DOE/ER-0046/5

JLS 11-17

Damage Analysis and Fundamental Studies

Quarterly Progress Report
Jan-Mar 1981

May 1981

U.S. Department of Energy
Assistant Secretary for Energy Technology
Office of Fusion Energy
Washington, DC 20545

NOTICE

Printed in the United States of America
Available from
National Technical Information Service
U.S. Department of Commerce
5285 Port Royal Road
Springfield, VA 22161

NTIS price codes
Printed copy: A l l
Microfiche copy: A01

DOE/ER-0046/5
UC-20,20c

Damage Analysis and Fundamental Studies

Quarterly Progress Report
Jan-Mar 1981

May 1981

U.S. Department of Energy
Assistant Secretary for Energy Technology
Office of Fusion Energy
Washington, DC 20545

FOREWORD

This report is the thirteenth in a series of Quarterly Technical Progress Reports on *Damage Analysis and Fundamental Studies* (DAFS), which is one element of the Fusion Reactor Materials Program, conducted in support of the Magnetic Fusion Energy Program of the U. S. Department of Energy (DOE). The first eight reports in this series were numbered DOE/ET-0065/1 through 8. Other elements of the Materials Program are:

- Alloy Development for Irradiation Performance (ADIP)
- Plasma-Materials Interaction (PMI)
- Special Purpose Materials (SPM).

The DAFS orogram element is a national effort composed of contributions from a number of National Laboratories and other government laboratories, universities, and industrial laboratories. It was organized by the Materials and Radiation Effects Branch, Office of Fusion Energy, DOE, and a Task Group on *Damage Analysis and Fundamental Studies,* which operates under the auspices of that Branch. The purpose of this series of reports is to provide a working technical record of that effort for the use of the program participants, the fusion energy program in general, and the DOE.

This report is organized along topical lines in parallel to a Program Plan of the same title so that activities and accomplishments may be followed readily, relative to that Program Plan. Thus, the work of a given laboratory may appear throughout the report. The Table of Contents is annotated for the convenience of the reader.

This report has been compiled and edited under the guidance of the Chairman of the Task Group on *Damage Analysis and Fundamental Studies,* D. G. Doran, Hanford Engineering Development Laboratory (HEDL). His efforts, those of the supporting staff of HEDL, and the many persons who made technical contributions are gratefully acknowledged. M. M. Cohen, Materials and Radiation Effects Branch, is the DOE counterpart to the Task Group Chairman and has responsibility for the DAFS Program within DOE.

Klaus M. Zwilsky, Chief
Materials and Radiation
Effects Branch
Office of Fusion Energy

CONTENTS

CONTENTS (Cont'd)

CONTENTS (Cont'd)

FIGURES

FIGURES (Cont'd)

Page

CHAPTER 4

1. Dual-Ion Irradiations of 316 Stainless Steel (W-ARD)

2. The Influence of Microchemical Evolution on the Swelling of AISI 316 and Its Dependence on Stress, Temperature and Heat Treatment (ANL-W, HEDL)

FIGURES (Cont'd)

FIGURES (Cont'd)

FIGURES (Cont'd)

TABLES

TABLES (Cont'd)

TABLES (Cont'd)

CHAPTER 1

IRRADIATION TEST FACILITIES

I. PROGRAM

Title: RTNS-II Operations (WZJ-16)
Principal Investigator: C. M. Logan
Affiliation: Lawrence Livermore National Laboratory

11. OBJECTIVE

The objectives of this work are operation of OFE's RTNS-II (a 14-MeV neutron source facility), machine development, and support of the experimental program that utilizes this facility. Experimenter services include dosimetry, handling, scheduling, coordination, and reporting.

RTNS-II is dedicated to materials research for the fusion power program. Its primary use is to aid in the development of models of high-energy neutron effects. Such models are needed in interpreting and projecting to the fusion environment engineering data obtained in other neutron spectra.

III. RELEVANT DAFS PROGRAM TASK/SUBTASK

TASK II.A.2,3,4.
TASK II.B.3,4.
TASK II.C.1,2,6,11,18.

IV. SUMMARY

Irradiations were performed for eight different experimenters from five different laboratories. These include five "piggyback" experiments. No major unscheduled outages occurred during this period.

V. ACCOMPLISHMENTS AND STATUS

A. Irradiations - M. W. Guinan, C. M. Logan, and D. W. Heikkinen (LLNL).

The HEDL-5 *two* zone furnace experiment for N. Panayotou (HEDL) was the dominant irradiation performed during this period. The present irradiation series for R. Jones (PNL) was completed. The following "piggyback" experiments were performed during this quarter:

1) Activation analysis of strontium nitrate, I. Bender (LANL).
2) Irradiation of electronic components, J. Srour (Northrop).
3) Radiation effects on the thermal/mechanical properties of TFTR insulators, G. Hurley (LANL).
4) Tritium-activated air detector instrumentation development, R. Jalbert (LANL)
5) A low fluence irradiation of Cu, Cu-A1 and Cu-Mn samples investigating cascade-cascade effects, H. Brager (HEDL).

B. RTNS-II Status - C. M. Logan and D. W. Heikkinen (LLNL).

The 50-cm target test assembly in the right target room is now virtually complete both mechanically and electrically. The Remotely Operated Vehicle Experiment Retriever (ROVER) has been completed and passed final tests. A new larger capacity horizontal turbo pump has been installed in the high voltage terminal. This replaces the original vertical turbo pump and is expected to be more reliable in addition to providing larger pumping capacity. The DFE radioactivity control review was completed satisfactorily. The panel's written report and recommendations are being prepared. No major deficiencies were found.

VII. FUTURE WORK

During the quarter, irradiations will be continued using the HEDL-5 furnace. In addition irradiations are planned for Barmore (LLNL), Jalbert (LANL) and Bradley (PNL). A further "piggyback" experiment for Srour (Northrop) will be done.

VIII. PUBLICATIONS

Effects of Fusion Neutrons on Thermocouples, C. M. Logan, D. W. Heikkinen, B. J. Schumacher, and P. A. House, UCRL 85452

I. PROGRAM

Title: Nuclear Data for Damage Studies and FMIT (WH025/EDK)
Principal Investigators: D.L.Johnson/F.M.Mann
Affiliation: Hanford Engineering Development Laboratory (HEDL)

II. OBJECTIVE

The objective of this work is to supply nuclear data needed for damage studies and in the design and operation of the Fusion Material Irradiation Testing (FMIT) facility.

III. RELEVANT DAFS PROGRAM PLAN TASK/SUBTASK

All tasks that are relevant to FMIT use, with emphasis upon:

SUBTASK	II.A.2.3	Flux spectra definition in FMIT
TASK	II.A.4	Gas Generation Rates
SUBTASK	II.A.5.1	Helium Accumulation Monitor Development
SUBTASK	II.B.1.2	Acquisition of Nuclear Data

IV. SUMMARY

Evaluation of deuteron-induced activation of gold and aluminum was done and residual doses were calculated.

The volume for regions of highest flux decreased by about a factor of 2 for 35-MeV operation as compared to 35-MeV operation.

V. ACCOMPLISHMENTS AND STATUS

A. Deuteron-Induced Activation of FMIT Materials -- D.L. Johnson (HEDL)

Activation of FMIT materials by deuterons will produce major contributions to residual gamma radiation doses following operation of the FMIT facility. Results of measurements of deuteron induced activation of various materials were described previously in the DAFS quarterly report for January-March 1980.[1] The following new results have been obtained.

In the FMIT facility small losses of the deuteron beam will occur all along the linear accelerator and the high energy beam transport system. Losses are currently estimated to be 3 μA per linear meter with 10 μA or more lost at certain hot spots. Large residual doses will result from direct deuteron activation of components exposed to beam losses and also from activation by neutrons produced by the same beam losses.

Gold is currently planned as the material to plate the surfaces of the linear accelerator drift tubes that are exposed to beam losses. Gold is known to have less deuteron induced activation and neutron production than when bare copper drift tubes are exposed to FMIT deuterons.

An updated analysis of measurements of the activation of gold by 35 MeV deuterons was completed. The residual gamma dose was then calculated using radionuclide production rates obtained from this experiment. Figure 1 shows the dose from a 20 year bombardment of thick gold by 35 MeV deuterons. The dose corresponds to a distance of 1 meter from a point source activated by a steady deuteron beam current of 1 μA. The dose is shown as a function of cooling time for the unshielded case and also for attenuation by various materials to illustrate their effectiveness for shielding.

The unshielded dose remains high for long cooling times. However, a small thickness of shielding such as lead or iron is very effective at reducing the dose, especially for cooling tirnes longer than

about 10 days. A large number of radionuclides contribute to the unshielded dose, however, many of these have low energy decay gamma rays that are easily attenuated. For example, for the dose through one inch of iron (similar to the tank wall of the linear accelerator) 5 radionuclides provide about 99% of the total. These radionuclides are respectively ^{196}Au(6.2 days), ^{198}Au(2.7 days), ^{195m}Hg(40 hours), ^{195}Hg(9.5 hours) and ^{194}Au(39.5 hours).

Aluminum is the material currently planned for the beam tubes between the accelerator and target and will also be activated by beam losses. Analysis of measurements of the activation of thick aluminum by 35-MeV deuterons was completed. Calculations of the residual gamma dose were then done using the measured radionuclide production rates. Figure 2 shows the dose as a function of cooling time for the same conditions described for activation of gold.

For cooling times less than about a week, the dose is dominated by ^{24}Na(15 hours). For longer cooling times, ^{22}Na(2.6 years) is the dominant contributor.

B. Flux-Volume Relations --
F.M.Mann (HEDL)

The spectra and flux-volume relations for 30 and 32 MeV incident deuterons were calculated. The volume for regions of highest flux decreases by about a factor of 2 for 32 MeV operation as compared to 35 MeV operation. The flux contours for 32 MeV, 100 mA operation are quite similar to 35 MeV, 80 mA operation.

VI. REFERENCES

1. D.L.Johnson and F.M.Mann, Damage Analysis and Fundamental Studies Quarterly Progress Report, January-March 1980, DOE/ER-0046/1 May 1980 pgs. 5-19.

2. D.L.Johnson and F.M.Mann, Damage Analysis and Fundamental Studies, Quarterly Progress Report, July-September 1980, DOE/ER-0046/3, Nov. 1980, pgs. 6-13.

VII. FUTURE WORK

Evaluation of activation and neutron sources associated with beam stops for accelerator tuning.

Resolve discrepancy between calculated and experimental results for the transmission of FMIT neutrons through thick iron (described in DAFS July-Sept. 1980 Quarterly Report(2).

Provide sources of radiation for use in beam diagnostics near the target.

VIII. PUBLICATIONS

C.Kalbach and F.M.Mann, "Phenomenology of Continuum Angular Distributions. I. Systematics and Parameterization," Phys. Rev. C23 (1981) 112.

C.Kalbach, "Phenomenology of Continuum Angular Distributions. II. Griffin Preequilibrium Model." Phys. Rev. C23 (1981) 124.

F.P.Brady, J.L.Romero, C.I.Zanelli, M.L.Johnson, G.A.Needham, J.L.Ullmann, P.P.Urone, and D.L.Johnson, "A Method for Measuring Neutron Total Non-Elastic Cross Sections." Nucl. Instr. & Methods 178 (1980) 427.

C.I.Zanelli, P.P.Urone, J.L.Romero, F.P.Brady, M.L.Johnson, G.A.Needham, J.L.Ullmann, and D.L.Johnson, "Total Non-Elastic Cross Sections of Neutrons on C, O, Ca, and Fe at 40.3 and 50.4 MeV," Phys. Rev. C23 (1981) 1015.

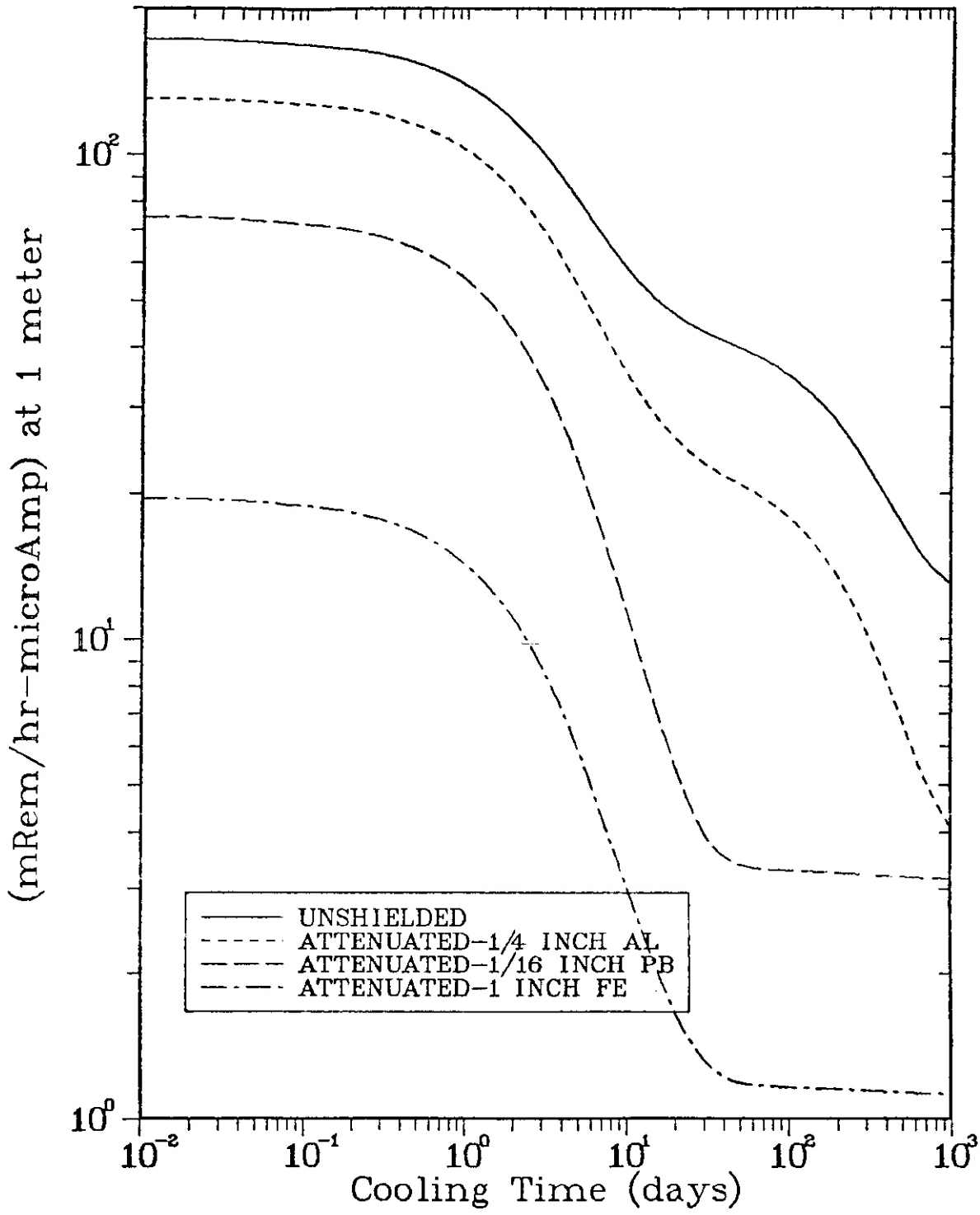

FIGURE 1. Dose After 20-Year Bombardment Time. (35 MeV deuterons on thick gold.)

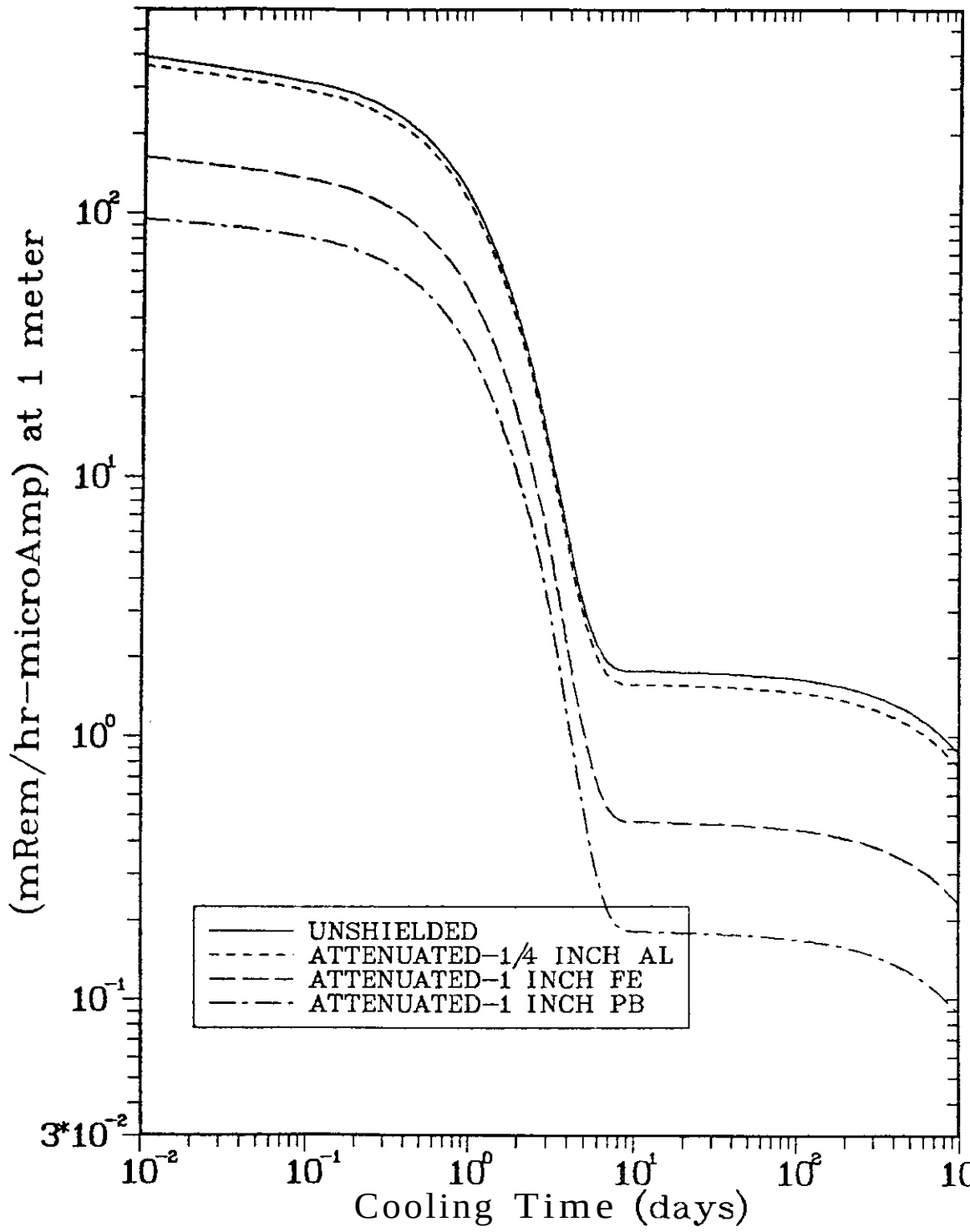

FIGURE 2. Dose After 20-Year Bombardment Time (35 MeV deuterons on thick aluminum.)

CHAPTER 2

DOSIMETRY AND DAMAGE PARAMETERS

I. PROGRAM

Title: Dosimetry and Damage Analysis
Principal Investigator: L. R. Greenwood
Affiliation: Argonne National Laboratory

II. OBJECTIVE

To establish the best practicable dosimetry for mixed-spectrum reactors and to provide dosimetry and damage analysis for OPE experiments.

III. RELEVANT DAFS PROGRAM TASK/SUBTASK

TASK II.A.1 Fission Reactor Dosimetry.

IV. SUMMARY

Dosimetry has been completed for the ORR-MFE2 irradiation. Reaction rates appear to be consistent with our previous spectral measurement at low power. Dosimeters have also been counted from the EBRII-X287 irradiation; analysis is now in progress. The status of all other fission reactor dosimetry is summarized in Table 1.

V. ACCOMPLISHMENTS AND STATUS

A. Dosimetry Results for the ORR-MFE2 Experiment
L. R. Greenwood (ANL)

Dosimeters have been counted from the ORR-MFE2 experiment which was irradiated from September 1, 1978 to March 24, 1980 in position E7 of the Oak Ridge Research Reactor. The sample was out of the reactor for 154 days; hence, the total time in core was 416 days. The average power level was 19.24 MW (26.4 MW in core) and the accumulated exposure was 10,972 MWD. Sixteen small dosimetry capsules (Co-Al, Fe, Ni, and Ti wires) were included with the experimental assemblies, one in each assembly on levels 1-4, labeled E-V. Two 30-cm long dosimetry tubes were welded to the outside of the assembly on the east side. One tube contained the above mentioned wires. The other contained helium accumulation

TABLE 1

STATUS OF REACTOR EXPERIMENTS

Facility/Experiment		Status and Comments
ORR	- MFE1	Analysis complete
	- MFE2	Analysis complete (3/81)
	- MFE3	Planning in progress
	- MFE4A,B	Samples expected 4/81
	- TBC07	Analysis complete
	- TRIO	Planning in progress
HFIR	- CTR 30,31,32	Irradiation in progress
	- T1,T2	Irradiation in progress
	- RB1	Planning in progress
Omega West	- Spectral Run	Analysis complete
	- HEDL/LLL1	Samples expected 4/81
	- ESG-OWR1	Planned for 6/81
EBR II	- X287	Samples counted by 4/81

monitors and radiometric wires. All radiometric samples have been gamma counted as well as selected helium samples. The latter have been sent to Rockwell International (D. Kneff and H. Farrar IV) for helium analysis.

Six reactions were analyzed from the dosimetry wires, namely, $^{59}Co(n,\gamma)$, $^{58}Fe(n,\gamma)$, $^{54}Fe(n,p)$, $^{46}Ti(n,p)$, $^{58}Ni(n,p)$, and $^{60}Ni(n,p)$. However, as was found with MFE1, the two nickel reactions have very large burnup corrections since ^{58}Co is converted to ^{60}Co in the high thermal flux,,. Hence, the nickel reactions are considered highly unreliable and have not been used. Additional measurements were obtained from the helium samples, namely, $^{63}Cu(n,\alpha)$ and $^{93}Nb(n,\gamma)$ at selected locations.

Table 2 lists the mean measured reaction rates for each level. Horizontal gradients on each level appear to be less than 10% in all cases and are usually less than the ±2% statistical variations in the data.

Fluence values can be derived from the reaction rates assuming that the spectrum is known. The spectrum was measured previously in position E7 at low power during January 1979.(1) A comparison of the present reaction rates with those measured previously should roughly scale with the difference in reactor power (19.24 MW/0.965 MW = 19.94). The measured ratio is 17.3 at the peak flux position (level 4), and vertical gradients appear to be quite close to those measured previously. This difference is probably due to differences in fuel loading.

The five reaction rates at each level in Table 2 were thus used with the STAYSL computer code to adjust the spectrum measured at low power with *28* reactions, cadmium covers, and fission foils. The final fluence values are listed in Table 3. The spectral analysis showed no evidence for any spectral shift between high power (30 MW) and low power (1 MW). In fact, all flux groups and reaction rates were adjusted by less than 10%.

Vertical flux gradient data is now being analyzed. Damage calculations will also be performed and detailed results will be circulated to the experimenters.

TABLE 2

MEAN REACTION RATES FOR ORR-MFE2

Position E7; average power = 19.24 MW (26.4 MW during reactor operation).

Values are mean of four samples on each level; accuracy ±5%.

		$\sigma\phi$[b] (atom/atom-s)				
Level	Height, cm[a]	$^{59}Co(n,\gamma)$ (x 10^{-9})	$^{59}Fe(n,\gamma)$ (x 10^{-11})	$^{54}Fe(n,p)$ (x 10^{-12})	$^{46}Ti(n,p)$ (x 10^{-13})	$^{63}Cu(n,\alpha)$[c] (x 10^{-14})
1	11.4	2.63	7.00	5.00	6.46	3.17
2	5.0	3.13	8.67	5.59	7.53	3.64
3	2.4	3.31	9.31	5.93	8.00	3.83
4	-9.1	3.82	10.89	6.38	8.80	4.06

[a] Height above vertical midplane. Capsules were located at the bottom of levels 1, 2, and 4 and at the top of level 3.

[b] Burnup corrections included; self-shielding negligible.

[c] Data extrapolated from helium tube position; accuracy ±7%.

TABLE 3

FLUENCES FOR ORR-MFE2
(STAYSL adjusted values based on reaction rates
in Table 2 and low power spectral measurement)

Level	Height, cm[a]	Fluence ($\times 10^{21}$ n/cm^2) Thermal[b] (±12%)	>.11 MeV (±12%)	>1 MeV (±15%)	Total (+9%)
1	11.4	3.27	5.13	2.44	12.59
2	5.0	3.99	5.92	2.78	14.75
3	2.4	4.26	6.28	2.95	15.64
4	-9.1	4.96	6.87	3.21	17.46

[a] Height above vertical midplane.

[b] Flux less than 0.55 eV.

VI. REFERENCES

1. L. R. Greenwood and R. R. Heinrich, DOE/ET-0065/6, p. 13, June 1979.

VII. FUTURE WORK

Radiometric samples are expected in April from ORR-MFE4A (M. Grossbeck) and from the first HEDL/LLL experiment in the Omega West Reactor (N. Panayotou). Most of the samples from the EBR II - X287 experiment have now been gamma counted; analysis is now in progress.

Fluence and damage parameter gradients will be generated for the ORR-MFE2 experiment. Results will also be combined with helium analyses from Rockwell International. More specific damage analyses will be furnished to experimenters on request.

VIII. PUBLICATIONS

None.

I. PROGRAM

Title: Helium Generation in Fusion Reactor Materials
Principal Investigators: D. W. Kneff and Harry Farrar IV
Affiliation: Rockwell International, Energy Systems Group

II OBJECTIVE

The objectives of this program are to measure helium generation rates of materials for Magnetic Fusion Reactor applications in the various neutron environments used for fusion reactor materials testing, *to* characterize these neutron test environments, and to develop helium accumulation neutron dosimeters for neutron fluence and energy spectrum dosimetry in these test environments.

III. RELEVANT DAFS PROGRAM PLAN TASK/SUBTASK

SUBTASK II.A.2.2	Flux-Spectral Definition in RTNS-II
SUBTASK II.A.4.2	T(d,n) Helium Gas Production Data
SUBTASK **II.A.4.3**	Be(d,n) Helium Gas Production Data

IV. SUMMARY

Helium analyses have been completed for all samples of Mo, Zr, and the seven separated isotopes of Mo irradiated in the RTNS-I, RTNS-II, and Be(d,n) neutron spectra, and for all V samples irradiated in the RTNS-I and Be(d,n) spectra. The RTNS-I data were then used to determine the total helium generation cross sections for these materials for 14.8-MeV neutrons. Helium analyses have been completed for the Cu, Ni, Fe, and Au helium accumulation dosimetry materials irradiated in the RTNS-II neutron characterization experiment. These results will be used in mapping the neutron fluence distribution for this irradiation and will provide additional cross section determinations for these materials.

V. ACCOMPLISHMENTS AND STATUS

Helium Generation Cross Sections for Fast Neutrons -- B. M. Oliver, D. W. Kneff, M. M. Nakata, and Harry Farrar IV (Rockwell International, Energy Systems Group)

Helium analyses have now been completed for all samples of zirconium, molybdenum, and the seven separated isotopes of molybdenum irradiated in the T(d,n) Rotating Target Neutron Sources-I and -II (RTNS-I, II), and in an ~0-32 MeV Be(d,n) neutron field produced with 30-MeV deuterons. Analyses have also been completed for all vanadium samples irradiated in the RTNS-I and Be(d,n) neutron spectra. These irradiations, performed at Lawrence Liveriiiore National Laboratory (LLNL) and the Crocker Nuclear Laboratory of the University of California at Davis, respectively, have been described in detail in previous reports and publications.(1-3) In general, the characterization of the neutron spectra and the analysis of helium in pure elements are sponsored by the Office of Fusion Energy. The cross section measurements for the separated isotopes are sponsored by the Office of Gasic Energy Sciences of the U.S. Department of Energy.

The irradiated materials were etched (to remove helium enhancement and depletion effects due to alpha recoils), segmented, and weighed before analysis. The analyses were performed using small resistance-heated graphite crucibles to release the helium. The use of these crucibles was based on the results of helium analysis tests described in the previous progress report for low-level helium measurements.(4) A total of 107 analyses were made for pure element and separated isotope molybdenum samples, 23 analyses were made for zirconium, and 15 were made for vanadium.

Cross section determinations have been made for the RTNS-I-irradiated materials, and the results are given in Table 1. Cross sections for the RTNS-II- and Be(d,n)-irradiated materials will be reported later when the

Material	Cross Section (mb)	Material	Cross Section (mb)
V	18.7 ± 1.4	^{92}Mo	31 ± 2
		^{94}Mo	22 ± 2
Zr	10.2 ± 0.8	^{95}Mo	17 ± 2
		^{96}Mo	11 ± 1
Mo	15 ± 2	^{97}Mo	10 ± 1
		^{98}Mo[a]	23 ± 2
		^{100}Mo	3.8 ± 0.5

[a]See text

fluence mapping and dosimetry correlations for these experiments have been completed. The RTNS-I cross sections were obtained by combining the helium generation measurements with the neutron fluence map[1] constructed for the irradiation volume. This map was based on a combination of helium accumulation and radiometric dosimetry included as a part of the experiment. The radiometric dosimetry data were provided by Argonne National Laboratory (ANL) and LLNL. The average neutron energy was 14.8 ± 0.1 MeV, and the spectrum distribution had a full-width-at-half-maximum of ~0.6 MeV.

The results presented in Table 1 are preliminary in that the data from the additional samples irradiated in RTNS-II have not yet been included. The results from the multiple sample analyses of the RTNS-I materials are in excellent agreement, having an average helium analysis reproducibility of 1%. The final results in Table 1 include the additional uncertainties associated with the neutron fluence. The results for the pure elements are in excellent agreement with those obtained from an earlier RTNS-I experiment[5] (viz. 18 ± 2, 10 ± 2, and 15 ± 2 mb for V, Zr, and Mo, respectively).

We believe that there is some basis for questioning the value obtained for ^{98}Mo (a value also obtained in preliminary RTNS-II results). The ^{98}Mo isotopic material had a different appearance and released significantly more non-helium gases during the analysis procedure than the other separated molybdenum isotopes. Its unexpectedly high cross section value could also explain the difference between the measured natural molybdenum cross section (15 ± 2 mb) and that derived from a weighted average of the measured isotopic cross sections (18 ± 1 mb). Chemical analyses conducted so far on the ^{98}Mo isotopic material indicate insufficient chemical impurity concentrations to generate significant helium. Other isotopes present in each separated isotope material were corrected for by solving a matrix of equations using the ORNL-supplied isotopic abundances.

Helium analyses have also been completed for the Cu, Ni, Fe, and Au pure element helium accumulation dosimetry rings irradiated in the RTNS-II neutron characterization experiment.[3] These analyses represent an additional 70 RTNS-II helium generation measurements performed to date. These results will be combined with the ANL and LLNL radiometric dosimetry data to construct the first comprehensive map of the neutron fluence distribution for this facility. The results will also provide additional cross section determinations for these materials.

VI. REFERENCES

1. O. W. Kneff, B. M. Oliver, M. M. Nakata, and H. Farrar IV, "Helium Generation Cross Sections for Fast Neutrons," in Proc. Symp. on Neutron Cross-sections from 10 to 50 MeV, M. R. Bhat and S. Pearlstein, eds., BNL-NCS-51245, Brookhaven National Laboratory, N.Y., p. 289 (1980).

2. D. W. Kneff, H. Farrar IV, L. R. Greenwood, and M. W. Guinan, "Characterization of the Be(d,n) Neutron Field by Passive Dosimetry Techniques," in Proc. Symp. on Neutron Cross-sections from 10 to 50 MeV, M. R. Bhat and S. Pearlstein, eds., BNL-NCS-51245, Brookhaven National Laboratory, N.Y., p. 113 (1980).

3. D. W. Kneff, B. M. Oliver, M. M. Nakata, and H. Farrar IV, "Characterization of the RTNS-II Neutron Field," in Damage Analysis and Fundamental Studies, Quarterly Progress Report July-September 1980, DOE/ER-0046/3, U.S. Department of Energy (1980).

4. D. W. Kneff, B. M. Oliver, M. M. Nakata, and H. Farrar IV, "Helium Production by Fast Neutrons," in Damage Analysis and Fundamental Studies, Quarterly Progress Report October-December 1980, DOE/ER-0046/4, Vol. 1, U.S. Department of Energy (1981).

5. H. Farrar IV and D. W. Kneff, "Helium Generation in Twelve Pure Elements by 14.8-MeV Neutrons," Trans. Am. Nucl. Soc. 28, 197 (1978).

VII. FUTURE WORK

Analyses of additional pure elements and their separated isotopes irradiated in the RTNS-I, RTNS-II, and Be(d,n) neutron spectra will continue during the next quarter, with emphasis on Nb, Co, and the separated isotopes of Fe, Ni, and Cu. Neutron fluence mapping of the high-flux region of the RTNS-II neutron environment will be initiated.

VIII. PUBLICATIONS

The following two abstracts were submitted during the quarter for the presentation of papers at upcoming conferences:

"Experimental Helium Generation Cross Sections for Fast Neutrons," by D. W. Kneff, B. M. Oliver, M. M. Nakata, and Harry Farrar IV, submitted to the Second Topical Meeting on Fusion Reactor Materials, Seattle, August 1981.

"A Review of Helium Accumulation Neutron Dosimetry for Fusion Neutron Test Environments," by D. W. Kneff, Harry Farrar IV (Rockwell International), and L. R. Greenwood (ANL), submitted to the Fourth ASTM-EURATOM Symposium on Reactor Dosimetry, Washington, D.C., March 1982.

I. PROGRAM

Title: Dosimetry and Damage Analysis
Principal Investigator: L. R. Greenwood
Affiliation: Argonne National Laboratory

II. OBJECTIVE

To establish standardized dosimetry procedures in order to reduce uncertainties in damage analysis and correlation procedures.

III. RELEVANT DAFS PROGRAM TASK/SUBTASK

TASK II.A.6 Dosimetry Standardization.

IV. SUMMARY

Dosimetry data have been provided to the international REAL-80 Project (IAEA) to compare spectral unfolding and damage analysis data and techniques. Data from our spectral analysis of ORR have been chosen as one test case. Cross section intercomparisons have revealed some minor problems with our multigroup computer code RESCAL, which have now been corrected.

V. ACCOMPLISHMENTS AND STATUS

A. International Comparison of Dosimetry Cross Sections (REAL-80)
L. R. Greenwood (ANL)

Argonne is participating in the REAL-80 Project sponsored by the International Atomic Energy Agency (Vienna) to compare dosimetry data and techniques. Our spectral measurement in ORR has been chosen as one test case due to the large number of reaction rates (28) and our development of the STAYSL computer code. Calculations have also been performed for the YAYOI reactor (M. Nakawaza, Japan). Data are being assembled for other reactors, and the first results of the exercise will be reported at the Fourth ASTM-EURATOM Symposium on Reactor Dosimetry in Washington, DC in March 1982. Such international comparisons have proven quite useful

in the past in uncovering differences in nuclear data and spectral unfolding computer codes. This exercise will also include nuclear cross section covariances and displacement damage rates.

As part of this comparison, our dosimetry cross sections were compared to those provided by W. L. Zijp (ECN, Petten).[1] Reaction rates generally agreed within a percent; however, unexplained differences in the data were clearly evident in the resolved resonance region. Most differences were traced to the fact that our multigroup processing code (RESCAL) used a fixed energy grid and, thus, can miss some narrow resonances at higher energies. Although these differences are relatively minor from the dosimetry point of view, it was felt that they should be eliminated since they complicate the whole comparison.

The RESCAL code[2] was thus improved to include an integral approximation of Breit-Wigner resonances when they are narrower than our subintervals (13,000 energy points). Since our subintervals are small enough that the neutron wave number, penetrability, and phase shifts are nearly constant over the interval, then the Breit-Wigner expression can be integrated in closed form as follows:

$$\bar{\sigma} = \int \sigma(E)\,dE / \int dE$$

$$= \frac{\pi\, g}{DE\, k^2}\, \Gamma_r\, [\arctan D_1 - \arctan D_2]$$

where k is the neutron wave number, Γ is the total resonance width, Γ_n is the neutron width, and Γ_r is the reaction width. D_1 and D_2 are equal to the difference between the end points of the interval and the resonance energy divided by one-half the total width. It can be shown that this approximation is accurate to within 0.1% for our broadest energy subintervals.

It was also found that the precision of our calculations could be improved by using integral expressions for the interpolation of the ENDF cross section files as listed in the following table.

ENDF Form	Integral Group Average
E vs. σ	$1/2\ (\sigma_1 + \sigma_2)$
ln E vs. σ	$\frac{(E_2\sigma_2 - E_1\sigma_1)}{(E_2 - E1)} - \frac{(\sigma_2 - \sigma_1)}{\ln E_2 - \ln E_1}$
E vs. ln σ	$\frac{\sigma_2 - \sigma_1}{\ln \sigma_2 - \ln \sigma_1}$
ln E vs. ln σ	$\frac{(E_2\sigma_2 - E_1\sigma_1)}{(E_2 - E1)} \frac{\ln (E_2/E_1)}{\ln (\sigma_2 E_2/\sigma_1 E_1)}$

where ln means the natural log to the base *e*. Care must be taken with all the above formulasinvolving the arctan and ln functions to ensure adequate precision.

All of our dosimetry multigroup cross sections have been re-evaluated with the above improvements in our RESCAL computer code. Detailed comparisons with 620 group files provided by W. L. Zijp show that most groups now agree within 1%. However, there are still a few unexplained differences which are being investigated. At the moment, no other data file is available for comparison. A file was released by B. Magurno (BNL);[3] however, errors have been detected and the file is now being redone. 'D. E. Cullen is presently preparing a file for comparison.[4]

In order to test our data in a dosimetry application, our spectral-averaged cross sections are compared to those calculated using Zijp's data in Table 1. As can be seen, except where different cross section data have been used, all integrals agree within 0.14% except for Np. Sharp differences were found in the unresolved resonance region for Np which are not presently understood.

TABLE 1

COMPARISON OF ORR SPECTRA - AVERAGED CROSS SECTIONS (BARNS)

(ANL data revised March 1981; 98 energy groups.)

Reaction	ANL	ZIJP[a]	DIFF (%) (ANL-ZIJP)
NA23G	1.2052-1	1.2048-1	0.03
MG24P	3.9024-4	3.8674-4	0.91[b]
AL27P	1.0423-3	1.0423-3	0
AL27A	1.7606-4	1.7605-4	0
SC45G	6.1173	6.1253	-0.13
TI46P	2.7293-3	2.7295-3	0
TI47P	5.6976-3	5.6954-3	0.04
TI48P	7.0949-5	7.0927-5	0.03
MN55G	3.1298	3.1662	-1.16[b]
FE54P	2.0075-2	2.0075-2	0
FE54A	1.9112-4	2.3336-4	22.1[b]
FE56P	2.5827-4	2.5828-4	0
FE58G	2.7298-1	2.7337-1	-0.14
CO59G	9.8302	9.8368	-0.07
CO59A	3.7286-5	3.7438-5	-0.41[b]
NI58P	2.6202-2	2.6201-2	0
NI60P	6.4037-4	6.4052-4	-0.02
IN115N	4.9146-2	4.9148-2	0
W186G	3.0562 +1	3.0558+1	0.01
AU1972	7.8009-4	7.7733-4	0.36[b]
AU197G	6.3395+1	6.3432+1	-0.06
U235F	1.3034+2	1.3034+2	0
U238F	8.2305-2	8.2293-2	0.02
U238G	1.0358+1	1.0368+1	-0.09
NP237F	4.2895-1	4.2782-1	0.26
NP237G	5.8902+1	5.8950+1	-0.08

[a] Data reported by D. E. Cullen (REAL 80).

[b] Different cross section data used.

VI. REFERENCES

1. W. L. Zijp (ECN, Petten); data transmitted by D. E. Cullen (IAEA) March 1981.

2. RESCAL computer code written by L. R. Greenwood (ANL), unpublished.

3. B. A. Magurno (BNL), private communication (March 1981).

4. D. E. Cullen, Program SIGMA1, UCRL-50400, Vol. 17, Part B, Rev. 2 (1979).

VII. FUTURE WORK

Although most data files agree closely with other available references, especially for dosimetry applications, an effort will be made to resolve the few remaining differences between our code and those of W. L. Zijp, B. A. Magurno, and D. E. Cullen.[4]

Additional calculations will be performed for the REAL-80 Project including reference spectra for CFRMF, BIG10, SIGMA-SIGMA, EBR II, and other facilities.

VIII. PUBLICATIONS

None.

I. PROGRAM

Title: Dosimetry and Damage Analysis
Principal Investigator: L. R. Greenwood
Affiliation: Argonne National Laboratory

II. OBJECTIVE

To describe the production of displaced atoms in materials and environments of interest in MFR development. Specifically, to include (n,γ) and beta-decay effects and revise all data according to ENDF/B-V.

III. RELEVANT DAFS PROGRAM TASK/SUBTASK

TASK II.B.1 Calculation of Defect Production Cross Sections.

IV. SUMMARY

All of our displacement cross sections are now being revised according to ENDF/B-V.

The theory is being developed to include (n,γ) and beta-decay displacements. Recoil atom energy distributions are being computed considering the effects of incident neutron energy, γ-γ angular correlations, and E-neutrino and β-γ angular correlations. Examples are shown for Al.

V. ACCOMPLISHMENTS AND STATUS

A. Description of Neutron Capture and Beta-Decay Processes Leading to Displacement Production

R. K. Smither and L. R. Greenwood (ANL)

Previous attempts[1,2] to include the (n,γ) reaction in the calculation of nuclear displacements have generally made a number of simplifying approximations. All gammas following capture are usually considered independently, regardless of cascades, γ-γ correlations, or lifetime considerations. The effect of the incident momentum of the incoming neutron has also usually been neglected. It is also interesting to note that many (n,γ) reactions (as well as other reactions) produce short-lived products

which beta-decay. If the end-point energy is high, then this subsequent beta-decay (and possibly further gamma decays) can significantly increase the number of displacements. We have developed a description of both processes for inclusion in our displacement cross section data files. Recoil atom energy distributions will also be included. Our treatment includes the effects of the momentum of the captured neutron, the angular correlation between the reaction momentum and the γ-ray recoil momentum, the γ-γ angular correlations, the lifetimes of intermediate states, and beta-neutrino angular correlations. Experimental measurements of the primary gamma spectrum, secondary branching ratios, sequential gamma-emission sequences, and measured lifetimes of intermediate states are used when possible. When experimental information is not available, a multistepped cascade model is used assuming level spacings and lifetimes for the intermediate states that are based on averages measured in similar nuclei. A second calculation is made for the 8-decay events that includes the angular correlation of the neutrino with the emitted 8-particle and also with the subsequently emitted γ-ray or gamma rays.

1. (n,γ) Recoils

Figure 1 illustrates the neutron capture process followed by multiple gamma emission where n represents the incoming neutron, A the capturing nucleus, A+1 the product nucleus, θ_1 the angle between the neutron induced recoil and the direction of the first gamma ray, θ_2 the angle between the neutron induced recoil and the second γ-ray, ϕ_1 the angle of the recoiling product nucleus A+1 after γ-emission measured from the initial neutron induced recoil, ϕ_2 the same following the emission of the second γ-ray, etc., a is the distance to the nearest neighbor nuclei, d_1 is the distance traveled by the recoiling nucleus before the first gamma ray is emitted, and d_2 the distance traveled between the emission of the first and second γ-rays, etc. The basic equation used to calculate the primary recoil energy is given by Equation (1):

$$E_{recoil}(n+\gamma) = \frac{1}{2(A+1)}\left[\frac{E_\gamma^2}{m_o c^2} + 2E_n - 2E_\gamma\sqrt{\frac{2E_n}{m_o c^2}}\cos\theta\right] \qquad (1)$$

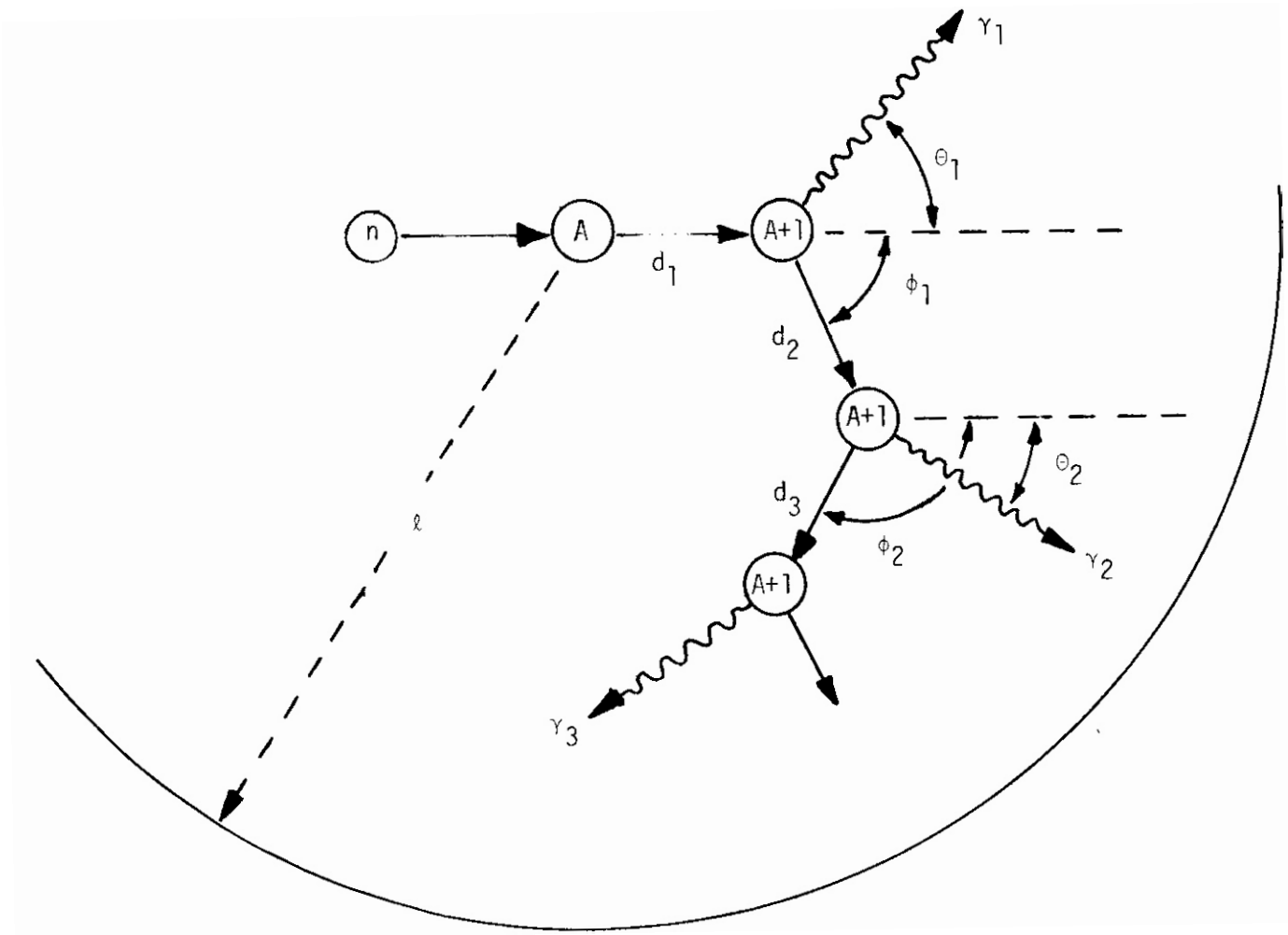

Figure 1. Schematic of the (n,γ) reaction with the emission of three gamma rays.

where E_γ is the y-ray energy, E_n the neutron energy, m_0 is one atomic mass unit, A the atomic weight of the initial atoms, and θ the angle between the direction of the incoming neutron and the direction of the y-ray. After each recoil event the distance traveled is calculated and this is added to the distance that will be traveled before the next y-ray is emitted. If the total distance traveled is less than the distance to the nearest neighbor atom, the process is continued. For the case of s-wave capture, the emission of the first gamma is isotropic. The appropriate weighting factor in this case is $2\pi\sin\theta d\theta$ and the average recoil energy will be given by Equation (2):

$$\overline{E\ \text{recoil}\ (n+\gamma)} = \frac{1}{2(A+1)}\left[\frac{E_\gamma^2}{m_0c^2} + 2E_n\right] \qquad (2)$$

For the case of p-wave capture, there will be an angular distribution of the emitted y-ray relative to the neutron momentum and a more general weighting factor $(1+\alpha_1\cos\theta)\ 2\pi\sin\theta d\theta$ must be used.

The recoil energy following the emission of the second y-ray is given by Equation (3):

$$E\ \text{recoil}\ (n+\gamma+\gamma) = \frac{1}{2(A+1)}\left[\frac{E_{\gamma 1}^2}{m_0c^2} + 2E_n - 2E_n\sqrt{\frac{2E_n}{m_0c^2}}\cos\theta + \frac{E_{\gamma 2}^2}{m_0c^2}\right.$$

$$\left. - 2\left(\frac{E_{\gamma 2}^2}{m_0c^2}\right)^{1/2}\left(\frac{E_{\gamma 1}^2}{m_0c^2} + 2E_n - 2E_{\gamma 1}\sqrt{\frac{2E_n}{m_0c^2}}\cos\theta\right)^{1/2}\cos(\theta_2 - \phi_1)\right] \qquad (3)$$

The angular distribution between the first and second y-ray must be taken into account at this point so an additional $(1+\alpha_2\cos\theta)$ term will appear in the weighting factor. The primary recoil spectrum resulting from the (n,γ) reaction will be a weighted average of the many y-ray cascades that follow neutron capture. Figure 2 compares the recoil energy spectrum produced by two y-rays in cascade when the half life of the intermediate

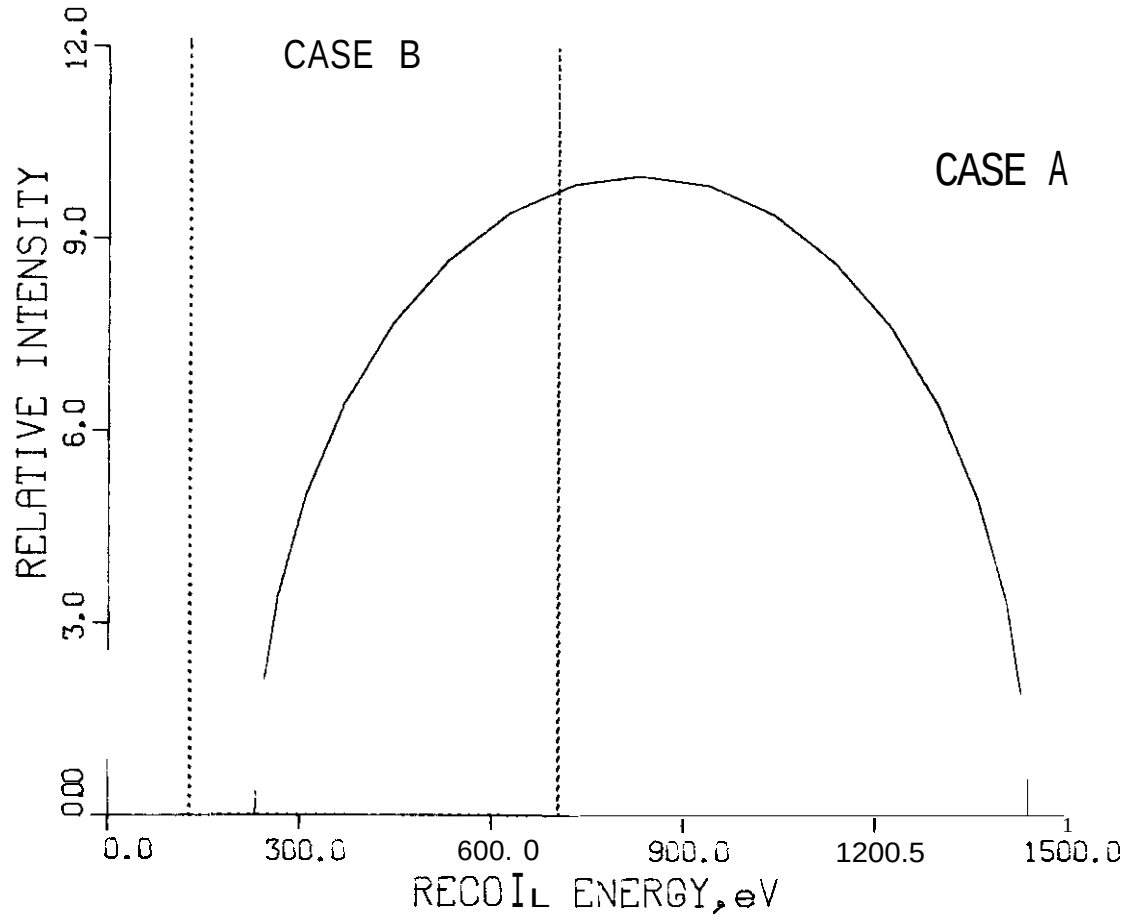

Figure 2. Recoil energy spectrum for a two step y-ray cascade where the primary γ-energy is 70% of the neutron binding energy (in ^{28}Al) and the energy of the second y-ray is 30% of the neutron binding energy. Case A is the spectrum produced when the half life of the intermediate state is short compared to the time between collisions, and Case B is the spectrum for the case when the lifetime of the intermediate state is long compared to the average collision time.

state is short compared to the time between collisions (case A) with the recoil energy spectrum produced when the half life of the intermediate state is long compared with the collision time and the recoiling nucleus comes to rest before the second y-ray is emitted (case B). The first spectra (case A) is a broad distribution whose upper limit is the same as the recoil energy for a gamma-ray whose energy is equal to the sum of the energies of the two cascading γ-rays. The recoil energy spectrum for the long-lived intermediate state cascade, case B, is just two sharp lines. There are twice as many events in case B as there are in case A, but average energy and peak energy of the spectrum are much higher in case A. The two effects tend to cancel each other, but the net effect is that more displacement damage will result in case B than in case A. It should be noted that the primary γ-ray spectrum following p-wave capture is different than that produced by s-wave capture, because the parity and the range of possible spins for the capture states are different.

2. 6-Decay Recoil

Quite frequently the (n,γ) reaction is followed by the β-decay of the product nucleus. If the end point energy of the 6-decay is a few MeV, there may be (depending on the mass of the product nucleus) enough recoil momentum from the 6-decay to displace the product atom. For light nuclei like ^{28}Al a displacement will occur for virtually every β-decay. The recoil energy of .the product nucleus following 6-decay is a function of both the E-energy and the neutrino energy, and it is necessary to take into account the appropriate angular correlation between the 6 and the neutrino in the calculation. This angular correlation is different for the different classes of 6-decay. The recoil energy is given by Equation (4):

$$E_{recoil}(\beta,\nu) = \frac{1}{2(A+1)m_o c^2}\left\{E(E+2m_e c^2) + (E_o - E)^2 + 2[E(E+2m_e c^2)]^{1/2}(E_o - E)\cos\theta\right\} \quad (4)$$

where E is the electron energy, E_0 is the end point energy, $(E_0 - E)$ is the neutrino energy, θ is the angle between the neutrino and the electron, and m_e is the mass of the electron and m_0 is the mass of one atomic mass unit. It is convenient to parameterize this expression in terms of the end point energy. Equation (5) is Equation (4) with the normalized energy parameter "a":

$$E_{recoil}(\beta,\nu) = \frac{E_0^2}{2(A+1)m_0c^2}\left\{a(a+b) + (1-a)2 + 2[a(a+b)]^{1/2}(1-a)\cos\theta\right\} \quad (5)$$

where $a = E/E_0$ and $b = m_ec^2/E_0$. The appropriate weighting factor for the recoil distribution in terms of this same normalized E-energy is given in Equation (6):

$$E_{recoil\ factor} = (a+b)^2(1-a)^2(1+c\beta\cos\theta)(2\pi\sin\theta)F_S(\beta) \quad (6)$$

where $\beta = Ve/c$, Ve = electron velocity, and $F_S(\beta)$ is, a slowly varying function of 6 and is approximately $\simeq 1$ in most cases. The coefficient c depends upon the character of the 8-decay process, allowed (Gamow-Teller), scaler, polar vector (Fermi), etc. Figure 3 shows the recoil spectrum for the E-decay of ^{28}Al [E_0 = 2.871 MeV, axial vector (Gamow-Teller)]. In this case "c" the coefficient in the angular correlation between the neutrino and the electron is equal to -1/3. The 8-decay of ^{28}Al to ^{28}Si is followed by the emission of a 1.8 MeV y-ray. The lifetime of the intermediate state is 0.5 x 10^{-12} sec; which is long enough so that most of the 6-related recoils have been stopped before the y-ray is emitted. In this case, the recoil caused by the y-ray is treated as a separate event.

B. Revision of Displacement Cross Sections with ENDF/B-V

L. R. Greenwood (ANL)

All of our cross section files are now being revised according to ENDF/B-V using the DISCS computer code.[3] Preliminary indications are

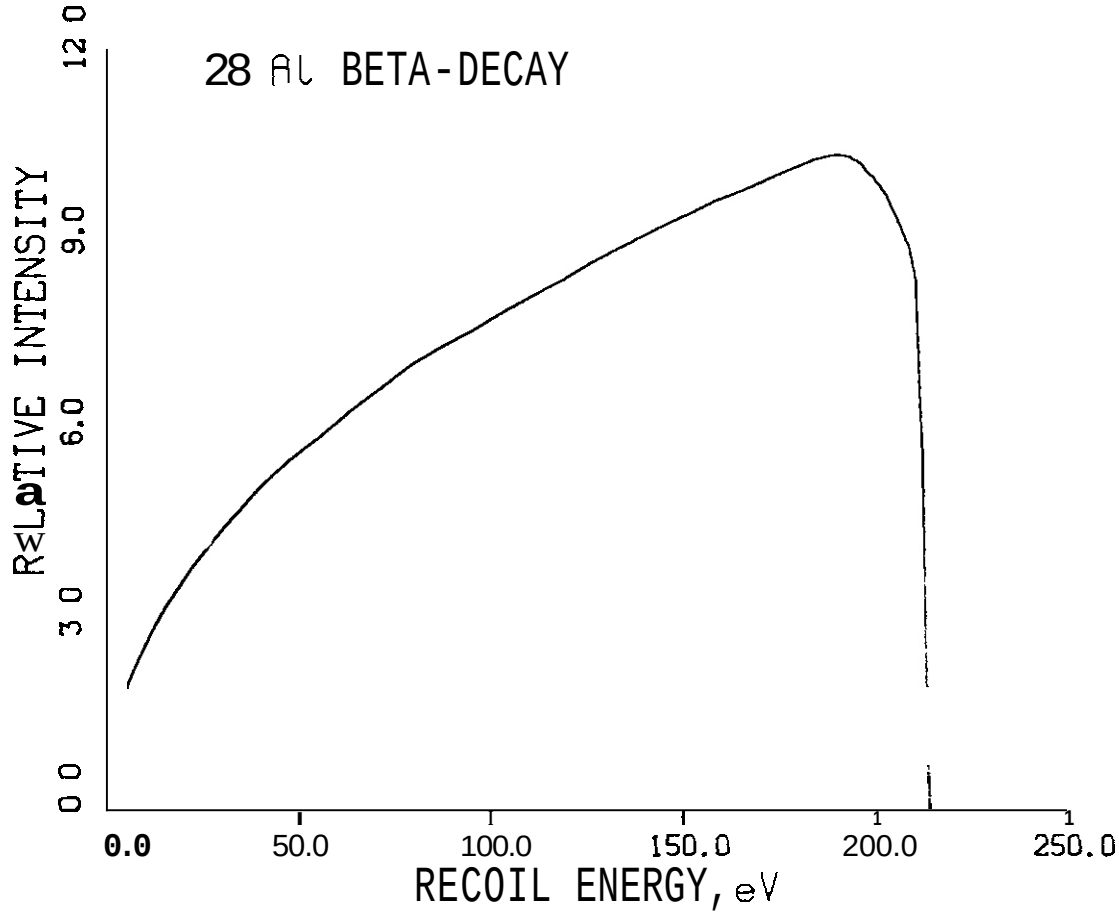

Figure 3. Recoil energy spectrum from ^{28}Al E-decay to ^{28}Si. The recoil spectrum of the gamma-ray transition in ^{28}Si is not included in this spectrum.

that most changes are relatively small and that spectral-averaged cross sections will generally agree within 10% of those computed using ENDF/B-IV. Several new elements have also been included; namely, Na, K, Ca, and Ta, bringing our list to 25. Following these revisions, we plan to extend as many files as possible to 50 MeV for applications at Be or Li (d,n) accelerators or spallation neutron sources.

VI. REFERENCES

1. D. G. Doran and N. J. Graves, HEDL-TME 76-60 (1976).
2. T. A. Gabriel (ORNL), private communication (1980).
3. G. R. Odette and D. R. Doiran, Nucl. Technol. 29, 346 (1976).

VII. FUTURE WORK

Displacement damage cross sections and recoil atom distributions will be computed for the 25 elements currently contained in our damage parameter data files. All cross sections will be based on ENDF/B-V, and the (n,γ) and E-decay effects will be included. All files will then be replaced at the Magnetic Fusion Energy Computer Center at Lawrence Livermore Laboratory.

VIII. PUBLICATIONS

None.

I. PROGRAM

Title: Radiation Damage Analysis and Computer Simulation

Principal Investigator: Don M. Parkin
Affiliation: Los Alamos National Laboratory of the University of California

II OBJECTIVE

The objective of this work is to develop displacement functions for polyatomic materials.

III. RELEVANT DAFS PROGRAM PLAN TASK/SUBTASK

SUBTASK II.B.2.3 Cascade Production Methodology
II.B.4.1 Interface with other designs and other tasks
II.B.4.2 Develop theory of spectral and rate effects

IV. SUMMARY

Analysis of displacement cascades in MgO, Al_2O_3 and TaO is reported using data obtained with the specified-projectile displacement function. This function describes the specific collision events that produce displacements. The results show that the importance of specific collision-pairs in producing displacements is a function of initial PKA energy and mass ratio.

V. ACCOMPLISHMENTS AND STATUS

A. Specified-Projectile Displacement Function Results for MgO, Al_2O_3 and TaO -- D. M. Parkin (Los Alamos) and C. A. Coulter (The University of Alabama)

The specified-projectile displacement function, $p_{ijk}(E)$, is defined as the average number of type-k atoms which are displaced from their sites by type-j atoms in a displacement cascade initiated by a PKA of type i and energy E. The definition of $p_{ijk}(E)$ was given in a previous report' and will not be repeated here. Results from calculations for MgO, Al_2O_3 and TaO will be presented.

To describe the role of the displacing collision-pairs it is convenient to define the displacing-atom fraction $R_{ijk}(E)$ as

$$R_{ijk}(E) = p_{ijk}(E) \Big/ \sum_{j=1}^{n} p_{ijk}(E)$$

This function gives the fraction of type-k displacements produced by type-j atoms for fixed i and k.

Values of $R_{ijk}(E)$ for MgO(62,62,62,62) are shown in Figs. 1 and 2. Asymptotic values of R_{ijk} are not equal to 0.5 and are not the same for Mg and 0 PKA's. This difference occurs because of the mass ratio effect described previously.' It is more efficient to have the kinetic energy residing as moving heavy atoms (Mg) than with the light atoms (0). Thus this effect is more pronounced for Mg PKA's than for 0 PKA's.

The largest values of $R_{ijk}(E)$ are for i=j=k, which just reflects that the energy transfer efficiency is less than one for unequal mass collisions. When the displaced atom is not the same as the PKA type, then $R_{iij}(E) > R_{ijj}(E)$ $i \neq j$. This shows that the low energy transfer collisions ($E \sim E^d$) between unlike atoms dominate over higher energy collisions ($E > E^d$).

Figs. 3 and 4 present data for Al_2O_3 (18,45,45,72). The important difference between these data and the MgO data is that for Al_2O_3 we have used different displacement threshold energies for Al(18 eV) and O(72 eV). Generally, the results are very similar to the equal displacement threshold case (e.g., MgO). However, the fact that Al atoms are easier to displace than 0 atoms does affect the results. $R_{121}(E)$ for Al_2O_3 is larger than for MgO. This reflects the fact that at energies near the threshold for displacing an 0 atom where $R_{121}(E)$ becomes greater than zero, Al displacement can be produced by the 0 atom with a much higher

probability than 0 displacements. As the PKA energy increases, this effect becomes less important. A similar effect for $R_{211}(E)$ is seen.

The results for TaO in Figs. 5 and 6 show the behavior when the mass ratio is large. In this case, $R_{111} >> R_{121}$, whereas for high PKA energies $R_{112} \approx R_{122}$. Relative to the small mass ratio results (MgO, Al_2O_3), for the Ta PKA's (heavy atom), displacement collisions between like atoms are the more frequent. The most striking difference occurs for the light atom (O) recoils. Here the dominant factor is the enhanced efficiency of getting energy into moving Ta atoms. $R_{211}(E)$ becomes much greater than $R_{221}(E)$.

For all the results, asymptotic values of $R_{ijk}(E)$ are reached for $E \gtrsim 10^5$ eV. Thus until rather large PKA energies are reached, the specific collision pairs that are producing displacementsarnchanging. This energy dependence is similar to that found for the distribution of displaced atom types.[3]

VI. REFERENCES

1. Don M. Parkin, OAFS Quarterly Progress Report, DOE/ET-0065/6 (1979).
2. C. Alton Coulter and Don M. Parkin, J. Nucl. Mater. 88, 249 (1980).
3. Don M. Parkin, OAFS Quarterly Progress Report., DOE/ER-0046/2 (1980).

VII. FUTURE WORK

Analysis of the nature of displacement cascades in polyatomic materials is nearing completion.

VIII. PUBLICATIONS

1. C. Alton Coulter and Don M. Parkin, "Total and Net Displacement Functions for Monatomic Materials," J. Nucl. Mater. 95, 193 (1980)

2. Don M. Parkin and C. Alton Coulter, "Total and Net Displacement Functions for Polyatomic Materials," submitted to J. Nucl. Mater.

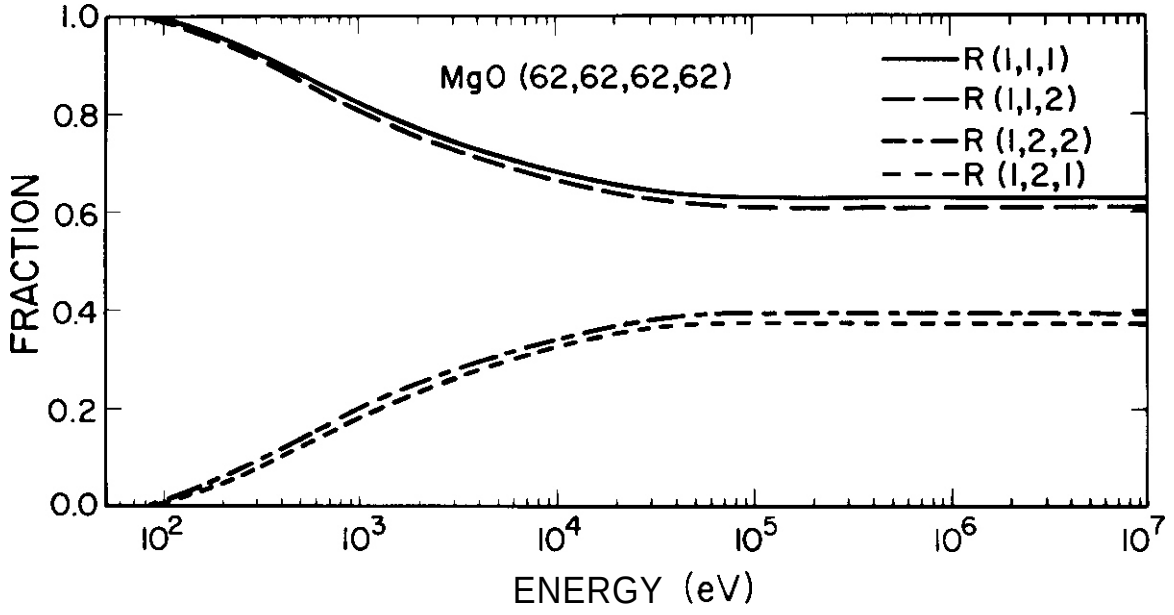

Figure 1. Values of R_{1ij} for MgO (62,62,62,62).

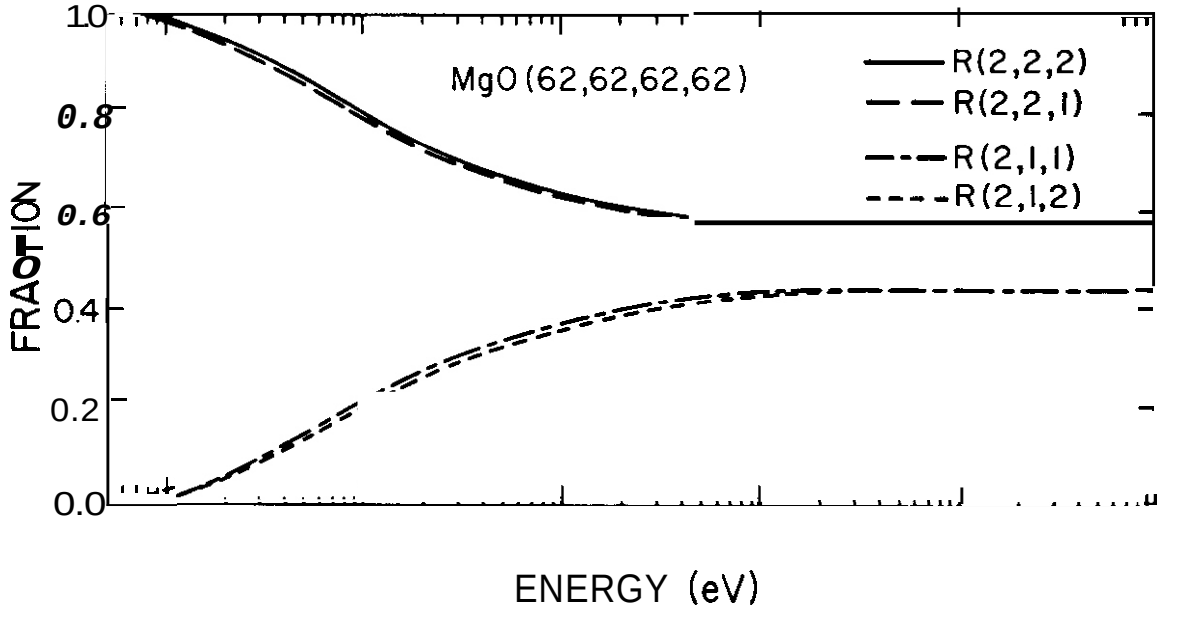

Figure 2. Values of R_{2ij} for MgO (62,62,62,62).

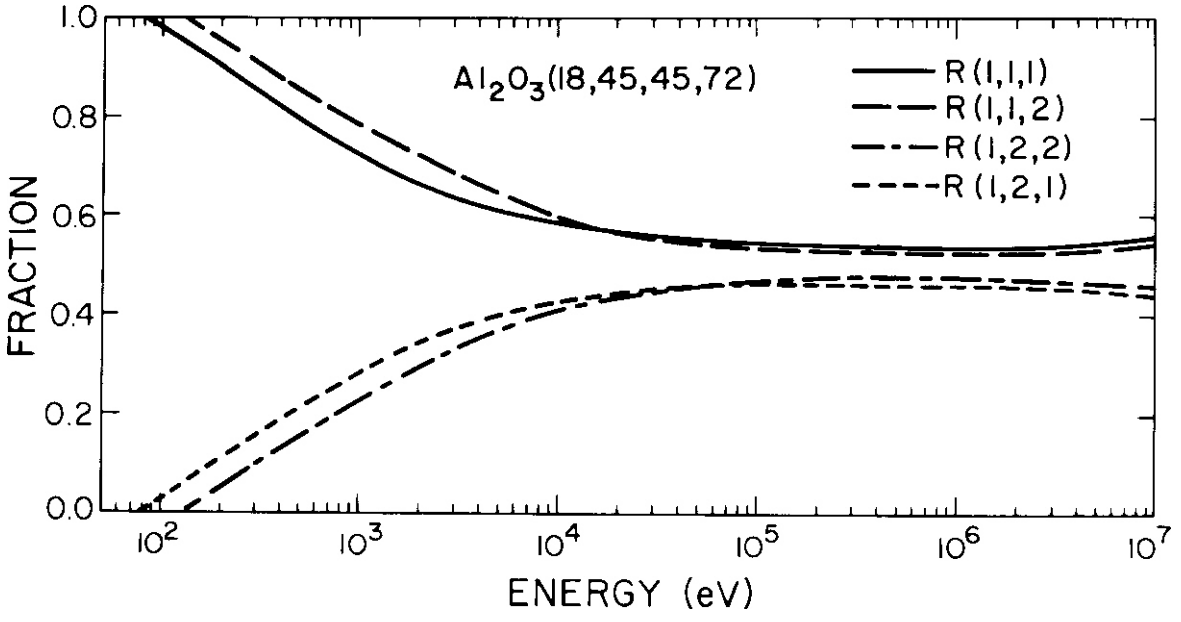

Figure 3. Values of R_{1ij} for Al_2O_3 (18,45,45,72).

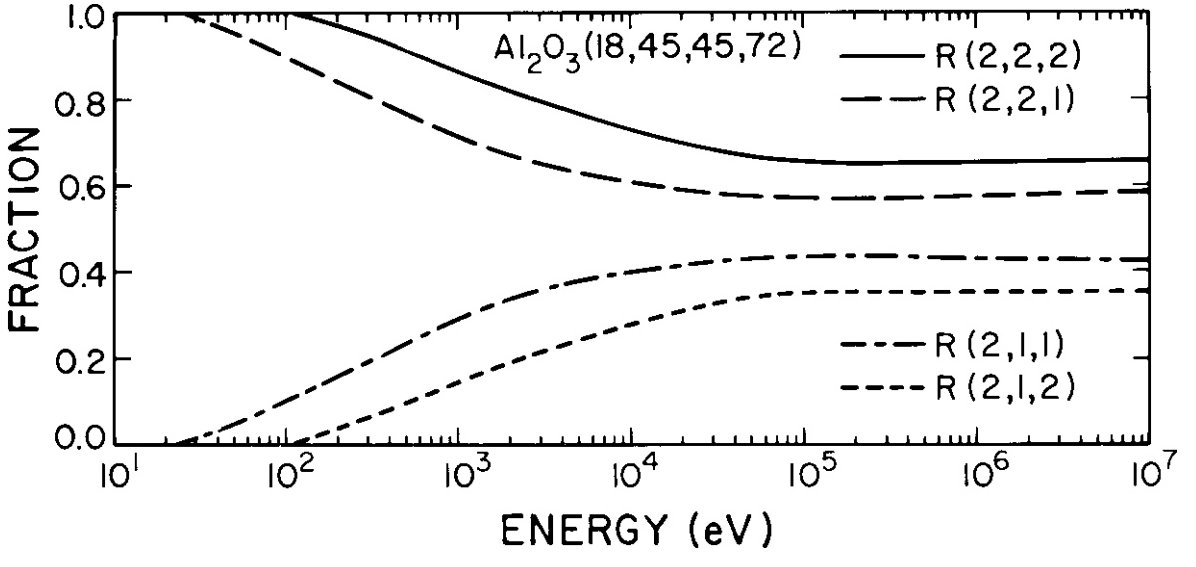

Figure 4. Values of R_{2ij} for Al_2O_3 (18,45,45,72).

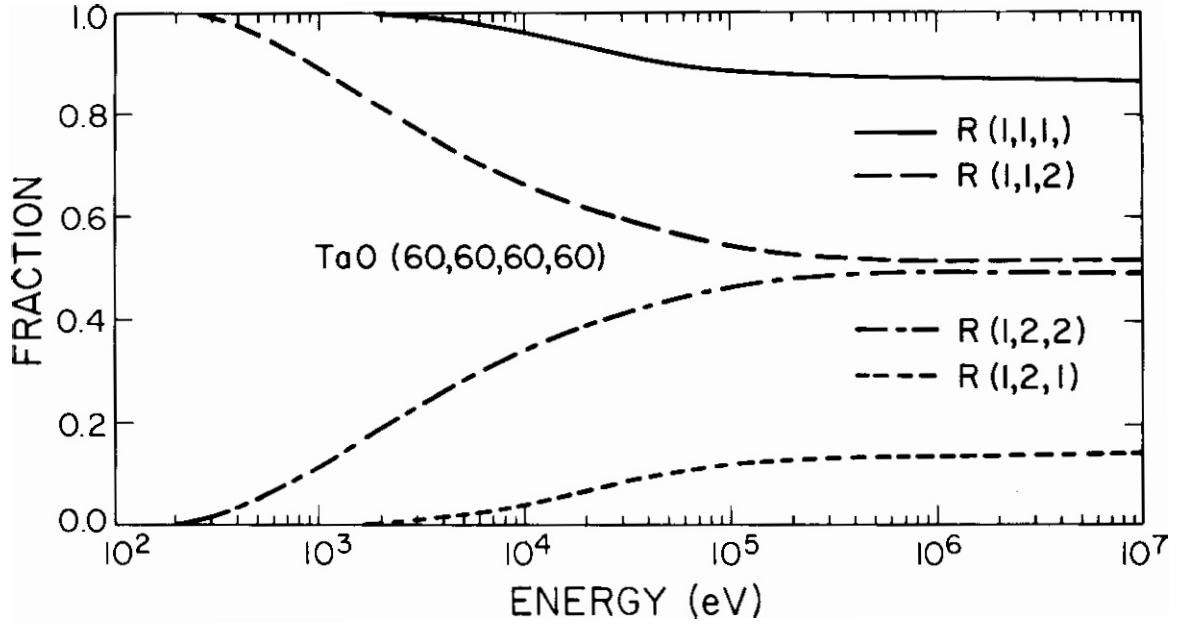

Figure 5. Values of R_{1ij} for TaO (60,60,60,60).

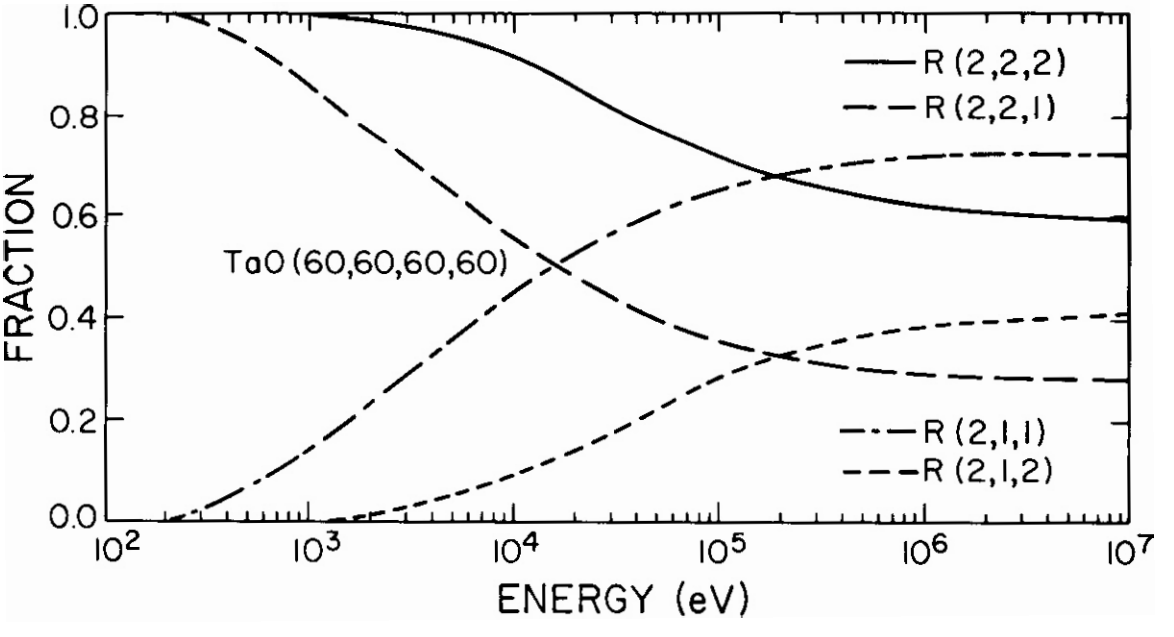

Figure 6. Values of R_{2ij} for TaO (60,60,60,60).

I. PROGRAM

Title: Nuclear Data for Damage Studies (AKJ)
Principal Investigator: D. G. Doran
Affiliation: Hanford Engineering Development Laboratory

II. OBJECTIVE

The objective of this work is to apply nuclear data to radiation damage studies.

III. RELEVANT DAFS PROGRAM PLAN TASK/SUBTASK

II.A.3 Sensitivity Studies
II.A.4.5 Gas Generation Rates
II.A.6.3 Dosimetry Standardization
II.B.l Calculation of Defect Production Cross Sections
II.C.4.1 Effects of Solid Transmutation Products on Microstructure

IV. SUMMARY

The nuclear data processing code NJOY is being updated to process cross sections induced by high energy neutrons.

A code to calculate solid and gas transmutation is being written.

An examination was made of potential self-shielding corrections to calculated displacement rates for specimens irradiated in FFTF. Monte Carlo calculations show that for 5-cm Fe spheres the volume averaged displacement rates will be about 15% lower than inferred from a knowledge of the surface flux and data from small samples. This reduction arises in approximately equal amounts from broad group flux modification due to downscattering and absorption and fine group flux modification due to resonance effects.

V. ACCOMPLISHMENTS AND STATUS

A. Calculation of Displacement Cross Sections -- F.M.Mann (HEDL)

The Los Alamos computer code NJOY[1] processes nuclear data from ENDF/B (the Evaluated Nuclear Data File) into formats usable by applications codes. ENDF/B is the standard nuclear data library for U.S. energy applications with evaluations approved by the DOE-sponsored Cross Section Evaluation Working Group (CSEWG). Besides producing data for reactor physics applications, NJOY calculates damage energy, helium production, and KERMA (Kinetic Energy Release in Materials) cross sections.

The MFECC version of the code is being revised to handle the new high energy neutron and charged particle formats being proposed by R.E.MacFarlane (LANL). Evaluations for Ca (ORNL), Cr (BNL), Fe (LANL), and Ni (LANL) for neutron energies to 40 MeV will be put into these new formats.

B. Solid and Gas Transmutation Production -- F.M.Mann (HEDL)

The computer code system REAC is being written to calculate the production of solid and gas transmutants for various reactor facilities. The code is heavily based on the NEUACT code") which is being used to calculate neutron activation. NEUACT cross section libraries will be extended to include stable nuclides as well as gaseous nuclides.

C. Damage Rates in Large Samples in the FFTF -- F.M.Mann (HEDL)

1. INTRODUCTION

Because of the large test volumes available, the Fast Flux Test Facility (FFTF) will be used to test materials that may be used in fusion facilities. Some of the samples may be much larger than have been used in previous irradiations and self-shielding may affect reaction rates for such large samples.

Reaction rates can be calculated from

$$R = \sum_i \langle \phi_v \sigma \rangle_i \qquad (1)$$

where R is the reaction rate, ϕ_v is the perturbed flux, a is the reaction cross section, and the brackets < > denote an average over the volume of interest and an integration over the energy group i. However, normally only the unperturbed surface flux $(\phi_s)_i$ is known. Equation 1 can be rewritten in terms of $(\phi_s)_i$,

$$R = \sum_i (\phi_s)_i (\sigma_o)_i \, f_i \, g_i \qquad (2)$$

where $(a_0)_i$ is the infinitely dilute cross section, f_i is the resonance self shielding factor for group i

$$f_i = \frac{\langle \phi_v \sigma \rangle_i}{\langle \phi_v \rangle (\sigma_o)_i} \, , \qquad (3)$$

and g_i is the broad group flux-modification factor for group i which provides the relationship between surface flux and the flux inside the sphere,

$$g_i = \frac{\langle \phi_v \rangle_i}{(\phi_s)_i} \qquad (4)$$

For very small volumes f_i and g_i tend to unity.

2. METHOD

To determine the magnitude of self shielding, the Monte Carlo code MCNP[3] using ENDF/B-IV cross sections was used to calculate (σ_o), f_i, and g_i as a function of radius for iron spheres immersed in Maxwellian fission spectra having temperatures of 0.5, 1.0, and 1.5 MeV. The resulting fluxes (ϕ_v and ϕ_s) and volume averaged reactions for elastic scattering and KERMA reaction rates $<\phi_v\sigma>$ were multigrouped into the 12 energy groups shown in Table I.

KERMA (total locally produced energy) cross sections were used instead of dpa cross sections as the MCNP libraries do not contain dpa cross sections. This substitution should still yield accurate results since below the (n,p) threshold at 3 MeV KERMA is solely due to nuclear recoil. Unfortunately the KERMA cross section in the MCNP library is void of resonances, and hence the effect of resonance self shielding (f_i) was estimated using the elastic cross section. KERMA in the Fe resonance region is mainly due to elastic scattering, so this should also be a good approximation.

3 DISCUSSION

The calculations show that, within the accuracies ($\sim$ 2-3%) of the Monte Carlo runs, the f_i are independent of the Maxwellian fission temperature but dependent on the radius of the Fe sphere. The broad group modification factors g_i depend on both the sphere radius and the Maxwellian temperature T. The infinitely dilute cross sections are independent of both r and T.

Table I presents the $f_i(r)$ and $g_i(r,T)$ multigroup values for r=5.0 cm and for T=0.5, 1.0, and 1.5 MeV. As can be seen, for the higher energy groups there is less flux inside the sphere than on the surface, while for the lower energy groups

downscattering has increased the flux inside the sphere. Since Fe has such a small absorption cross section, the total flux is nearly conserved, resulting in only a shape change. The resonance self-shielding factor varies from 0.74 to 1.00 for a 5 cm sphere.

4. APPLICATIONS

The FFTF core spectrum is not a pure Maxwellian fission spectrum; however, between 0.2 and 2 MeV the core spectrum closely resembles a Maxwellian fission spectrum with a temperature of 1 MeV.

Table II presents the relative (to r=0.001 cm) KERMA reaction rate as a function of sphere radius using the g_i factors corresponding to T=1 MeV and the collapsed FFTF core center spectrum. The total self-shielding effect is statistically not important for Fe spheres of 0.5 cm or less. If a softer spectrum is used (Maxwellian temperature = 0.5 MeV), the relative reaction rate decreases from 0.85 to 0.83. A harder spectrum (T=1.5) increases the relative rate to 0.91. Such a hard spectrum is not typical of a mixed-oxide reactor like FFTF.

The typical experiment will not have pure Fe samples. As other elements are added, the resonance self-shielding effect will increase toward unity. Using the Bondarenko method, the resonance self-shielding correction for stainless steel is predicted to be 0.96 for a 5 cm sphere as compared to 0.93 given in Table II for pure Fe. Because the major constituents of stainless steels have cross sections similar to Fe for FFTF energies, the broad group flux modification factors should not significantly change.

VI. REFERENCES

1. R. E. MacFarlane, R. J. Barrett, D. W. Muir, and R. M. Borcourt, The NJOY Nuclear Data Processing System: User's Manual. LA-7584-M, Los Alamos Scientific Laboratory, 1978.

2. D. L. Johnson and F. M. Mann, DAFS Quarterly Progress Report for period ending September 30, 1980, (DOE/ER-004613), p.9.

3. LASL Group X-6, "MCNP - A General Monte Carlo Code for Neutron and Photon Transport," LA-7396-M, Los Alamos Scientific Laboratory, 1979.

VII. FUTURE WORK

Finish modification of NJOY computer code and process high energy evaluations.

Produce transmutation histories for typical MFE irradiation facilities.

TABLE 1

MULTIGROUP CORRECTION FACTORS FOR Fe SPHERES FOR r=5.0 cm@

Upper Energy (MeV)	g_i $\langle\phi_v\rangle/\phi_s$			f_i $\left(\frac{\langle\phi_v\sigma_e\rangle/\phi_v \mid r=5.0}{\langle\phi_v\sigma_e\rangle/\phi_v \mid r=0.0}\right)$
	T^+=0.5 MeV	T^+=1.0 MeV	T^+=1.5 MeV	
20.0	.75	0.76	0.78	1.00
5.0	0.85	0.89	0.88	0.99
2.0	0.91	0.93	1.00	0.95
1.5	0.97	0.96	1.02	0.91
1.2	0.97	1.00	1.01	0.90
1.0	0.95	1.02	1.06	0.92
0.8	1.00	1.02	1.16	0.86
0.6	0.98	1.08	1.05	0.91
0.4	0.98	1.05	1.10	0.80
0.3	1.02	0.96	1.15	0.87
0.2	0.94	1.02	1.04	0.74
0.1	1.00	1.10	1.30	0.74
0.01	---	---	---	---

@ uncertainties are ~3%

+ T is the temperature of a Maxwellian fission spectrum

The resonance self-shielding factors were computed for a Maxwellian fission temperature of 1.50 MeV.

TABLE 2

RELATIVE KERMA REACTION RATE AS A FUNCTION OF RADIUS+

FOR AN FFTF CORE SPECTRUM

r (cm)	Resonance Shielding only	Spatial Shielding only	Both
0.001	1.0	1.0	≡1.0
0.01	1.0	1.0	1.0
0.1	1.0	1.0	1.0
0.5	0.98	1.0	0.98
1.0	0.97	0.99	0.96
2.0	0.95	0.96	0.92
5.0	0.93	0.95	0.85

+ Monte Carlo uncertainties are ∿ 3% for all numbers

I. PROGRAM

Title: Irradiation Effects Analysis (AKJ)
Principal Investigator: D. G. Doran
Affiliation: Hanford Engineering Development Laboratory

II. OBJECTIVE

The objective of this work is to develop computer models for the simulation of high energy cascades which will be used to generate defect production functions for correlation analyses of radiation effects.

III. RELEVANT DAFS PROGRAM TASK/SUBTASK

Subtask II.B.2.3 Cascade Production Methodology

IV. SUMMARY

Cascade sizes, as represented by the dimensions of the distributions of defects in simulated cascades in ordered Cu_3Au, were compared with dimensions of disordered regions measured in recent TEM experiments in ordered Cu_3Au irradiated with Cu^+ ions having energies from 5 to 200 keV. The average areas of the simulated and observed cascades, measured transverse to the incident ion direction, compare favorably at all energies, but the maximum dimensions of the simulated cascades are much larger than those experimentally measured at the higher energies. When the small foil thickness necessary for the observations is taken into account, much better agreement is obtained.

V. ACCOMPLISHMENTS AND STATUS

A. A Comparison of Simulated and Experimental Cascade Dimensions in Cu_3Au - H. L. Heinisch and M. P. Morford (HEDL)

Disordered zones resulting from individual displacement cascades can

be imaged in an electron microscope because of the difference in structure factor for super lattice reflections between the disordered zones and the ordered matrix. Through this technique, microscopy can yield information on the sizes and shapes of displacement cascades, as exemplified in the results of the recent investigations of ion irradiated ordered Cu_3Au.[1-3]

This information can be directly compared with the sizes and shapes of computer simulated cascades, thus providing a vital link between modeling and experiments.

In principle, it is possible to determine the configuration of the disordered region produced by a high energy displacement cascade modeled at an atomistic level. In practice, the binary collision computer code MARLOWE, which we use to model high energy cascades, is not set up to do this, so we have simply compared the spatial distribution of point defects produced with MARLOWE to the observed disordered regions for cascades of the same energy. The experiments on Cu^+ ion irradiations at room temperature of ordered Cu_3Au by Jenkins et al.[1-2] were simulated with MARLOWE by Cu primary knock-on atoms (PKAs) of the same energies in ordered Cu_3Au.

The TEM was done on very thin (20-30 nm) areas of specimens which had been irradiated by Cu^+ ions at normal incidence. The disordered regions observed are thus representative of the lateral dimensions of the cascades. The MARLOWE cascades were therefore analyzed by measuring the extent of regions containing defects projected onto a plane normal to the randomly chosen PKA directions.

To make a fair comparison, the visibility criteria of the TEM image must be considered. The visibility of a disordered region depends on the thickness of the disordered region and its average level of disorder, as well as on its lateral dimension.[1] The depth of the zone within the foil and the foil thickness are also important. Regions thinned to about 30 nm or less are necessary. Jenkins et al. studied specimens bombarded with Cu^+ ions with energies from 5 to 200 keV. No disordered regions were observed for 5 keV Cu^+ ions, but at and above 10 keV each ion apparently produced a visible zone

of disorder. Above about 30 keV, and especially at the higher energies, closely separated disordered zones were identified as subcascades resulting from a single ion. The multiple zones representing subcascades were treated collectively as a single zone by Jenkins et al. Two measurements were reported at each ion energy, the average diameter $\overline{D}$ and the average maximum dimension $\overline{D}_{max}$ of the cascade. D is the diameter of a circle having the same area as the disordered zone (or the sum of the areas of the individual subcascades) for a cascade. D_{max} is the maximum extent of the disordered zone (or of the total region occupied by the multiple zones representing sub-cascades from a single event).

Cascades generated with MARLOWE from 5 to 100 keV were initially analyzed by determining numerically the areas of simple geometric shapes containing the defects for each cascade. This was found to be unsatisfactory because of the irregular ,shapes and subcascades of the higher energy cascades. The following method was then devised: the cascade region was divided into a grid of squares and the number of defects in each square was determined. A plot showing the number of defects in each square was made (Figure 1), which produced a density profile for the cascade. These density profiles were then analyzed much as if they were TEM micrographs. That is, visibility criteria based on the density of defects and the sizes and regularity of the dense regions were applied uniformly to the cascades at all energies. Simply measuring the total area containing defect densities greater than some minimum value is not sufficient, because the dense areas of a single cascade are not always contiguous. The criteria were determined by choosing a minimum visible defect density which produced a good fit to the experimental value of $\overline{D}$ at 20 keV, and by using the fact that 5 keV cascades produced no disordered zones visible by TEM. This graphical approach was found necessary in order to not include (i.e., to deem invisible) some small isolated areas of high density as well as to include as part of the visible region those small, less dense areas which are enclosed within dense regions.

The results for about ten cascades at each energy are shown in Figure 2, compared to the experimental results (smooth lines). There is good agreement for

$\bar{D}$ at all energies, and for $\bar{D}_{max}$ for energies of about 20 keV or less. However, the differences between the theoretical and experimental values of $\bar{D}_{max}$ become much larger with increasing energy.

The microscopy must be done in extremely thin regions of the foil, and there is a possibility that some high energy cascades may not be completely contained within the inspected region. To simulate this, the 50 and 100 keV cascades were analyzed after allowing only the defects occuring in the first 30 nm along the PKA direction to be included. For two of the ten cascades at 100 keV the additional assumption was made that several subcascades were widely enough separated from each other that they would be considered as individual cascades in a micrograph. The results of this analysis are shown in Figure 3, where there is considerably better agreement for $\bar{D}_{max}$.

Of course, the simulation has shortcomings. For example, thermal effects were not included, and the interatomic potentials, while plausible, are untested against other experimental data. Also, the number of simulated cascades examined is small; larger statistical samples are needed, along with three-dimensional graphical examinations of the simulated cascades to establish better visibility criteria for the analysis. The foil thickness used in the analysis is conservative, 30 nm being the upper limit of thicknesses reported for the observations. The dependence on foil thickness of the simulation results should be determined.

The significant result of the investigation so far is that the values of $\bar{D}_{max}$ for the simulated cascades changed dramatically when the foil thickness was taken into account. While Jenkins et al. were certainly aware of the possibility that the high energy cascades might not be totally contained within the thin foils, they apparently underestimated this effect. Thus, the necessity of thin foils for this TEM technique would seem to place a severe limitation on its usefulness for high energy cascades.

VI. REFERENCES

1. M. L. Jenkins, K. H. Katerbau and M. Wilkens, Phil. Mag., 34, 1141 (1976).

2. M. L. Jenkins and M. Wilkens, Phil Mag., 34, 1155 (1976).

3. M. L. Jenkins, N. G. Norton and C. A. English, Phil Mag., 40, 131 (1979).

VII. FUTURE WORK

More cascades will be analyzed for better statistics, and higher recoil energies will be investigated.

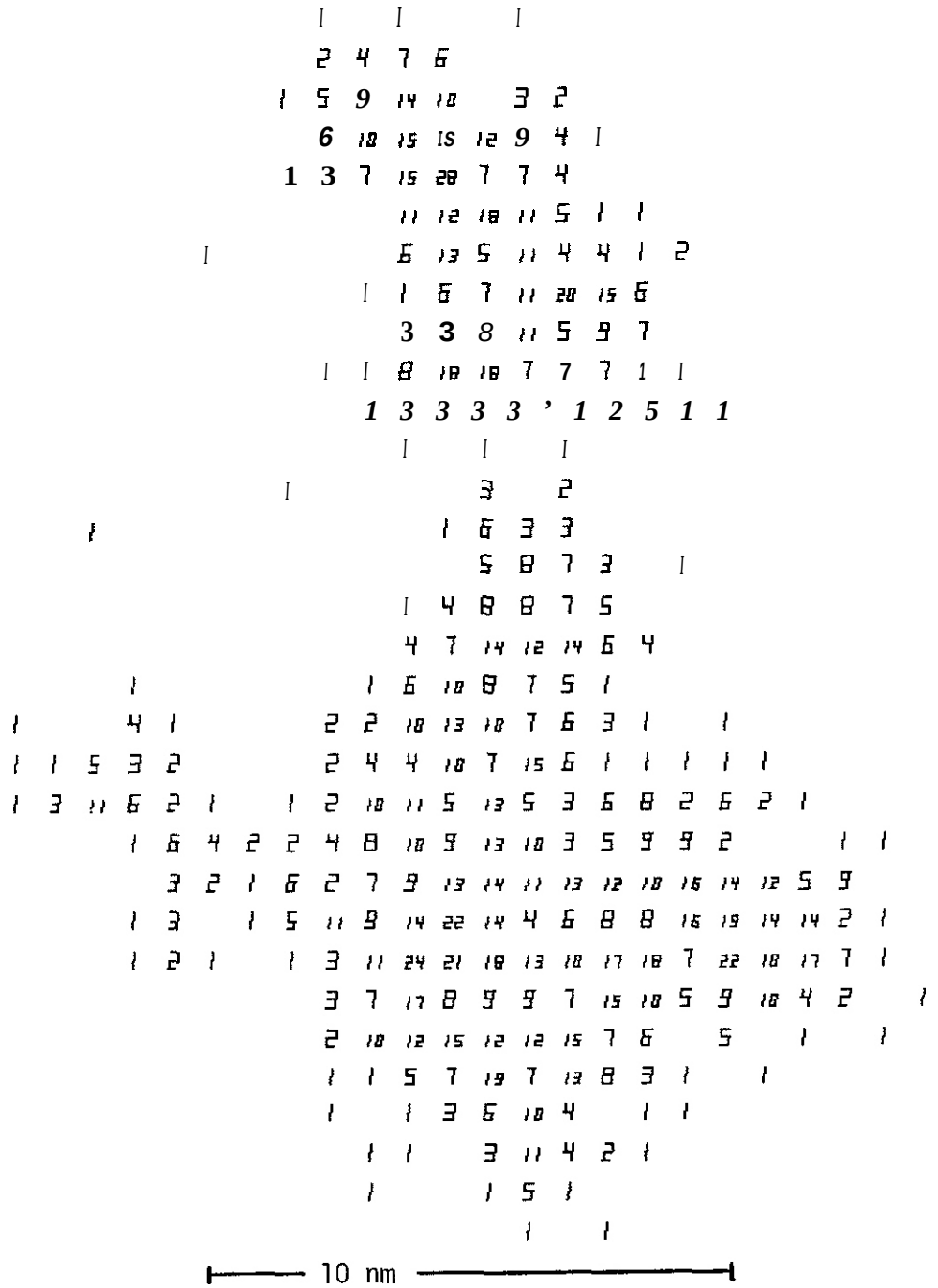

FIGURE 1. Density Profile for Point Defects Projected Normal to the PKA Direction far a 50-keV Cu PKA in Ordered Cu_3Au. Each number refers to the number of defects in a square of side 2 lattice parameters at that location. Squares containing 10 or more defects were considered visible in the analysis.

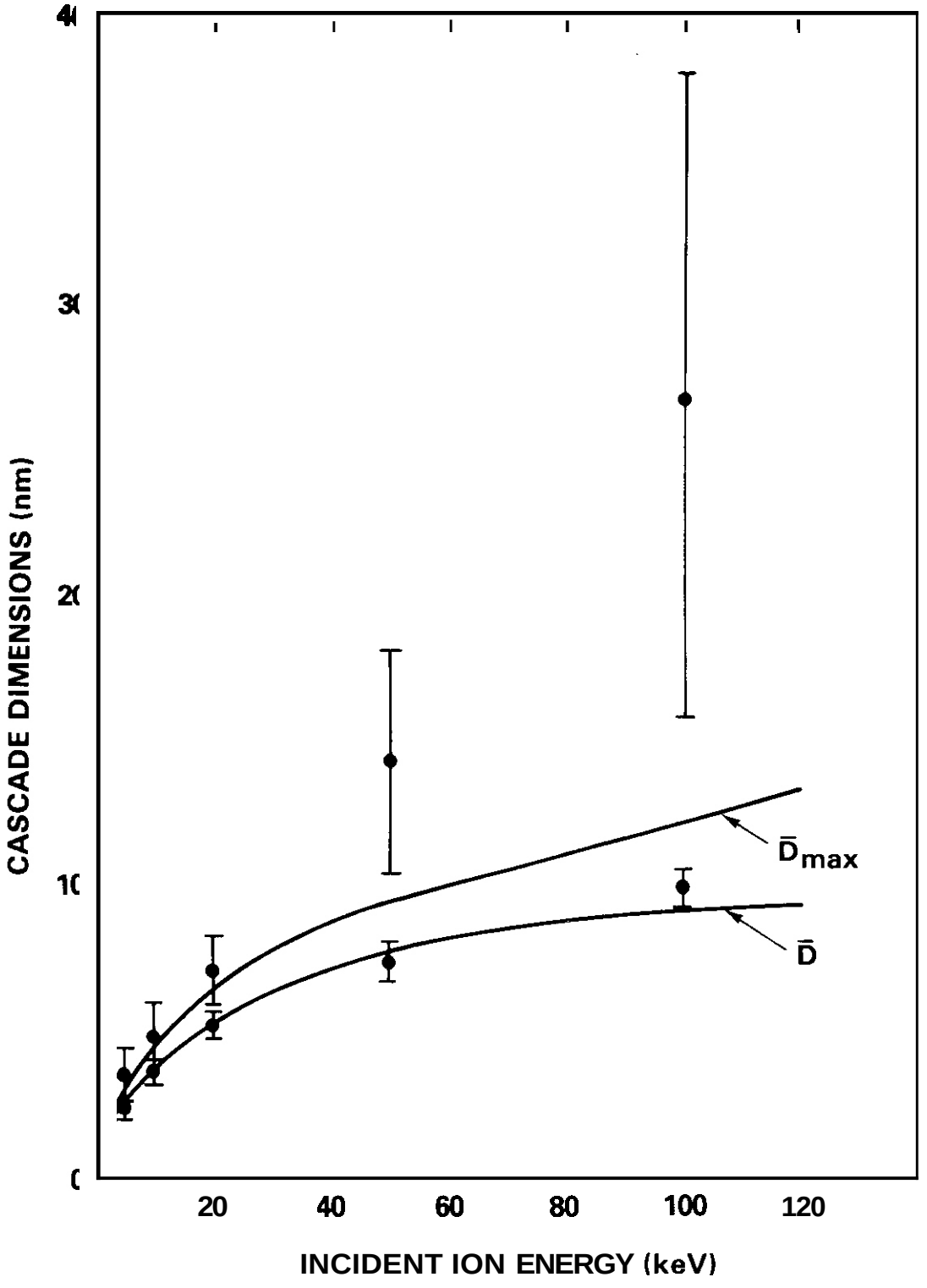

FIGURE 2. Average Diameter $\bar{D}$ and Average Maximum Dimension $\bar{D}_{max}$ as a Function of Energy. The curves summarize the experimental measurements *of* Jenkins et al.[1-3] of disordered zones produced by Cu^+ ions in ordered Cu_3Au. The points refer to the distributions of point defects for simulated Cu PKAs in ordered Cu_3Au. Error bars are $\pm$ one standard deviation.

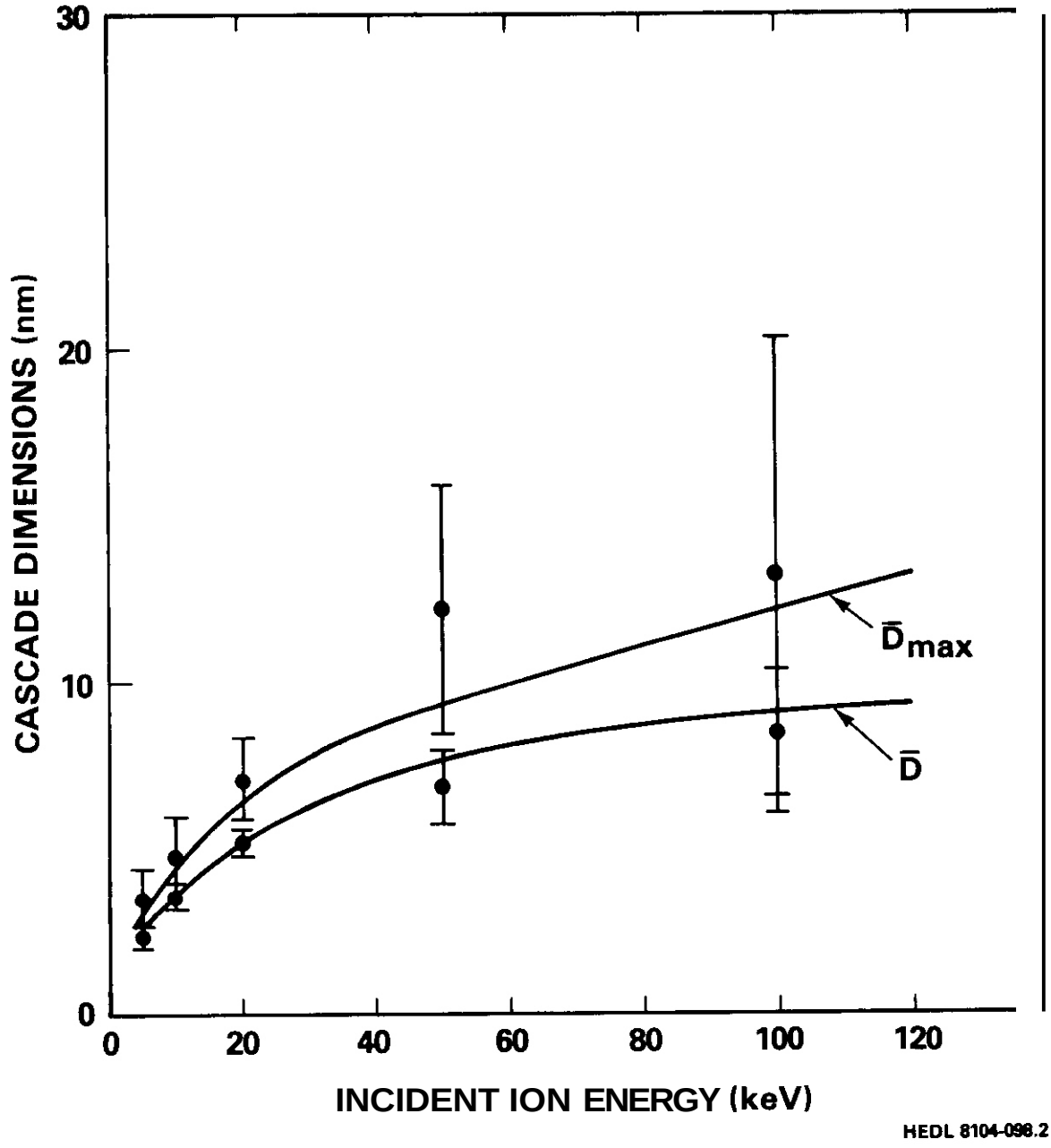

FIGURE 3. $\bar{D}$ and $\bar{D}_{max}$ as a Function of Energy, Where the Simulation Has Been Adjusted to Correspond to a 30-nm Film Thickness.

I. PROGRAM

Title: Irradiation Effects Analysis (AKJ)
Principal Investigator: D. G. Doran
Affiliation: Hanford Engineering Development Laboratory (HEDL)

II. OBJECTIVES

1. Determine defect survivability in copper alloys irradiated at 25°C and the influence of solute additions and neutron fluence.

2. Determine the validity of using TEM and microhardness measurements to study the dependence of survivability on neutron energy and solute additions.

3. Study the nature of microstructural evolution during 14 MeV neutron irradiations for later comparison to fission reactor data.

III. RELEVANT DAFS PROGRAM PLAN TASK/SUBTASK

SUBTASK II.B.3.2 Experimental Characterization of Primary Damage State; Studies of Metals

II.C.6.3 Effects of Damage Rate and Cascade Structure on Microstructure; Low-Energy/High-Energy Neutron Correlations.

IV. SUMMARY

Additional examinations of the copper-alloy series irradiated in RTNS-II at 25°C confirm the validity of conclusions drawn in previous studies of point defect production and clustering. Microscopy has been performed on four specimens from the nickel-alloy series and analysis is in progress.

V. ACCOMPLISHMENTS AND STATUS

A. Microstructural Analysis of Specimens Irradiated in RTNS-II - H. R. Brager and F. A. Garner.

1. Introduction

In a previous report it was shown that microscopy and microhardness measurements had been made on pure copper and copper with 5% of either Al, Ni, or Mn. All of these metals had been irradiated in RTNS-II at 25°C to fluences as large as 7.5 x 10^{17} n/cm^2.(1) The analysis of these data showed that a substantial fraction of the defects were below the resolutionlimit of the microscope and accounted for a large amount of the hardening that results from irradiation. It also appeared that each cascade event and its subsequent internal rearrangements could be considered at this flux and fluence to be a separate event, both in time and space. It was shown that some solutes such as aluminum lead to substantial differences in clustering of point defects within the cascade and thus affect the subsequent visibility of the clusters. There did not appear to be any substantial effect of any solute studied on the number of defects surviving the cascade event. The fraction of defects surviving the original cascade event appeared to be at least 9%.

Since that time the effort has been continued. Several other specimens of the copper alloy series have been examined to assess the validity of the earlier conclusions. The effort has also been expanded to include an alloy series based on nickel rather than copper.

2. Pure Copper Irradiated to a Lower Fluence Level

In the previous report(1) pure copper was examined after irradiation to a fluence of 2.7 x 10^{17} n/cm^2 (14 MeV). A specimen has now been examined after irradiation to 0.76 x 10^{17} n/cm^2. Typical defect populations are shown in Figure 1. As shown in Table I the mean diameter

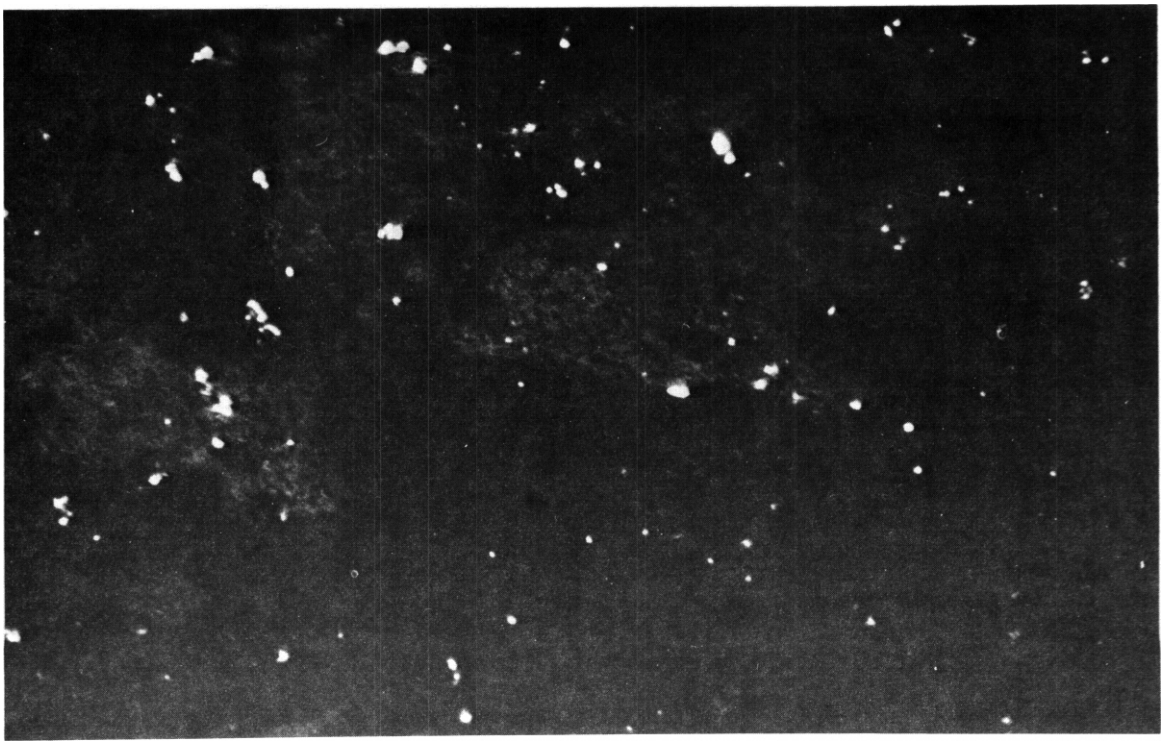

FIGURE 1. Weak Beam Dark Field Imaging of Defect Clusters Formed in Copper Irradiated at 25°C to 7.6 x 10^{16} n/cm^2 (E = 14 MeV)

TABLE 1

MICROSCOPY DATA - RTNS-II COPPER BINARY SERIES

Alloy	ϕt Neutron Fluence (10^{17} n/cm^2)	$\bar{d}$ Cluster Diameter (nm)	ρ Cluster Conc. (10^{17}/cm^3)	$(\rho/\phi t)$ Cluster Conc. per Unit ϕt
cu	2.7	2.6	1.3	0.48
cu*	0.76	3.0	0.25	0.33
Cu + 5% Mn	7.4	2.7	3.4	0.46
Cu + 5% Ni	7.6	2.3	3.6	0.47
Cu + 5% Al	7.1	2.0	7.7	1.08
Cu + 5% Al*	6.8	2.5	6.2	0.91

*Denotes new specimens

of the defects in the lower fluence specimen was ~3.0 nm at a density of 2.5 x 10^{16} defects/cm^3. These numbers are considered to be preliminary estimates at this time but confirm the conclusion drawn before that each cascade event is roughly independent of all other cascade events. Note that the mean size of the clusters does not increase with accumulated fluence. The slightly lower number density per unit fluence may reflect either an overestimated foil thickness or the larger uncertainty associated with the smaller number of defects counted in this specimen.

3. Examination of Another Copper + 5% Aluminum Specimen

As shown in Table I, the previous study concluded that aluminum additions to copper lead to enhanced visibility of defect clustering while nickel and manganese additions do not. In order to confirm this conclusion another specimen of this alloy was examined at a similar fluence of 6.8 x 10^{17} n/cm^2. As shown in Table I an aluminum addition of 5% leads to substantially enhanced visible number densities per unit fluence. This indicates that aluminum plays a role that is substantially different from that played by nickel and manganese.

4. Examination of the Nickel Series Alloys

A similar analysis is proceeding on the nickel-5% solute series irradiated in RTNS-II to fluences as large as 6.6 x 10^{17} n/cm^2 at 25°C. To date four specimens have been examined. Analysis of the micrographs is in progress.

5. Conclusions

Additional examinations of the copper-alloy series irradiated in RTNS-II at 25°C confirm conclusions drawn in previous studies of point defect production and clustering. Microscopy has been performed on four specimens from the nickel solute series and analysis is in progress.

TABLE 2
NICKEL SERIES SPECIMENS

Identification Code	Alloy	Neutron Fluence n/cm^2
ITVZ	Pure Ni	2.6×10^{17}
55Vu	Ni + 5% Si	6.6×10^{17}
53UZ	Ni + 5% Al	6.1×10^{17}
59x3	Ni + 5% Mn	6.9×10^{17}

VI. REFERENCES

1. H. R. Brager, F. A. Garner and N. F. Panayotou, "14 MeV Neutron Irradiation of Copper Alloy at EBR-II," OAFS Quarterly Progress Report, DOE/ER-0046/3, p. 81.

VII. FUTURE WORK

The analysis of the copper-solute and nickel-solute series will continue. The identity of the point defect clusters will be pursued using the black-white contrast technique. The theoretical considerations of solute size, weight, and interaction with point defects will also be examined.

VIII. PUBLICATIONS

An abstract entitled, "Damage Development and Hardening in 14 MeV Neutron Irradiation of Copper Alloys at 25°C," (HEDL-SA-2357A) has been submitted for presentation at the Second Topical Meeting on Fusion Reactor Materials to be held August 9-12, 1981 in Seattle, Washington.

I. PROGRAM

Title: Irradiation Effects Analysis (AKJ)
Principal Investigator: D. G. Doran
Affiliation: Hanford Engineering Development Laboratory

II OBJECTIVE

The objective of this work is to determine the effects of high energy neutrons on damage production and evolution, and the relationships of these effects to effects produced by fission reactor neutrons. Specific objectives of the current work are the development of techniques to extract from miniature specimen geometries information on the change in mechanical properties of neutron irradiated metals.

III. RELEVANT DAFS PROGRAM PLAN TASK/SUBTASK

SUBTASK	II.B.3.2	Experimental Characterization of Primary Damage State; Studies of Metals
	II.C.6.3	Effects of Damage Rate and Cascade Structure on Microstructure; Low-Energy/High-Energy Neutron Correlations
	II.C.11.4	Effects of Cascades and Flux on Flow; High-Energy Neutron Irradiations
	II.C.18.1	Relating Low- and High-Exposure Microstructures; Nucleation Experiments

IV. SUMMARY

A major goal of the DAFS program involves obtaining accurate measurements of the changes in the flow behavior of neutron irradiated metals from miniature specimen geometries. Indenter type hardness techniques have been applied to TEM disk type specimens in an effort to extract relative hardening data. Since microhardness tests are localized, they do not preclude

either the continued irradiation or the further study of the TEM disk specimens by other post irradiation analytical techniques.

It has been determined that the relative increase in the Vickers hardness of copper irradiated to a dose level of 1×10^{17} n/cm^2, E~14 MeV, is directly proportional to the increase in the 0.2 percent offset yield strength of copper. This finding resolves a previously reported discrepancy between measured changes in the offset yield strength and estimates based on hardness measurements. It remains to be shown that similar correlations can also be obtained, both at higher dose levels and for metals other than copper.

V. ACCOMPLISHMENTS AND STATUS

Prediction of the Change in the Offset Yield Strength of Copper Due to High Energy Neutron Irradiation Using Vickers Microhardness Data --

N. F. Panayotou (HEDL)

A. Introduction

In a previous quarterly report a discrepancy was reported between measurements of the increase in the 0.2 percent offset yield strength of Cominco and LLNL copper irradiated at 25°C at RTNS-I and values of the 0.2 percent offset yield strength calculated from hardness measurements on OAFS copper irradiated at 25°C at RTNS-II[1]. For convienience the result of the original attempt to correlate these strengthening results is reproduced in Figure 1. Possible causes for this discrepancy include differences in the composition and/or the prior history of the metals and the assumed relationship between offset yield strength and hardness.

The solute content of Cominco and LLNL copper is on the order of 500 ppm while OAFS copper has a solute content of about 25 ppm. All three types of copper were irradiated in an annealed condition. Although it could be argued that the difference in composition could be the basis of

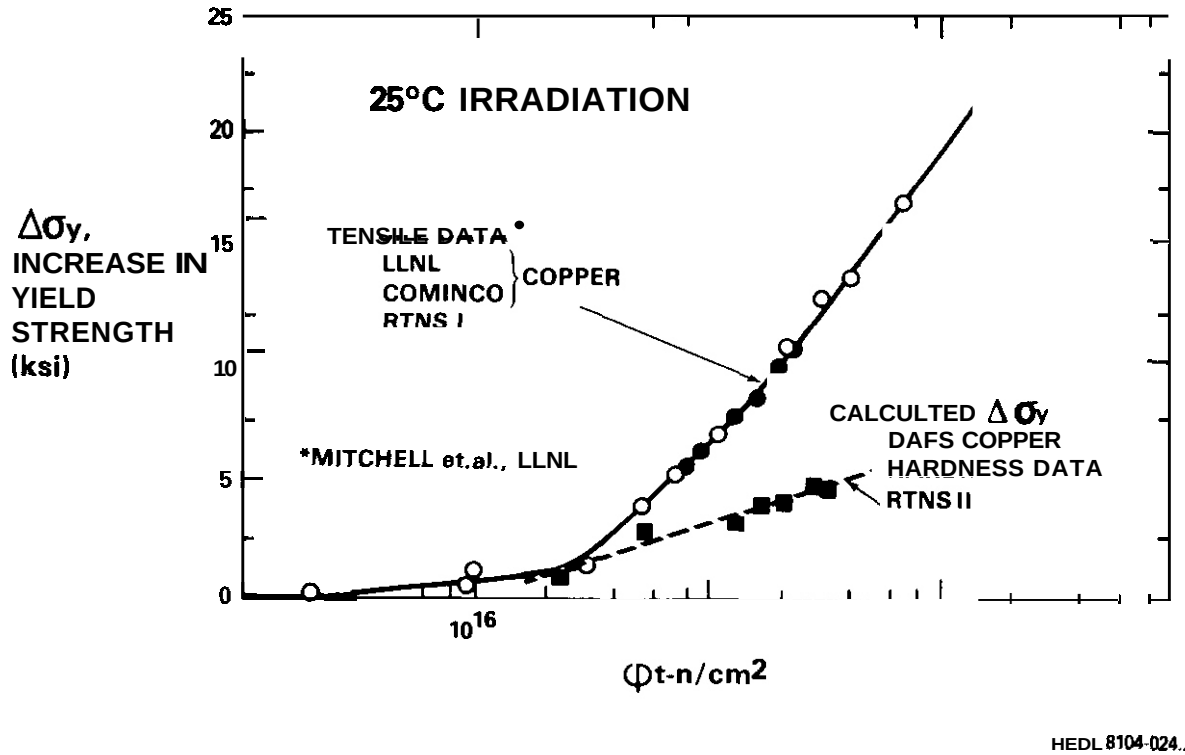

FIGURE 1. Original Attempt to Correlate Measured Strengthening and Calculated Strengthening Based on Hardness Data for Irradiated Copper.
Calculation assumes $a = K(DPH)B^{n}$.[1]

the reported discrepancy, the microstructure of the irradiated metals showed no significant differences in the number or size of visible defects.[1] Furthermore recent work, a confirmation of which appears in this quarterly report, indicates that a much larger addition of solute, up to 5 atomic percent, does not affect the relative irradiation induced hardening of copper or copper binary alloys.[2] It appears therefore, that the relatively small differences in solute content of the Cominco or LLNL and DAFS copper is not responsible for the reported discrepancy in strengthening results. Another potential source of the reported discrepancy is the assumed relationship between offset yield strength and hardness.

The calculated values of the increased in offset yield strength shown in Figure 1 assumed that

$$a_Y = K\ DPH\ (B)^n \qquad (1)$$

where σ_Y is the 0.2 percent offset yield strength expressed in MPa, K is a numerical constant equal to 3.27, DPH is the Vickers hardness number in kg/mm^2, B is a constant and n is the work hardening coefficient. The values of both B and n were taken to be constant and equal to 0.1 and 0.414 respectively. The calculated values of Strengthening, Figure 1, did not aqree with the data of Mitchell et.al. However, as will be discussed below, a good correlation between measured and calculated values of strengthening based on hardness can be obtained by assuming that

$$\Delta\sigma_Y(MPa) = 3.27\ \Delta DPH(kg/mm^2) \qquad (2)$$

where no$_Y$ and ΔDPH are the changes in the 0.2 percent offset yield strength and the Vickers hardness number, respectively.

B. Experimental Procedure and Results

Tensile data for LLNL and Cominco copper obtained by Mitchell et.al. which were taken from plots of $\Delta\sigma_y$ versus dose are summarized in Table 1 and appear in Figure 2 as a trend curve. The tensile specimens of Cominco and LLNL copper were irradiated at 25°C at the RTNS-I facility. The details of the experimental procedure of Mitchell et.al. have been reported elsewhere.[3] According to Mitchell, the yield strengths of unirradiated Cominco and LLNL copper were 52 and 62 MPa, respectively. Hardness data for DAFS copper are also summarized in Table 1 and plotted in Figure 2. The specimens used to obtain hardness data were 3 mm diameter TEM disk type specimens. The disks were punched from 0.254 mm thick annealed sheet stock of high purity copper obtained from A. D. Mackey Co. The total solute content of the stock was about 25 ppm. In order to minimize specimen deformation during the punching operation, a punch which supports both sides of the stock material was used. Specimens were also given a stress relief heat treatment, 400°C/15 min/Air Cool, after forming. This treatment produced a grain size of ASTM 5-6 (agerage grain diameter of 55 μm) and an initial Vickers hardness of $56.6\pm2.3\ kg/mm^2$ at a load of 50 gm. The average grain diameter of the LLNL and Cominco copper was about 50 μm. All hardness

TABLE 1

COPPER STRENGTHENING DATA

Tensile Data (3)			Hardness Data			
Copper Type	Dose 10^{17} n/cm^2	$\Delta\sigma_y$ MPa	Copper Type	Dose 10^{17} n/cm^2	ΔDPH kg/mm^2	$\Delta\sigma_y$ MPa
Cominco	0.11	6				
LLNL	0.24	8	OAFS	.25	0±5.5	0±18
Cominco	0.30	10	OAFS	.25	8k5.9	26±19
Cominco	0.55	26	DAFS	.58	Oi-4.2	Oi-14
Cominco	0.70	36	OAFS	.59	15±3.0	49±10
LLNL	0.90	41				
LLNL	0.95	45				
Cominco	1.1	48				
LLNL	1.4	55				
LLNL	1.6	61	OAFS	1.7	19t3.3	62±11
LLNL	2.0	69	OAFS	1.7	24t4.4	79±14
Cominco	2.1	74	DAFS	1.9	11±2.9	36±10
LLNL	2.3	76	DAFS	2.1	24t3.8	79±12
Cominco	3.0	88	OAFS	2.8	26±2.9	85±10
Cominco	4.0	95	OAFS	3.0	26t4.4	85±14
Cominco	6.5	117	OAFS	4.0	27t2.9	88±10

tests were performed using a Tukon type hardness tester fitted with a standard Vickers indenter and at a load of 50 gm. The lengths of the diagonals of each indent were measured using a Filar type eyepiece accurate to ±0.5 μm. The disk type specimens of OAFS copper were irradiated at 25°C at the RTNS-II facility.

The hardness data summarized in Table 1 are the average of at least five indents. The uncertainty reported is the 1σ spread of the measured hardness and the calculated strength values. The tabulated values of $\Delta\sigma_Y$ were calculated using Equation 2. Using this relationship, changes in the 0.2 percent offset yield strength of copper calculated from hardness

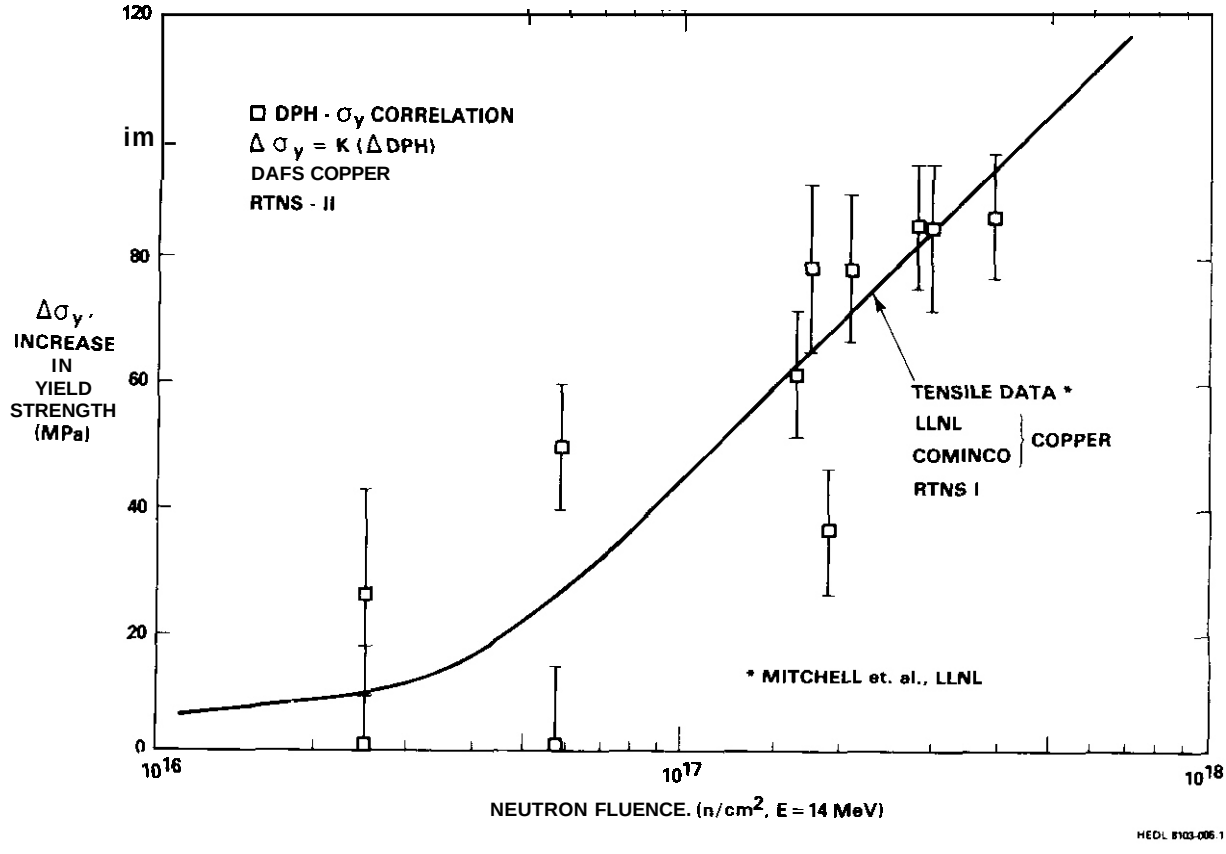

FIGURE 2. Correlation Between Measured Strengthening and Calculated Strengthening Based on Hardness Data for Irradiated Copper. Calculation assumes $\Delta\sigma \sim \Delta DPH$.

data were found to be generally within ±10 percent of the values measured by Mitchell et.al. using tensile specimens.

C. Discussion

Equation 2 is based on the well known relationship between indenter hardness DPH, and the true flow stress, σ, of a metal, $\sigma \sim DPH/3$.[4,5] Essentially, the indenter hardness number (units of pressure) is taken to be proportional to the true flow stress at the true strain value which is characteristic of the indentation. For a Vickers type indenter, the average strain is about 8%. This relationship between the strength measured by a Vickers hardness indenter and the 0.2% offset yield strength is illus-

strated in Figure 3, curve a. Clearly, in order to calculate σ_Y, the 0.2 percent offset yield strength, directly from DPH/3, the form of the stress-strain curve between yield and 8 percent strain must be known. However, if the stress-strain behavior of the metal changes only slightly with hardening, e.g. curve b Figure 3, it can be argued that the change in the flow stress at 8 percent strain, $\Delta\sigma_{DPH}$, should be proportional to the change in the offset yield strength, $\Delta\sigma_y$. Qualitatively, this type of change in stress-strain behavior has been observed for copper which was irradiated to dose levels where its yield strength had increased by a factor of four.[6] The maximum strengthening reported by Mitchell et.al. was about a factor of two. Therefore it is reasonable to expect that ΔDPH or $\Delta\sigma_{DPH}$ should be proportional to $\Delta\sigma_Y$ for the dose level covered by this work. It should also be noted that, in the limit of high neutron dose, DPH/3 can become a direct measure of σ_Y. Makin reports that highly irradiated copper shows little strain hardening during tensile testing.[6] This type of stress-strain behavior is illustrated in Figure 3, curve c. Clearly, the strength at 8 percent strain is a good approximation to the yield strength in this case. An attempt to extend this type of correlation to other metal systems is in progress. Preliminary results for both irradiated DAFS nickel and cold worked AISI 316 stainless steel show good correlations between measured strengthening and calculated strengthening based on hardness. The initial hardness and work hardening coefficients of these metals are significantly different than those of annealed copper. Accordingly, it appears that the relationship $\Delta\sigma_Y \sim \Delta DPH$ may be valid for metals other than just annealed copper.

The original attempt to develop a hardness-strength correlation made several assumptions which have since been determined to be invalid. The value of n, in Equation 1, was originally assumed to be constant, independent of irradiation. Actually n decreases as a metal is hardened.[7] Even though a reasonable correlation can be obtained using Equation (1), if n is allowed to decrease as a function of fluence, a further problem remains in that Equation (1) implicity assumes a power law type stress-strain behavior. It has been determined that such an assumption is not valid for copper.[8] In order to verify this assessment, measurements of

D. Conclusions

The original attempt to correlate hardness and strength data of irradiated copper was determined to be inadequate. However, by simply assuming that $\Delta\sigma_Y \sim \Delta DPH$, a correlation, accurate to about ±10%, was obtained between measured strengthening and the strengthening of irradiated copper calculated from indenter type hardness data. Preliminary results indicate that this correlation may be valid for other metal systems which have sustained a comparable degree of hardening.

VI. REFERENCES

1. H. R. Brager, H. L. Heinisch and N. F. Panayotou, "Microstructural Development in Copper Irradiated in RTNS-II," DAFS Quarterly Progress Report, DOE/ER-0046/1 (January-March 1980), p. 76.

2. H. R. Brager, F. A. Garner and N. F. Panayotou, "Microstructural Development in Copper Irradiation in RTNS-II," DAFS Quarterly Progress Report, DOE/ER-0046/3 (July-September 1980), p. 82.

3. J. B. Mitchell, R. A. Van Konynenburg, C. J. Echer and D. M. Parkin, "DT Fusion Neutron Radiation Strengthening of Copper and Niobium," UCRL Preprint UCRL-77357 Rev. 1.

4. F. A. McClintock and A. S. Argon, Mechanical Behavior of Materials, Addison-Wesley, Reading, Mass, pp 443-465.

5. G. E. Dieter, Mechanical Metallurgy, 2nd Edition McGraw-Hill, NY pp 389-402.

6. M. J. Makin, "The Hardening of Metals by Irradiation," Proceedings of the Conference on Irradiation Embrittlement and Creep in Fuel Cladding and Core Components, British Nuclear Energy Society, London, 1973.

7. R. W. Hertzberg, Deformation and Fracture Mechanics of Engineering Materials, John Wiley & Sons (1976), p. 18.

8. H. J. Kleemola, M. A. Niemineu, Met. Trans. 5 (1974), 1863

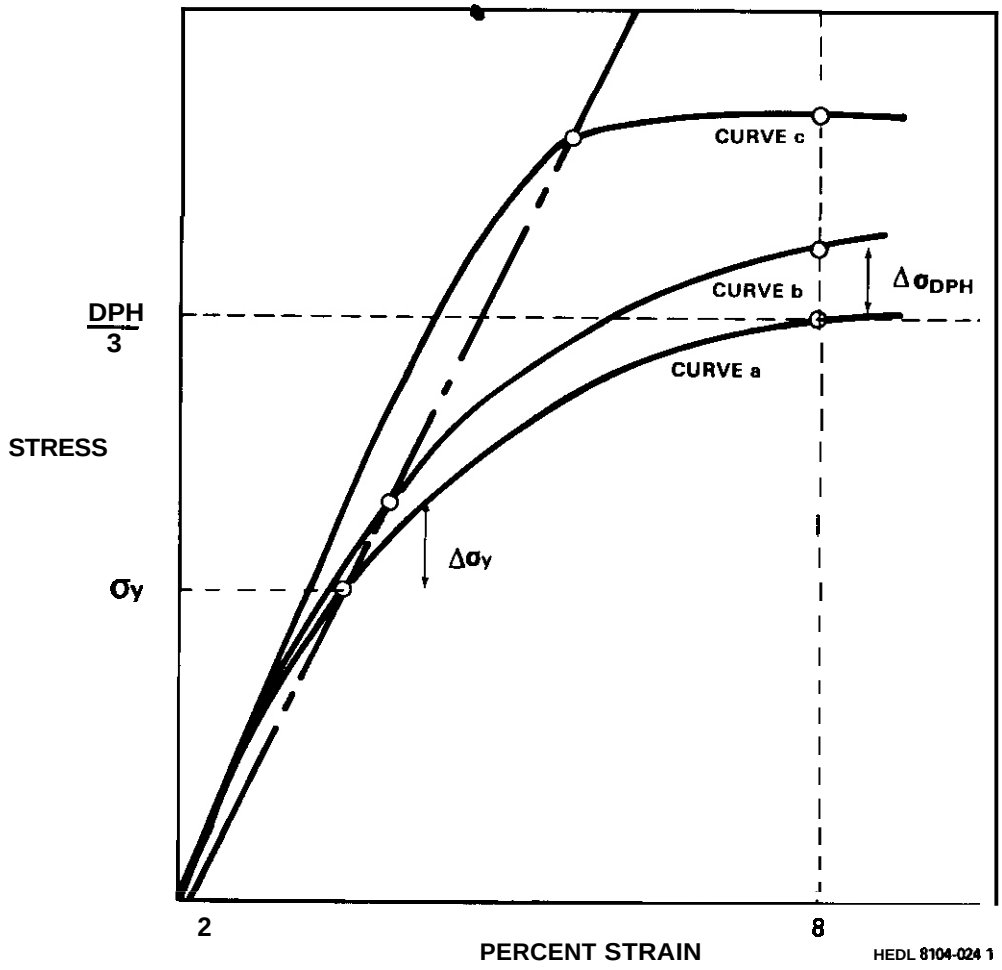

FIGURE 3. Typical Schematic Stress-Strain Curves for Copper: Curve a, Unirradiated Copper; Curve b, Slightly Irradiated Copper; Curve c, Highly Irradiated Copper.

the value of n for irradiated copper TEM disk specimens are in progress using the Meyers hardness technique.[6] Tha ability to measure n and An is also important since values of n can be correlated with tensile ductility and can be used to evaluate the effect of irradiation on stress-strain behavior.

VII. FUTURE WORK

Extend $\Delta\sigma_Y \sim \Delta$DPH correlation to other metal systems.

Continue development of techniques to measure work hardening coefficients using irradiated TEM disk specimens.

CHAPTER 3

FUNDAMENTAL MECHANICAL BEHAVIOR

I. Title: Effects of Irradiation on Fusion Reactor Materials

Principal Investigator: A. P. L. Turner
Affiliation: Argonne National Laboratory

II. OBJECTIVE

The objective of this work is to establish the effects of changes in irradiation flux on the rate of radiation assisted creep.

III. SUMMARY

Two types of creep rate transients were observed at the termination of irradiation during creep deformation of Ni-4 at. % Si alloy at 350°C. A short term transient saturated in less than one minute and a long term transient lasted for about 10 hours. The rapid transient appears to be too large to be explained by a change in temperature distribution (shear modulus change) in the specimen. It may be evidence for enhanced creep resulting from glide of dislocations released from obstacles by the climb caused by the absorption of surplus vacancies after the irradiation was stopped. The long term transient may have resulted from a change in the dislocation structure. A change in structure in the opposite sense may also be responsible for a creep transient with a moderate duration observed at the onset of irradiation.

V. ACCOMPLISHMENTS AND STATUS

A. Irradiation Creep Transient in Ni-4 at. % Si -- J. Nagakawa and V. K. Sethi

1. Introduction

There have been reports on a significant creep rate enhancement at the initiation and termination of irradiation[1] or by

a cyclic irradiation flux[2] during irradiation creep. Such a cyclic enhancement added to the irradiation creep is very detrimental for fusion reactor materials because irradiation conditions in at least the initial generation of fusion reactors will be cyclic. Rapid creep during cyclic irradiation has been explained in terms of the transients in the flow of point defects to sinks when the irradiation flux is changed.[1,2] Dislocation climb is enhanced by a surplus interstitial flux when the irradiation is turned on and by a surplus vacancy flux when the irradiation is stopped. If the enhanced climb liberates dislocations from pinning points allowing strain by glide, an enhanced creep rate can result from climb in either vacancy or interstitial absorbing directions.

In the course of a light-ion irradiation creep study of Ni-4 at. % Si alloy at 350°C creep transients were observed at the beginning and at the end of irradiation. These creep transients are analyzed in this report.

2. Experimental Procedure

Details of experimental procedures and the torsional creep apparatus have been described in previous progress reports. All experiments were performed with 21 MeV deuterons and a specimen temperature of 350°C. In order to eliminate sample to sample variations all experiments were performed using the same specimen (Ni-4Si-9), after it had been irradiated to 0.031 dpa which is sufficient to nearly saturate the irradiation induced hardening. The postirradiation creep rate of this specimen showed a stress exponent of 3 throughout the stress range examined.

3. Results and Discussion

Figure 1 shows strain vs. time curves for the last portions of irradiation creep experiments and the beginnings of

subsequent postirradiation thermal creep experiments. Two different creep transients can be seen: an abrupt change in strain when the beam is turned off which is neglibibly small at low stress, and a long term transient which is significant at any stress. The short transients were almost completed within a minute whereas the long transients lasted for nearly 10 hours. Accelerated transient creep of rather moderate duration (about 30 minutes) was observed at the beginning of irradiation as has been reported previously.(3)

It is possible that the short term transient could result from a change in temperature distribution in the specimen associated with the termination of irradiation. Such a temperature distribution change can cause a change in elastic strain (rotation) through a change in the shear modulus. However, the detailed analysis described below indicates that the amount of strain observed is too large to result entirely from the temperature change and does not have the proper dependence on the applied stress. Figure 2 shows a schematic representation of the temperature distribution in the specimen during irradiation creep at 1.3×10^{-6} dpa s^{-1} and a subsequent thermal creep experiment. Before irradiation, the specimen is heated only by a helium gas at 290°C. After the deuteron beam is aligned on the specimen, Seam heating of 30°C is added to the irradiated gauge portion ℓ_{irr} of the specimen. ℓ_{irr} is defined by a slit. The sample is then heated further by direct resistance heating to bring the gauge section to 350°C. When the irradiation is completed, the resistance heating is increased simultaneously as the beam is shut off in order to keep the gauge section at 350°C. A rapid increase in strain (rotation) was observed when the specimen temperature was increased to 350°C by turning on the direct resistance heating at the beginning of irradiation after completion of beam alignment. The amount of this strain, which is denoted by $\Delta\gamma_T^S$, is plotted in Fig. 3 as a function of the maximum shear stress. The straight line in the figure shows the calculated increase in strain associated with the temperature distribution change. Although there

is a rather large scatter resulting from unstable conditions during the early period of irradiation, coincidence between the observed and the calculated $\Delta\gamma_T^S$ is remarkably good. A linear stress dependence is obtained as expected. The strain associated with the short transient, denoted by $\Delta\gamma_S$, is not linear in stress and is much larger than the strain increase expected from the temperature distribution effect, denoted by $\Delta\gamma_T^F$ in Fig. 4. Therefore, the short creep transient is very unlikely to be a result of temperature distribution change.

This short creep transient may result from a surplus flux of vacancies to dislocations during the initial stage of the beam-off period after the interstitial defects have rapidly drained from the lattice. Vacancy flow enhances dislocation climb so that the dislocations can overcome pinning points and produce strain by a subsequent glide motion. Point defect concentrations during this point are given by

$$C_i = o,$$

$$C_v = (C_v^* - \overline{C}_v^e) \exp(-D_v Z_v^o \rho_t t) + \overline{C}_v^e, \tag{1}$$

where C_v^* is the vacancy concentration at the onset of annealing period, $\overline{C}_v^e$ is the equilibrium vacancy concentration a an average dislocation, D_v is the vacancy diffusivity, Z_v^o is the vacancy bias factor, and ρ_t is the total dislcoation density.[2] The climb-glide creep rate $\dot{\varepsilon}_{cg}$ is expressed by

$$\dot{\varepsilon}_{cg} = \rho_m(\lambda/h)b[V_c], \tag{2}$$

where ρ_m is the mobile dislocation density, λ/h is the ratio of the

obstacle spacing to its height, b is the strength of the Burgers vector, and V_c is the climb rate of an average dislocation. V_c under the condition of Eq. (1) is[2]

$$V_c = \frac{Z_v^o D_v}{b} (C_v^* - \bar{C}_v^e) \exp(-D_v Z_v^o \rho_t t) \quad . \qquad (3)$$

Thus, from Eqs. (2) and (3)

$$\dot{\varepsilon}_{cg} = \rho_m (\lambda/h) Z_v^o D_v C_v^* \exp(-D_v Z_v^o \rho_t t) \quad , \qquad (4)$$

where $\bar{C}_v^e$ is neglected because $C_v^* >> \bar{C}_v^e$. The transient creep strain, $\Delta\varepsilon_{cg}(t)$, is given by integrating Eq. (4) with respect to time, t,

$$\Delta\varepsilon_{cg}(t) = (\rho_m/\rho_t)(\lambda/h) C_v^* \{1 - \exp(-D_v Z_v^o \rho_t t)\} \quad . \qquad (5)$$

The time dependence of $\Delta\varepsilon_{cg}$ originates from the term $\{1 - \exp(-D_v Z_v^o \rho_t t)\}$ and $\Delta\varepsilon_{cg}$ saturates at the value $\{(\rho_m/\rho_t)(\lambda/h) C_v^*\}$ which must be dependent on stress. Figure 5 shows $\{1 - \exp(-D_v Z_v^o \rho_t t)\}$ vs. t for $Z_v^o = 1.76$, $\rho_t = 1 \times 10^{14} m^{-2}$ and $D_v = 3.72 \times 10^{-15} m^2/s$[2] and also for $D_v = 2.74 \times 10^{-16} m^2/s$ which was calculated from a migration energy of 1.38 eV[4,5] and vibration frequency factor of $5 \times 10^{13} s^{-1}$.[6] Both cases indicate that $\Delta\varepsilon_{cg}$ has nearly reached saturation in a minute as has been observed in the experiments. Therefore, the duration of the short creep transient observed at the onset of the beam-off (annealing) period agrees well with that predicted to result from surplus vacancy flux which causes enhanced climb-glide of dislocations. The magnitude of the strain produced depends on details of the model and the quantities ρ_m/ρ_t and λ/h which cannot be estimated accurately enough to make comparison

meaningful.

The long term transient, $\Delta\gamma_L$, cannot be explained by the transients in point defect fluxes to sinks because it persists for too long. It may be the result of a change in dislocation structure. The transient creep of moderate duration observed at the onset of irradiation also persists for too long to be related to transients in the point defect fluxes because these should reach their steady state values under irradiation more quickly. This transient might also be the result of a change in dislocation structure. A creep transient associated with surplus interstitial flux at the onset of irradiation[1,2] may have occurred, but not been recognized because of the non-steady conditions during the alignment of the deuteron beam pn the sample.

VI. REFERENCES

1. S. R. Maciwen and V. Fidleris, Phil. Mag., 31, 1149 (1975).

2. E. P. Simonen, J. of Nucl. Mater., 90, 282 (1980).

3. J. Nagakawa, V. K. Sethi, F. V. Nolfi, Jr. and A. P. L. Turner, OAFS Quarterly Progress Report for Period Ending September 31, 1980.

4. W. Wycisk and M. Feller-Knieprneier. Phys. Stat. Sol. (a), 37, 183 (1976).

5. K. Maier, H. Mehrer, E. Lessman and W. Schule, Phys. Stat. Sol. (b), 78, 689 (1976).

6. A. Seeger and H. Mehrer, Vacancies and Intersitials in Metals, (A. Seeger et al., eds., North-Holland Publishing Co., Amsterdom, 1970) p. 1.

VII. PUBLICATIONS

1. J. Nagakawa, V. K. Sethi and A. P. L. Turner, "Irradiation Creep and Solute Segregation in Ni-4 at. % Si", Proc. Irrad. Phase Stability Symposium, TMS-AIME, Pittsburgh, PA, October 5-9, 1980.

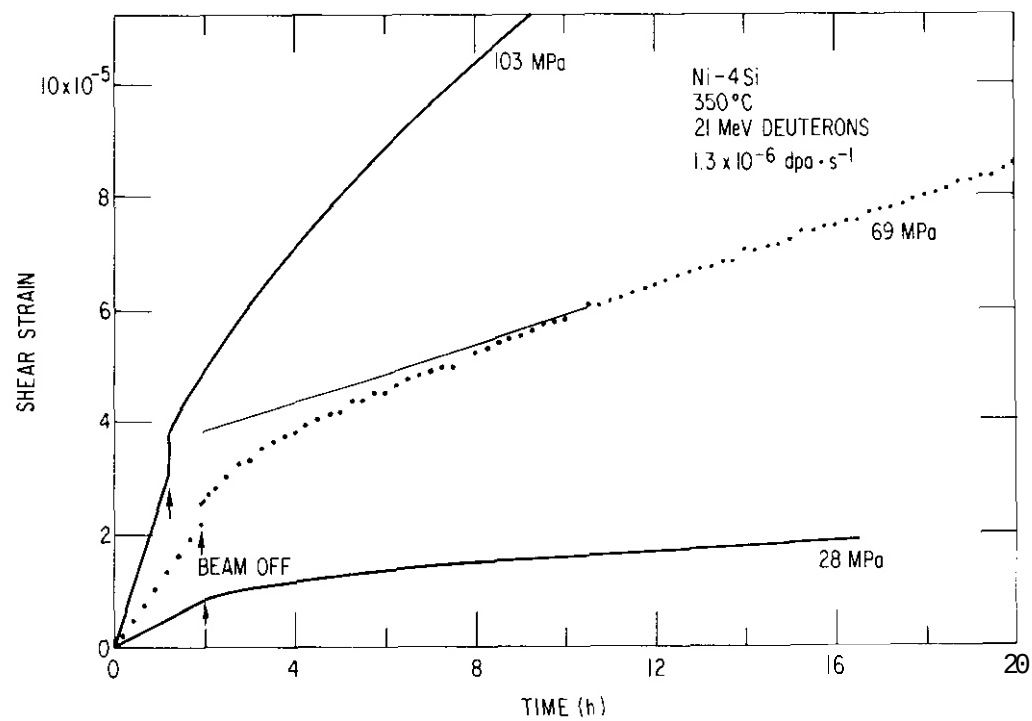

Figure 1. Creep curves showing the last portion of irradiation creep experiments and the initial portion of postirradiation thermal creep tests. Short term and long term transients can be seen. The short transient is clearly larger than the data fluctuations as indicated in the curve for 69 MPa which is expressed by data points from the digital data 1ogger.

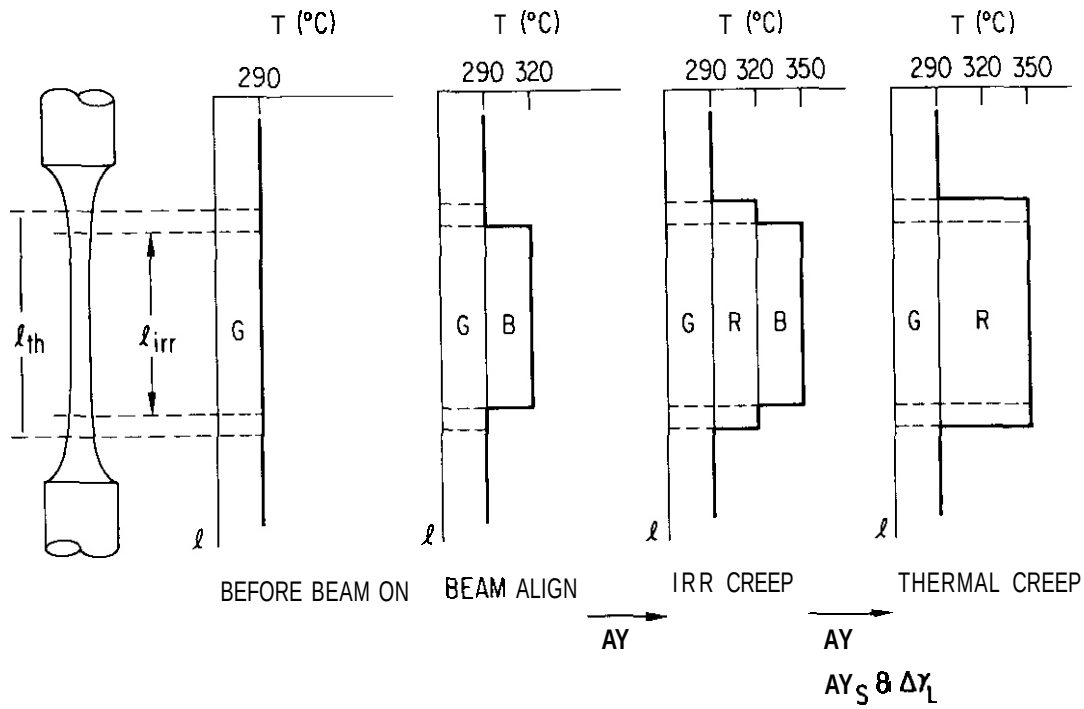

Figure 2. Schematic representations of the temperature distributions during irradiation creep and thermal creep experiments. The letters G, B and R denote helium gas heating, beam heating and resistance heating, respectively. Ay_T^S and $\Delta\gamma_T^F$ denote changes in elastic strain (rotation) due to a temperature distribution (shear modulus) change. $\Delta\gamma_S$ and $\Delta\gamma_L$ denote observed short and long term transient strain, respectively.

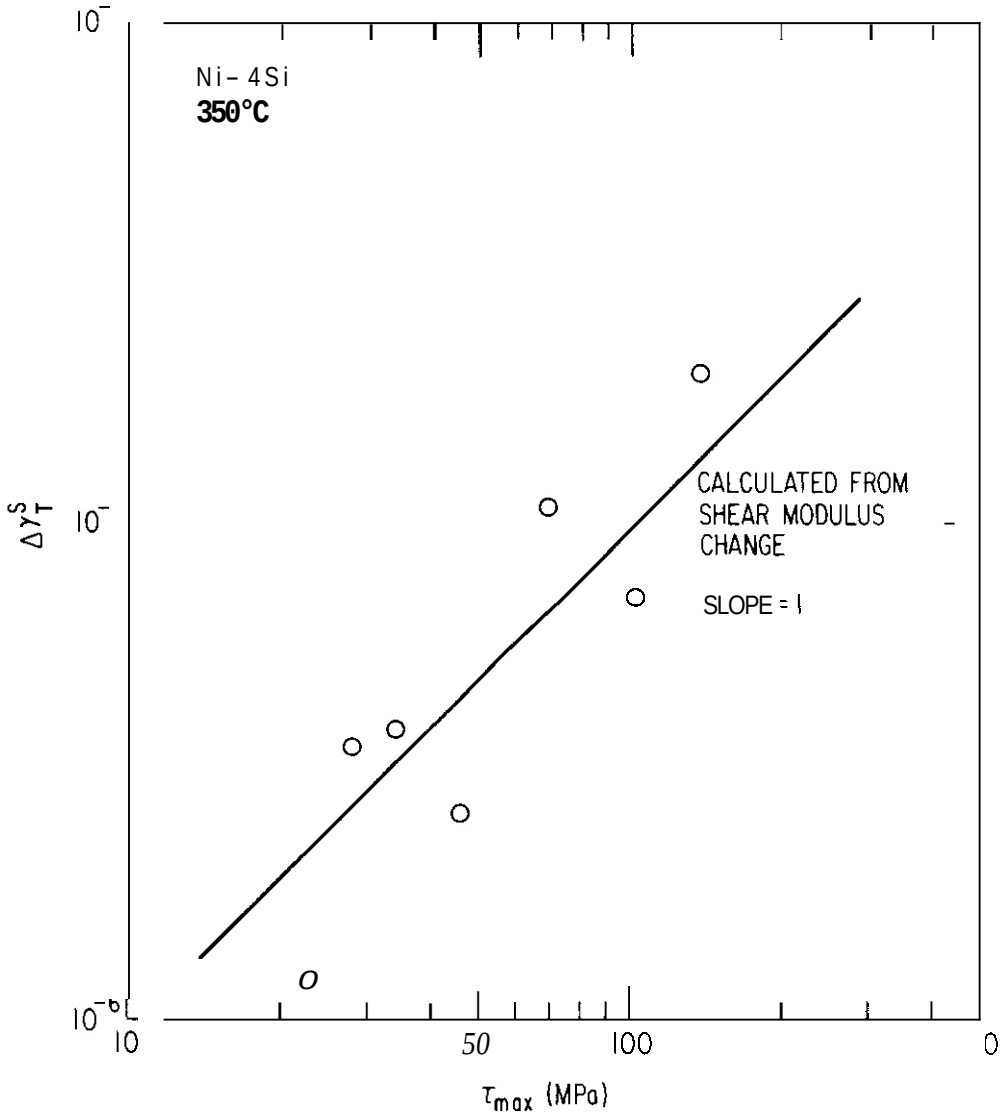

Figure 3. The magnitude of the rapid strain increase observed when the specimen temperature was increased to 350°C by turning on the resistance heating after the beam was aligned. The strain increase calculated from the shear modulus change associated with the temperature distribution change is shown by a straight line with a slope of one. Fairly good agreement between the observed and the calculated values can be noticed.

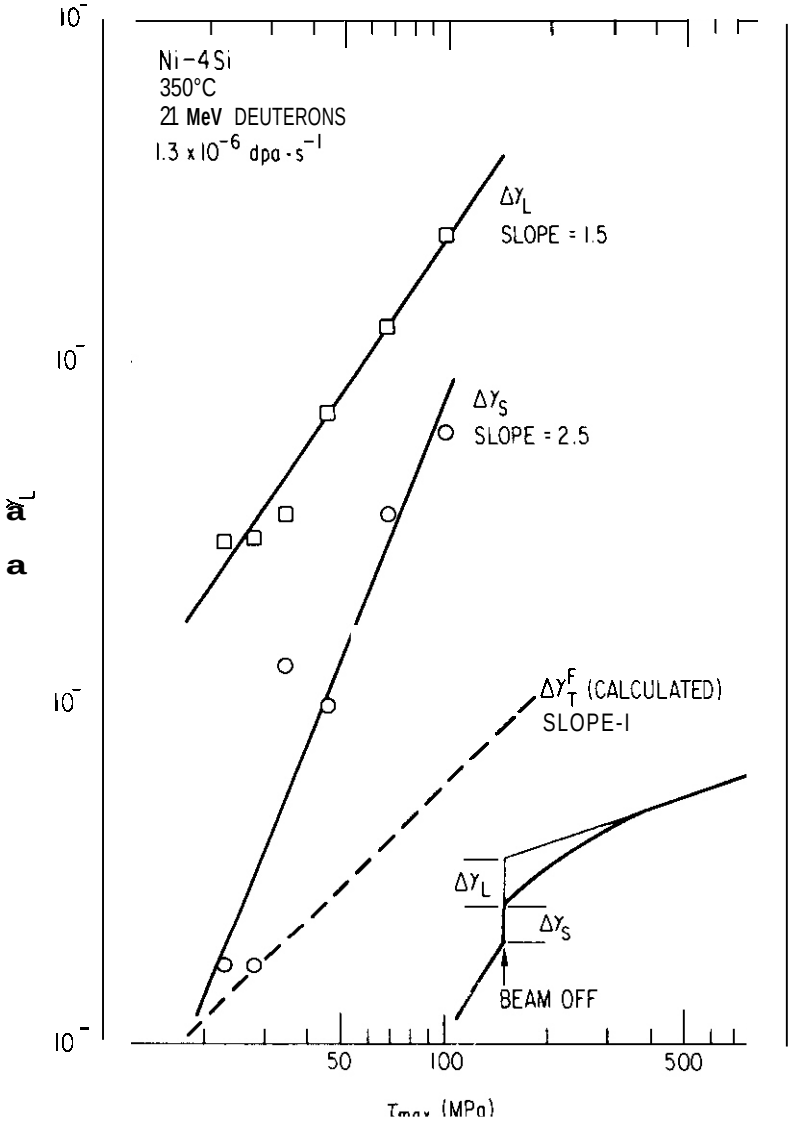

Figure 4. Stress dependencies of the observed strain associated with the short-($\Delta\gamma_S$) and long-($\Delta\gamma_L$) term transients as well as the calculated strain change due to temperature distribution change ($\Delta\gamma_T^F$) when the beam was turned off. Both $\Delta\gamma_S$ and $\Delta\gamma_L$ are much larger than $\Delta\gamma_T^F$ and are not linear in stress.

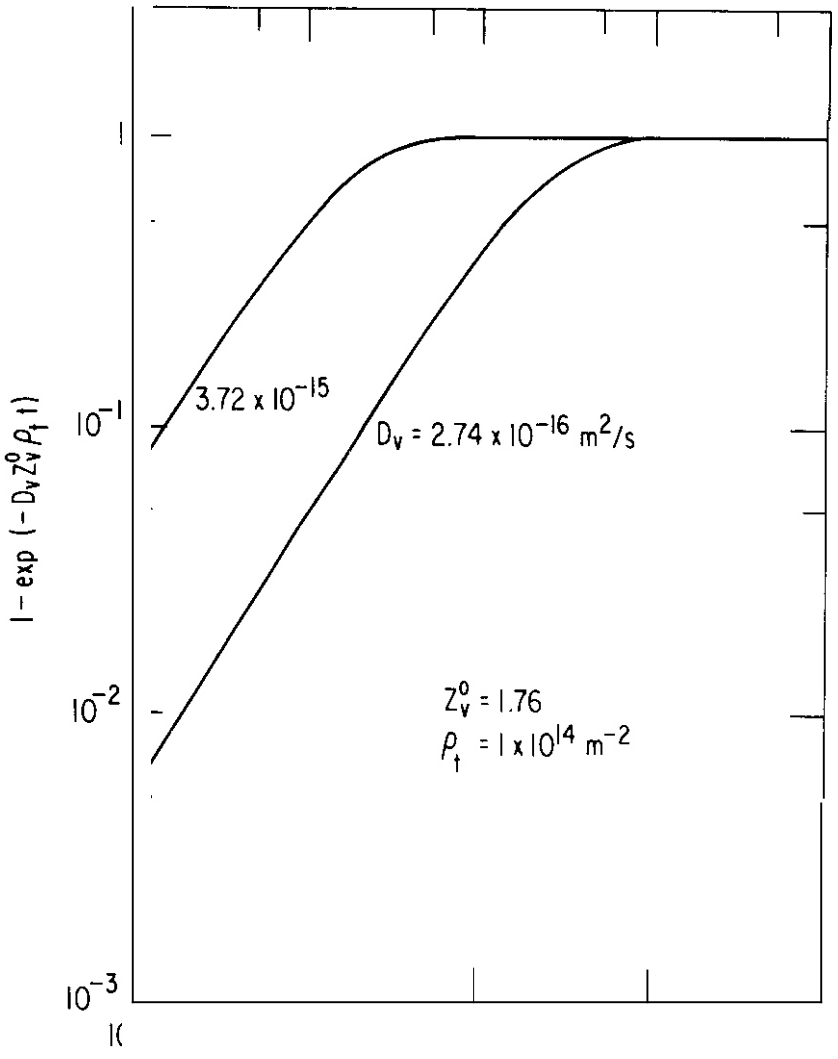

Figure 5. Time dependencies of creep transient caused by surplus vacancy flux for two different vacancy diffusivities. Both cases indicate that the creep transient almost reaches saturation within one minute.

I. PROGRAM

Title: Fundamental Studies of Radiation Damage Analysis
Principal Investigators: G.R. Odette and G.E. Lucas
Affiliation: University of California, Santa Barbara

11. OBJECTIVE

The objective of this work is to develop physical models describing the influence of metallurgical and irradiation variables on the alteration of mechanical properties. These models will be used to correlate available data, to plan and analyze new experiments and, ultimately, to extrapolate to fusion reactor conditions.

III. RELEVANT OAFS PROGRAM PLAN TASK/SUBTASK

SUBTASK II.C.14.1 Modeling of Flow and Fracture Under Irradiation-Model Development
SUBTASK II.C.16.1 Composite Correlation Models and Experiments-Correlation Model Development

IV. SUMMARY

Mechanical Properties Modeling

Creep fracture behavior of both unirradiated and irradiated (and helium implanted) austenitic stainless steel has been modeled using simple creep fracture mechanisms. A creep fracture map for the solution annealed 316 stainless steel has been developed and the predictions of the map are in good agreement with the experimental data on times-to-fracture. An irradiated rupture model has been developed based on 1) a size distribution of pre-existing helium bubbles, 2) stress induced nucleation of creep cavities on helium bubbles, and 3) a creep constrained cavity growth mechanism. The predictions of the model are in excellent agreement with the rupture times and ductilities for both the helium injected and neutron

irradiated Ti-stabilized stainless steel. However, the models developed are preliminary and they do not include all the critical processes, such as phase instabilities.

V. ACCOMPLISHMENTS AND STATUS

Creep Fracture Mechanisms in Unirradiated and Irradiated Stainless Steels -- S.S. Vagarali and G.R. Odette
(University of California, Santa Barbara).

A. Introduction

Commercial fusion reactor structural components will operate at temperature-stress regimes in which creep fracture is one of the significant failure modes. Fracture mechanism maps are convenient for representing the major mechanistic regimes [1]. A regime of prime engineering significance is at intermediate temperatures and at low stresses characteristic of service conditions; however, because of the very long rupture times implicit, very little data is available for these conditions. Limited experimental data indicates that grain boundary cavitation failure dominates this regime [2,3]. A fracture map for unirradiated solution annealed 316 stainless steel was recently developed by us as shown in Figure 1 [4]. The map indicates that at intermediate temperatures and low stresses, diffusion controlled cavitation fracture is dominant. However, recent studies have shown that cavitation fracture may often be creep controlled [5-7]. In the present work, the map given in Figure 1 is modified by incorporating creep controlled cavitation fracture mechanism.

Of course, the major concern is the creep-rupture properties of materials in actual service including, but not limited to, the effects of irradiation. It is well established that the microstructural and microchemical evolution which occurs in irradiated alloys can significantly alter fracture modes and generally reduce creep ductilities and rupture times. Unfortunately, the effects of irradiation are highly complex and not well understood. For example, significant differences have been

observed between the results of in-situ versus post-irradiation creep rupture testing [8]; in some cases irradiation has been observed to increase rupture times [9].

In spite of such complexity, there may be some circumstances which one particular aspect of irradiation damage is dominant and amenable to simple modeling. This may occur, for example, when there are high concentrations of transmutant helium leading to a significant increase in the number of grain boundary creep cavities which form on preexisting helium bubbles. Hence, a creep rupture model has been developed based on: 1) a size distribution of preexisting helium bubbles; 2) stress induced formation of creep cavities on a fraction of this bubble distribution; and 3) a creep constrained cavity growth mechanism. The predictions of the model are compared with rupture times and ductilities for both helium injected and neutron irradiated Ti-stabilized stainless steel.

8. Creep Fracture Mechanisms

Elevated temperature fracture behavior of polycrystalline materials may be divided into two categories: a) transgranular creep fracture; b) intergranular creep fracture.

The fracture process involves nucleation and growth of voids or cracks, viz. time-to-fracture, t_f, is essentially determined by the time required for the voids or cracks to form, grow and coalesce.

B.1 Transgranular Creep Fracture

In this mode of fracture, voids nucleate at second phase particles and grow by local creep of matrix. Ashby [1] has analyzed the fracture process and t_f is given by

$$t_f = \left[\varepsilon_n + \frac{1}{1.8}\,\frac{n}{n-1}\,\ln\left(\frac{0.7}{\sqrt{f_v}} - 1\right)\right]/\dot{\varepsilon}_c \qquad (1)$$

where ε_n an effective nucleation strain", f_v is volume fraction of second phase particles, $\dot{\varepsilon}_c$ is the creep rate and n is the stress exponent; the second term in the brackets is a post-nucleation ductility parameter which is the strain needed to grow matrix voids to final fracture instability.

B.2 Intergranular Creep Fracture

For intergranular fracture mode voids or cracks nucleate and grow in the plane *of* the grain boundary. Failure often occurs suddenly without neck formation. There are two types of intergranular fracture mechanisms: 1) triple point cracking; 2) cavitation fracture.

B.3 Triple Point Cracking

This mode of fracture is important at low temperatures and high stresses. Grain boundary sliding in polycrystals leads to stress concentration at the grain boundary triple junctions which may often be relieved by nucleation of a crack, and following nucleation, the crack grows by wedging action of the sliding process. Williams [10,11] has analyzed the fracture process and time-to-fracture is given by

$$t_f = \left[\frac{2\,\gamma_{eff}}{\sigma\, d\, \xi} + \varepsilon_n\right]\dot{\varepsilon}_c^{-1} \qquad (2)$$

here γ_{eff} is the effective surface energy of fracture, ξ is the ratio of the strain contribution due to sliding to the total strain, σ is applied stress and d is grain size. Note that the value of ε_n may not be the same for the various mechanisms; it is often set at zero for triple point cracking.

B.4 Cavitation Fracture

Cavitation fracture occurs under conditions of low stresses and high temperatures by nucleation and growth of cavities on grain boundaries

* Of course, primary creep rates are higher than the steady-state $\dot{\varepsilon}_c$ values used to estimate void nucleation times; hence, the ε_n value should be viewed as an 'effective' strain parameter in the present context.

Nucleation of creep cavities is not well understood. Several phenomenological models and considerable experimental evidence suggest that nucleation is strain controlled, and perhaps continuous during early stages of creep [12]. Other models are based on stress induced nucleation at favored "low-energy" sites [13]; however, even in this case some local strain, for example due to boundary sliding, is probably needed to produce stress concentrations sufficient to induce nucleation. Hence, it is likely that both stress and strain are necessary to nucleate creep cavities. For either mechanism there is a clear association between creep cavities and grain boundary microstructural features such as triple points, precipitates and slip-band intersections.

Because of this complexity, we have modeled the nucleation process parametrically. For unirradiated steels, creep cavity grain boundary densities are taken as a constant independent of stress and temperature. Typical values are $\sim 10^{10}$ m^{-2} or a mean cavity half spacing A = 5μm; this is consistent with experimental observation. In the case of irradiated alloys containing grain boundary helium bubbles, a stress dependent creep cavity model is used as discussed in Section 111. Nucleation times are calculated based on an effective nucleation strain divided by creep rate relation as in Equation (1).

The modes of cavitation fracture are further subdivided into two types depending on the cavity growth mechanism as: a) unconstrained diffusion growth; and b) constrained diffusion growth.

In general, these two mechanisms operate together in sequence; that is, the mechanism predicting lower cavity growth rate or higher time-to-fracture will be rate limiting.

8.4.1 Unconstrained Diffusion Growth

In this model the growth of cavities is assumed to occur by vacancy diffusion along the grain boundary. Diffusion growth model was first proposed by Hull and Rimmer [14] and has been further modified by several workers [15-17]. Raj et al. [18] have estimated time-to-fracture assuming a fixed number of cavities per unit area of the boundary as

$$t_f = \frac{0.05kT\,\lambda^3}{\delta D_B\,n\Omega} - \varepsilon_n/\dot{\varepsilon}_n \qquad (3)$$

where λ is the average half-spacing between the cavities. As in case of triple point cracking this model also assumes that the nucleation strain for cavities is negligible. In this case, the nucleation strains are often set equal to zero.

8.4.2 Constrained Diffusion Growth

For unconstrained diffusion growth of cavities the grain boundaries must be perfect sources for vacancies and the plating of atoms on the grain boundary must occur freely and uniformly. The latter condition requires that the cavity distribution is uniform along the grain boundary. These conditions may be met only rarely in practice. Commercial alloys such as 316 stainless steel contain intergranular precipitates which may inhibit the ability of grain boundaries to act as perfect sources for vacancies [19]. Further, the cavity spacing is not uniform and they are observed on a fraction of grain boundaries oriented normal to the stress axis [12,20]. These factors will result in cavity growth rate lower than that predicted by unconstrained diffusion growth model and give rise to constrained diffusion growth. Oyson [5] has analyzed this problem for a boundary containing cavities which is surrounded by boundaries without cavities. However, Edward and Ashby [6] have considered local constraints around a cavity in which the cavity growth rate is limited by a cage of surrounding material which is deforming by power law creep. The results of both these constrained growth models, although developed for different mechanisms, give roughly similar results. Thus, even though the cavity growth occurs by vacancy diffusion along the grain boundaries, its rate is limited by the creep of surrounding matrix. In this work we adopt the model of Edward and Ashby [6] model which is given by

$$t_f = \left[\varepsilon_n + \frac{1}{n} \ln \frac{(1+P)^n}{(1+P)^n - (1-n f_i)} \right] (\dot{\varepsilon}_c)^{-1} \qquad (4)$$

where f_i is the initial area fraction of grain boundary cavities and P is a dimensionless quantity given by

$$P = \frac{1}{10}\left[\frac{4\delta D_B \Omega}{\lambda^3 kT}\frac{\sigma_o}{\dot{\varepsilon}_o}\left(\frac{\dot{\varepsilon}_o}{\dot{\varepsilon}_c}\right)^{\left(1-\frac{1}{n}\right)}\right]^{\frac{2}{n}} \tag{5}$$

where $\dot{\varepsilon}_o$, σ_o are related to steady state creep rate, $\dot{\varepsilon}_c$, and stress, σ, as

$$\dot{\varepsilon}_c = \dot{\varepsilon}_o\left(\frac{\sigma}{\sigma_o}\right)^n . \tag{6}$$

Further it can be shown that

$$\frac{\sigma_o}{\dot{\varepsilon}_o}\left(\frac{\dot{\varepsilon}_o}{\dot{\varepsilon}_c}\right)^{\left(1-\frac{1}{n}\right)} = \frac{\sigma}{\dot{\varepsilon}_c} . \tag{7}$$

Substituting equation (7) into (5), the parameter P is given by

$$P = \frac{1}{10}\left[\frac{4\delta D_B \Omega}{\lambda^3 kT}\frac{\sigma}{\dot{\varepsilon}_c}\right]^{\frac{2}{n}} \tag{8}$$

Table 1 summarizes the rate equations for the high temperature deformation mechanisms, viz. dislocation creep and grain boundary sliding and equations for the times-to-fracture for the creep fracture mechanisms are given in Table 2. The basis for these equations is given in Reference [4].

Note that we have not exhausted all possible mechanisms; for example, at high stresses grain boundary cavities may grow by pure creep mechanisms [1]. Further, surface diffusion kinetics may be rate limiting in some cases [21,22]; in order to model this situation where elongated crack-like cavities may form a number of additional parameters are needed and the mathematical formulation is rather complex. Hence, we have treated only the less complex mechanisms in this work.

TABLE 1

HIGH TEMPERATURE DEFORMATION MECHANISMS

Mechanisms	Rate Equation for Steady-State **Creep** Rate
Dislocation **Creep**	$\dot{\varepsilon}_c = 10^{33} \left(\frac{\sigma}{G}\right)^6 \left[1+2\times10^{15} \left(\frac{\sigma}{G}\right)^6\right] \exp\left(-\frac{450000}{RT}\right) \ s^{-1}$
Grain Boundary **Sliding**	$\varepsilon_{gbs} = \xi \times \dot{\varepsilon}_c$
where :	$\xi = 5.7 \times 10^{-8} \left(\frac{\sigma}{G}\right)^{-2.2} \left(\frac{b}{d}\right)^{-1} \exp\left(\frac{100000}{RT}\right)$

TABLE 2

HIGH TEMPERATURE FRACTURE MECHANISMS

Mechanism	Equation for Time-to-Fracture	
Transgranular	$t_f = \{\varepsilon_n + \frac{1}{1.8}\frac{n}{n-1}\ln(\frac{0.7}{\sqrt{f_v}} - 1)\}\ (\dot{\varepsilon}_c)^{-1}$	[1]
Triple Point Cracking	$t_f = \left[\frac{2\ \gamma_{eff}}{\sigma\ d\ \xi} + \varepsilon_n\right] J\ (\dot{\varepsilon}_c)^{-1}$	[7]
Cavitation (Diffusion Control)	$t_f = \frac{0.05kT\ \lambda^3}{\sigma\Omega\delta D_B} + \frac{\varepsilon_n}{\dot{\varepsilon}_c}$	[13]
Cavitation (Creep Control)	$t_f = \left[\varepsilon_n + \frac{1}{n}\ln\ \frac{(1+P)^n}{(1+P)^n - (1-nf_i)}\right]\ (\dot{\varepsilon}_c)^{-1}$	[3]

C. Creep Fracture Map

A creep fracture map is constructed for annealed type 316 stainless steel with a 50-μm grain size using the method suggested by Ashby [1] as shown in Figure 2. The two mechanisms of cavitation fracture, viz. creep and diffusion control, operate sequentially *so* that the model predicting higher time-to-fracture will determine the mode of cavitation fracture. Further, the three fracture modes, viz. transgranular creep fracture, triple point cracking and cavitation fracture were assumed to be operating independently of each other, so that the failure occurs by the process predicting the lowest value for time-to-fracture. As noted by Ashby [1], this is an oversimplification of the real situation since mixed modes of fracture are very common in practice and the damage introduced by one process may influence operation of other modes of fracture. Further, it was assumed that at $\sigma/G \geq 6.3 \times 10^{-3}$ low temperature ductile fracture is dominant. The parameters used in the construction of the map are given in Table 3.

At this point it is important to note the influence of grain size on the fracture map. Of the three fracture mechanisms considered here, two of them, viz. transgranular creep fracture and cavitation fracture predict t_f at independent of grain size, the remaining process, triple point cracking, predicts $t_f \alpha 1/d$ (Table 2). Since the rate equation for grain boundary sliding has the same grain size dependence, t_f for this process will also be independent of grain size. This might suggest that the fracture map given in Figure 2 is independent of grain size and hence can be applied for 316 stainless steel of any grain size. However, the rate equations for dislocation creep and grain boundary sliding, given in Table 1, and used in the construction of the map were based on the analysis of experimental data over a narrow grain size range of 50-120 μm. Hence, the map given in Figure 2 is applicable over the same grain size range.

The fracture map is divided into several fields within which one fracture mode is dominant. At the field boundaries the fracture modes on either side of the boundary predict equal times to fracture. Contours of

TABLE 3

PARAMETERS USED IN THE CONSTRUCTION OF CREEP FRACTURE MAP

Parameter	Values	Reference
Ω	$1.20 \times 10^{-29}\ m^3$	
b	2.58×10^{-10}	
T_m	1810 K	
R	$8.314\ J\ mole^{-1}\ K^{-1}$	
k	$1.38 \times 10^{-23}\ J\ K^{-1}$	
G	$8.1 \times 10^{4}[1 - 4.7 \times 10^{-4}(T-300)]$ Mpa	[30]
D_ℓ	$4.4 \times 10^{-5} \exp(-280000/RT) m^2\ s^{-1}$	[31]
δD_B *	$3.6 \times 10^{-14} \exp(-193000/RT) m^3\ s^{-1}$	[31]
ε_n	0.10	
ε_n +	0.0	
f_v	0.05	
γ_{eff}	$70\ J\ m^{-2}$	[32]
λ	2.5×10^{-6} m	
f_i	10^{-3}	
γ_s	$2.572 - (T-273) \times 3.6 \times 10^{-4}\ J\ m^{-2}$	[29]

* for transgranular and creep controlled cavitation fracture modes.

\+ for triple point cracking and diffusion controlled fracture modes.

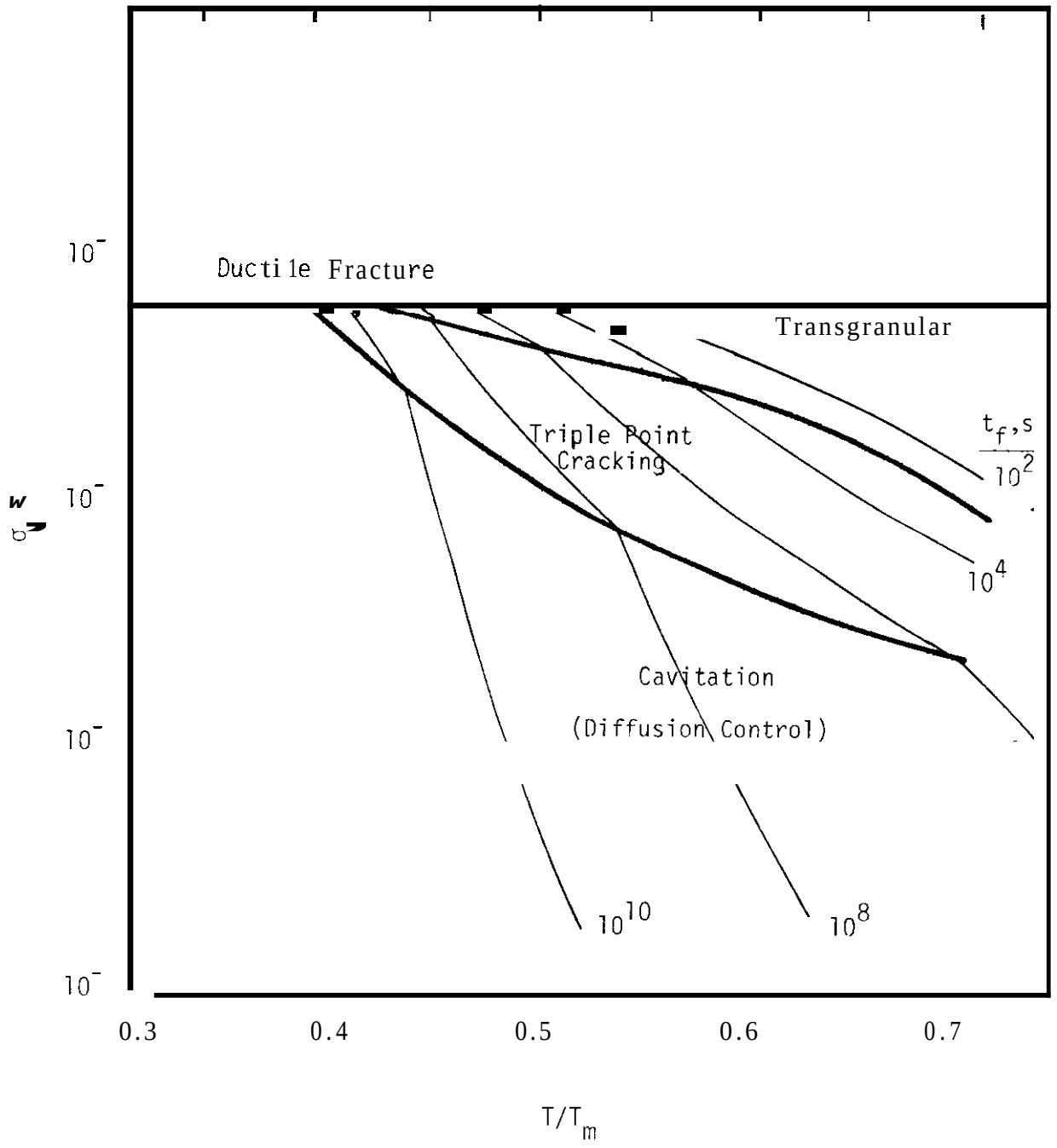

Figure 1. A creep fracture map for solution annealed 316 stainless steel having grain size of 50 μm developed earlier [4].

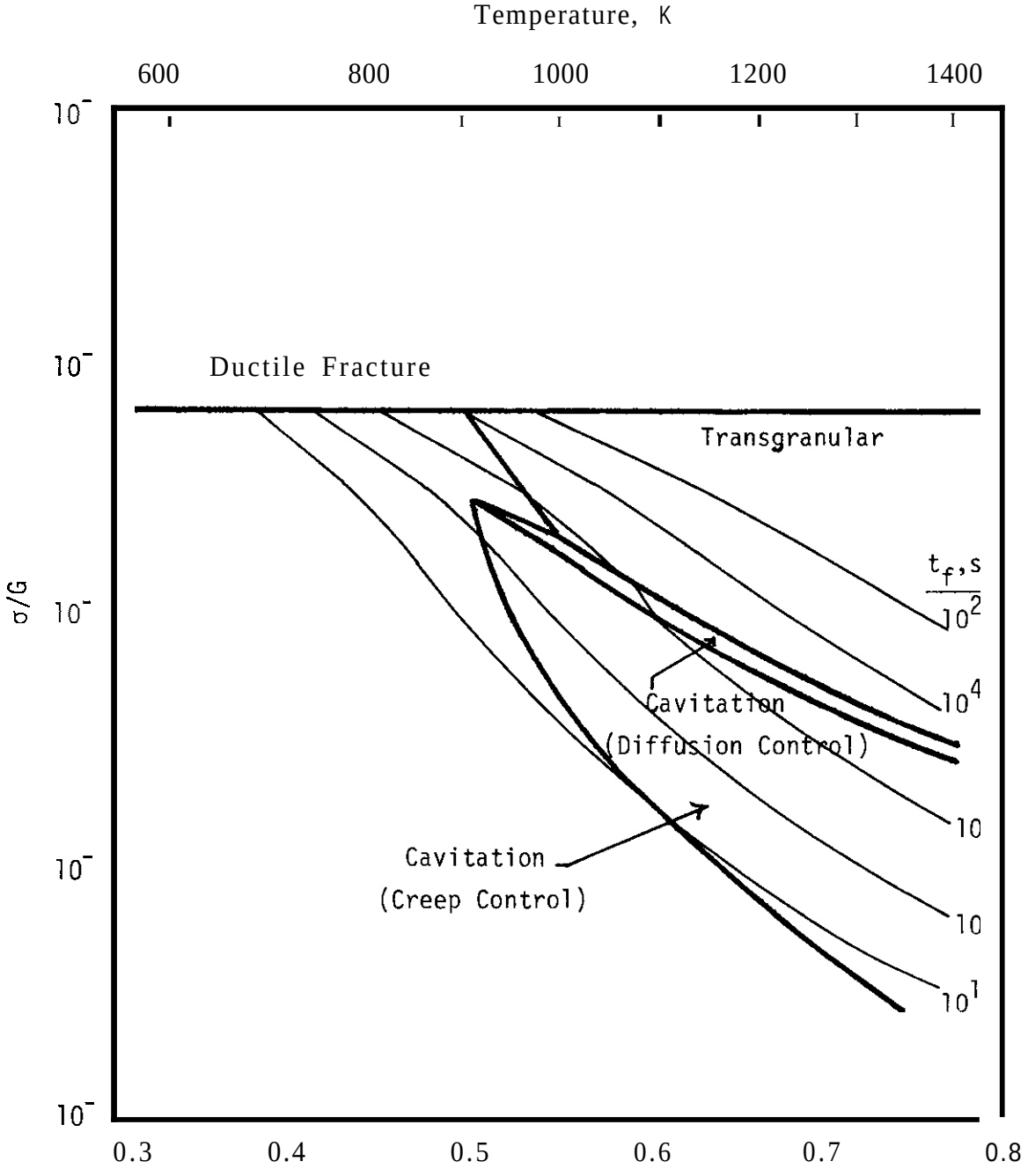

Figure 2. Revised creep fracture mao for solution annealed 316 stainless steel with grain size 50 μm treating creep controlled cavity growth.

constant time-to-fracture (10^2-10^{10} seconds) are shown on the map in the form of thin lines and these lines cover the entire range of practical interest.

The fracture map highlights several important features. Transgranular fracture occurs at high stresses and high temperatures, and generally has a small time-to-fracture ($t_f < 10^5$ sec.) and intergranular fracture is dominant at low stresses. Of the two modes of intergranular fracture, triple point cracking is dominant at high stresses and low temperatures in contrast to cavitation fracture which mainly occurs at low stresses and high temperatures. further, creep controlled cavitation fracture occurs over much wider range of stress and temperature than the diffusion controlled cavitation fracture mode. The region of diffusion controlled cavitation fracture is very narrow and is sandwiched between regions of transgranular creep fracture and creep controlled cavitation fracture. This would suggest that with increasing stress there will be changes in fracture mode from creep controlled cavitation fracture to diffusion controlled cavitation fracture to transgranular creep fracture. Such a behavior has been qualitatively suggested by Miller and Langdon [7]. Furthermore, the narrow region of diffusion .controlled cavitation fracture may be in part responsible for the absence of experimental evidence for this mode of fracture. It was also observed that the region of diffusion controlled cavitation fracture was fairly insensitive to cavity half-spacing parameter, A, over the range from 1 to 5 μm. This occurs because with change in A, the shift in boundary between transgranular and diffusion controlled cavitation fracture and that between diffusion and creep controlled cavitation fracture occur in the same direction. For example, lowering of A will result in lower t_f for both diffusion and creep controlled fracture modes and hence will shift the boundaries upward i.e. higher stresses. Hence, the region of diffusion controlled cavitation fracture is insensitive to cavity half-spacing parameters. Of course, the actual fracture times are a sensitive function of cavity spacing.

The creep fracture map shown in Figure 2 differs in several respects from the map shown in Figure 1. One important difference is in

the region of cavitation fracture. Figure 1 shows that diffusion controlled cavitation fracture is dominant at low stresses whereas the map developed in the present work indicates that creep controlled cavitation is dominant at low stresses and diffusion controlled cavitation fracture occurs over a very narrow range of stress and temperature. Another notable difference is in the region of triple point cracking. Figure 2 shows that triple point cracking is dominant at low temperatures where as figure 1 indicates that it is important even at high temperatures.

The predictions of the model based map were compared with the experimental data on creep fracture. The creep fracture of annealed 316 stainless steel with grain size in the vicinity of 50 μm has been investigated by several workers [3,23-25]. Logarithmic values of experimentally obtained times-to-fracture to base ten are superimposed on the fracture map as shown in figure 3. for simplicity only a few values of time-to-fracture, t_f, have been given. Excellent agreement is obtained between the experimental and the predicted values of time-to-fracture. Most significantly in contrast to Figure 1, the data in figure 2 spans all three significant creep fracture mode regimes, and the map is more consistent with fractography observations. further, in extrapolating beyond the data base to longer rupture times no large change in stress dependence is indicated.*

D. Creep Fracture of Helium Implanted and Irradiated Stainless Steel

While it is well established that the microstructural and the microchemical changes which take place in irradiated alloys significantly alter the fracture modes, creep ductilities and rupture times [8,24,25]. The processes are quite complex and are not well understood. Generally, creep ductility is reduced and intergranular failure is enhanced [24].

* These models do not contain all mechanisms which may be significant; for example, under some conditions the temperature (and perhaps stress) controlled rate at which brittle phases precipitate may govern fracture times.

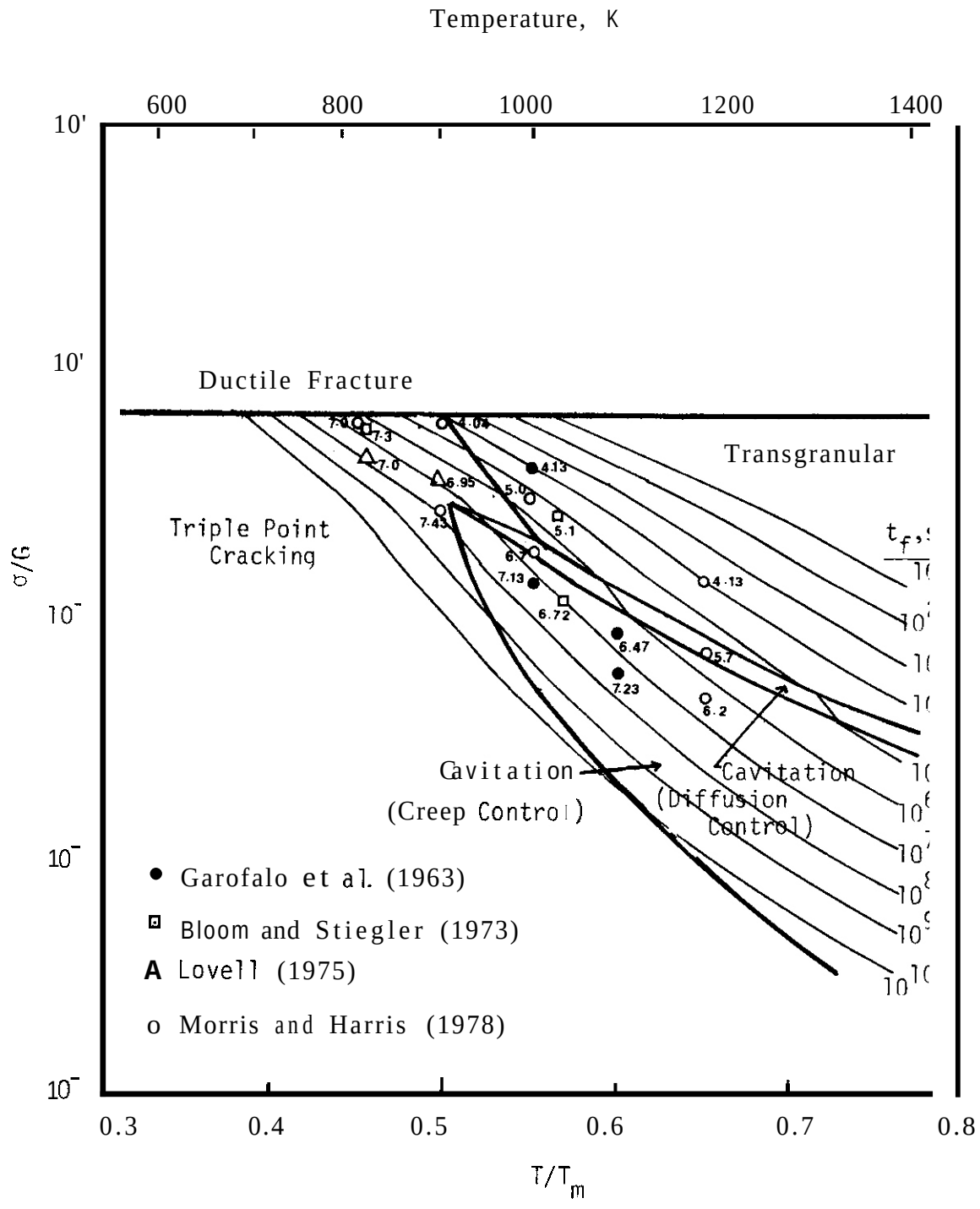

Figure 3. Comparison of the experimental creep rupture data and the model predictions for solution-annealed 316 stainless steel.

However, the effect of irradiation on rupture times is not simple. It is observed that irradiation under some conditions may retard rupture or may enhance it [9]. For conditions involving high helium concentrations, the dominant effect *of* irradiation is to significantly increase the number *of* grain boundary creep cavities because helium bubbles act as nucleation sites. Hence, irradiation and/or helium implantation promotes intergranular cavitation fracture mode. A creep rupture model is presented here based on a distribution of helium bubbles and creep constrained cavity growth mechanism.

In this model it is assumed that the helium bubbles on the grain boundaries act as preferred sites for cavity nucleation. Further, it is assumed that the helium bubbles are distributed in size and/or gas content. Various distributions might be assumed, i.e. gaussian, exponential, or others which have been derived specifically for gas bubble characteristics; further, one might utilize directly experimentally observed distributions.

For simplicity in the present work, the distribution of helium bubbles is assumed to be exponential such that the bubble density, N_b, is given by

$$N_b = No \cdot \exp(-R/R_o) \tag{9}$$

where N_o is the number of helium bubbles per unit area of grain boundary and R_o is the average radius of the helium bubble. The creep cavity density is given by

$$Nc = N_o \exp(-r^*/R_o) \tag{10}$$

where r^* is the critical radius given by the instability criterion for stress induced growth of bubbles as

$$r^* = \frac{0.77\ \gamma_s}{\sigma} \tag{11}$$

where γ_s is surface energy. Figure 4 illustrates this model schematically.

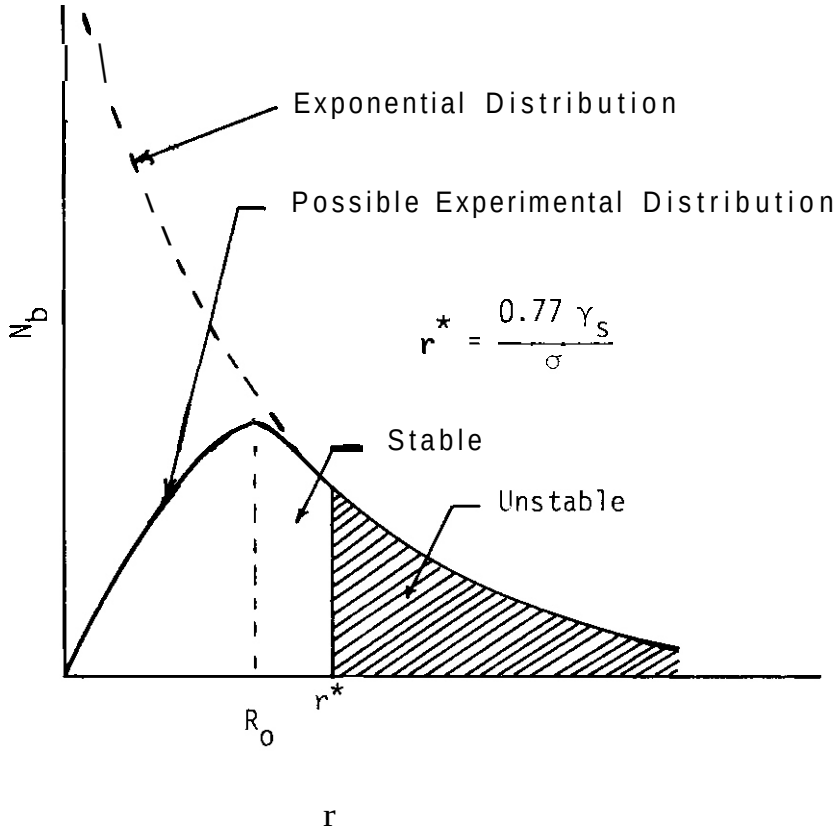

Figure 4. Schematic illustration *of* size distributions of helium bubbles and the fraction which form creep cavities.

Hence bubbles with $r > r^*$ act as creep cavities and grow under the influence of applied stress by creep constrained cavity growth mechanism. Thus the model predicts increase in cavity density at higher stresses. Further, the cavity half-spacing, λ, and the initial area fraction of grain boundary cavities, f_i, change with stress and are given by

$$\lambda = \frac{1}{2\sqrt{N_c}} \tag{12}$$

$$f_i = \left(\frac{R_o}{\lambda}\right)^2 \tag{13}$$

The time-to-fracture predicted by the model is given by

$$t_f = \left[\frac{1}{n} \ln \left\{\frac{(1+P)^n}{(1+P)^n - (1-nf_i)}\right\}\right] \left(\dot{\varepsilon}_c\right)^{-1} \tag{14}$$

where P is given by Equation (8). Equation (14) is the same as Equation (4) except the nucleation strain has been set to zero $\varepsilon_n = 0$.

The predictions of the model are compared with the post-irradiation creep rupture data of Andreko et al [26] and Wassilew and Schirra [27] and post-helium implantation creep rupture data of Sagues [28] on a Titanium stabilized austenitic stainless steel as shown in Fig. 5. The parameters used in the correlation are

$$N_o = 10^{13}\ m^{-2}$$
$$R_o = 3 \times 10^{-9}\ m$$

which are consistent with TEM observations of Sagues [28]. The creep rate, ε_c, for the material was fit to data given by Sagues [28] and is

$$\varepsilon_c = 0.35\ \sigma^9 \exp\left(-\frac{523000}{RT}\right) s^{-1} \tag{15}$$

where σ is in MPa. The surface energy, γ_s, for the alloy is taken as [29]

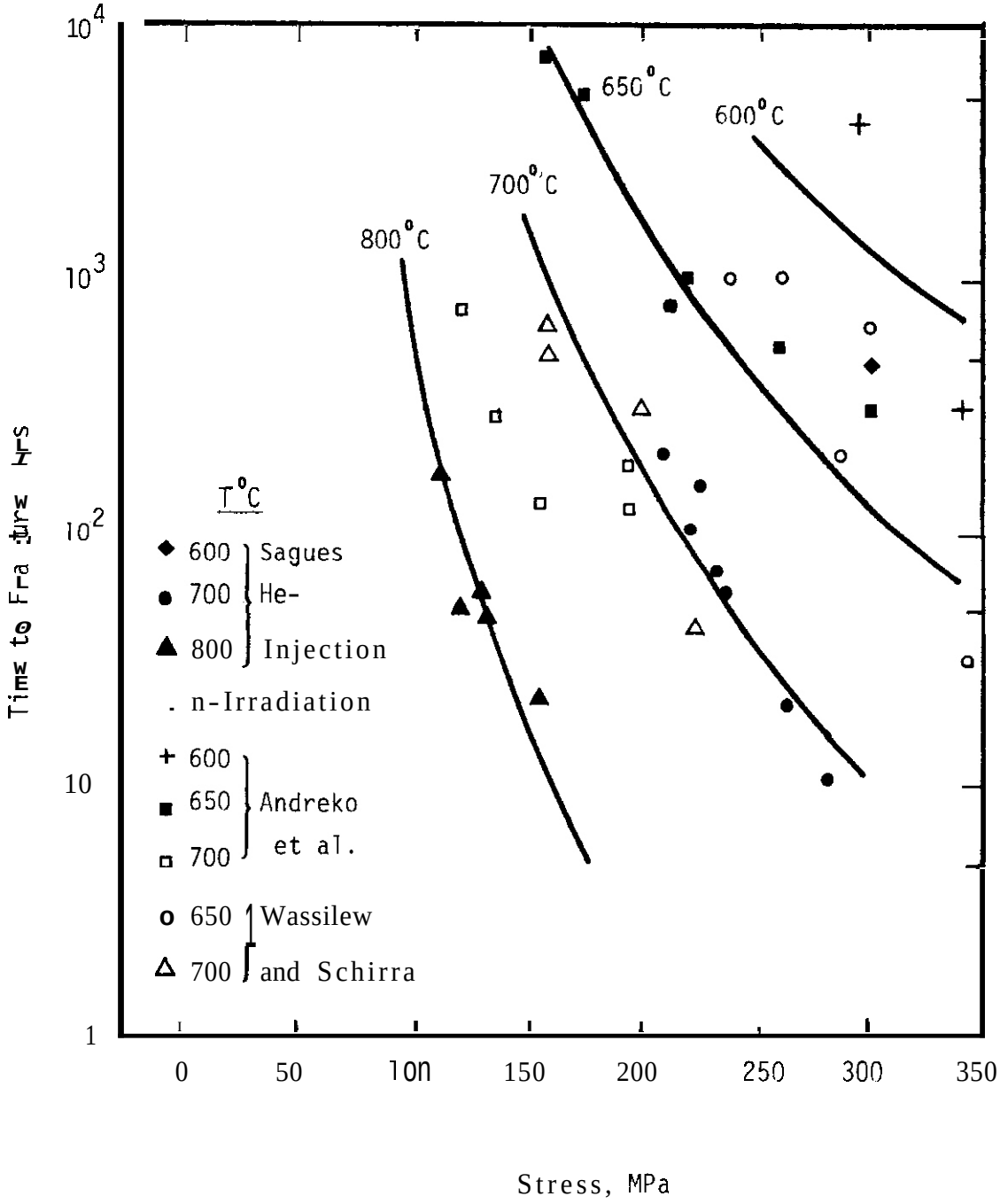

Figure 5. Correlation of model predictions and post-irradiation and helium injected creep rupture data for a titanium-stabilized stainless steel.

$$\gamma_s = 2.572 - (T-273) \times 3.6 \times 10^{-4} \text{ J m}^{-2}. \quad (16)$$

The times-to-fracture predicted by the model are in excellent agreement with the data particularly for temperatures from 650 to 800°C. Further, the creep ductilities predicted by the model are in the range of 0.1 to 3% which is consistent with the ductilities reported by Andreko et al [26] and Sagues [28]. However, a discrepancy is observed between the cavity spacings predicted by the nucleation model and the experimental observations. Sagues [28] has reported cavity spacings of 0.5 - 1.0 μm for a creep test at 130 MPa at 800°C. The nucleation model predicts cavity spacing decreasing with increase in stress from 0.75 μm at 350 MPa to 3.3 μm at 125 MPa at 800°C. However, these are somewhat smaller than typical creep cavity spacings of ∿ 5-10 μm in stainless steels.

The significance of the model as a correlation tool is as follows: simply using the minimum creep rate and rupture time data from relatively short-time tests, supplemented by direct microstructural observations when available, reasonable estimates of long-term behavior may be possible. Of course, this requires that the model accurately describe the basic mechanism of creep rupture for the material condition of interest.

The rupture times found by Sagues [28] for uninjected specimens were about the same as the injected specimens. However in this case, the mode of fracture was transgranular rather than grain boundary cavitation. Notably, this observation is consistent with the map for normal 316 solution annealed stainless steel shown in Figure 2; however, the significance of this agreement is difficult to establish due to both possible material differences, and the atypical form of Sagues' specimens (thin foils which failed by propagation of edge cracks).

As an exercise of the basic approach, however, a fracture map for 316 steels was constructed using Equations 9 to 14 and the parameters used to fit the irradiated/injected data; parameters for the noncavitation regimes and the deformation equations were taken as the same as in Section A2. (See Tables 1 and 2.) The map is shown in Figure 6. It is evident that the major effect of the irradiation/injection-induced microstructure is primarily a shift to lower temperatures in the regime of

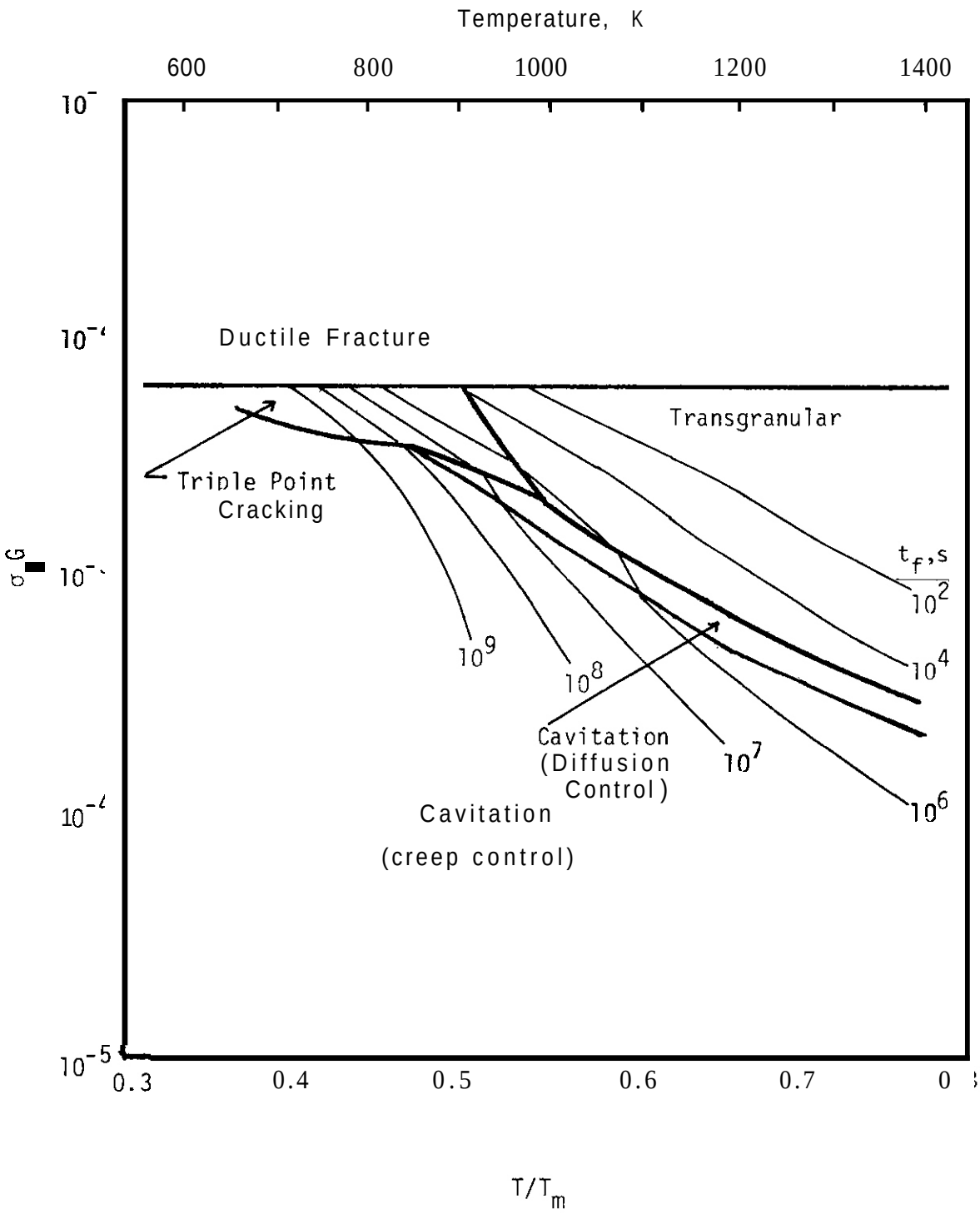

Figure 6. Modification of the creep fracture map given in Figure 2 by considering an exponential distribution *of* cavities.

dominance of creep controlled cavitational fracture and a small reduction in the rupture life in this fracture regime; the behavior in the transgranular regime is, of course, not affected.

We must emphasize that this preliminary model for PI creep rupture behavior does not treat a member of potentially important factors including effects of in-situ irradiation creep, competitive process of thermal, stress and irradiation induced damage structures (microstructural and microchemical), etc. The possible influence of these factors will be investigated in future research.

E. Summary and Conclusions

A creep fracture map for solution annealed 316 stainless steel has been developed. Unlike previous maps, the regime of creep constrained cavitation fracture is dominant at intermediate temperatures and low stresses. The predictions of the map are in good agreement with experimental data on creep fracture for the alloy.

A creep rupture model has been developed based on the nucleation of creep cavities on the distribution of helium bubbles and their growth by creep constrained grain boundary diffusion. Application of the model to both helium injected and neutron irradiated titanium stabilized stainless steel data also produced good agreement between the predicted and the measured post-injection/irradiation rupture times and ductilities.

VI. REFERENCES

1. M.F. Ashby, Report #CUED/C/MATS/TR34, Cambridge University, Engineering Department, Cambridge, England (1977).

2. W.E. White, I. LeMay and Bassett, "Elevated Temperature Properties of Austenitic Stainless Steels," Ed. A.D. Schaefer, p. 1, The American Society for Mechanical Engineers, New York (1974).

3. D.G. Morris and D.R. Harries, Metal Sci., 12, 1587 (1977).

4. S.S. Vagarali and G.R. Odette, Department of Energy, Quarterly Progress Report, May 1979.

5. B.F. Dyson, Can. Met. Quart., 18, 31 (1979).

6. G.H. Edward and M.F. Ashby, Acta Met., 27, 1505 (1979).

7. D.A. Miller and T.G. Langdon, Scripta Met., 14, 143 (1980).

8. M.L. Grossbeck, J.O. Stiegler and J.J. Holmes, Proceedings of International Conference Radiation Effects in Breeder Reactor Materials," Eds. M.L. Bleiberg and J.W. Bennett, p. 95, Scottsdale, Arizona (1977).

9. E.R. Gilbert and B.A. Chin, Nuc. Tech., 52, 273 (1981).

10. J.A. Williams, Phil. Mag., 15, 1289 (1967).

11. J.A. Williams, Acta Met., 15, 1559 (1967).

12. B.J. Cane and G.W. Greenwood, Metal Sci., 9, 55 (1975).

13. R. Raj, Acta Met., 26, 995 (1978).

14. D. Hull and R.E. Rimmer, Phil. Mag., 4, 673 (1959).

15. J. Weertman, Scripta Met., 7, 1129 (1973).

16. R. Raj and M.F. Ashby, Acta Met., 23, 653 (1975).

17. M.V. Speight and W. Beere´, Metal Sci. 9, 190 (1975).

18. R. Raj, and H.M. Shih and H.H. Johnson, Scripta Met., 11, 839 (1977).

19. I.G. Crossland and D.G. Harris, Metal Sci., 13, 55 (1979).

20. D.A. Miller and R. Pilkington, Met. Trans 9A, 489, (1979).

21. T.J. Channg, K.I. Kagawa, J.R. Rice and L.B. Sills, Acta Met., 27, 265 (1979).

22. S.H. Goods and W.D. Nix, Acta Met., 26, 739 (1978)

23. F. Garofalo, C. Richmond, W.E. Domis and F. Von Gemmingen, Proc. Joint International Conference on Creep, Institute of Mechanical Engineers, London (1963), p. 31.

24. E.E. Bloom and J.D. Stiegler, ASTM STP529, 360 (1973).

25. A.J. Lovell, Nuc. Tech., 26, 297 (1975).

26. K. Andreko, L. Schaefer, C. Wassilew, K. Ehrlich and H.J. Bergmann, Proceedings of International Conference on Radiation Effects in Breeder Reactor Structural Materials, Eds. M.L. Bleiberg and J.W. Bennett, p. 65, Scottsdale, Arizona (1977).

27. C. Wassilew and M. Schirra, European Conference on Irradiation Behavior of Fuel Cladding and Core Component Materials, p. 169, Karlsruhe, Germany (1974).

28. A.A. Sagues, Unpublished research.

29. L.E. Murr, "Interfacial Phenomena in Metals and Alloys," p. 125, Addison-Wesley, Reading, Massachusetts (1975).

30. H.J. Frost and M.F. Ashby, "Fundamental Aspects of Structural Alloy Design," edited by R.J. Jaffe and B.A. Wilcox, p. 27, Plenum Press, New York (1977).

31. D. Juve-Duc, D. Trehenx and P. Guiraldeq, Scripta Met., 12, 1107 (1978).

32. D.G. Morris and D.R. Harries, J. Mater. Sci., 12, 1587 (1977).

VIII. FUTURE WORK

Deformation and fracture maps will be developed for unirradiated 20% CW 316 stainless steel. Data on post-irradiation creep rupture of 20% CW 316 will be used, along with the model, to develop a preliminary map for this material condition.

A large creep rupture data base is being assembled from the literature for both irradiated and unirradiated stainless steels, including some in-situ data. This data will be analyzed with the model to test its ability to correlate and predict data as described above.

Finally, the model will be extended to treat other irradiation induced mechanisms - e.g. irradiation creep.

I. PROGRAM

Title: Mechanical Properties

Principal Investigator: R. H. Jones

Affiliation: Pacific Northwest Laboratories
Operated by Battelle Memorial Institute

II. OBJECTIVE

The purpose of this work is to determine the effect of irradiation on the grain boundaries segregation of minor and impurity elements in fusion reactor alloys.

III. RELEVANT DAFS PROGRAM PLAN TASK/SUBTASK

SUBTASK II.C.14 Models of Flow and Fracture Under Irradiation

SUBTASK II.C.I Effect of Material Parameters on Microstructure

IV. SUMMARY

The effect of radiation on surface segregation of minor and impurity elements has been studied in four alloys. Radiation induced surface segregation of phosphorus was found in both 316 type stainless steel and in Nimonic PE-16. Segregation and depletion of the other alloying elements in 316 stainless steel agreed with that reported by other investigators. No significant radiation enhanced or induced segregation was observed in the ferritic HT-9 or Ti-6A1-4V alloy.

V. ACCOMPLISHMENTS AND STATUS

A. Radiation Enhanced Segregation to Grain Boundaries - J. L. Brimhall (PNL).

The influence of irradiation on the segregation or depletion of minor and impurity elements was investigated in four alloys: 316 type stainless steel, Nimonic PE-16, Ferritic HT-9 and Ti-6Al-4V. The alloys were heat treated to a stable metallurgical condition prior to ion bombardment with 5 MeV Ni^{++} ions. The dose at the surface was 2 atom displacements per atom (dpa) and the irradiation temperature varied from 450-650°C, depending on the alloy. Auger Electron Spectroscopy (AES) combined with a continuous sputter removal of the surface was used to determine the concentration gradient of elements away from the surface region. A maximum of six elements could be continuously monitored during the sputter profiling. A complete AES scan for all elements was periodically taken during the sputter removal. Thermal control specimens that were annealed in the irradiation chamber for a time equivalent to the irradiation time were also analyzed.

Enhanced segregation of Si and depletion of Mo near the surface after irradiation was noted in the 316 stainless steel, Fig. 1. Some enhancement of nickel and depletion of iron as a result of irradiation was also observed but are not shown for the sake of clarity. These observation are in qualitative agreement with the results of similar studies on 316 stainless steel reported by Okamoto and Rehn.[1] There was no significant effect of irradiation on the Cr or S concentration profiles. Phosphorus was not analyzed in the sputter profiling but the AES scans taken at periodic time intervals do show an enhanced phosphorous concentration just below the surface, Table 1. Evidence of phosphorous segregation to grain boundaries in neutron irradiated 304 stainless steel has been reported.[2]

An enhanced surface segregation of phosphorous and surface depletion of molybdenum were the main effects of the irradiation in PE-16, Fig 2. These results are similar to those from 316 stainless steel. Al, Ti, Cr and S were also analyzed but there was no marked difference between the irradiated and the thermal control specimens. In both cases, Al, Ti and

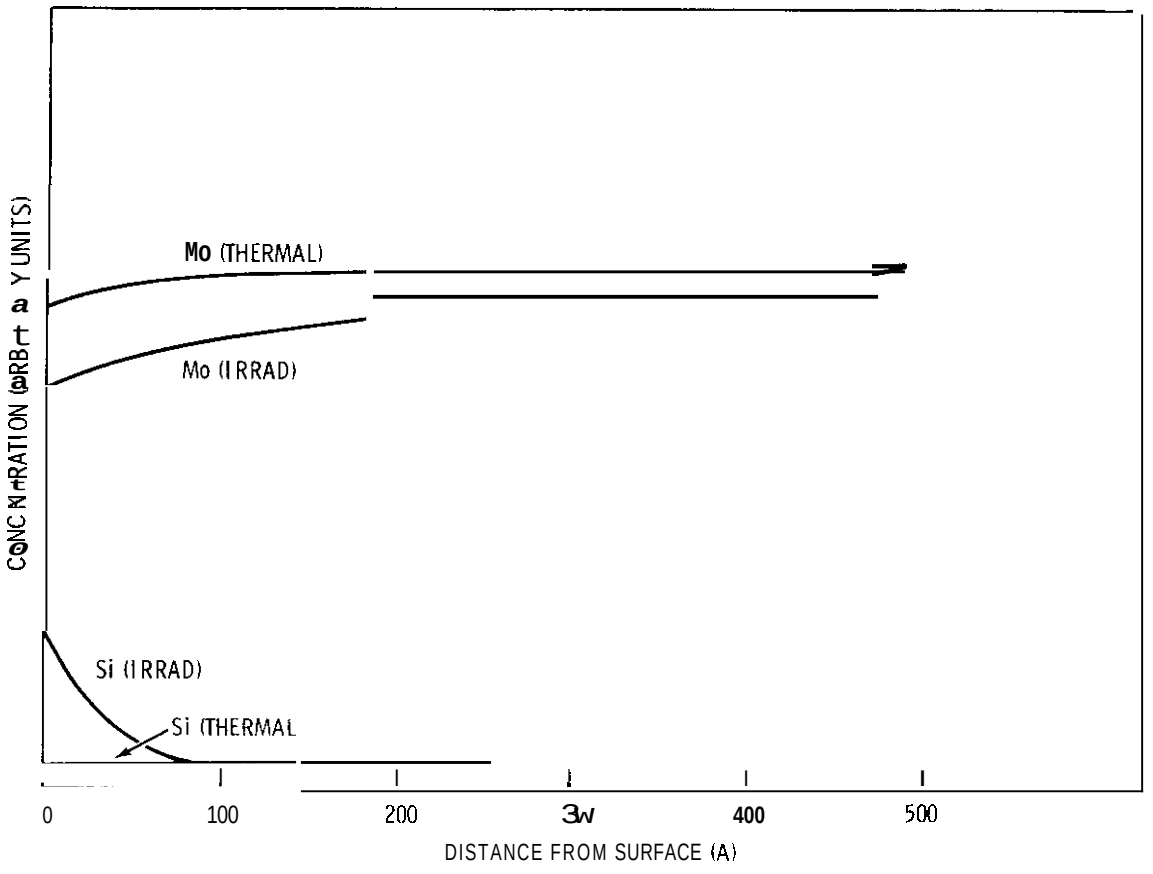

FIGURE 1. AES Sputter Profiles of Si and Mo in Type 316 Stainless Steel, Ion Bombarded at 500°C. Profiles of thermal specimen also shown.

TABLE 1. PHOSPHORUS CONCENTRATION IN 316 STAINLESS STEEL AT VARIOUS DEPTHS FROM SURFACE

	% Phosphorus		
Condition	Surface	20-40A	180-250A
Irrad 500°C	0.4	7.75	0.09
Irrad 600°C	0.6	1.63	0.22
Non Irrad (500°C)	0.5	0.37	0.27

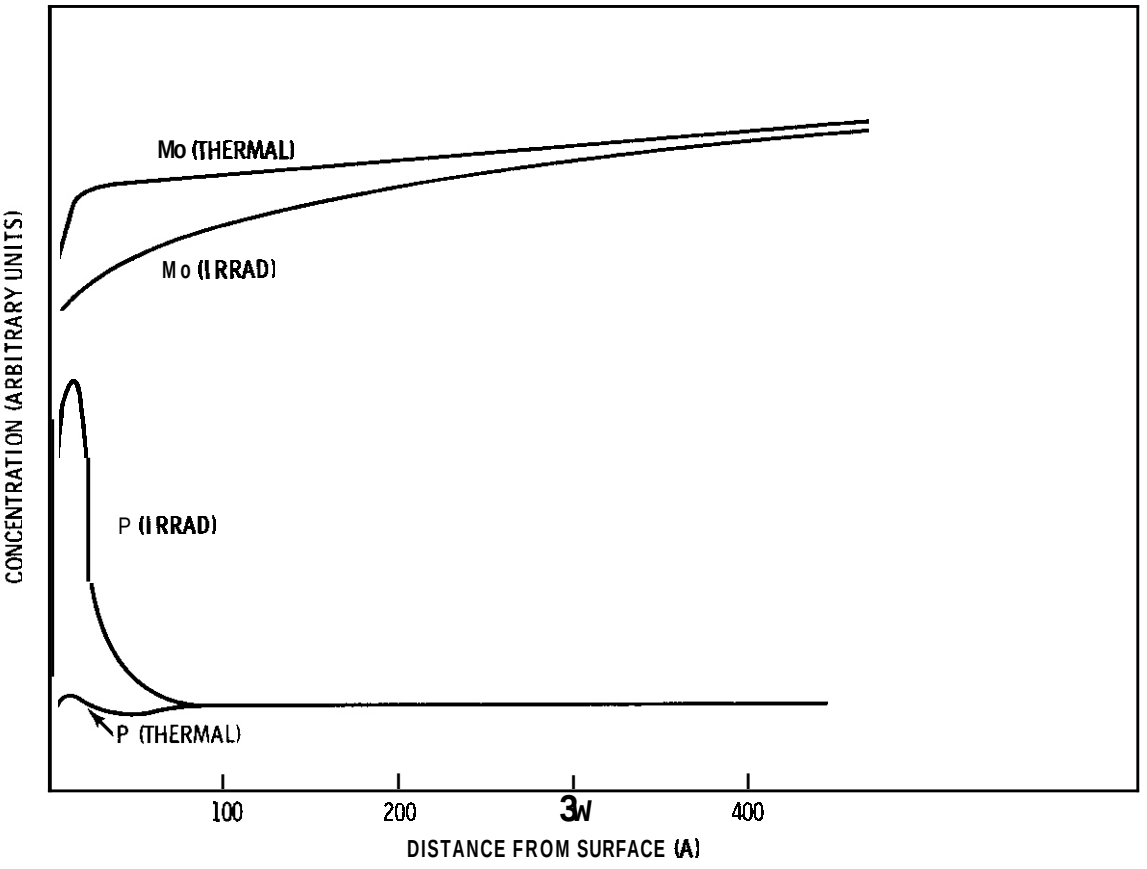

FIGURE 2. AES Sputter Profiles of P and Mo in **PE-16,** Ion Bombarded at 500°C. Profiles of thermal control specimen also shown.

Cr showed marked segregation very close to the surface and are probably combined in an oxide.

Neither the HT-9 nor the Ti-6Al-4V alloy showed any marked radiation enhancement of a segregation phenomena. Si, S, P, N, Mo and Cr were analyzed in the HT-9 and the results were similar in both the irradiated and the thermal control specimens. However, there was some evidence that nitrogen surface segregation was enhanced by irradiation. In the titanium alloy, carbon, oxygen and sulfur showed high surface concentration in both the irradiated and the thermal control specimens. There was also evidence for significant oxide formation which greatly complicated the analysis.

VI. REFERENCES

1. P. R. Okamoto, and L. E. Rehn, "Radiation-Induced Segregation in Binary and Ternary Alloys," J. Nucl. Mat. 83, p. 2 (1979).

2. R. E. Clausing and E. E. Bloom, "Auger Electron Spectroscopy of Fracture Surfaces in Irradiated Type 304 Stainless Steel," Grain Boundaries in Engineering Materials, J. L. Walter, J. H. Westbrook and D. A. Woodford, eds., pp. 491-506, Claitors Pub Div., Baton Rouge, 1975.

VII. FUTURE WORK

Experiments on 316 type stainless steel will be repeated with particular emphasis on the analysis of phosphorous segregation using sputter profiling. Some experiments on HT-9 will also be repeated to confirm the current observations.

CHAPTER 4

CORRELATION METHODOLOGY

I. PROGRAM

Title: Irradiation Response of Materials

Principal Investigators: S. Wood, J. A. Spitznagel, W. J. Choyke
Affiliation: Westinghouse Research and Development Center

II. OBJECTIVE

The objective of this work is to assess the phenomenology and mechanisms of microstructural evolution in materials exposed to simultaneous helium injection and creation of atomic displacement damage by a second ion beam.

III. RELEVANT DAFS PROGRAM TASK/SUBTASK

SUBTASK II.C.1, II.C.2, II.C.3, II.C.5, II.C.9, II.C.18.

IV. SUMMARY

Analytical electron microscopy of acicular precipitates in dual ion bombarded SA 316 SS shows them to be rich in Ni, Si and P. The results are in qualitative agreement with acicular precipitate compositions in austenitic stainless steels after long term aging or fission reactor irradiation. An unexpected inhomogeneity in Ti concentration in SA 316 from the MFE heat has been observed. Regions with high Ti content exhibit more than one precipitate morphology and do not experience rapid anomolous cavity growth. Parametric studies of the dependence of critical cavity size on the magnitude and temperature dependence of surface energy and Van der Waals exclusion volume are reported. It is demonstrated that large variations in these parameters have only a minimal effect at temperatures below $\sim$ 650°C.

V. ACCOMPLISHMENTS AND STATUS

A. Precipitation in 316 SS

Acicular or needle-like precipitates have been observed in aged,[1] neutron-irradiated[2] and ion-bombarded[3,4] austenitic stainless steels. Bentley and Leitnaker[1] observed a phase in 321 SS whose composition was 27Ti-4Cr-27Fe-17Ni-7P and 18As. In comparison, Lee et al[2] investigated 316 + Ti and observed a phase whose average composition was 16Si-19Cr-29Fe-27Ni-5P-4S. The elements Si, P, S and Ni were all highly enriched in this phase with respect to the composition of the base matrix. These results are in good agreement with some recent data obtained in this study from SA 316 SS from the MFE heat. The specimen was solution annealed at 1050°C for 0.5h prior to being simultaneously bombarded with 20 MeV O^{+4} and $\leq$ 2 MeV helium at 600°C. All microscopy and compositional data were obtained at a section depth corresponding to $\sim$ 4 dpa and 83 appm He (i.e. $\sim$ 1.2 x 10^{-4} dpa/s and 2.4 x 10^{-3} appm He/s). Figure 1 shows some typical scanning transmission electron microscopy (STEM) images of the acicular phase observed in this material, together with the locations of various energy dispersive X-ray spectroscopy (EDS) analyses (performed with a 100 Å diameter probe size on a Philips 400 STEM). Comparison of the compositions at points 5 and 7 or 6 and 8, for example, always revealed an enrichment of Si, P and Ni at the precipitate (i.e. at 5 and 6). Thus, although it is recognized that, for an in-foil analysis of this type, the matrix is contributing a large portion of the total X-ray counts, the statistical evidence clearly shows that the precipitates are enriched in these elements. Figure 2 compares typical EDS spectra from matrix and precipitate illustrating this point. Quantitative compositional information cannot be obtained without extracting the second phase particles from the matrix. This technique is currently being developed and further work will follow. It should also be noted that the Ni, Si, P enrichment is in agreement with earlier unreported data on Si^{+6} bombarded 316 SS. Orientation of the precipitates was determined (Figure 3) to be along <001> directions in the 316 SS which

agrees with previous results in 321 and 316 + Ti.[1,2] (Note that the area shown in Figure 3c had a (001) orientation).

A further interesting fact revealed by the EDS analyses (Figure 2) is the very high Ti content of the austenite matrix (calculated by the thin foil program to be ~ 2.3 to 2.7 wt%). This value is not at all consistent with the bulk matrix composition determined earlier to be < 0.001 wt% by spectrographic analysis.[5] It is also not due to either specimen contamination during preparation or to some anomalous effect in the microscope because a 304 SS specimen examined under identical conditions yielded a composition with absolutely no Ti. Thus, it is deduced that the MFE heat of 316 SS is not as homogeneous as previously thought. Additional matrix analyses on other specimens are now in progress to elucidate this point. In particular, specimens showing the anomalous cavity growth phenomenon[4] are being examined. The oxygen bombarded specimen investigated in this report was bombarded under conditions expected to yield the explosive growth observed at 600°C in samples damaged by Si^{+6} ions. However, the resultant microstructure was instead composed of a very high number density of small bubbles (generally < 60 Å diameter) with only a few larger cavities (Figure 3). Many of the bubbles are associated with precipitates, which appear to be of two types: the acicular phase examined by EDS plus small, blocky particles (indicated by the arrows) often sympathetically nucleated with the needle precipitates. It is now suspected that the equiaxed phase is MC carbide which precipitated because of the high Ti content of the matrix and that the basic matrix chemistry prevented explosive cavity growth from occurring.

B. Variation of Maximum Equilibrium Bubble Size with Surface Energy and Van der Waals Constant

The concept of a critical cavity size (D_c^c) for a transition from gas-driven to bias-driven cavity growth and the necessity of experimentally obtaining an estimate of D_c^c to determine helium partitioninq was discussed in a previous report.[6] A multi-key access computer code has been used

continually in conjunction with the dual ion experiments on 316 SS to calculate D_c $(= 2r_c)$, the maximum equilibrium bubble diameter which is regarded as an upper estimate of D_c^c.[7,8] The code utilizes the Van der Waals equation of state to calculate the number of helium atoms in a cavity of a given size:

$$n_1 = \frac{8\pi r_i^2 \gamma}{3(RT + 2B'\gamma/r_i)} \qquad (1)$$

where:

n_i = number of helium atoms in a bubble of radius r_i
r_i = radius of bubble in class i in cm
γ = surface energy in ergs cm^{-2}
R = gas constant = 1.38 x 10^{-16} erg $atom^{-1}$ deg^{-1}
T = absolute temperature in °K
B' = Van der Waals constant in cm^3/atom

By means of an iterative procedure, the code then sums n_i over all cavities in the size distribution, assuming that even those cavities with $D > D_c$ contain an amount of helium sufficient to have stabilized them as equilibrium bubbles when their diameter was equal to D_c^c. The process is continued until the helium accounted for is equal to the amount of helium available. In its most simple form, the code uses the total implanted helium concentration at that section for this latter value. However, a subsequent modification was made whereby some of the helium was partitioned to dislocations.[8] The fraction of helium partitioned to cavities was defined as

$$Q^{-1} = \frac{\sum_i 4\pi r_i N_i}{\sum_i 4\pi r_i N_i + \rho_D} \qquad (2)$$

where:

N_i = number of cavities in class i
ρ_D = dislocation density

Thus, when $Q = 1$, all helium was allocated to cavities and when $Q \neq 1$ ($Q > 1$) some of the helium was partitioned to dislocations, depending on ρ_D. Curves in this report are simply labeled according to $Q = 1$ or $Q \neq 1$ consistent with the above approach.

Since there has recently been some concern expressed about utilization of specific surface energy values and values of B', in this reporting period the code was used to investigate the dependence of D_c on γ and B' for the cavity size distributions observed in dual-ion bombarded 316 SS. Three material conditions were investigated - SA 316 SS (1050°C for 0.5h), 20% CW 316 SS and aged 316 SS (50%cold rolled + SA at 1050°C for 0.5h + aged at 800°C for 10h). Cavity size distributions were obtained from sections corresponding to 12-15 dpa and appm He/dpa ratio of 11-15. Results for the aged 316 SS are presented in Figures 4, 5 and 6. Five different surface energy - temperature dependencies were used. In Figure 4a, γ was set at 1000 ergs/cm^2 and made independent of T; in Figure 4b, γ was set at 1200 ergs/cm^2 at 750°C and made linearly dependent on T with a slope of -1.9 ergs . cm^{-2} . deg^{-1}; similarly, in Figures 4c and 5b, γ was set at 2750 ergs/cm^2 or 500 ergs/cm^2, respectively, at 750°C with the same slope; and finally, in Figure 5a, γ was set at 500 ergs/cm^2, constant. All curves presented in Figures 4 and 5 were calculated with B' = 16.4 cm^3/atom. Figures 4c and 6b represent data obtained 'normal' values for γ and B' (i.e. those which are believed to be most accurate). Comparison of Figures 4 and 5 shows that, for temperatures $\leq$ 650°C, there is essentially no change in D_c with γ for either $Q = 1$ (no partitioning to dislocations) or $Q \neq 1$ (partitioning included). At 700°C, some dependence was observed for both cases, but more for $Q = 1$. Variation of B' to simulate softer or harder interatomic potentials (within the range of published values) (Figure 6) utilizing the normal γ values (2750 ergs/cm^2 at 750°C, etc.) yielded no dependency of D_c. All curves show the typical temperature dependence predicted by the rate theory for D_c^C.[9] These results, particularly for the drastic surface energy changes invoked were rather surprising, and it is believed that their explanation is directly linked to the cavity size distributions

observed in these specimens, as well as the inherent dependencies within the Van der Waals equation.

Inspection of equation 1 intuitively suggests that a decrease in γ for a given r_i, T and B' should yield a reduction in n_i since the γ-term in the denominator is small. A quick calculation, taking T = 923°C, r_i = 3.5 nm, B' = 16.4 x 10^{-24} cm^3/atom and γ = 2925 and 500 ergs/cm^2, shows that the corresponding n_i values are *7.48* x 10^3 and 2.95 x 10^3 atoms, respectively. Thus, since n_i does decrease with decreasing γ (by a factor of 2.5 in this example), D_c is expected to increase as γ decreases, and vice versa. This trend was, in fact, observed (see Table 1 for better clarification).

At 650°C (923°K), the change in D_c is relatively small, however, because (a) D_c is not large even for γ = 2925 ergs/cm^2 and (b) because of the shape of the size distribution (Figure 7a). This specimen has a bimodal cavity size histogram with a high number density of small cavities. Thus, since D_c (γ = 2925 ergs/cm^2, Q = 1) is located at the center of this large peak in the number density, the extra helium atoms made available to other cavities by a reduction in γ are rapidly taken up (numerically) by the next size class and thus, no extreme change in D_c is manifested. This argument is further supported by the Q $\neq$ 1 case, since here, D_c is of course smaller for γ = 2925 ergs/cm^2 and thus has an even higher relative number density in the next size class to accommodate the 'extra' helium.

At 700°C, the cavity size histogram is not bimodal and *is* more bell-shaped (Figure 7b). Here, the lack of a strong dependence of D_c on y is due to the high number of cavities with $D_i > D_c$ (which, according to the code calculation, all contain the same number of helium atoms as a bubble with $D_i = D_c$ because they passed through this size class). Here, changes in n_i for a size class around $D_i = D_c$ will be accommodated by the remainder of the cavities in the distribution, although not quite so rapidly as in the previous example because D_c is much larger (29.6 nm

for γ = 2750°C at 750°C). A quick calculation shows that for T ≈ 973°K, γ = 2925 ergs/cm^2 and r_i = 15 nm, n_i = 2.69 x 10^6 atoms. However, reducing γ to 500 ergs/cm^2 reduces n_i to 6.49 x 10^4 atoms - a very large change compared to that which occurs for the smaller bubbles. Thus, one anticipates a greater dependence of D_c on γ for the distribution shown in Figure 7b compared to that in Figure 7a which is what is observed.

Figure 6 and Table 2 document the variation of D_c with B' and temperature for γ = 2750 ergs/cm^2 at 750°C and a linear variation of γ with T. For both Q = 1 and Q ≠ 1 (no partitioning and partitioning to dislocations, respectively), essentially no dependence of D_c on B' was found. This is because the dependence of n_i on B' is inherently weak in equation 1, particularly for $r_i \geq$ 15 nm since the second term in the denominator then becomes very small. Thus, it could be predicted that at 700°C, where D_c is comparatively large, its dependence on B' should be less than at the lower temperatures, which was indeed observed. It is thus concluded that, despite current controversy about the value of B' utilized for these types of calculations, for the cavity size distributions observed in the 316 SS, this is not an important consideration.

Results obtained for SA and CW 316 SS were very similar to those presented for the aged material. Representative curves are shown in Figures 8 and 9 for the case where B' = 16.4 cm^3/atom and γ has a linear temperature dependence such that γ = 2750 ergs/cm^2 at 750°C. Specimen 105 (Figure 9, 600°C) was a beam history experiment in which the helium was implanted during the first and last quarters of the Si^{+6} bombardment only, although the total amount of helium implanted was the same as the other specimens (∼ 20 appm at that section). Fluences were 2.5-5 dpa. Figure 9 suggests that this sample has a much higher D_c value than might be predicted by the theory for dual *ion* bombardment because of the increase in the curve at 600°C.[9] This is contrary to some recent results in 304 SS[10] which yielded little dependence of D_c on beam history for a given fluence, helium concentration and temperature, and this result in the 316 SS is being analyzed further. With the exception

of data points from this specimen, both 20% CW and SA 316 SS yielded a dependence of D_c on temperature predicted by the rate theory for the critical cavity size, D_c^c. It is interesting to note that for a given temperature, D_c appears to be relatively insensitive to the condition of the material (compare Figures 6b, 8, 9).

VI. REFERENCES

1 J. Bentley and J. M. Leitnaker in "The Metal Science of Stainless Steels," Met. Soc. AIME (1978), Edited by E. W. Collings and H. W. King, pp. 70-91.

2. E. H. Lee, P. J. Maziasz and A. F. Rowcliffe, "The Structure and Composition of Phases Occurring in Austenitic Stainless Steels in Thermal and Irradiation Environments," to be published in the Proceedings of a Symposium on "Irradiation Effects on Phase Stability," TMS-AIME, 1981.

3. W. J. Choyke, J. N. McGruer, J. R. Townsend, J. A. Spitznagel, N. J. Doyle and F. J. Venskytis in "Fusion Reactor Materials," Proc. of the First Topical Meeting on Fusion Reactor Materials, Miami Beach, Florida, Jan. 1979 (North Holland)

4. S. Wood, J. A. Spitznagel and W. J. Choyke, DAFS Quarterly Report No. 7, November 1979.

5. S. Wood, J. A. Spitznagel, W. J. Choyke, N. J. Doyle, J. N. McGruer and J. R. Townsend. "Microstructural Oevelopment in Dual-Ion Bombarded 316 SS," to be published in the 10th International Symposium on Effects of Radiation on Materials, ASTM, 1981.

6. S. Wood, J. A. Spitznagel and W. J. Choyke, DAFS Quarterly Report No. 8, October-December 1979.

7. S. Wood, J. A. Spitznagel and W. J. Choyke, DAFS Quarterly Report No. 9, January-March 1980.

8. J. A. Spitznagel, S. Wood and W. J. Choyke, DAFS Quarterly Report No. 10, April-June 1980.

9. M. R. Hayns, M. H. Wood and R. Bullough, J. Nuc. Mat., Vol. 75 (1978), p. 241.

10. W. J. Choyke, J. A. Spitznagel, S. Wood, N. J. Doyle, J. N. McGruer and J. R. Townsend, "Implantation Rate Effects on Microstructure," to be published in Nuclear Instruments and Methods, 1981.

VII. FUTURE WORK

Analytical microscopy measurements of precipitate and matrix compositions and crystal structures at different helium levels and damage rates in dual ion bombarded 316 SS (SA, 20% C.R. and aged conditions) will continue. A set of algorithms to deduce self-consistent average helium distances from microstructural data will be developed.

VIII. PUBLICATIONS

None.

TABLE 1

MAXIMUM EQUILIBRIUM BUBBLE SIZES IN AGED 316 SS
CALCULATED WITH B' = 16.4 x 10^{-24} cm^3/atom

Specimen	Temp °C	γ=1000 ergs/cm^2 constant		γ=500 ergs/cm^2 constant		γ=500 ergs/cm^2 at 750°C		γ=1200 ergs/cm^2 at 750°C		γ=2750 ergs/cm^2 at 750°C	
		Q = 1	Q ≠ 1	Q = 1	Q ≠ 1	Q = 1	Q ≠ 1	Q = 1	Q ≠ 1	Q = 1	Q ≠ 1
113 2*	850	5 ≤	4 ≤	6.7	5.3	5.7	4.6	5.2	4.3	4.9	4.0
115.1	900	≅ 4	3 ≤	13.4	4.3	10.4	3.8	7.8	3.4	6.3	3.2
117.1	950	≤ 3	≅ 4	11.8	6.6	9.9	5.9	7.4	5.0	6.4	4.6
119.2	000	44 0	1 5	62.7	23.2	56.6	21.4	39.2	17.3	29.6	13.2

*Indicates Specimen 113, Se tion z

TABLE 2

MAXIMUM EQUILIBRIUM BUBBLE SIZES IN AGED 316 SS
CALCULATED WITH γ = 2750 ergs/cm^2 AT 750°C

Specimen	Temp °C	$B' = 13.6 \times 10^{-24}$ cm^3/atom $\times t^{1/3}$		$B' = 16.4 \times 10^{-24}$ cm^3/atom $\times t^{1/3}$		$B' = 19.2 \times 10^{-24}$ cm^3/atom $\times t^{1/3}$	
		Q = 1	Q ≠ 1	Q = 1	Q ≠ 1	Q = 1	Q ≠ 1
113.2*	550	4.6	3.8	4.9	4.0	5.1	4.2
115.1	600	5.8	3.0	6.3	3.2	6.9	3.4
117.1	650	6.0	4.4	6.4	4.6	6.7	4.8
119.2	700	28.8	12.7	29.6	13.2	30.3	13.6

* Indicates Specimen 113, Section 2.

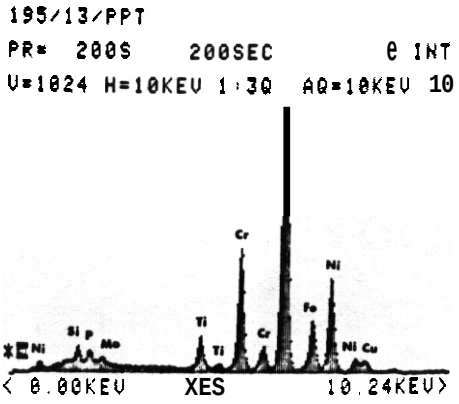

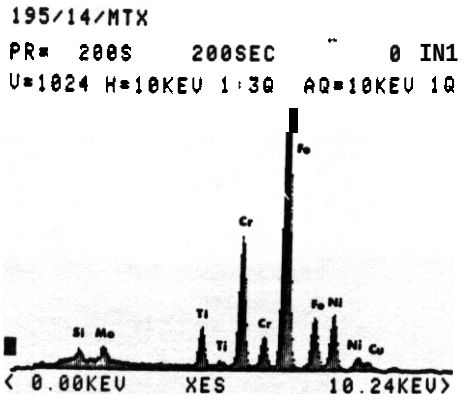

FIGURE 2. EDS Analyses.

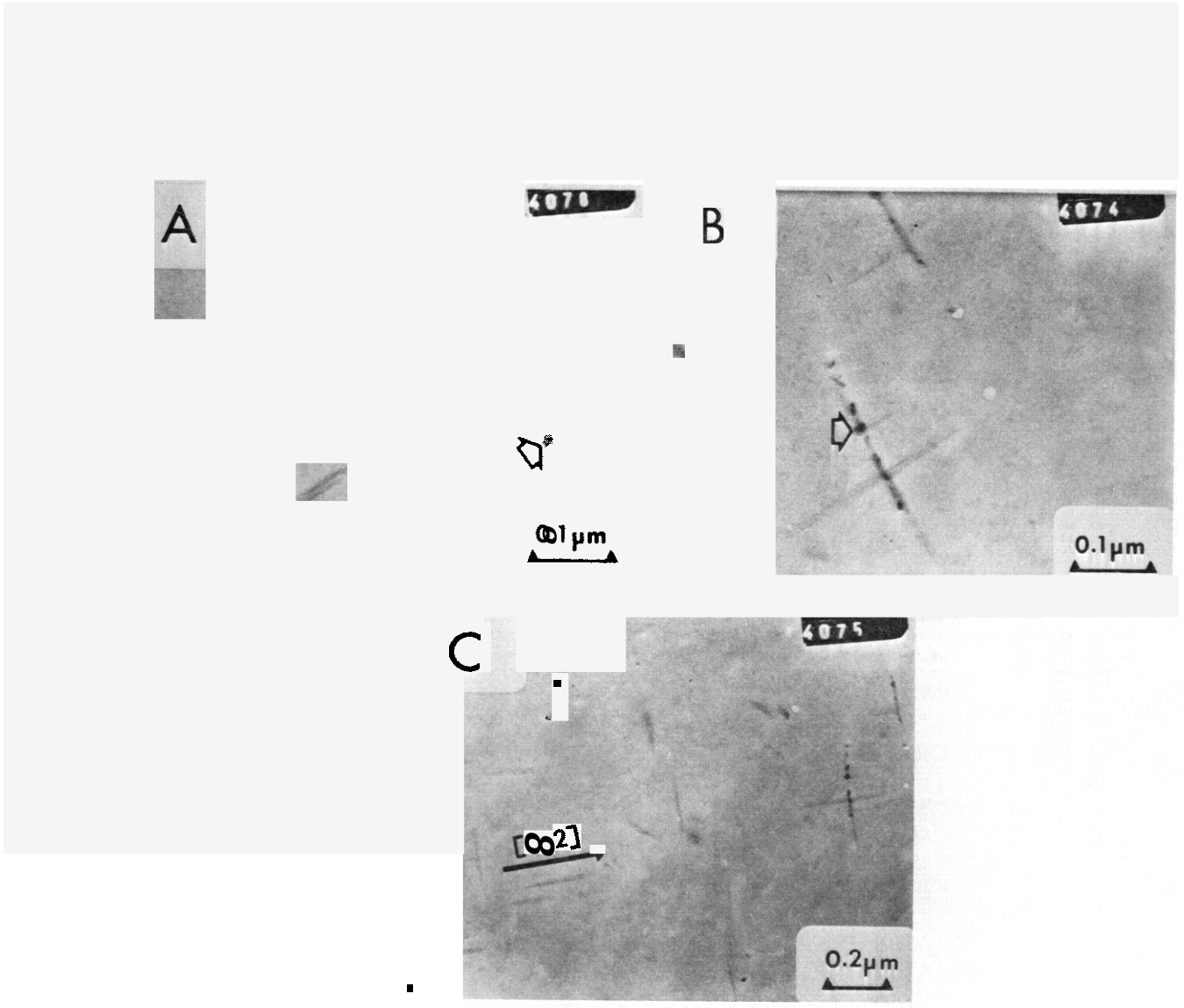

FIGURE 3. TEM Micrographs of an SA 316 SS Specimen Dually Bombarded with O^{+4} and Helium, Showing Precipitates and Bubbles (∿4 dpa, 83 appm He at 600°C).

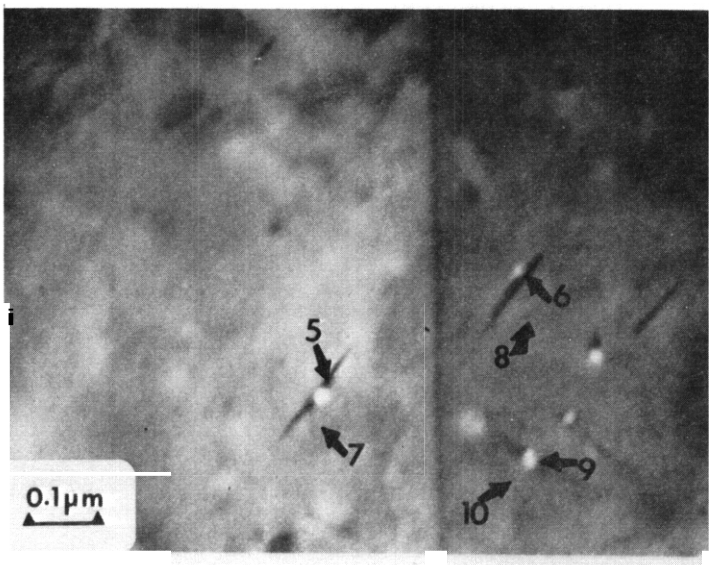

a

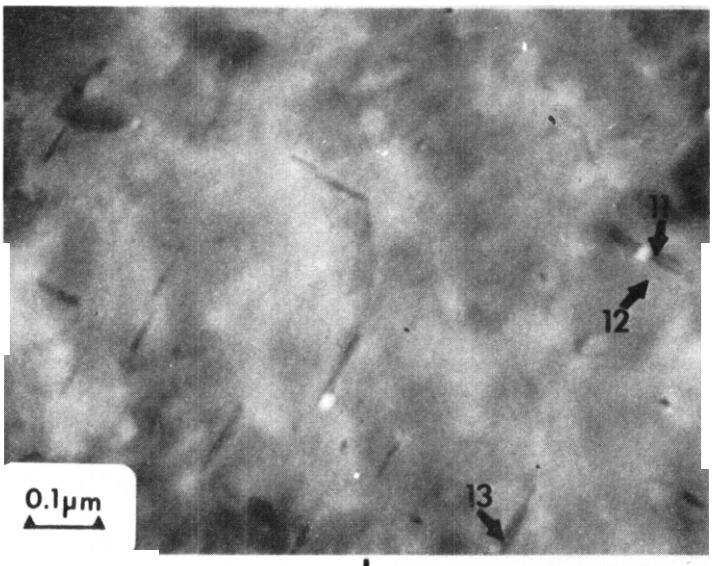

b

FIGURE 1. STEM Micrographs Obtained From SA 316 SS Dually Bombarded With C^{+4} and Helium at 600°C to ~4 dpa and 83 appm He. Arrows indicate locations of EDS analyses on acicular precipitates and the matrix.

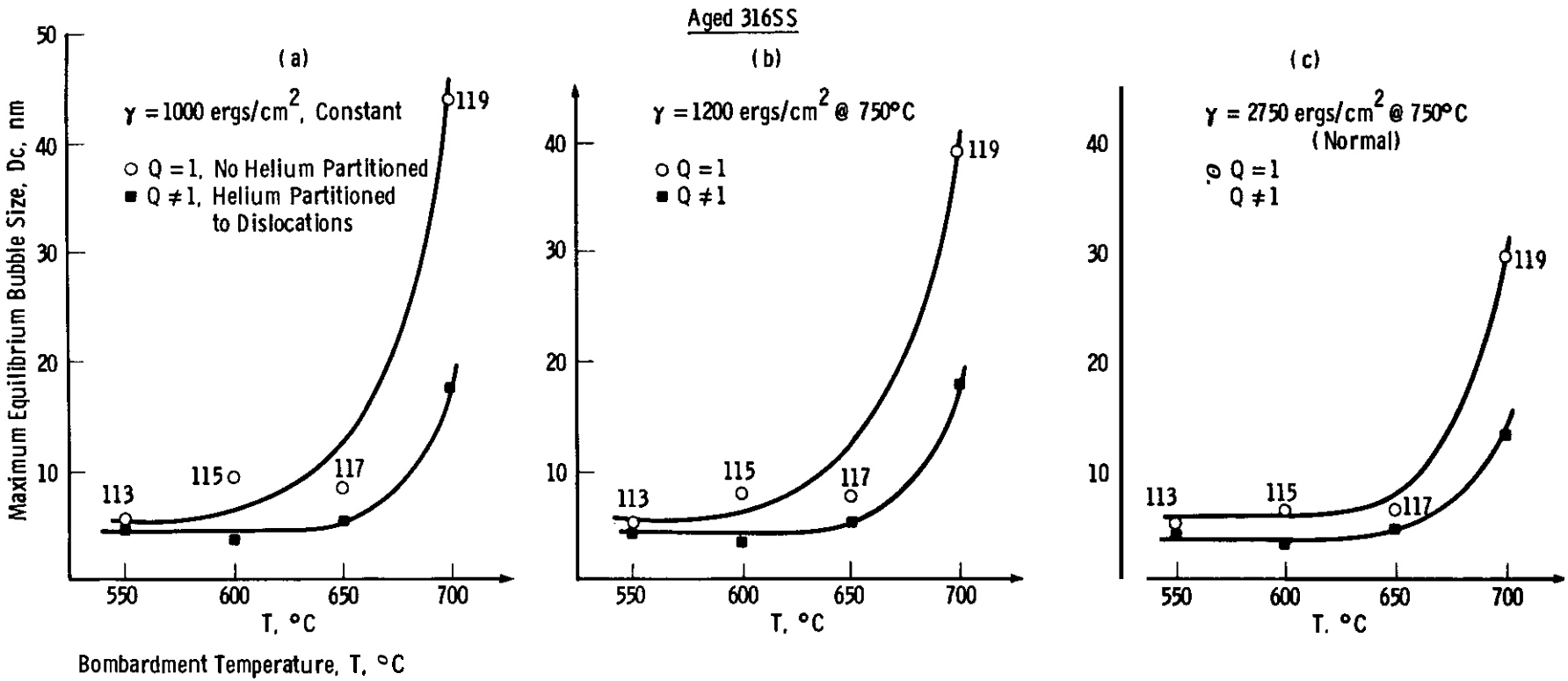

FIGURE 4. Variation of the Maximum Equilibrium Bubble Size, Dc, With Temperature and Surface Energy, γ Calculations were performed with the Irwin code using B' = 16.4 x 10^{-24} cm^3/atom.

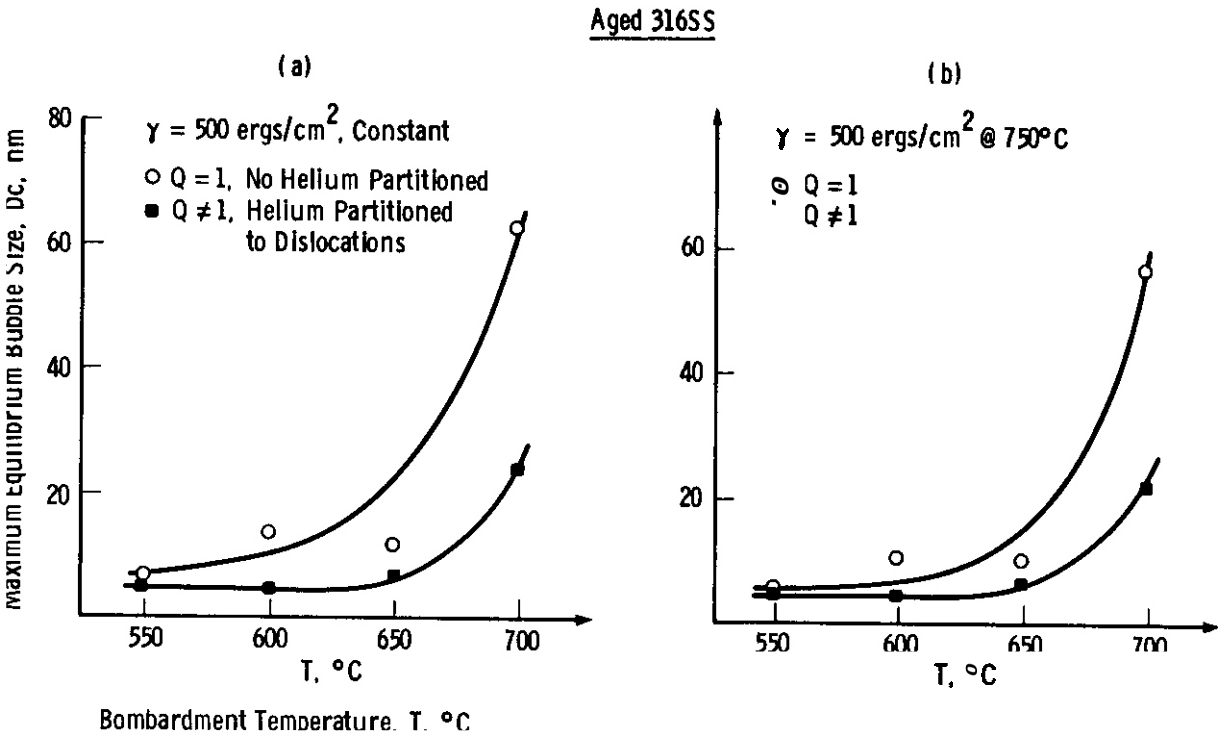

FIGURE 5. Variation of the Maximum Equilibrium Bubble Size, Dc, With Temperature and Surface Energy, γ Calculations were performed with the Irwin code using B' = 16.4 cm^3/atom.

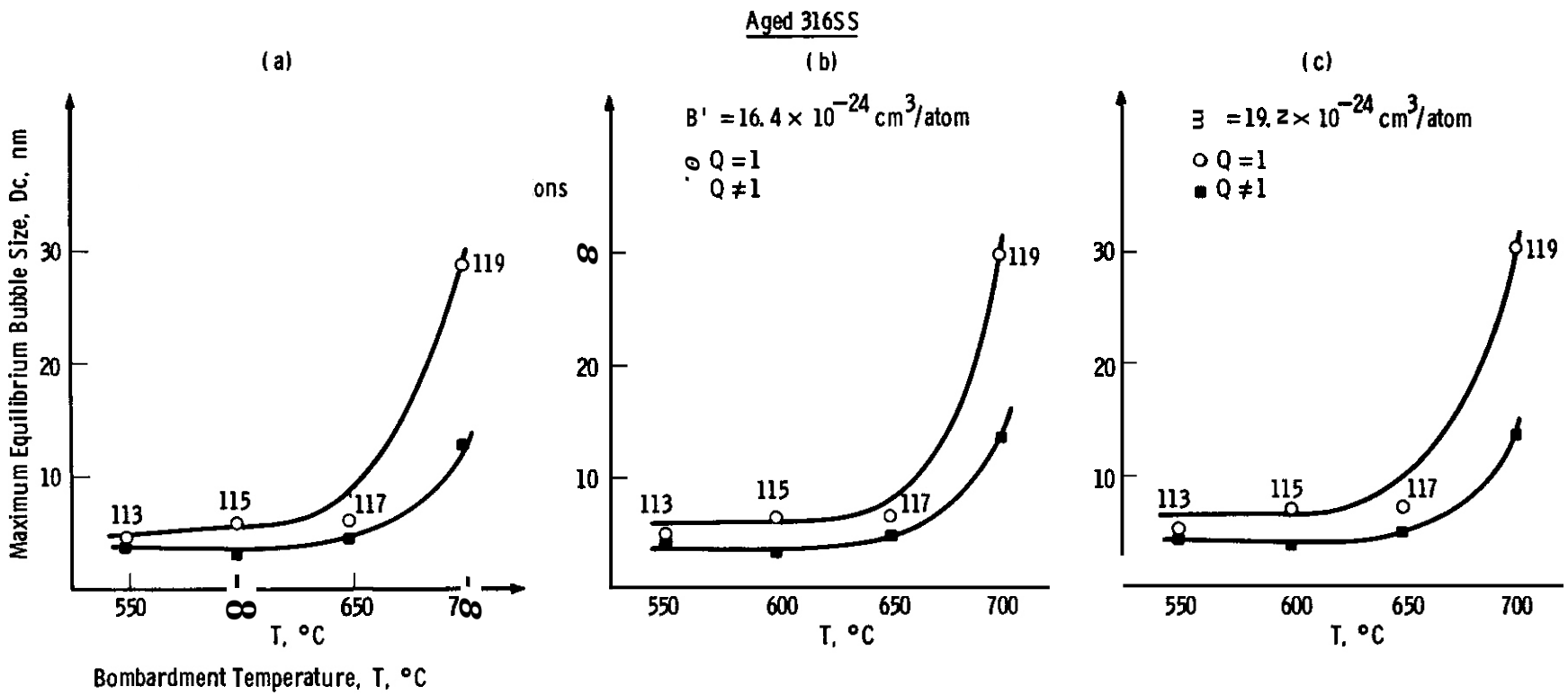

FIGURE 6 Variation of the Maximum Equilibrium Bubble Size, Dc, With Temperature and B', the Van de Waal Constant. Calculations were performed with the Irwin computer code using γ = 2750 ergs/cm^2 at 750°C, and a linear dependence of γ on temperature.

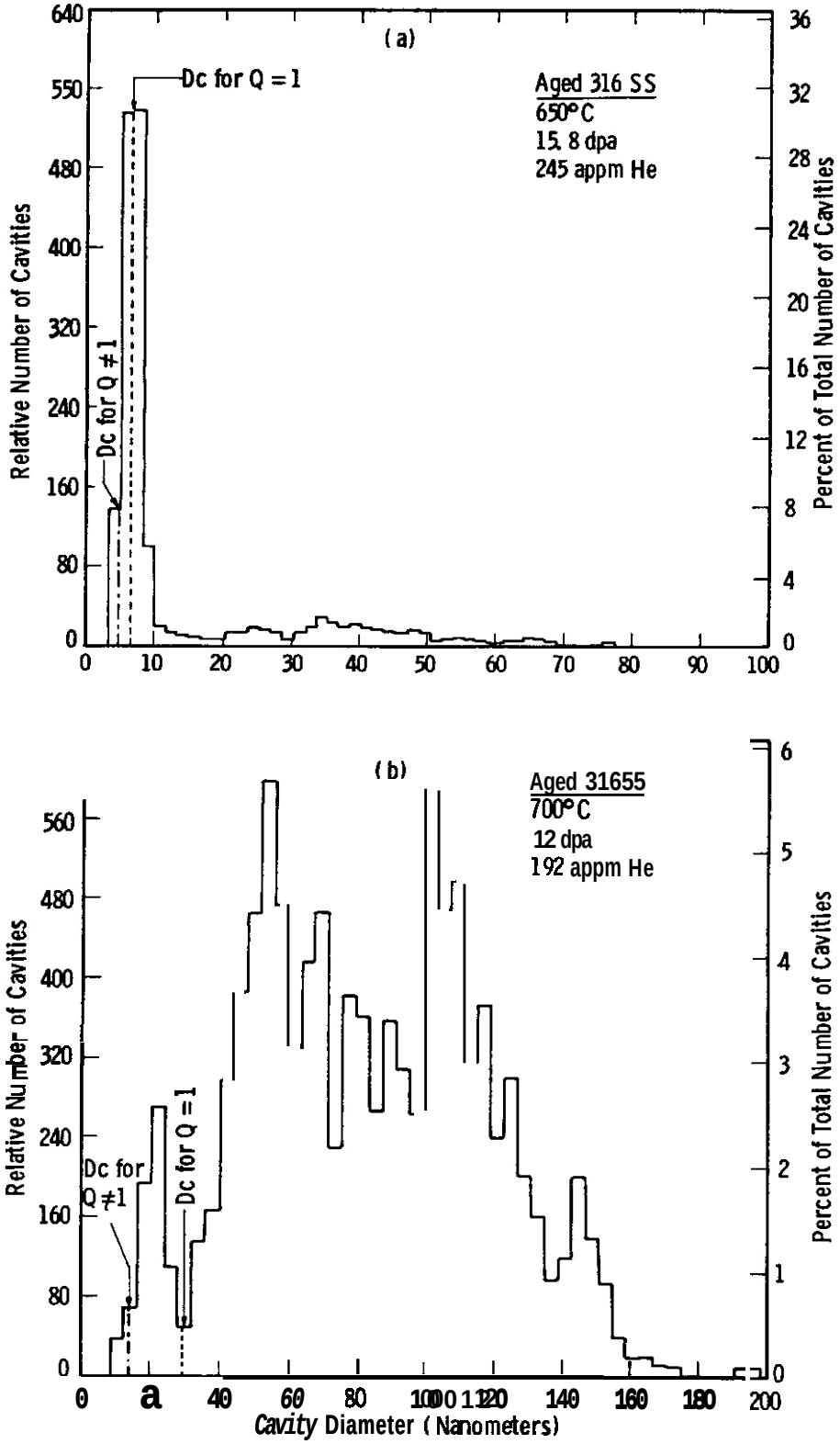

FIGURE 7. Cavity Size Histograms for Aged 316 SS Specimens Dually Bombarded with 28 MeV Si^{+6} and ≤ 2 MeV He ions at a) 650°C and b) 700°C. (Dc values shown were calculated with γ = 2750 ergs/cm^2 at 750°C and B' = 16.4 cm3/atom.)

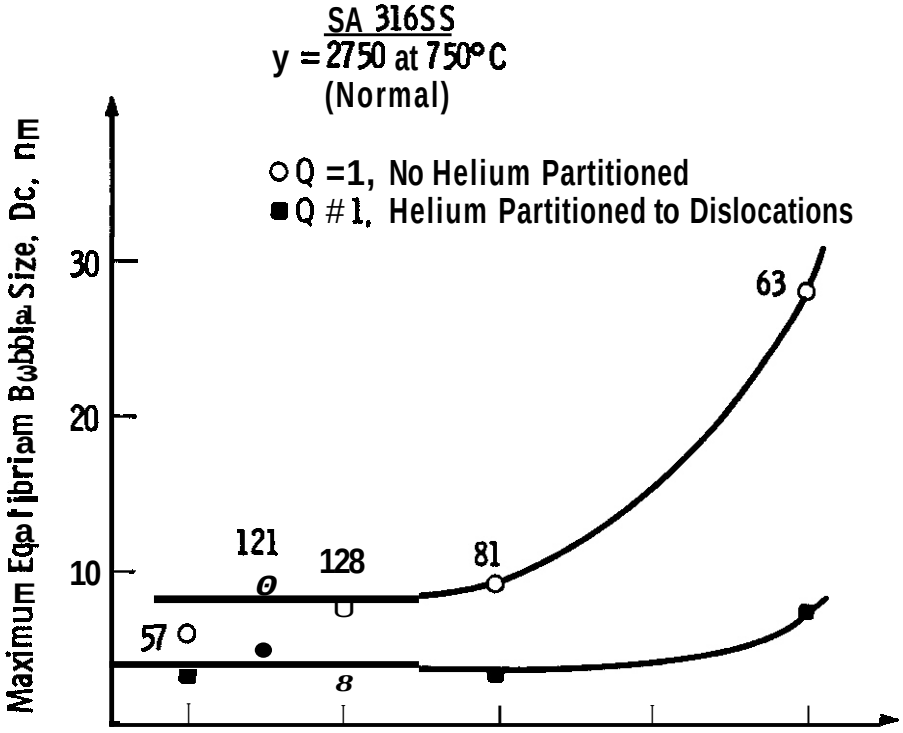

FIGURE 8. Variation of the Maximum Equilibrium Bubble Size, Dc, With Temperature for SA 316 SS. Calculations were performed with the Irwin code using $B' = 16.4\ cm^3/atom$.

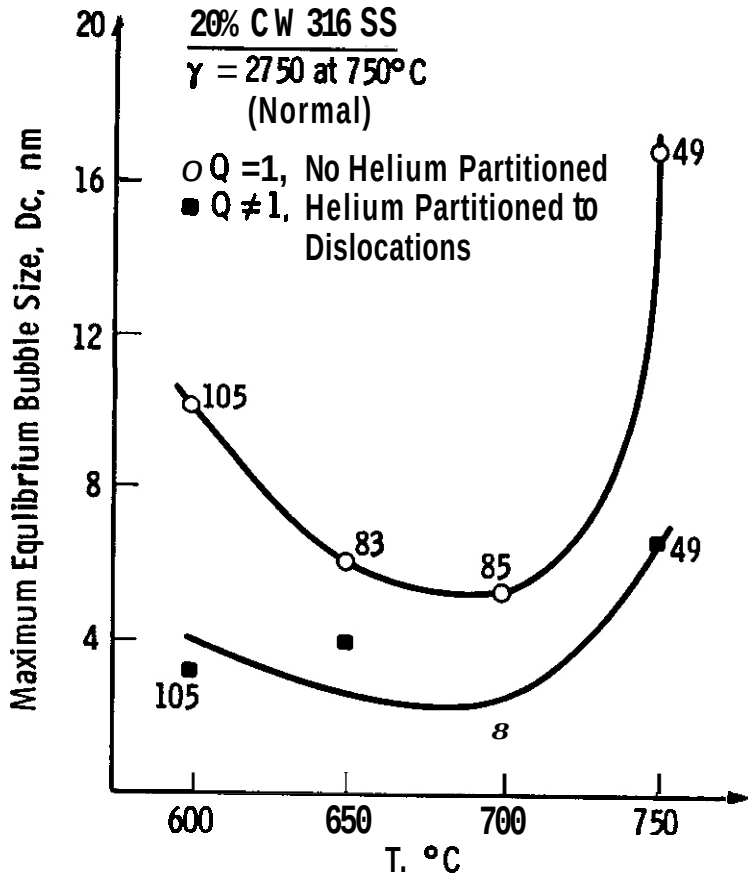

FIGURE 9. Variation of the Maximum Equilibrium Bubble Size, Dc, With Temperature for 20% CW 316 SS. Calculations were psrformed with the Irwin code using B' = 16.4 cm^3/atom.

I. PROGRAM

Title: Irradiation Effects Analysis (AKJ)
Principal Investigator: D. G. Doran
Affiliation: Hanford Engineering Development Laboratory

11. OBJECTIVE

To determine the dependence of the radiation-induced microchemical evolution of AISI 316 on variables such as thermal-mechanical starting condition, temperature, stress, neutron flux and fluence.

111. SUMMARY

Extraction and analysis of precipitates in irradiated AISI 316 have shown that the microchemical evolution is sensitive to some variables but not others. There is an acceleration with applied stress of the radiation-induced nickel removal process at 550°C but not at 400°C, an observation which is in agreement with the results of other studies. The relative swelling behavior of various specimens can be correlated with the amount of nickel removal from the alloy matrix. At 400°C there appears to be a sensitivity of the level of precipitation to neutron flux and/or time in reactor. At 400°C the microchemical evolution is very sluggish and still in progress at 14×10^{22} n/cm^2 (E >0.1 Mev). At 550°C the evolution is not so sluggish and still in progress at 7×10^{22} n/cm^2.

IV. ACCOMPLISHMENTS AND STATUS

A. The Influence of Microchemical Evolution on the Swelling of AISI 316 and Its Dependence on Stress, Temperature and Heat Treatment - D. L. Porter (ANL-Idaho Falls) and F. A. Garner (HEDL)

1. Introduction

It has been recently shown that the onset and acceleration of void swelling in AISI 316 can be correlated to the microchemical evolution of the precipitate and matrix compositions, and that the influence of various material and environmental parameters on swelling and irradiation creep can be observed in their concurrent effect on precipitate evolution.[1-4] The majority of the data supporting this correlation come from comparative irradiations at single fluence levels and are usually based on microscopy observations of very small but presumably typical specimen volumes.

Another type of data has recently become available which not only gives bulk-averaged microchemical data but also is available over a range of neutron fluences. In these experiments the precipitates are extracted and their volune and metallic element composition are determined.[5-6] There is no assurance as yet that all of the precipitates are extracted. The identity of the various precipitates is also not determined, but these are in general known from the microscopy studies. The material described in this report is AISI 316 in several starting conditions, and was used to construct pressurized tubes. These tubes were maintained at constant temperatures of either 400 or 550°C. The length of the 400°C tubes was forty inches and that of the 550°C tubes was ten inches. The steel is the V87210 reference heat used in the U.S. Breeder Reactor Program. It was irradiated in EBR-II either as solution-annealed, 10%or 20%cold-worked, or Heat Treat D. The HTD condition was 20% cold worked and then aged (24 hours at 482°C, air quenched, 216 hours at 704°C, air quenched).

In general the relative swelling of this material is HTD >annealed >10% cold worked >20% cold worked.[8]

2. Experimental Results

Although the full compositional data are available and will be presented in later reports, it is sufficient for the present purpose to

focus only on the nickel content of the precipitates and their relative fractional amount. The total nickel removal appears to be a very reliable index of the extent of the microchemical evolution. In the following graphs the stress shown beside each data point is the nominal hoop stress of the tube. Subsequent analyses will use the actual, slightly different hoop stresses determined upon postirradiation examination.

Figure 1 shows the mole fraction of nickel (relative to the total of iron, nickel, chromium and molybdenum atoms only) in 10 and 20%cold worked AISI 316 during irradiation at 400°C. Note that the single curve drawn through these data signifies an independence of stress and cold-work level in the 10-20%range. The total precipitate levels are only available for 10%cold work at this time and show no discernible dependence on stress level, as shown in Figure 2. It is significant that the evolution at 400°C is still in progress at 14×10^{22} n/cm^2 (E >0.1 MeV). This demonstrates that the evolution is very sluggish and is proceeding toward yet a higher level of nickel enrichment. It is this potentially higher level of nickel removal that can be reached in not quite so sluggish a fashion for certain temperature histories which give substantially higher levels of swelling.[4,7]

Figure 3 shows a comparison of the cold-worked data at 400°C with that of HTD. The effect of stress, if one exists, cannot be discerned from this data set. The onset of an accelerated microchemical evolution to a much higher precipitate nickel level is obvious however and is consistent with the higher swelling of HTD compared to that of both annealed and cold worked material.[8] Figure 4 shows that at 550°C the nickel concentration process proceeds at a higher rate than that observed at 400°C. There is also some hint that stress may accelerate the precipitation process. Note that at 7.3×10^{22} n/cm^2 there is a slight increase in both the amount of precipitate and the nickel mole fraction with increasing stress level.

In 10%cold worked AISI 316 at 550°C the effect of stress on swelling is much more obvious as shown in Figure 5. At 3.9×10^{22} n/cm^2 the effect

of stress on the total nickel removal is hard to discern but at 6.3 x 10^{22} n/cm^2 a late term acceleration of both the precipitate amount and mole fraction of nickel has occurred. The very high nickel level of ~50% has been observed in G-phase precipitates[9-10] or may represent an average of several phases, some of which are as high as 75% nickel (Ni_3Si). Brager and Garner earlier found that the formation of Ni_3Si was apparently insensitive to stress at 500°C however.[3,4]

Figure 6 shows that at 550°C both solution-annealed and 20% cold worked steels continue to develop precipitates which are progressively richer in nickel content. As expected the nickel content of precipitates in the annealed steel is somewhat ahead of that in the 20% cold worked steel The annealed curve may represent material which was not stressed at the nominal 207 MPa level however. Although this tube started at a hoop stress of 207 MPa, it leaked at some unknown time and rate during irradiation and had only 24.4 MPa at the end of the experiment. If the stress was reduced prior to the end of the swelling incubation period, then the nickel removal and swelling levels might be larger (than shown in Figure 6) for conditions of constant stress.

The relative swelling behavior of each condition [8] and the observed stress dependence of swelling[11-12] are quite consistent with the concept of earlier swelling with accelerated nickel removal. There is also some data that indicate a sensitivity to displacement rate or time in reactor at 400°C in 20% cold-worked AISI 316. As shown in Table I the amount of precipitate is greatest for low flux irradiation. Whereas one might expect more precipitates to form in those specimens exposed to the highest fluence, the lower fluence specimens which spent a long time in reactor at lower flux had roughly twice as much precipitate.

4. Conclusions

Extraction and analysis of precipitates in irradiated AISI 316 have shown that the microchemical evolution is sensitive to some variables but

not others. There is an acceleration with stress of the radiation-induced nickel removal process at 550°C but not at 400°C, an observation which is in agreement with the results of other studies. The relative swelling behavior of various specimens can be correlated with the amount of nickel removal from the alloy matrix. At 400°C there appears to be a sensitivity of the level of precipitation to neutron flux and/or time in reactor. At 400°C the microchemical evolution is very sluggish and still in progress at 14×10^{22} n/cm^2 (E >0.1 MeV). At 550°C the evolution is not so sluggish and still in progress at 7×10^{22} n/cm^2.

V. REFERENCES

1. H. R. Brager and F. A. Garner, "Swelling as a Consequence of Gamma Prime (γ') and $M_{23}(C,Si)_6$ Formation in Neutron Irradiated 316 Stainless Steel," J. Nucl. Mat., 73, (1978) 9-19.

2. H. R. Brager and F. A. Garner, "Dependence of Void Formation on Phase Stability in Neutron Irradiated Type 316 Stainless Steel," ASTM STP 683, Proc. ASTM 9th International Symposium on Effect of Radiation on Structural Materials, Richland, WA, July 10, 1978, p. 207.

3. H. R. Brager and F. A. Garner, "Microchemical Evolution of Neutron-Irradiated 316 Stainless Steel," Effects of Radiation on Materials, Tenth Conference, ASTM STP 725, D. Kramer, H. R. Brager and J. S. Perrin (Eds) ASTM (1981) (in press).

4. F. A. Garner, "The Microchemical Evolution of Irradiated Stainless Steels," this report (also see reference 9).

5. D. L. Porter, J. Nucl. Mat., 92, (1980) 155-159.

6. D. L. Porter and E. L. Wood, J. Nucl. Mat., 83, (1979) 90-97.

7. F. A. Garner, E. R. Gilbert, O. S. Gelles and J. F. Foster, "Effect of Temperature Chanaes on Swellina and Creeo of AISI 316," Effect of Radiation on Materials, Tenth Conference,' ASTM STP 725, D. Kramer, H. R. Brager and J. S. Perrin (Eds) ASTM (1981) (in press).

8. G. L. McVay, R. E. Einziger, G. L. Hofman and L. C. Walters, J. Nucl. Mat., 78, (1978) 201-209.

9. W. J. S. Yang, H. R. Brager and F. A. Garner, "Radiation-Induced Phase Development in AISI 316," HEDL-SA-2157, presented at Symposim on Irradiation Phase Stability, October 5-9, 1980, Pittsburgh, PA, (in press).

10. L. E. Thomas, "Irradiation-Induced Phase Instabilities in Austenitic Stainless Steels," Proc. Thirty-Seventh Annual EMSA Meeting, August 13-17, 1979, San Antonio, TX, 422-423.

11. F. A. Garner, E. R. Gilbert and D. L. Porter, "Stress Enhanced Swelling of Metals During Irradiation," DAFS Quarterly Report DOE/ER-0046/4, p. 103 (see also reference 7).

12. F. A. Garner, "Extrapolation of Stress-Affected Swelling Models Into Compressive and Cyclic Stress States," this report.

VI. FUTURE WORK

This work will continue as more data becomes available.

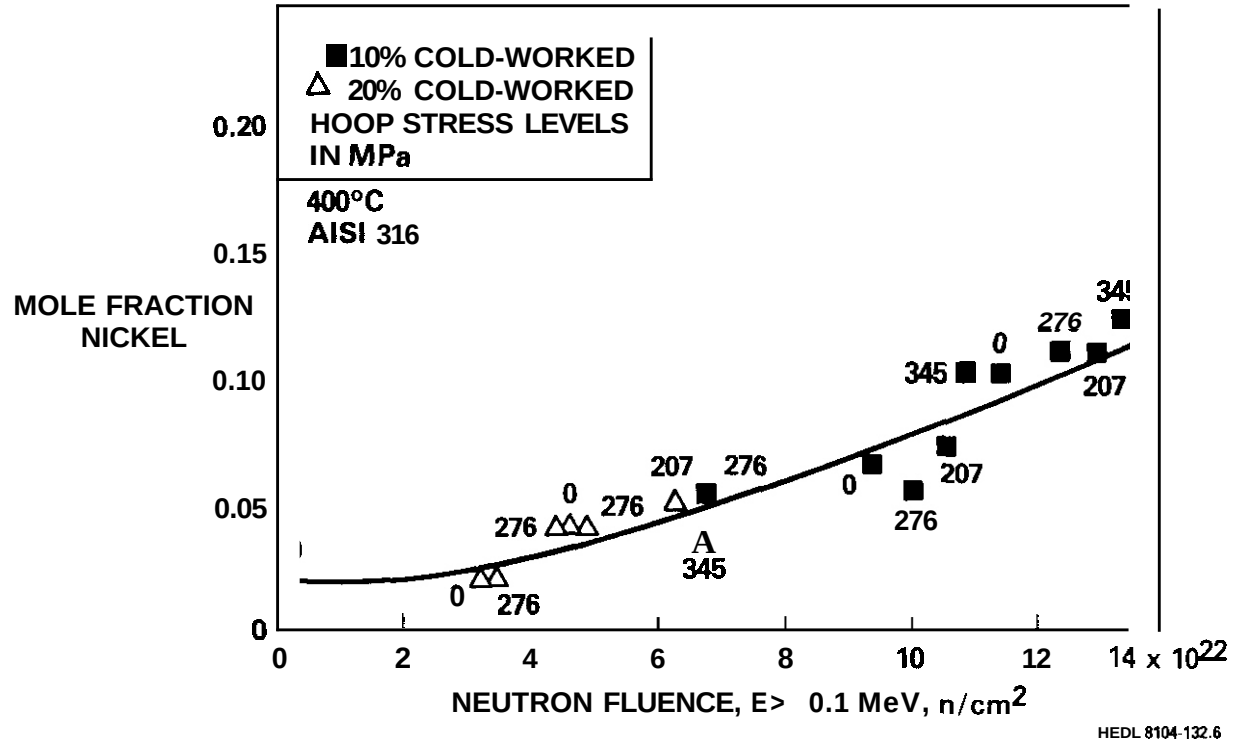

FIGURE 1. Nickel Content of Extracted Precipitates Formed at 400°C in 10 and 20% Cold-Worked AISI 316. (Stress levels given beside each datum).

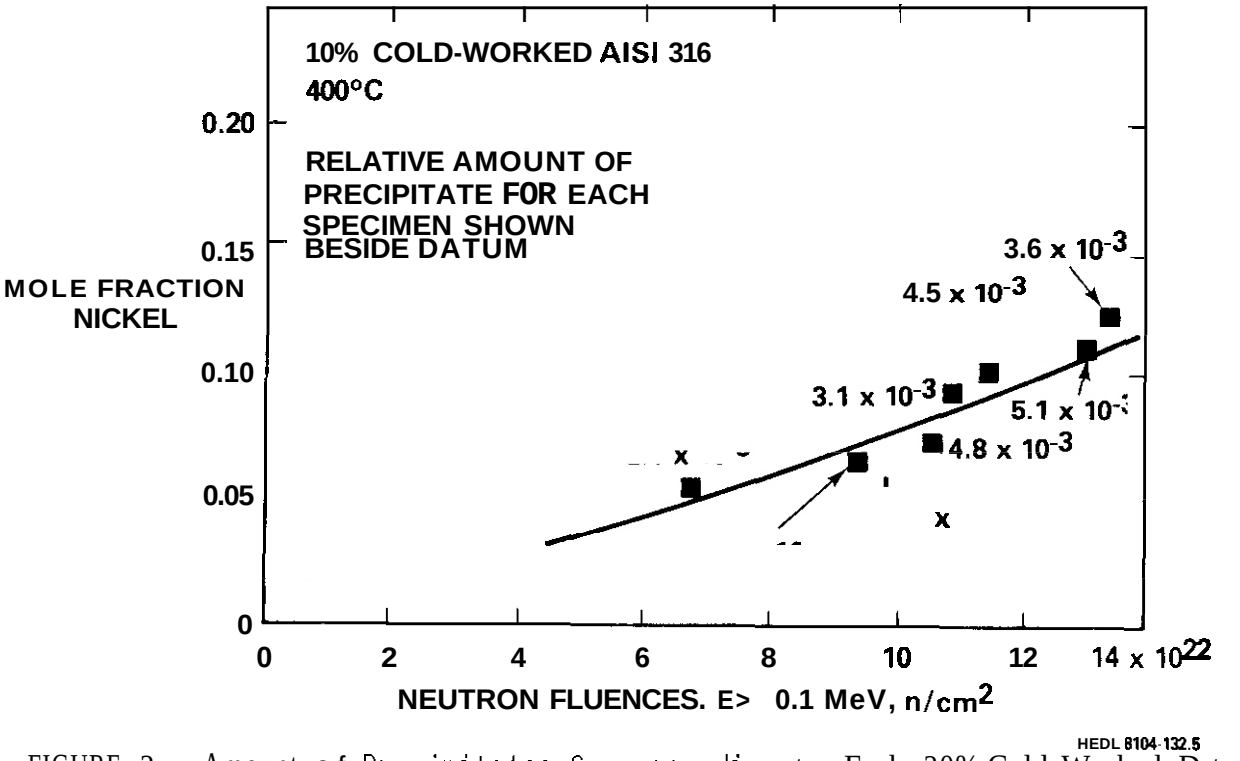

FIGURE 2. Amount of Precipitates Corresponding to Each 20% Cold-Worked Datum of Figure 1.

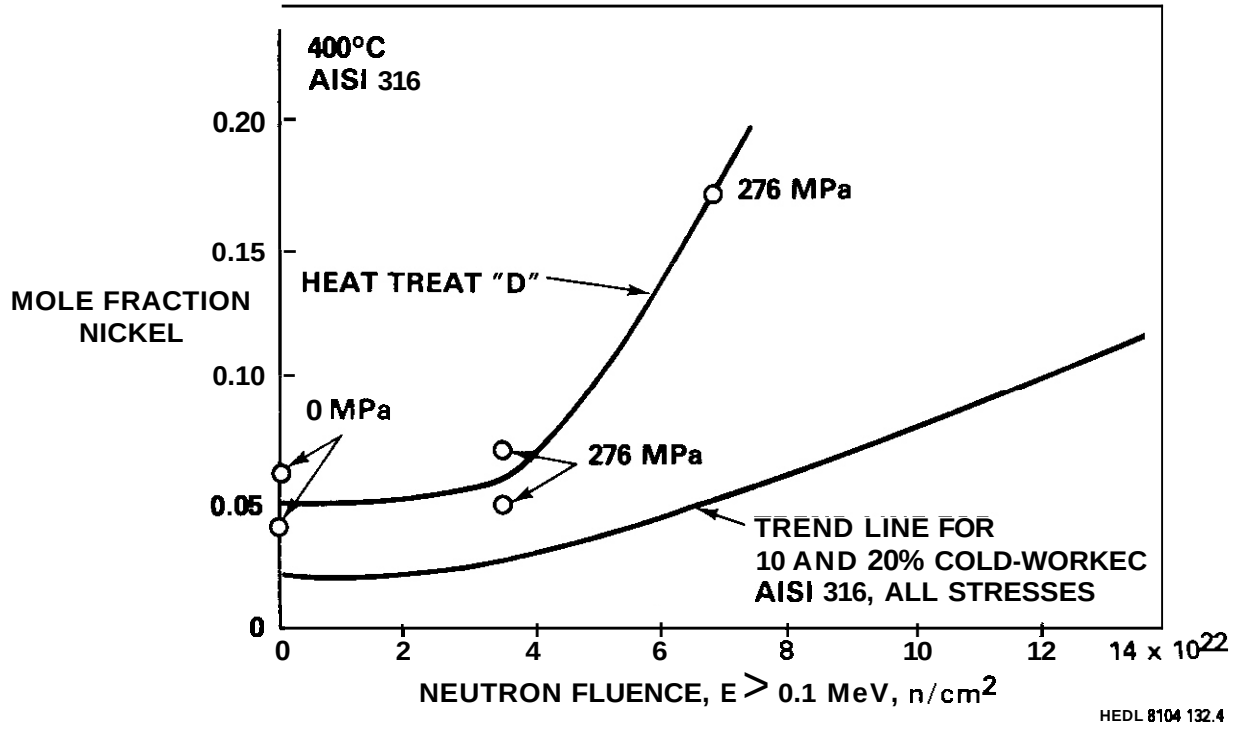

FIGURE 3. Comparison of Nickel Content of Precipitates in Heat-Treat D and Cold-Worked AISI 316 at 400°C.

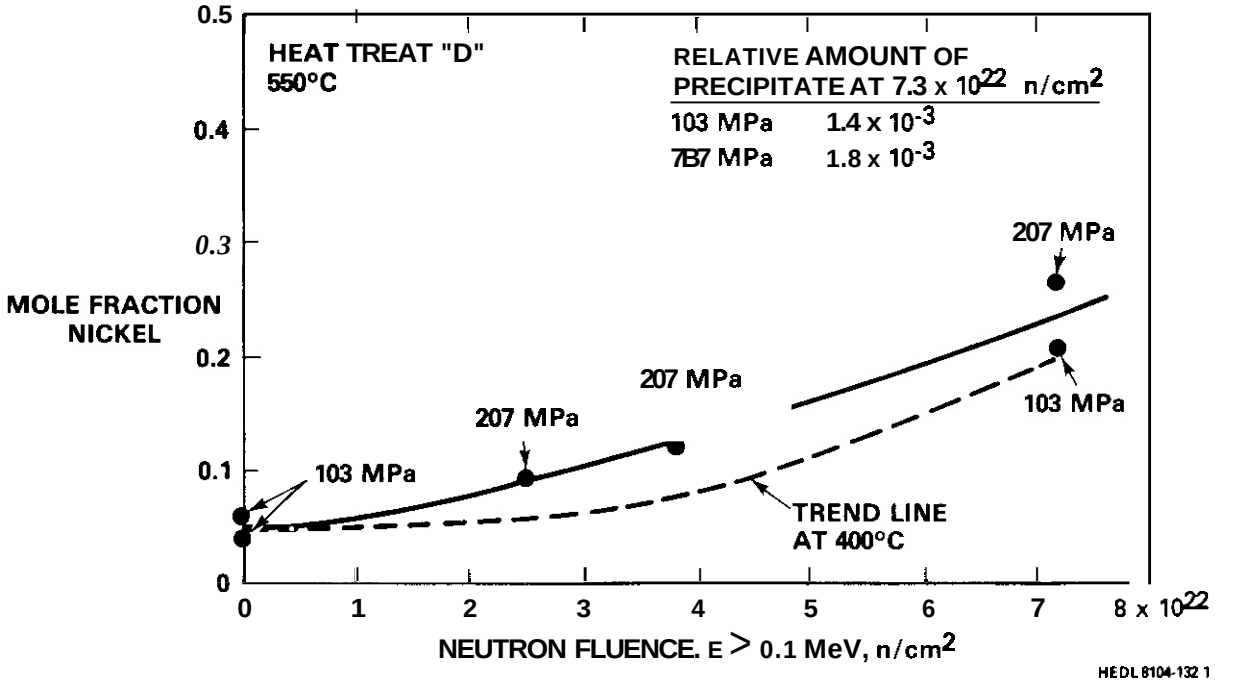

FIGURE 4. Comparison of Nickel Segregation Behavior in Heat-Treat D at 400°C and 550°C.

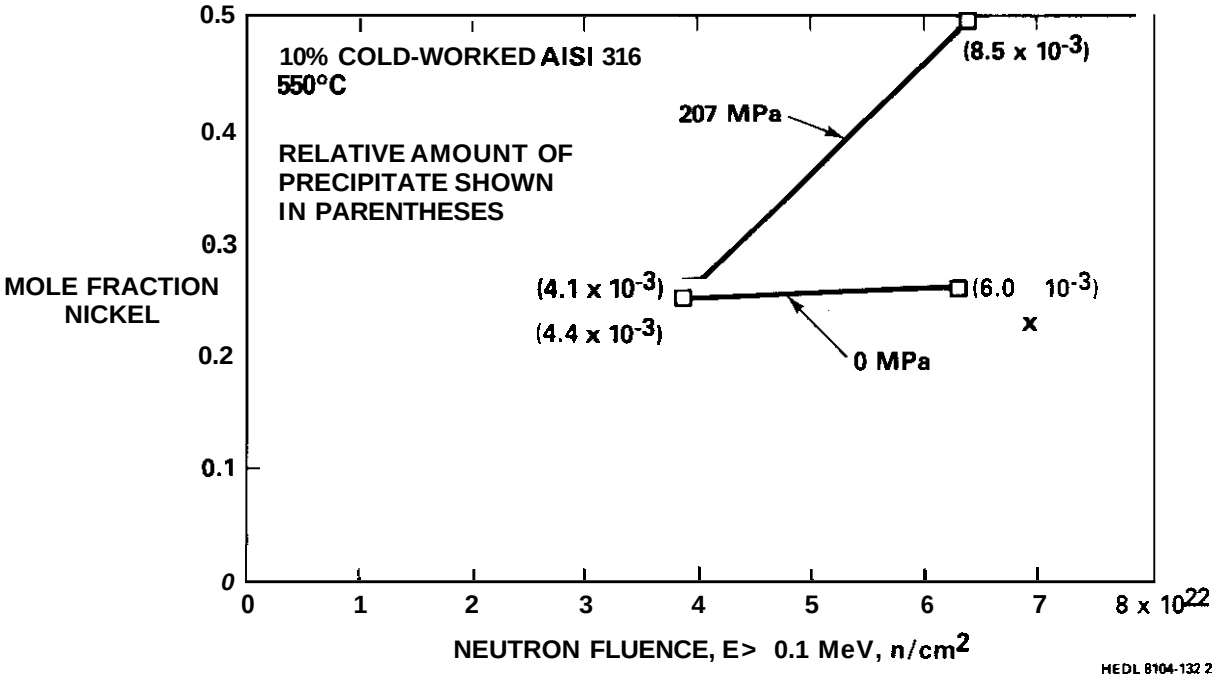

FIGURE 5. Effect of Stress on Nickel Segregation Into Precipitates in 10% Cold-Worked AISI 316 at 550°C.

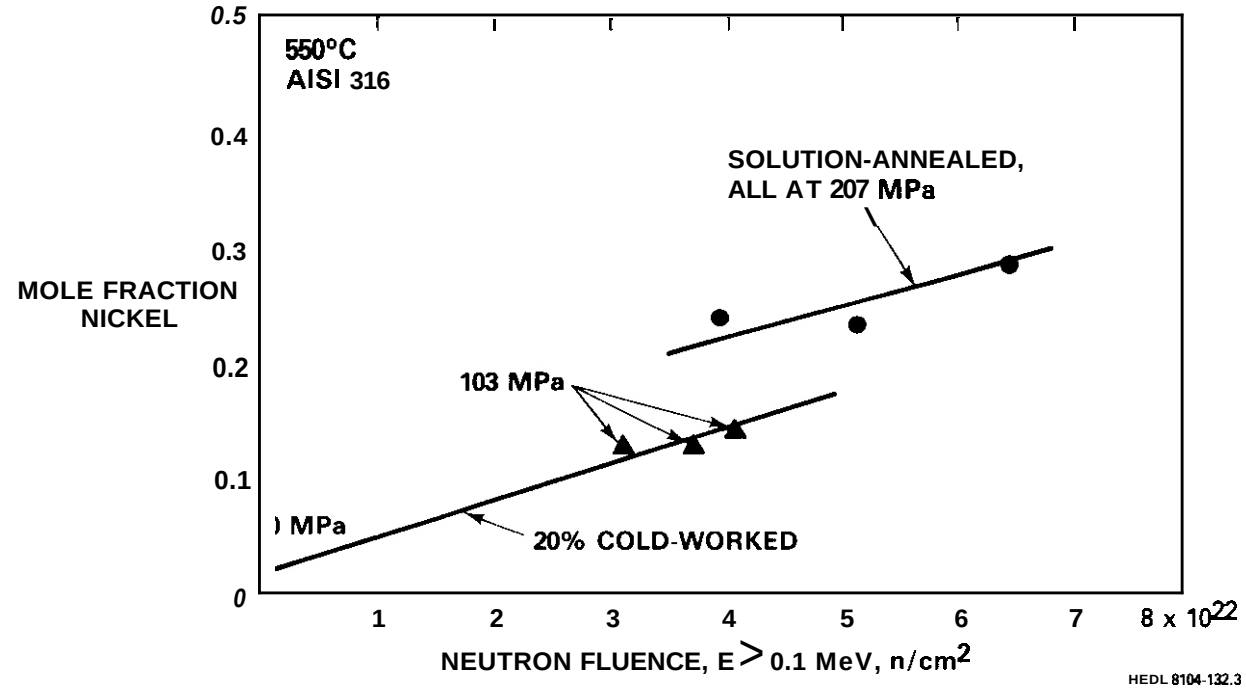

FIGURE 6. Comparison of Nickel Segregation Behavior of Annealed and 20% Cold-Worked AISI 316 at 550°C.

TABLE 1

PRECIPITATION IN 20% COLD-WORKED
AISI 316 AT 400°C

ϕt (E >0.1 MeV) (10^{22} n/cm^2)	Time at Temperature hours	ϕt/time	Relative Amount of Precipitation	Mole Fraction Nickel
4.6	12,185	3.78×10^{18}	5.5×10^{-4}	0.040
4.15	12,185	3.41×10^{18}	6.1×10^{-4}	0.030
3.2	16,522	1.94×10^{18}	1.39×10^{-3}	0.033
3.1	16,522	1.88×10^{18}	1.06×10^{-3}	0.048

I. PROGRAM

Title: Irradiation Effects Analysis (AKJ)
Principal Investigator: D. G. Doran
Affiliation: Hanford Engineering Development Laboratory

II. OBJECTIVE

The objective of this effort is to explore the role and impact of the radiation-induced microchemical evolution on the development of changes in either dimension or mechanical property in stainless steels.

III. RELEVANT DAFS PROGRAM PLAN TASK/SUBTASK

II.C.1 Effect of Material Parameters on Microstructure
II.C.2.4 Modeling
II.C.14 Models of Flow and Fracture Under Irradiation
II.C.16 Composite Correlation Models and Experiment

IV. SUMMARY

It recently has been shown that the precipitates that develop during irradiation play the dominant role in the response of 300 series alloys. This role is expressed primarily in a large change in matrix composition that may significantly alter the diffusional properties of point defects. It may also substantially alter the rate of acceptance of point defects flowing to dislocations and voids. The major elemental participants have been identified as carbon, nickel and silicon. Carbon appears to function as a major governing factor of the route and rate by which the radiation-induced evolution proceeds. It is the sensitivity of carbon's response to a wide range of variables that accounts for much of the variability observed in the swelling of 316 stainless steel.

Silicon's role is two-fold. While in solution it depresses void

nucleation and determines the duration of the void incubation period. It also coprecipitates with nickel. The eventual level of nickel in the alloy matrix appears to control the steady-state swelling rate and is determined by the silicon and carbon content. The other participating elements appear to affect primarily the distribution and activity of carbon. Dislocations introduced either by irradiation or cold work likewise appear to influence the role of carbon.

In these studies, several new physical mechanisms appear to be operating. These are the Inverse Kirkendall effect, interstitial-altered phase stability, solute-interstitial binding, the infiltration-exchange process, and the creation of radiation-stable precipitates. The sensitivity of the latter phenomenon to temperature and flux has been shown to account for much of the unusual behavior of AISI 316 during irradiation.

V. ACCOMPLISHMENTS AND STATUS

A. The Microchemical Evolution of Irradiated Stainless Steel - F. A. Garner (HEDL)

1. Introduction

The neutron irradiation on various 300 series stainless steels in fast breeder reactors has recently been shown to lead to two concurrent and interactive evolutions, one involving the microstructural components associated with swelling and irradiation creep [1] and another "microchemical" evolution involving extensive repartitioning of elements between the matrix and various precipitate phases. While the majority of the published data on the microchemical processes have been concerned with AISI 316 stainless steel [2-14] data have also been published on silicon and titanium modifications of AISI 316 [15-17], AISI 304 [12,18], and the niobium-stabilized alloy FV548.[19]

Microscopy and energy dispersive X-ray studies have now provided a basis for understanding the nature of the processes driving the evolution of

these steels. The wide range of void swelling behavior observed in AISI 316 has been shown to arise from the inherent metastability of this steel, a condition which is not only substantially altered and accentuated by irradiation, but one which is very sensitive to many material and environmental variables.

The magnitude of this metastability and its consequences on alloy behavior during irradiation have not previously been fully appreciated, particularly in theoretical descriptions. In the modeling of irradiation-induced dimensional and mechanical property changes, several implicit assumptions are often incorporated into theoretical descriptions. In effect it is assumed that the property change of interest can be described in terms of a microstructural scenario in which precipitates are assigned relatively small roles such as sites for void nucleation or reservoirs for minor solute atoms. The major components of the microstructure (voids, Frank loops, dislocations) are also assumed to have preferences or "biases" for point defects which are not strong functions of alloy matrix composition. It is also implicitly assumed that the concentrations of the major elements in the matrix do not change during irradiation. In such scenarios the diffusional properties of the matrix are thought to be influenced only by the irradiation temperature, displacement rate, and the matrix level of solute atoms which act as traps for point defects.

It is the purpose of this paper to show that the precipitates that develop during irradiation in AISI **316** and other alloys play a dominant role in the alloy response. This role is expressed primarily in a large change in matrix composition that may significantly alter the diffusional properties of point defects. It may also substantially alter the rate of acceptance of point defects at dislocations and voids.

The major elemental participants in the microchemical evolution have been identified as well as most of the participating phases and the physical mechanisms driving the evolution. These will be reviewed along with examples of consequences of the sensitivity of this evolution as seen in the swelling, creep and yield stress of AISI 316.

In the majority of what follows, the conclusions are firmly supported by data. In a few instances the conclusions presented are either inferred from macroscopic property changes or possible coincidental correlations. Speculative conclusions or proposals are identified as such.

2. Overview of the Microstructural/Microchemical Evolution

Although there are many similarities between the response of the various 300 series alloys to irradiation, there are small but significant divergences that reflect differences in alloy composition. Since the data on alloys other than AISI 316 are rather sparse, the evolutionary scenario presented here is based only on the observed response of AISI 316. Divergent behavior in other alloys will be discussed in the following sections where appropriate.

During irradiation, the development of dislocation and loop microstructure proceeds toward a saturation state, composed of number densities and component identities which eventually become independent of starting microstructure.(') Both the rate of approach to saturation and the saturation level of Frank loops are strongly dependent on temperature, stress and displacement rate but surprisingly the saturation dislocation network that evolves is essentially independent of these variables.[1,20-22] The microchemical evolution induced by radiation also appears to proceed toward a saturation state but at a much more sluggish pace,[3,5-6] although certain temperature paths or preirradiation treatments can short-circuit the sluggishness.[4-5,23]

Long-term thermal aging of AISI 316 has shown the alloy to be metastable and to form second-phase precipitates of various carbides and intermetallic compounds.[24-25] These phases segregate specific elements from the matrix. When this alloy is placed in reactor, however, the radiation-induced microstructural components interact with the defect fluxes. Those components which act as sinks induce in their vicinity point defect gradients which function as a new and potent driving force for segregation. The element nickel seems particularly prone to concentrate at the bottom of such gradients.[2,6]

The matrix nickel content away from sinks is then reduced, although not by much unless solutes such as silicon and carbon are present.[15] These elements coprecipitate with nickel at microstructural sinks such as dislocations, loops and precipitates. Such sinks form a microchemical reservior capable of removing from the matrix approximately three atoms of nickel for each silicon (and possibly carbon) atom. In AISI 316 with a nominal silicon level of 0.5 weight percent, this leads to a reduction in matrix nickel from typically 13.5 to approximately 9 weight percent.

The most interesting feature of the precipitate-related segregation process is that the path by which the segregation proceeds does not appear to greatly influence the eventual nickel composition of the matrix. The saturation level of 9% has been observed in 20% cold worked 316 at four temperatures spanning different phase regimes. It has also been observed in solution annealed steel at several temperatures. This independence of path has also been demonstrated on a microscopic level [2] in AISI 316 and will be discussed in a later section. Porter [12-13] has also shown that in AISI 316 the saturation amount of precipitate and its nickel content are the same in aged, solution annealed or 20% cold worked steels. As shown in Figure 1, the nickel level of the precipitates evolves with fluence in each alloy but is independent of the amount of precipitate. Porter [13] notes that large pre-existing chromium-rich carbides in the aged steel dissolve during irradiation at 550°C to accomodate the new nickel-rich precipitates.

A large variety and balance of phases can develop in AISI 316, depending strongly on irradiation temperature and history as well as minor variations in composition and preirradiation thermal-mechanical treatment.[5-7] The balance of phases can also change within a single grain.[6-7]

The precipitate types formed in AISI 316 during irradiaiton can be summarized into four classes.[7] There are precipitates such as $M_{23}C_6$ and Laves phase which retain their expected crystal structure but which are progressively changed in composition during irradiation. There are precipitates which may form during thermal aging but which are accelerated by irradiation,

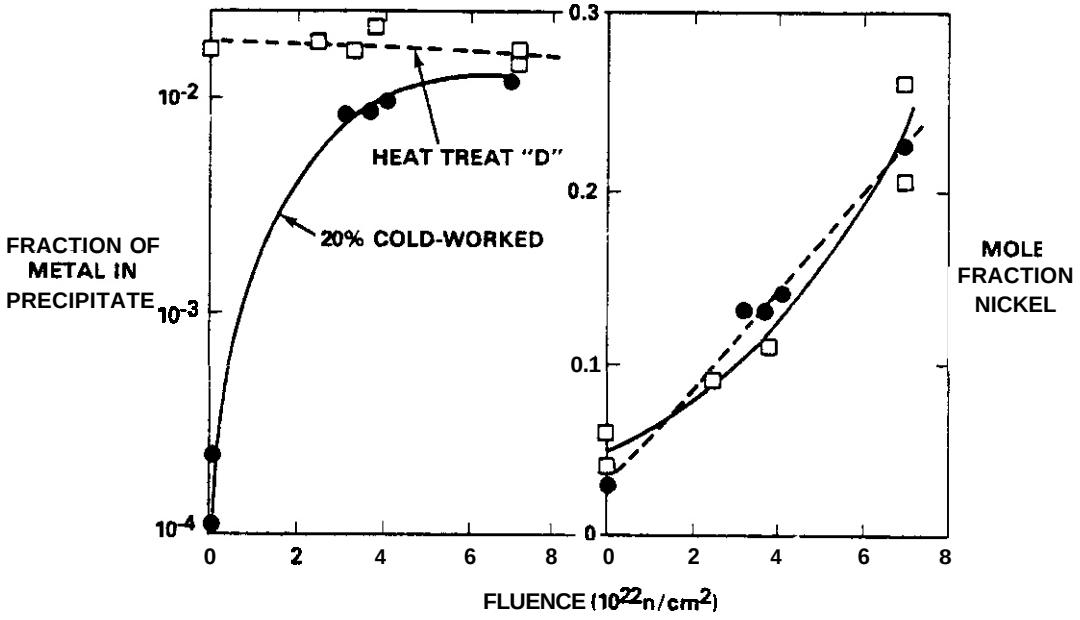

FIGURE 1. Measurements of Extracted Precipitates and Their Nickel Content For Both 20% Cold-Worked and Aged (24 hr at 482°C, air quenched, 216 hr at 704°C, air quenched) AISI 316 After Irradiation at 550°C. (13) The nickel level of the precipitates is independent of the amount of precipitation.

such as η-silicide. Another class of precipitates is induced by and only stable under irradiation, such as γ' (Ni_3Si) and G-phase (nickel-rich metal silicide). It also appears that some precipitates may form from the crystallographic transformation of other particles whose composition has been substantially changed by irradiation, such as M_6C from transformed $M_{23}C_6$. The slowest phase to form in this steel is generally the γ' phase, although there are substantial heat-to-heat differences in the irradiation time required to develop this phase.(3,11)

All of these phases exhibit one characteristic, however. They either form as nickel and silicon-rich phases or become progressively richer in these elements as the irradiation proceeds. With one significant exception, this characteristic has also been observed in all precipitates in all 300 series alloys referenced in this study. The exception is titanium-rich MC precipitates that form in titanium-modified stainless steel.(26) This precipitate in both irradiated and unirradiated conditions is strongly enriched in Ti, Mo, V and Nb and depleted in Si, Ni, Cr and Fe. The significance of this observation

will be discussed later.

The identity of the various phases formed during irradiation is sensitive to major changes in alloy composition as well. While all the phases formed in AISI 304 have not yet been definitively identified, it appears that there exists a range of precipitates as varied as that in AISI 316. Note that in Figure 2 the nickel content of extracted precipitates not only shifts with temperature and fluence but falls into two distinct categories.

No γ' has yet been found in AISI 304, which has the same silicon level but a lower nickel content than AISI 316 (9% versus 13-14%). In AISI 316 the presence of γ' is only observed at moderate to high silicon levels [5] and extends to some high temperature limit which increases with the silicon level.[15] An increase in stability is predicted (and observed in binary alloys) for Ni_3X-type phases as the concentration of either element is increased or as the displacement rate is raised.[27] The titanium and niobium-modified alloys appear to develop not only titanium and niobium carbides but also the G-phase. This latter phase forms only under irradiation, and corresponds to known stable phases such as $Nb_6Ni_{16}Si_7$ [28] and $Ti_6Ni_{16}Si_7$ [17] in other alloy systems.

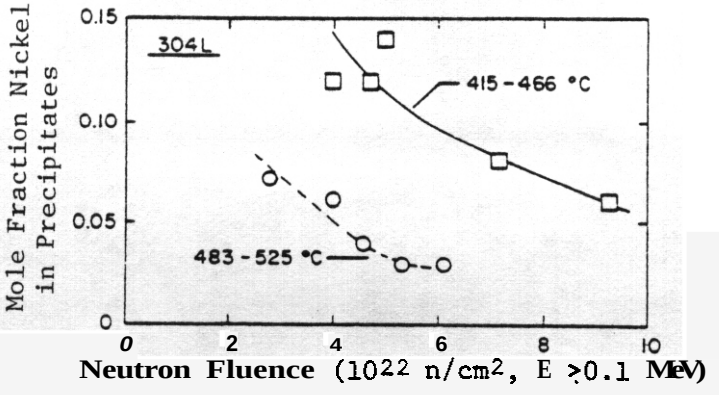

FIGURE 2. Measurement of the Nickel Concentration of Precipitates Extracted From Irradiated Annealed AISI 304L.[12] There appears to be two types of precipitates existing in different temperature ranges. The apparent fluence dependence reflects the strong temperature dependence of precipitation of each phase rather than rejection of nickel from the precipitates. The total precipitate volume increases with fluence and is relatively insensitive to irradiation temperature.[12] (The temperatures increase from left to right on each curve).

The precipitation and segregation sequences that develop during irradiation have important consequences on the further evolution of the alloy matrix. The first of these consequences has been discussed in detail elsewhere [2-6] and will be only briefly discussed here. There is almost always a correlation between the onset of swelling and the formation of nickel-rich precipitates. Figure 3 shows a typical example of this correlated microstructural development. As shown in the inset, two adjacent points along a fuel pin clad tube suffered a large difference in swelling over a temperature interval of only 25°C. The neutron fluxes and fluences at these positions were essentially identical. The large amount of swelling at one position was accompanied by a substantial amount of precipitates of the γ' phase. The low swelling position had just begun to develop precipitates.

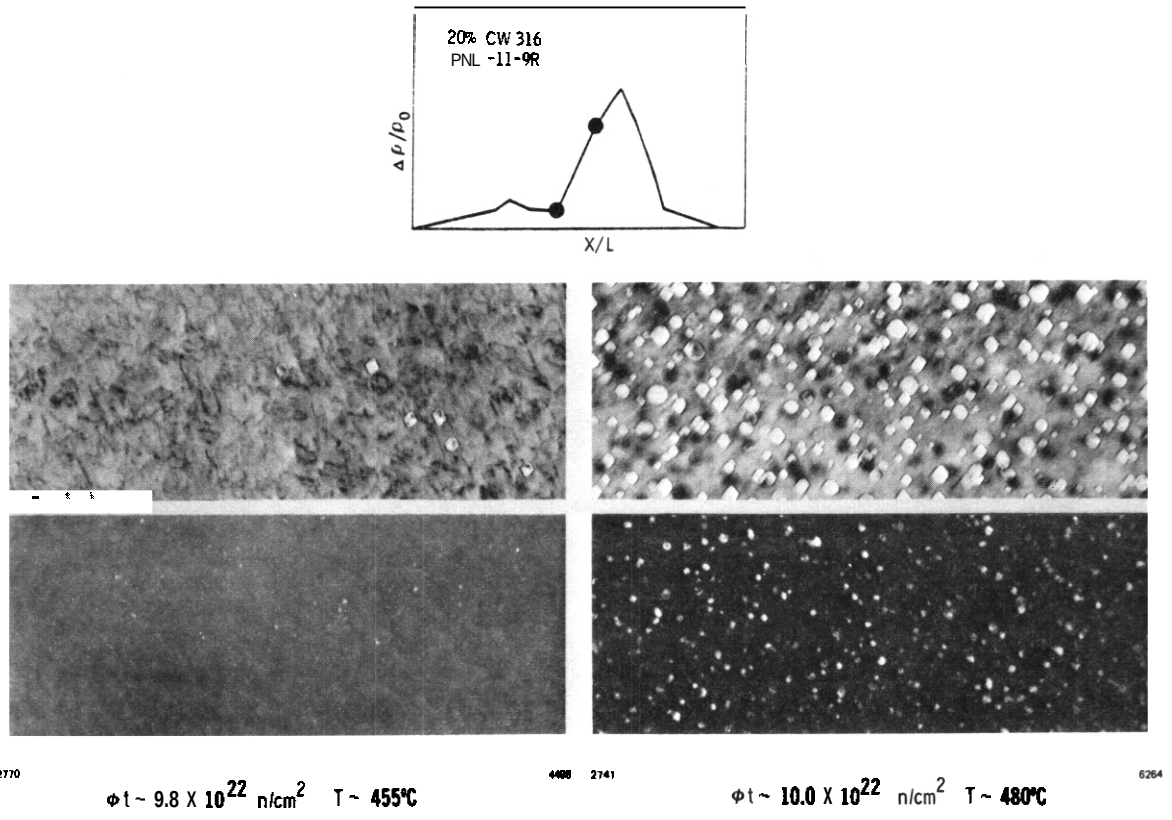

FIGURE 3. Correlated Development of Voids and γ' Precipitates (shown in dark field) Observed in Cladding of the PNL-11-9R Fuel Pin. The density change profile shown in the inset shows that the swelling varies strongly as a function of position.

Another consequence of the nickel segregation process on phase stability can be quite significant. If the silicon content is increased over the nominal specification for AISI 316, the matrix nickel content can be driven so low as to initiate the transformation of substantial amounts of matrix austenite to ferrite.[15] In AISI 304 the initial nickel level is only 9 weight percent and the nominal 0.5 percent silicon is sufficient to cause the transformation.[13,18] In both alloys, the segregation of nickel to void surfaces causes the voids to remain encased in austenite shells. The higher nickel content near the void surface resists the transformation.

Once ferrite forms the swelling rate of the transformed regions decreases sharply.[15] This decrease is comouflaged initially by the 2% volume increase that accompanies the transformation. Magnetic measurements of neutron irradiated AISI 316 have also indicated the formation of ferritic phases at relatively low fluences in AISI 316 of moderate silicon content. In these studies, microscopy was either not performed[29] or revealed no observable ferritic phases.[12,30-31] In one of these experiments[29] there was also no correlation found between the magnetic profile and that of the swelling.

3. Mechanisms Driving the Microchemical Evolution

The data indicate that there appears to be a number of new phenomena peculiar to irradiation environments that operate in addition to more ordinary mechanisms which may also be altered by irradiation.

Diffusional processes based on vacancy exchange mechanisms will obviously be accentuated, but not necessarily unaltered in nature by the presence of irradiation-induced point defects. The use of line-of-sight integrated measurements through a thin foil using energy dispersive X-ray (EDX) determination[6] of concentration profiles near microstructural sinks has conclusively demonstrated that the inverse Kirkendall[32] effect operates in AISI 316 during irradiation.[2,6,15] This results in the concentration of slower diffusing species such as nickel at the bottom of vacancy gradients near microstructural sinks. The concentration of these slower atoms is balanced by an outflow of faster

diffusing species such as chromium. The evidence also supports the segregation of silicon by binding interactions with point defects, probably interstitials.

Since silicon in known to be both a fast-diffusing element [34] and a possible candidate for binding reactions with interstitials,[32-33] one would expect that the competition between these two processes would be dependent on temperature and lead to a different segregation behavior at each type of sink. In AISI 316 void surfaces have not been found to segregate silicon but the γ' phase (Ni_3Si) appears to form on dislocations and Frank loops.[3,11] This suggests that the slight excess of vacancies arriving at voids causes the transport of silicon away from the void by the inverse Kirkendall effect to overwhelm silicon transport toward the void by interstitial binding. The corresponding excess of interstitials arriving at dislocations could then cause a reversal of the silicon flow, leading to the coprecipitation of silicon and nickel. The element nickel is postulated to be concentrated by both inverse Kirkendall and binding with interstitials.[33]

The balance of these two competing segregation mechanisms at dislocations may in itself be sufficient to explain the phenomenon of radiation-stable phases such as γ' and G-phase. Perhaps it is only fortuitous that the number densities and sizes of γ' precipitates in AISI 316 vary with temperature [14,35] in a manner similar to that of Frank loops [1] and the γ' phase inhabits the temperature regime [3] characteristic of Frank loops for nominal silicon concentrations. However, as shown in Figure 4, Lee has provided microscopy evidence of the nucleation of γ' on the edge of Frank loops in AISI 316.

P. J. Maziasz and W. J. S. Yang have speculated on a direct role of the interstitial in the formation of radiation-stable phases. Whereas $M_{23}C_6$ and Laves in unirradiated alloys grow by a mechanism involving absorption of vacancies from the matrix,[36] it is possible that γ' and G-phase grow by incorporating the excess interstitials, particularly elements of the desired identity. The magnitude and sign of the precipitate-matrix misfit would determine whether vacancies or interstitials contributed to the altered stability of any phase.

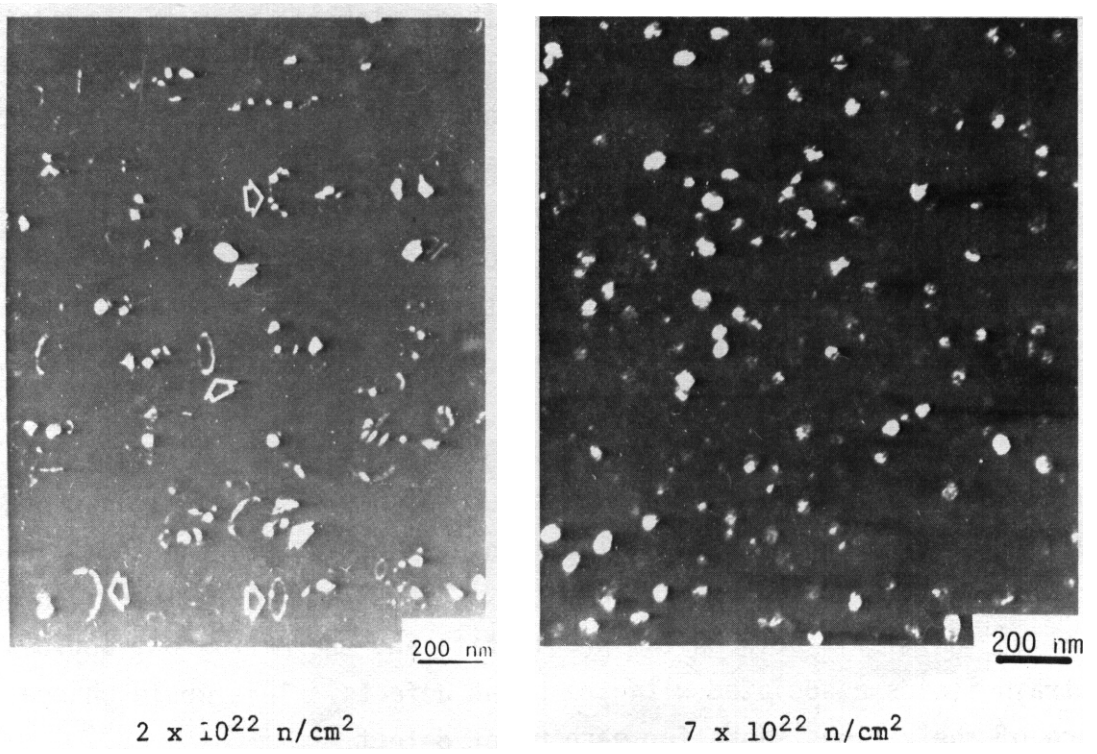

FIGURE 4. Formation of γ' on the Edge of Frank Loops in Silicon-Modified AISI 316 Irradiated in EBR-II at 482°C. (Courtesy of E. H. Lee of ORNL).

An interesting feature of the radiation-stable phases is their instability in the absence of irradiation. Postirradiation aging of both the G-phase and the γ' phase in AISI 316 has shown them to slowly dissolve at the temperature of their in-reactor formation.[5,7] There also appears to be a limitation to the temperature range of γ' stability at a given displacement rate.[3,7] Both the γ' and nickel-rich $M_{23}C_6$-formed in neutron-irradiated 316 were also observed to dissolve when irradiated with nickel ions at higher displacement rates.[37] This indicates that the stability of a given precipitate in any alloy may be confined to a certain regime of damage rate and temperature.

Another new phenomenon observed in these studies is the infiltration-exchange process,[2,6] wherein precipitates such as $M_{23}C_6$ and Laves become progressively enriched in nickel and silicon at the expense of other elements such as chromium and molybdenum. Porter's data clearly show this evolution in measurements of extracted precipitates.[13] Line-of-sight EDX profiles show that this

process manifests itself in gradients of these elements near the precipitate surfaces, particularly when swelling is at low levels.[2,6] At higher fluences and levels of swelling the gradients are no longer maintained and the matrix conpositions of the participating elements are established at new levels. The use of line-of-sight profiles has not yet allowed the identification of the balance of mechansims involved. It is expected, however, that inverse Kirkendall, solute-defect binding and perhaps even interstitial-altered phase stability may all contribute to the phenomenon.

It might be speculated that the operating processes are self-accelerating in that the removal of various elements such as nickel and silicon changes the diffusivities of both the elemental components and the point defects, and also alters the lattice parameter of the matrix. This latter consideration would not only alter the misfit between the precipitate and the matrix but would also alter the strain fields associated with the point defects. This would change the preference of the various sinks for each point defect.

4. The Microchemical Role of Carbon, Silicon and Nickel

Although the swelling of AISI 316 has been found to be sensitive to the concentration of many elements,[38-39] it appears that the microchemical evolution primarily involves the action of carbon, silicon and nickel. It has been shown that even in Fe-Ni-Cr alloys without solute the swelling is critically dependent on the nickel concentration at levels below approximately 35%.[40] This suggests that the nickel level strongly affects either the diffusional properties of the matrix or the capture efficiencies of each microstructural component. The former possibility has been discussed by Venker and Ehrlich[41] but experiments directed toward this proposal do not support the concept of a substantial modification of diffusional properties with nickel content.[42-43] A large dependence of the irradiation-induced dislocation density on nickel content has also not been observed. Since many properties of Fe-Ni-Cr alloys (stacking fault energy, modulus, lattice constant, thermal expansion coefficient, and magnetic properties) show a pronounced sensitivity to the nickel content, it appears that the point defect capture efficiencies of dislocations and voids

might also be sensitive to the nickel content. As shown in Figure 5, it appears that a parallel can be drawn between the dependence of swelling on initial nickel content and the acceleration of swelling with declining nickel content. Just as the initial nickel concentration C^{o}_{Ni} has been shown to be the major factor determining the magnitude of swelling,[39] the declining instantaneous nickel content in a specific alloy has been correlated with the acceleration of the swelling rate.[2,6]

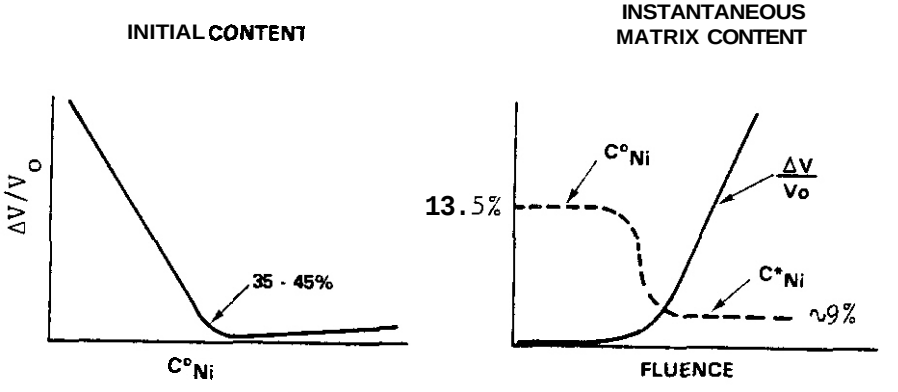

FIGURE 5. Schematic Representation of the Correlation Observed Between Swelling Versus the Original Alloy Nickel Content and Swelling Versus the Average Instantaneous Nickel Content in the Matrix of AISI 316.[40]

In examination of AISI 316 of nominal composition,[3,5-6] AISI 316 of varying silicon levels,[15] and the titanium and silicon-modified 316 designated LSI [16-17] a rough correlation has been developed which predicts the nickel saturation level.[2] When the average matrix nickel content reaches the level $C^{*}_{Ni} \simeq C^{o}_{Ni} - 3(C_{Si} + C_{C})$, where C_{Si} and C_{C} are the atomic concentrations of silicon and carbon, the steady state swelling is essentially established.

The decomposition of the austenite matrix of AISI 316 has been shown to occur in a very inhomogeneous manner, particularly in the cold worked condition. On a microscopic level, however, the correlation between the onset of void growth and the local nickel content has been demonstrated quite clearly in a study where the elemental concentrations in many small volumes throughout the matrix of irradiated AISI 316 were sampled by energy dispersive X-ray analysis. In Figure 6, the distribution of matrix nickel contents is presented for two AISI 316 specimens made from identical material but of different

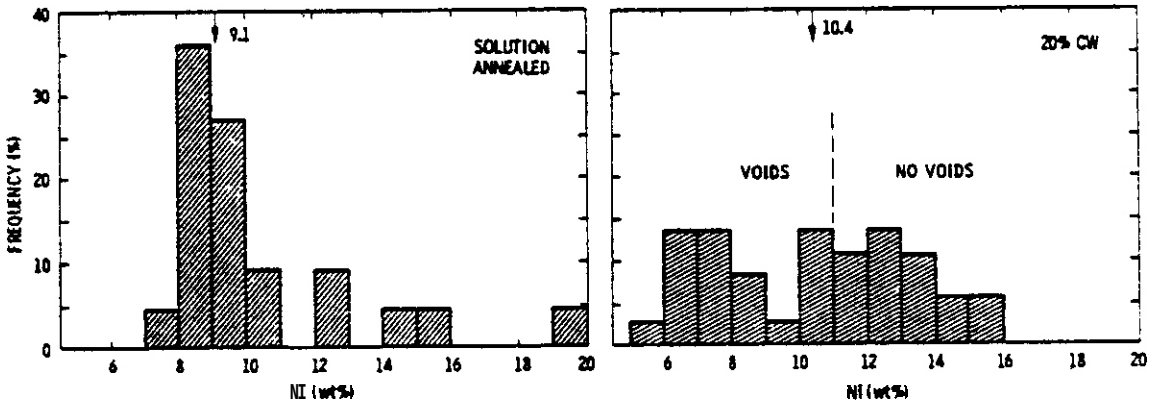

FIGURE 6. Distribution of Nickel Content in Many Small Matrix Locations in Irradiated AISI 316 Specimens Irradiated at 650°C to a Fluence of 1.0×10^{23} n/cm^2 (E >0.1 MeV).[2] Voided regions exist in areas with nickel contents below ~11%.

starting conditions. They were irradiated together. Both the solution annealed and 20% cold worked specimens wen? found to contain Laves precipitates which were substantially enriched in nickel and silicon. The mean levels of these elements in the precipitates of the solution annealed specimens were higher than those of the 20% cold worked specimen. Note that the average nickel level of the matrix of the annealed specimen has been reduced from the original 13.5% level to about 9%. The cold worked specimen at these conditions has a matrix nickel content that has been reduced to an average of 10.4%, a value approaching that of the solution annealed matrix, but the distribution is much broader. The void swelling of the annealed specimen was about 8% and relatively homogeneously distributed, while the void swelling of the cold worked specimen was only 0.6% and quite nonuniformly distributed. In general, X-ray analysis of voided precipitate-free areas (about 0.5 microns in diameter) in the cold worked specimenshowedthe nickel content to be in the <10% range while areas containing >11% nickel had not yet begun to swell.

The role of silicon appears to be two-fold as shown in Figure 7. While in solution the silicon causes a suppression of void nucleation.[15] As the matrix silicon level is increased, the void incubation period is extended.[15,39-40] This behavior has been explained in terms of silicon's simultaneous role in interstitial-solute binding and enhanced vacancy mobility.[44-45] When silicon leaves

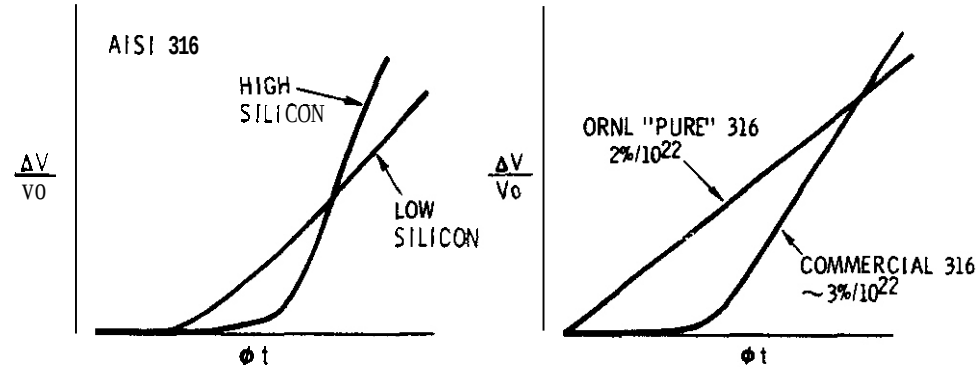

FIGURE 7. Schematic Representations of the Dual Role of Silicon in Void Swelling of AISI 316. The addition of silicon leads to an extension of the incubation period but a later increase in the swelling rate.(15) The "pure" 316 data are presented in Reference 46 and establish that the swelling rate is independent of temperature over a wide range of temperatures. The "comnercial" 316 curve is drawn for the peak swelling rate which occurs at approximately 590°C.(65)

solution the effective vacancy diffusivity decreases and void nucleation rates increase. At the same time, the coprecipitation of nickel and silicon results in a substantial reduction in the matrix nickel content. This causes an increased swelling rate at higher fluence. Therefore, any short-term benefit of reduced swelling with additional silicon is lost at higher fluences. For example, Figure 7 also shows a comparison between the observed swelling behavior of two nominally similar steels, both with the same major element composition, but one without solutes (carbon and silicon). The "pure" 316 alloy exhibits a very short incubation period and a swelling rate of only $2\%/10^{22}$ n/cm^2 (E > 0.1 MeV) which is essentially independent of irradiation temperature.(46) The "commercial" 316 alloy, on the other hand, exhibits the expected long incubation period and a swelling rate that was 50%higher, as would be expected for an alloy matrix with a much lower saturation level of nickel. As shown in Figure 8, the simultaneous removal of nickel and silicon can also be observed on a microscopic level.

Carbon appears to control the rate, path and extent of the initial phase development. This role shifts with temperature. At relatively low temperatures (<525°C) the addition of carbon depresses swelling in AISI 316,(35,38,47) primarily by extending the incubation period, as shown in Figure 9. The mechanism

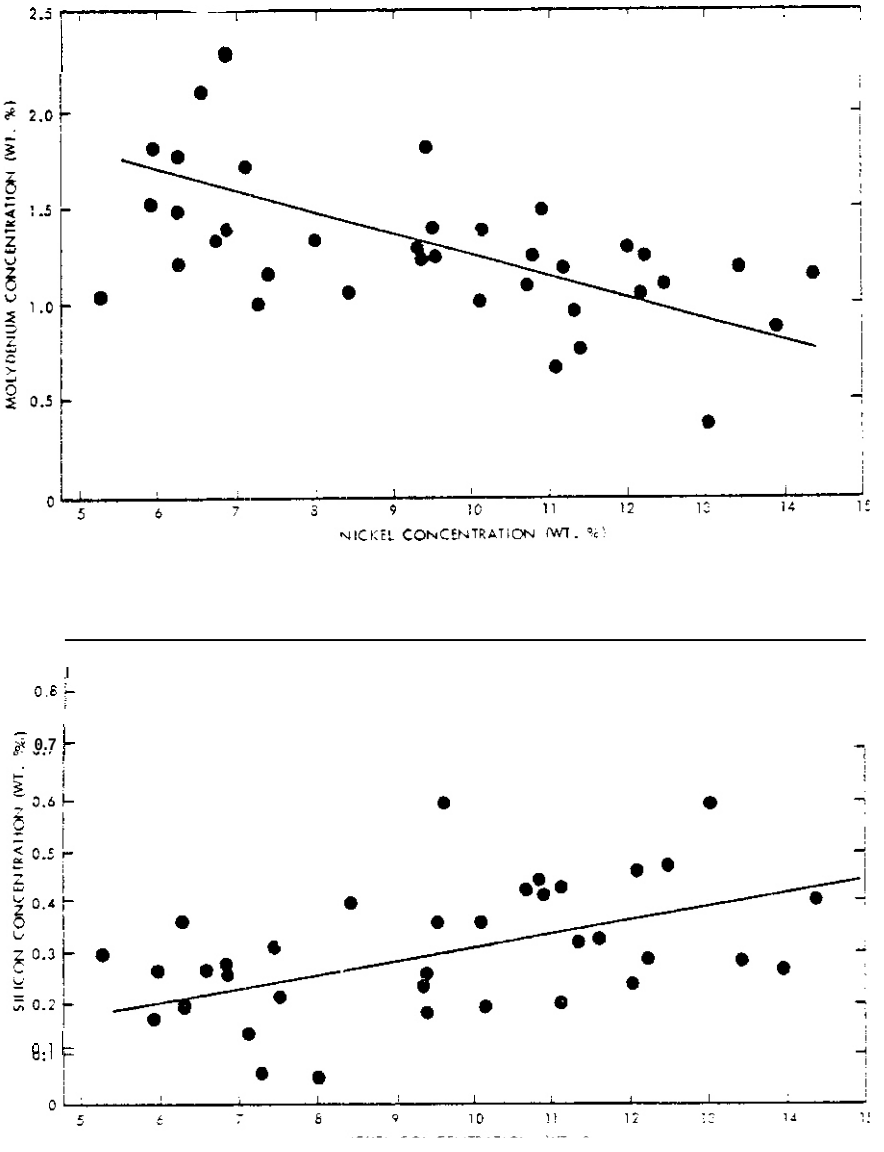

FIGURE 8. Simultaneous Determinations of Elemental Compositions at Many Areas in 20% Cold-Worked AISI 316 Irradiated at 650°C to a Fluence of 1.0 x 10^{23} n/cm^2 (E >0.1 MeV).(2,6) The lines are determined by least squares fit. Note that nickel and silicon tend to be high together while molybdenum is low. This indicates that nickel and silicon flow together and against the flow of molybdenum. There are large local variations in all elements, however.

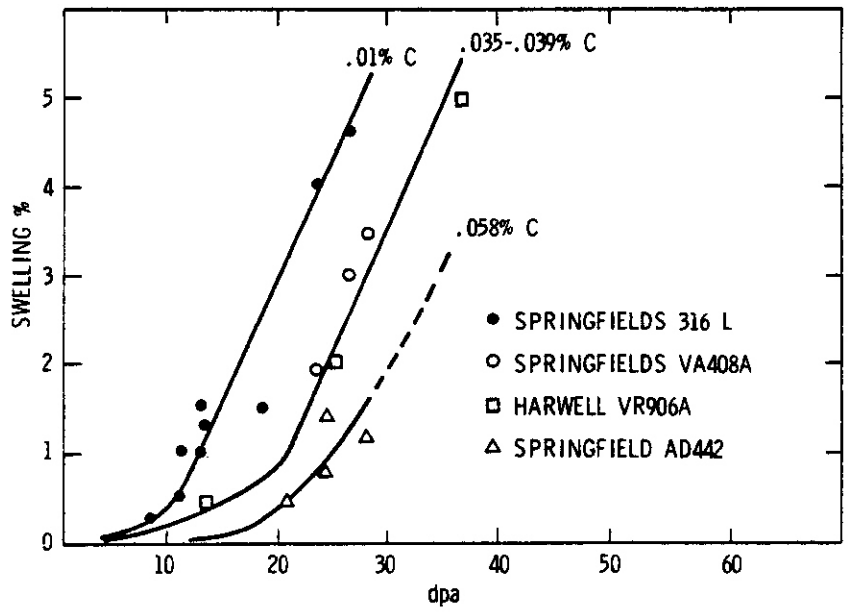

FIGURE 9. Effect of Carbon Content on the Swelling of Four British 316 Stainless Steels Irradiated at 425°C.[35]

proposed to explain this behavior is steel somewhat speculative but it appears that carbon interferes with the development of the dominant precipitate that forms at low temperature in annealed AISI 316. This precipitate has been found at 6 x 10^{22} n/cm^2 and 385°C to be 40.3Cr-17.5Fe-26.9Ni-8.3Si-6.4Mo (wt.%).[5-7] The lattice constant (1.13 nm) and the fcc crystal structure appear to signal another G-phase, this one based on chromium. Cold work has been also shown to completely **suppress** the formation of this phase and its associated swelling.[4-5]

At higher temperatures (>550°C) carbon additions increase the swelling of AISI 316,[39] as shown in Figure 10. At these temperatures carbides are precursors to the formation of intermetallic phases such as Laves. It is the infiltration of these phases by nickel and silicon that controls the swelling rate at temperatures above approximately 550°C.[2,6] Thus, adding carbon accelerates the microchemical evolution by accelerating the development of the carbide and Laves phases. The reversal in carbon's role occurs in the regions near 550°C and this probably accounts for the lack of consistent swelling behavior versus carbon content observed at temperatures of 525 ±25°C.[35]

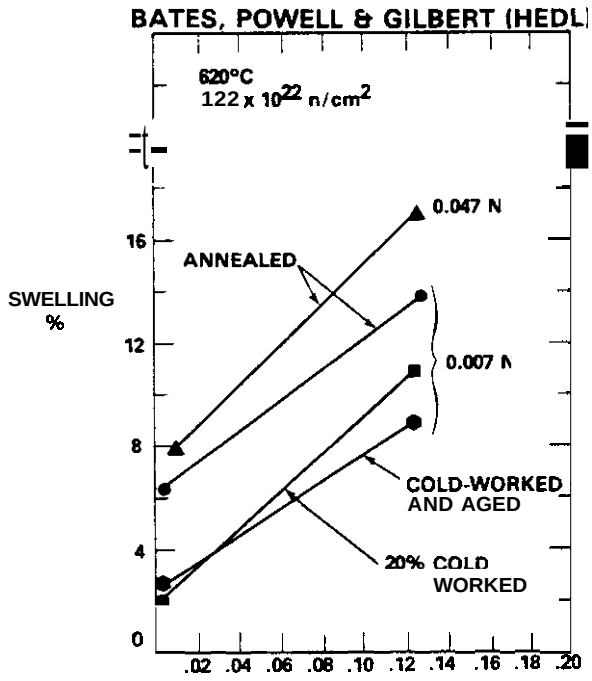

FIGURE 10. Carbon Increases Swelling of AISI 316 in Various Starting Conditions at High Temperature and Fluence.(39) Note the synergism with nitrogen.

Although the possible roles of carbon while in solution have not been identified at this time, it appears that carbon's major role in swelling of AISI 316 is to trigger or influence the path and time by which the initial phase development occurs. Irradiation temperature, displacement rate, and thermal-mechanical starting condition are variables expected to be important in the initial distribution of carbon and the rate and route by which it precipitates. The relationship between carbon precipitation and the temperature dependence of swelling has been studied by Hofman and coworkers.(48-49)

The reversal of carbon's role with increasing temperature leads to the prediction that the relative magnitude of the two swelling peaks(47-51) observed in annealed AISI 316 will be strongly affected by the carbon content. Low carbon steels will have accentuated low temperature peaks and smaller peaks at high temperatures. High carbon steels will exhibit the opposite behavior. This behavior was observed in U.S.,(48-49) British and French fuel pin cladding.(35,47,50) As shown in Figure 11, the double-peaked behavior of annealed AISI 316 can be linked to similar peaks in the nickel removal processes.(51)

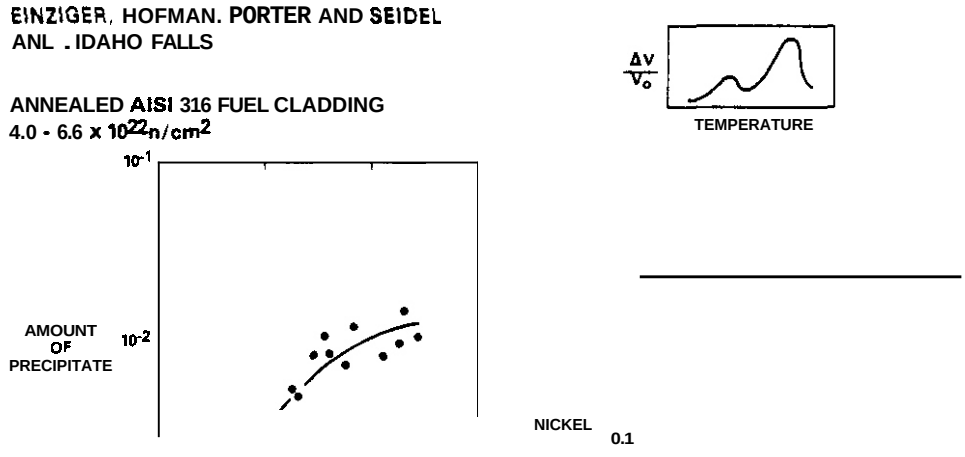

FIGURE 11. Relative Measurements of Extracted Precipitates and Their Nickel Content in Annealed AISI 316 Fuel Pin Cladding.(12,51) The schematic at the upper right shows that annealed 316 for high peak cladding temperatures exhibits two swelling peaks.(48-49,51) Researchers at ANL correlate these peaks to the peaks seen in the mole fraction and total nickel removal curves.

It is important to note that the actions of nickel, silicon, and carbon are all highly interactive with each other. One example will suffice to show that ignorance of the synergism between these elements caused many of theearlierconflicting conclusions concerning the role of these elements.

Recently, comparative irradiation data on various British steels have shwon that during irradiation at 425°C, the role of carbon is clearly to extend the incubation period of swelling (see Figure 9).[35] In the interpretation *of* these data, however, the investigators inadvertently spotlighted one *of* the apparent inconsistencies which arise as a result of the Ni-C-Si synergism. Although two of the steels have essentially identical carbon levels and exhibit identical swelling behavior, the silicon levels are substantially different (0.32 versus 0.63 wt.%). This led the authors *of* that report to conclude that silicon plays no great role at that temperature. This conclusion is inconsistent with all other British, U.S. and European data. The low silicon steel, however,

was also low in nickel relative to that of the high silicon steel. Using the previous definition for the coprecipitation relationship and a factor of two to convert silicon weight percentages to atomic percentages, the saturation nickel content for the two steels can be determined. Therefore, the effect of silicon

Springfields VA408A:	$C^*_{Ni} \simeq (13.7) - (3)(0.63)(2) = 9.9\%$
Harwell VR906A:	$C^*_{Ni} \simeq (11.4) - (3)(0.32)(2) = 9.5\%$

in each alloy is to reduce the predicted matrix nickel content to almost identical saturation levels. It appears that the influence of silicon in this experiment was therefore obscured by the corresponding nickel variations.

5. The Microchemical Role of Other Elements

The element molybdenum plays a large role in the formation of the carbide and intermetallic phases.[24] The swelling behavior of AISI 304 is significantly different from that of AISI 316 and may reflect not only its lower nickel content but also the absence of molybdenum. Molybdenum appears to play no direct role in the formation of the radiation-stable precipitates. Molybdenum flows out of caribde and Laves precipitates during irradiation, however, signalling that it plays some active role in the evolution. Molybdenum is not only a relatively fast diffusing element in γ-iron [52] but has the largest degree of misfit or lattice dilation *of* any element in AISI 316.[53] It would therefore be expected to migrate up a gradient of either interstitials or vacancies. This may account for the outflow observed of molybdenum.

It also appears that at low concentrations some elements such as phosphorus and nitrogen exert a surprisingly large effect on swelling.[39] For instance, it has been shown that phosphorus changes the critical temperature for self-nucleation of homogeneous precipitation of $M_{23}C_6$ in 18Cr-9Ni-4Mn-stainless steels.[54] It appears that such elements may increase the effective interstitial content of the steel, either increasing the effective supersaturation of carbon or by entering the precipitate to form $M_{23}(C,P)_6$.[54]

The titanium and niobium-stabilized austenitic alloys have exhibited swelling behavior substantially different from that of AISI 316 of nominal specification. Since the MC carbides formed are quite stable at normal irradiation temperatures, this might be expected. There is, however, one remarkable coincidence in the swelling behavior of these alloys. As illustrated in Figure 12, titanium-modified steels routinely exhibit a low-temperature swelling peak. They also develop less swelling at high temperature than observed in unmodified AISI 316.[55-56] This is the behavior expected of low carbon steel. While it would be unrealistic to propose that the only role of titanium is to reduce the carbon content of the alloy matrix, it is hard to ignore the parallel. It is also quite significant that TiC precipitates resist the infiltration-exchange process while other phases cannot.[26]

Note that for each of the elements considered above, the central role proposed is that of influencing the activity or distribution of carbon. This tends to confirm the proposed role of carbon as one of the major determinants of the swelling behavior.

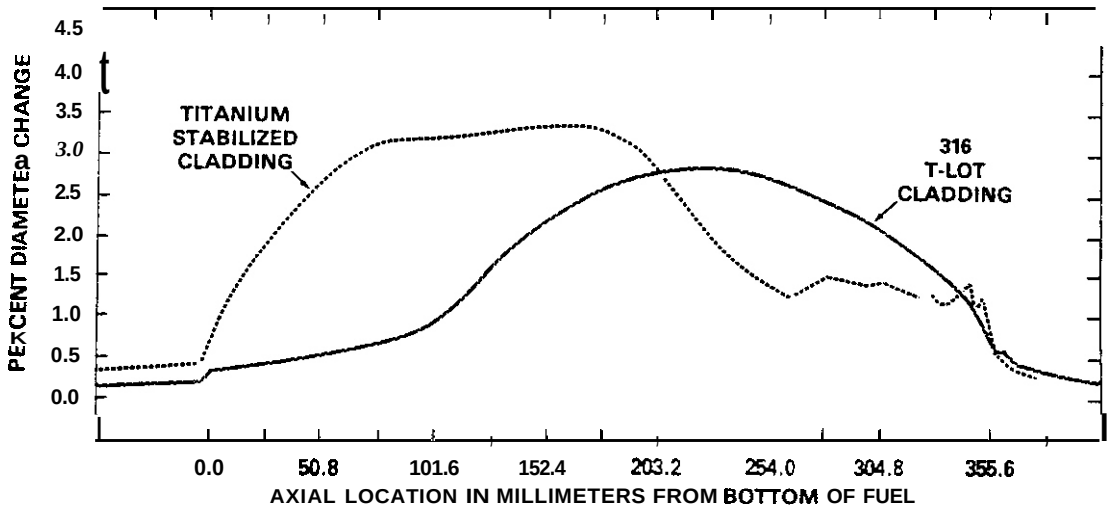

FIGURE 12. Diameter Measurements From a Fuel Pin Clad With Titanium-Stabilized 20% CW 316 Stainless Steel and From a Fuel Pin Clad With T-Lot 20% CW Stainless Steel.[55,60] (T-lot pins were constructed from the same heat of steel used in the experiments described in figures 3, 6, 8, 20 and 21). Both pins were irradiated side by side to 10.5 x 10^{22} n/cm^2.

6. The Microchemical Role of Dislocations

The role of dislocations cannot be defined as confidently as that of other parameters; therefore, this section is by nature somewhat speculative. The data do present strong clues, however. First of all, cold working of pure metals (Al, Mg, Cu, Ni, V) does not lead to changes in neutron-induced swelling.[57] (Ion and electron irradiation of cold worked pure metals has yielded rather ambiguous results and reflects the difficulty in establishing or maintaining high near-surface dislocation densities). While the role of cold work is always to reduce swelling in AISI 316, the swelling of AISI 304 and AISI 321 can actually be increased, particularly at low temperatures.[46]

Brager and Garner [4-5] have definitively shown that the role of cold work is to alter the phase evolution associated with swellling in AISI 316. In one case, the low temperature radiation-stable and nickel-rich phase that evolves easily in annealed steel was totally suppressed by cold working, requiring that the microchemical evolution proceed via the more sluggish γ' route. At other temperatures, the carbide-Laves sequence and the ensuing infiltration-exchange process were merely delayed by cold work, therefore extending the incubation period for void swelling. It was also shown in this steel that preirradiation aging of 20% cold worked steel under some conditions accelerated the formation of the normally sluggish γ' phase.[4-5] This acceleration leads to swelling levels greater than that of annealed steel. This was quite surprising since the aged steel prior to irradiation still possessed dislocation densities typical of the 10% cold worked condition.

The data also strongly suggest an interrelationship between dislocation density and carbon.[47,50] Note in Figure 13 that both increasing cold work and carbon levels have similar effects on the swelling of AISI 316. It is proposed here that the role of cold working is two-fold. The carbon dispersed in the matrix during annealing probably begins to cluster during the subsequent rather rapid cool-down. Cold work not only redistributes the carbon more effectively but the dislocations also bind a large fraction of the carbon due to its large degree of misfit in this alloy.[53] The effect of this binding with dislocation

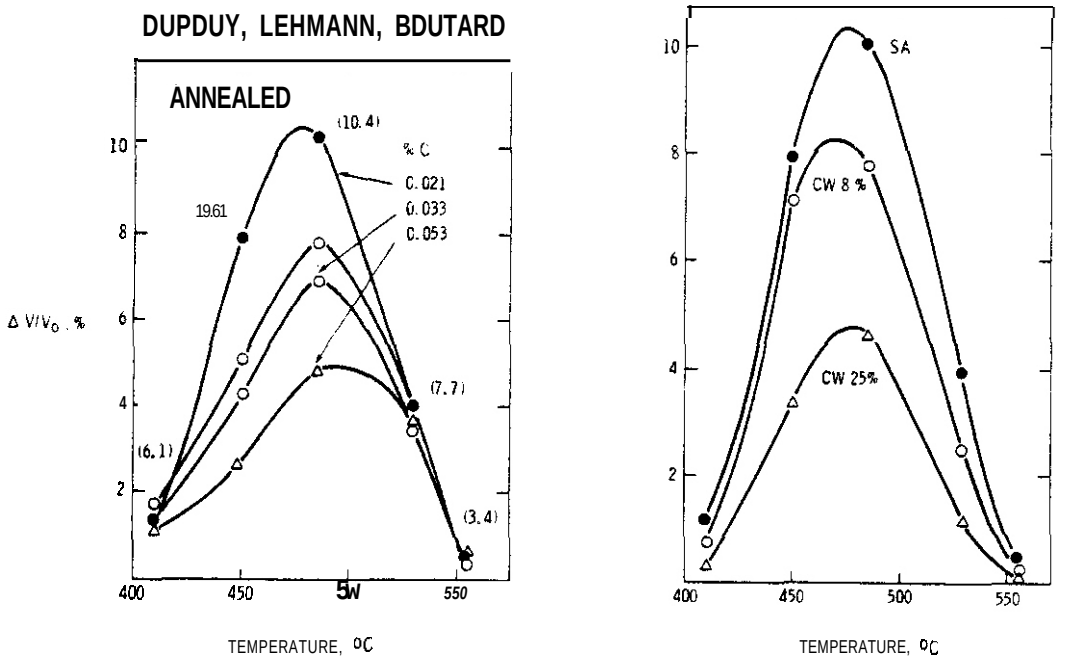

FIGURE 13. Similar Influence of Carbon Content and Cold Work on Swelling of AISI 316.(50) The effect of carbon content on 20% cold-worked steel is equally dramatic as that of annealed steel. The neutron fluence in units of 10^{22} n/cm^2 (E >0.1 MeV) is shown in parentheses

densities on the order of 3×10^{11} cm^{-2} is to elevate the solubility of carbon in the matrix at low irradiation temperatures, thereby reducing the supersaturation of carbon and altering the rate of its segregation. The high density of dislocations and Frank loops generated by cold working is maintained by the radiation at levels $\geq 6 \times 10^{10}$ cm^{-2}.(1)

If this argument is to have any validity, one would expect that the effect of cold work on swelling should saturate when the dislocation density saturates. The data shown in Figures 14(a) and 14(b) support this concept. The effect of cold work on swelling saturates around 30% cold work (58) and so does the dislocation density and its associated strain.(59)

The best test of this concept would be to demonstrate that cold working of pure Fe-Ni-Cr ternaries leads to no change in swelling behavior. Unfortunately, such an experiment does not appear to have yet been performed.

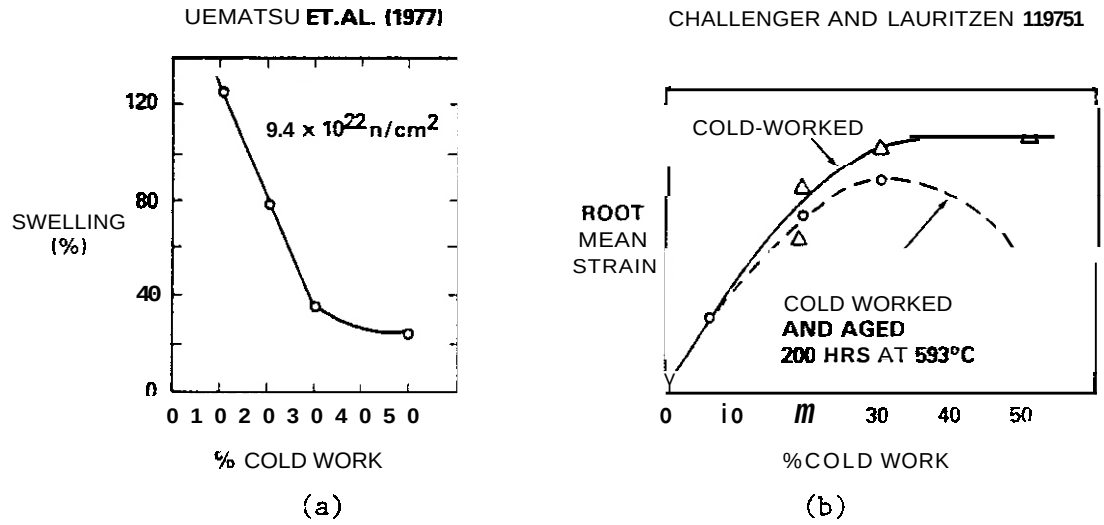

FIGURE 14. (a) Effect of Cold Work on Swelling of Type 316 Stainless Steel at High Fluences.(58) (b) Root Mean Strain as a Function of the Degree of Cold Work and Aging for Type 316 Stainless Steel.(59)

The typical diameter change profiles observed in fast reactor irradiations (Figure 15) can now be explained in terms of the diversity of the phase evolution and its sensitivity to cold work as well as processing and irradiation temperature. The double-bump profile of annealed steel is a reflection of two precipitation regimes influenced by the carbon level. The relative prominence of the two peaks is dependent not only on the carbon level but also the flux and temperature profiles. The region between the peaks is the regime of the sluggish γ' phase, which has been found to be insensitive to the cold work level. Earlier it was noted that the γ' precipitates appear to have nucleated on Frank loops. The Frank loop density is eventually independent of starting condition after a short period of irradiation.(1) This may account for the independence of γ' formation on cold work.

Cold working of this steel suppresses the low temperature radiation-stable phase and delays the microchemical evolution at all temperatures, probably by influencing the distribution and activity of carbon. Note that in Figure 15 the cold worked swelling peaks above core center, reflecting the sluggish evolution of the phases around 500°C in the heats of steel originally employed in the U.S. Breeder Program.(7) In AISI 316 steels with much shorter incubation periods

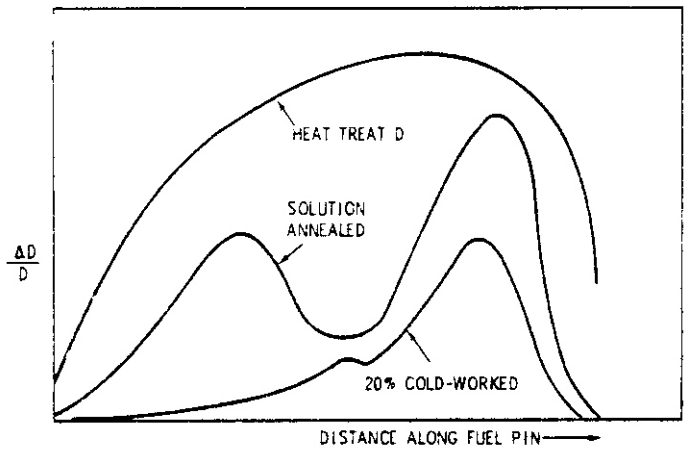

FIGURE 15. Schematic Illustration of Deformation Profiles Observed in AISI 316 Fuel Pins Irradiated in a Typical Fast Reactor.

employed in construction of the core of the Fast Flux Test Facility, the swelling peaks in the EBR-II reactor occur near the peak flux position.(60)

It also appears that the Frank loops formed early in the irradiation at low temperature may provide nucleation sites for the radiation-stable G-phase formed in annealed steel. Beckitt and Clark (36) have shown that interstitial loops (formed during aging by internal stresses generated by volume changes accompdnying the growth of $M_{23}C_6$) are instrumental in nucleating new $M_{23}C_6$ particles. Perhaps the radiation-produced loops provide the nucleation sites for both carbides and silicides. The high temperature side of the low temperature swelling peak corresponds rather closely to the temperature dependence of Frank loop density.

7. Sensitivity to Environmental Parameters

Now that an understanding is emerging as to the origin of the variability of swelling response to irradiation, the available data must be analyzed with an eye toward the influence of uncontrolled variables within the data. Figure 16 demonstrates that the displacement rate affects swelling of AISI 316 probably through flux-time effects on phase evolution.(61) In data reduction efforts the neutron flux is usually not considered a variable.

It is safe to forecast that when design correlations developed to

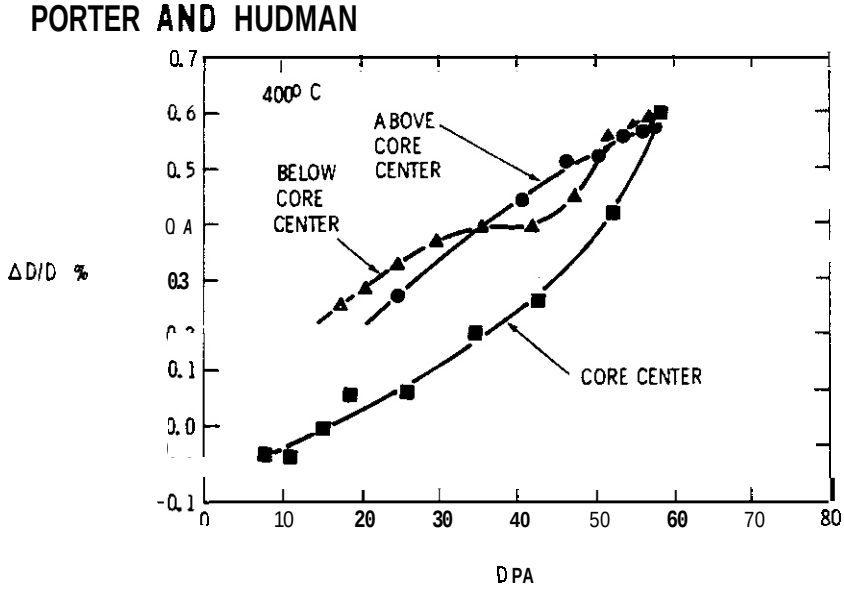

FIGURE 16. Diameter Change Data (61) for 5% Cold-Worked AISI 316 Suggesting That the Swelling is Sensitive to Displacement Rate and Time In Reactor as Well as the Total Number of Displacements (dpa).

describe the behavior of this steel are applied to new environments, the predictions and the material response will diverge due to the sensitivity of the microchemical evolution to many environmental variables. It must also be recognized that the majority of the available data fall into two categories, irradiation of experimental specimens under relatively isothermal conditions and irradiation of fuel pin cladding. The time, temperature, stress and flux histories experienced by these materials are not an adequate representation of all potential in-reactor histories.

In order to be able to attempt predictions of the behavior for any new environment and history, a new approach is being employed. The phases observed in a given class of steels are cataloged and their sensitivities determined. This provides some guidance when extrapolating into new environments. The pronounced flux and temperature sensitivities of the radiation-stable phases leads to the conclusion that one would anticipate that at higher fluxes a shorter incubation period would result at low temperatures. As shown in Figure 17, flux-sensitive incubation periods have been observed in comparative irradiations in two French fast reactors,(47)

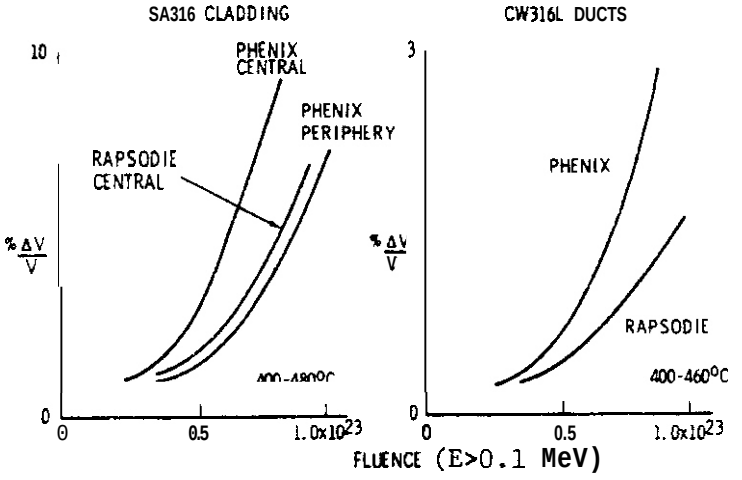

FIGURE 17. Flux-Dependent Swelling Behavior Observed in Irradiation of French Solution-Annealed Cladding and Cold-Worked 316L Ducts. (47)

but no microstructural data are available to confirm that the sensitivity can be correlated with changes in the γ' or G-phase. In these irradiations, the temperature increased slowly with dose and was approximately the same for the various curves at a given dose. The authors of the original report note that when comparisons are made at constant dose and temperature the swelling is always greater when the displacement rate is greater. (47)

One would also expect that the intermetallic phases, the precursors to the infiltration-exchange process, would be very sensitive to time-at-temperature. In higher flux reactors a component would spend less time in reactor to reach a given fluence. As a consequence, the high temperature swelling peak would recede somewhat. This behavior has also been observed in comparative Phenix/Rapsodie irradiations. (47)

The most pronounced demonstrations of the temperature sensitivity of the γ' phase are provided by the response of both swelling and irradiation creep to decreases in temperature which cross the γ' phase boundary in a manner shown in Figure 18. Both the swelling (Figure 19) (62) and the irradiation creep (Figure 20) coefficient (63) were found to vary strongly with the magnitude of the temperature drop. The sensitivity of void swelling was shown to be directly correlated with the onset of accelerated γ' formation. (63) In this experiment

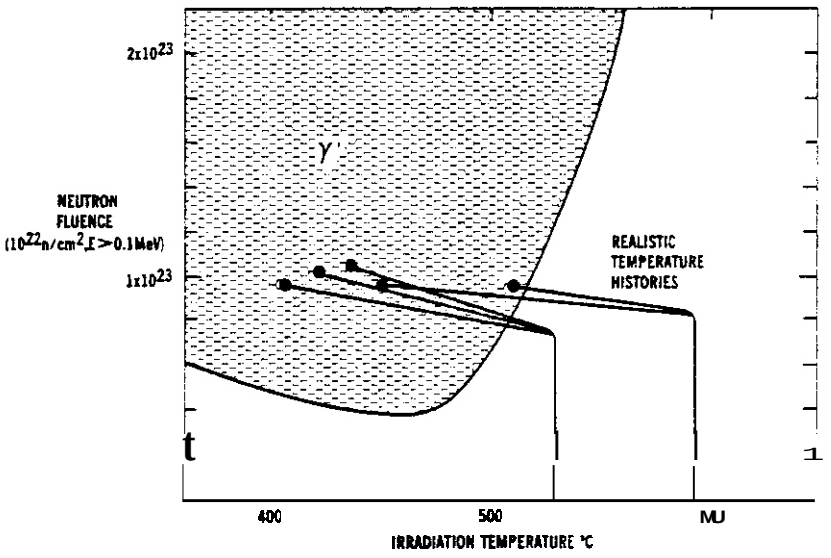

FIGURE **18.** Typical Temperature Histories *of* 20% CW AISI 316 Specimens Subjected to Gradual Temperature Reduction During Irradiation. (63) The shaded region represents the regime *of* isothermal formation of γ' in this heat. (3)

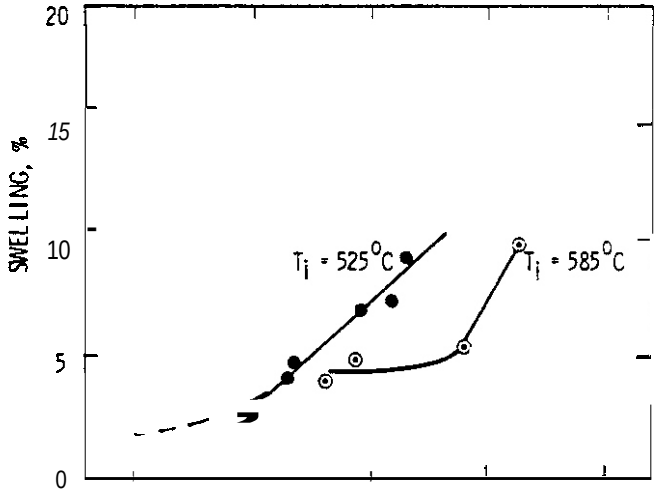

FIGURE 19. Enhancement of Swelling **by** Gradual Temperature Reductions During Neutron Irradiation of 20% Cold-Worked AISI 316 (replotted from Reference 62). T_i is the starting temperature.

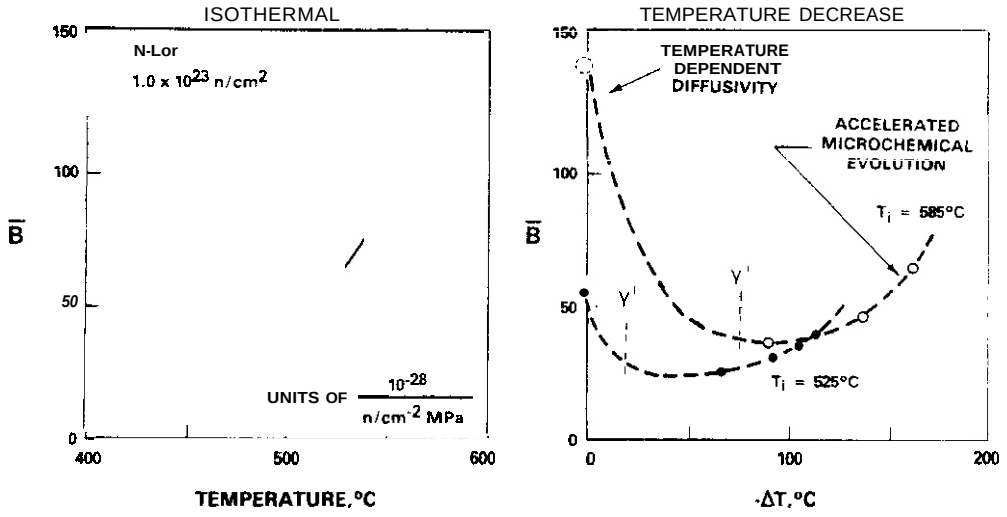

FIGURE 20. Comparison of Average Creep Coefficients of 20% CW AISI 316 Obtained in Response to Isothermal and Gradually Declining Irradiation Temperatures.(62) The onset of γ' formation is shown.

the onset of the gradual temperature drop preceeded the onset of swelling, but not the onset of irradiation creep. As shown in Figure 20, the average creep coefficient over the constant and declining portions of the temperature history initially falls with decreasing temperature, in agreement with rate theory predictions for an alloy of constant composition. However, the average creep coefficient again increases for temperature histories that form γ' and change the matrix composition of the alloy.

Similar swelling and creep behavior was found in fuel pin cladding subjected to cyclic temperature decreases.(63-64)

One conclusion concerning development of swelling correlations was drawn from the temperature change data. The large values of swelling observed for large temperature decreases cannot be explained by any small modification of the currently available empirical descriptions of isothermal swelling.(65) In particular, the "steady-state" swelling rates contained in these correlations must be changed to reflect the possibility that the low swelling rates observed in cold worked AISI 316 are merely a manifestation of a very slowly evolving precipitate microstructure, but one that can be short-circuited by certain temperature histories.

The flux and temperature dependency of the radiation-stable phases has also been shown to account for much of the fluence, temperature and flux dependence of the yield stress of **AISI** 316. (66-67)

The effect of tensile stress on swelling of AISI 316 and other alloys has recently been definitively determined to be related to changes in the incubation behavior.[68] **As** shown in Figure 21, the effect of stress is most pronounced at high temperatures. This sensitivity has been shown to be related to the stress sensitivity of intermetallic phase formation.[68] This insight requires that the correlation developed for non-tensile stress states be quite different than originally envisioned. The low-temperature radiation-stable precipitates do not appear to be stress-sensitive. This has been verified experimentally for the γ' phase in **AISI** 316 and has been inferred for the G-phase from the relative stress-insensitivity of swelling of annealed **AISI** 316 at **low** temperatures.[47]

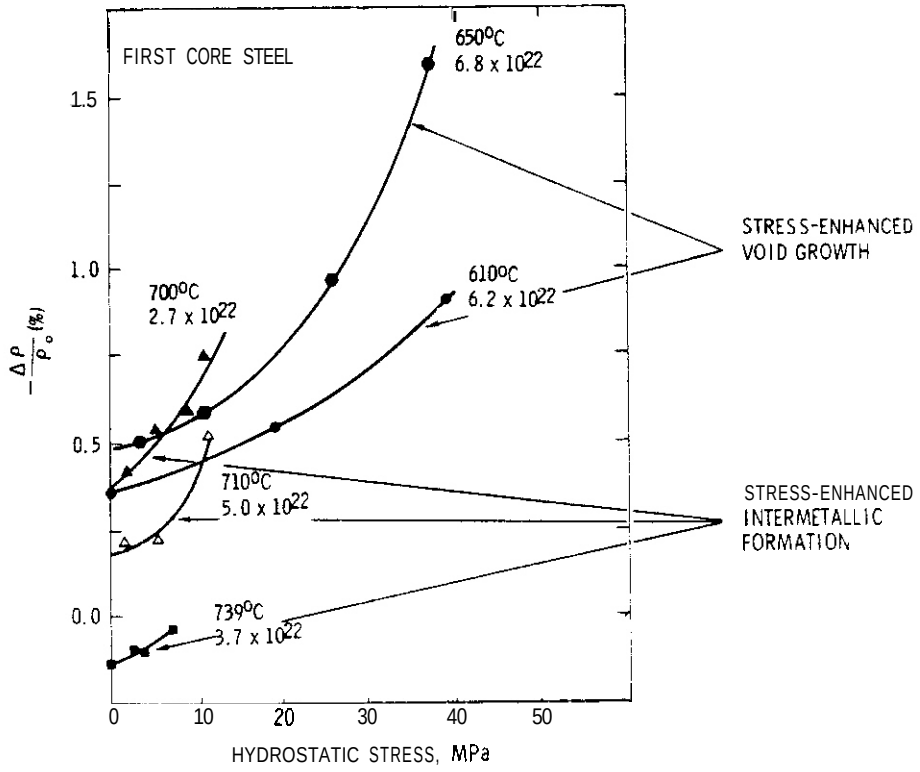

FIGURE 21. Stress-Enhanced Density Changes Observed in 20% Cold-Worked AISI 316.(68) Note that dilational strains associated with formation of intermetallic phases can be observed at temperatures and fluences where void swelling has not commenced.

8. Conclusions

In the foregoing sections, it has been shown that the precipitates that develop during irradiation play the dominant role in the alloy response. This role is expressed primarily in a large change in matrix composition that may significantly alter the diffusional properties of point defects. It may also substantially alter the rate of acceptance of point defects at dislocations and voids.

The major elemental participants have been identified as carbon, nickel and silicon. Carbon appears to function as a major governing factor of the route and rate by which the evolution proceeds. It is the sensitivity of carbon's response to a wide range of variables that accounts for much of the variability observed in the swelling of AISI 316 stainless steel, particularly in response to preirradiation thermal-mechanical treatment.

Silicon's role is two-fold in that while in solution it depresses void nucleation and determines the duration of the void incubation period. It also coprecipitates with nickel. The eventual level of nickel in the alloy matrix appears to control the steady-state swelling rate.

The other participating elements appear to affect primarily the distribution and activity of carbon. Dislocations introduced either by irradiation or cold work likewise appear to influence the role of carbon.

In these studies, several new physical mechanisms appear to be operating. These are the inverse Kirkendall effect, interstitial-altered phase stability, solute-interstitial binding, the infiltration-exchange process, and the creation of radiation-stable precipitates. The sensitivity of the last phenomenon to temperature and flux has been shown to account for much of the unusual behavior of AISI 316 during irradiation.

VI. REFERENCES

1. H. R. Braoer. F. A. Garner. E. R. Gilbert. J. E. Flinn, and W. G. Wolfer, in Radiation-Effects in Breeder Reactor Structural Materials, M. L. Bleiberg and J. W. Bennett (Eds), the Metallurgical Society of the America1 Institute of Mining, Metallurgical and Petroleum Engineers (1977), pp. 727-755.

2. H. R. Brager and F. A. Garner, "Microchemical Evolution of Neutron-Irradiated 316 Stainless Steel," Effects of Radiation on Materials, ASIM STP 725, D. Kramer, H. R. Brager and J. S. Perrin (Eds), ASIM (1981).

3. H. R. Brager and F. A. Gamer, J. Nucl. Mat., 73 (1978), p. 9.

4. H. R. Brager and F. A. Garner, Trans ANS, 28 (1978), p. 151.

5. H. R. Brager and F. A. Garner. "Deoendence of Void Formation on Phase Stability in Neutron-Irradiated Type 316 Stainless Steel," Effects of Radiation on Structural Materials, ASIM STP 683, J. A. Sprague and D. Kramer (Eds), ASIM (1979), pp. 207-232.

6. H. R. Brager and F. A. Garner, "Analysis of Radiation-Induced Microchemical Evolution in 300 Series Stainless Steel," Proc. Symposium on Advanced Techniques for the Characterization of Irradiated Materials, February 24-28, 1980, Las Vegas, NV, to be published in TMS-AIME Conference Proceedings Series.

7. W. J. S. Yang, H. R. Brager and F. A. Garner, "Radiation-Induced Phase Development in AISI 316," Proc. AIME Symposium on Irradiation Phase Stability, October 5-9, 1980, Pittsburgh, PA (in press).

8. P. J. Maziasz, Scripta Met., 13 (1979), p. 621.

9. P. J. Maziasz, J. Nucl. Mat., 85 and 86, (1979), p. 713.

10. P. J. Maziasz. "Precipitation Response of Austenitic Stainless Steels to Simulated Fusion Irradiation," in The Metal Science of Stainless Steels, E. W. Collins and H. W. King (Eds), Proc. 107th AIME Annual Meeting, Denver, CO, March 2, 1978.

11. D. S. Gelles, "Gamma Prime Formation in AISI 316 Stainless Steel: An Example of Radiation-Enhanced Solute Segregation," Ref. 10.

12. D. L. Porter and W. L. Wood, J. Nucl. Mat., 83 (1979), p. 90.

13. D. L. Porter, "Irradiation-Induced Microstructural Changes in Neutron-Irradiated Cold Worked and Aged Type 316 Stainless Steel," accepted for publication in J. Nucl. Mat.

14. C. Cawthorne and C. Brown, J. Nucl. Mat., 66 (1977), p. 201.

15. H. R. Brager and F. A. Garner, "Radiation-Induced Evolution of the Austenite Matrix in Silicon-Modified AISI 316 Alloys," Ref. 7.

16. L. E. Thomas, Trans ANS, 28 (1978), p. 151.

17. L. E. Thomas, "Irradiation-Induced Phase Instabilities in Austenitic Stainless Steels," Proc. 37th Annual EMSA Meeting, August 13-17, 1979, San Antonio, TX, p. 422.

18. D. L. Porter, J. Nucl. Mat., 79 (1979), p. 406.

19. T. M. Williams, J. M. Titchmarsh and D. R. Arkell, J. Nucl. Mat., 82 (1979), p. 199.

20. H. R. Brager, F. A. Garner and G. L. Guthrie, J. Nucl. Mat., 66 (1977), p. 301.

21. D. S. Gelles, F. A. Garner and H. R. Brager, "Frank Loop Formation in Irradiated Metals in Response to Applied and Internal Stresses," Ref. 2.

22. F. A. Garner, W. G. Wolfer and H. R. Brager, "A Reassessment of the Role of Stress in Development of Radiation-Induced Microstructure," Ref. 5, p. 160.

23. F. A. Garner, E. R. Gilbert, D. S. Gelles and J. P. Foster, "The Effect of Temperature Changes on Swelling and Creep of AISI 316 Stainless Steel," Ref. 2.

24. B. Weiss and R. Stickler, Met. Trans, 3 (1972), p. 851.

25. J. E. Spruiell, J. A. Scott, C. S. Ary and R. L. Hardin, Met. Trans, 4 (1973), p. 1533.

26. P. J. Maziasz, "Helium-Trapping at Ti-Rich MC Particles in Ti-Modified Austenitic Stainless Steel," Ref. 7.

27. G. Martin, J. L. Bocquet, A. Barbu and Y. Adda, "Fundamental Aspects of the Evolution of, and Phase Changes in, Metals and Alloys Under Irradiation," Ref. 1, p. 899.

28. F. X. Spiegel, D. Bardos and P. Beck, Trans Met. Soc. AIME, 277 (1963), p. 575.

29. J. L. Baron, R. Cadalbert and J. Delaplace, J. Nucl. Mat., 51 (1974), p. 266.

30. J. T. Stanley and K. R. Garr, Met. Trans A, 6A (1975), p. 531

31. J. T. Stanley, J. Nucl. Mat., 85 and 86 (1979), p. 787.

32. A. D. Marwick, R. C. Pillar and P. M. Sivall, J. Nucl. Mat., 83 (1979), p. 35.

33. P. R. Okamoto and L. E. Rehn, J. Nucl. Mat., 83 (1979), p. 2.

34. R. A. Swalin, A. Martin and R. Olsen, Trans AIME (1957), p. 936.

35. J. I. Bramman, C. Brown, J. S. Watkin, C. Cawthorne, E. J. Fulton, P. J. Barton and E. A. Little, "Void Swelling and Microstructural Changes in Fuel Pin Cladding and Unstressed Specimens Irradiated in DFR," Ref. 2, p. 479.

36. F. R. Beckitt and B. R. Clark, Acta Met., 15 (1967), p. 113.

37. E. H. Lee, A. F. Rowcliffe and E. A. Kenik, J. Nucl. Mat., 83 (1979), p. 79.

38. J. F. Bates, "Irradiation-Induced Swelling Variations Resulting from Compositional Modifications of Type 316 Stainless Steel," ASTM STP 570 (1975), pp. 369-387.

39. J. F. Bates, R. W. Powell and E. R. Gilbert, "Reduction of Irradiation-Induced Creep and Swelling by Compositional Modifications," Ref. 2.

40. J. F. Bates and W. G. Johnston, "Effects of Alloy Composition on Void Swelling, Ref. 1, p. 625.

41. H. Venker and K. Ehrlich, J. Nucl. Mat., 60 (1976), p. 347.

42. S. J. Rothman, L. J. Nowicki and G. E. Murch, J. Phys. F: Metals Physics, 10 (1980), pp. 383-398.

43. J. Rothman, L. J. Nowicki and G. E. Murch, "Tracer Diffusion of Cr, Ni and Fe in Austenitic Fe-Cr-Ni Alloys," presented at Fall AIME Meeting, St. Louis, MO, October 15-19, 1978.

44. F. A. Garner and W. G. Wolfer, "The Effect of Solute Additions On Void Nucleation," accepted for publication in J. Nucl. Mat.

45. L. K. Mansur, "Effective Diffusion Coefficients of Point Defects in Impure Materials," ORNL-TM-7247, March 1980.

46. W. K. Appleby, E. E. Bloom, J. E. Flinn and F. A. Garner, "Swelling in Neutron-Irradiated 300 Series Stainless Steels," Ref. 1.

47. J. L. Boutard, G. Brun, J. Lehman, J. L. Seran and J. M. Dupouy, "Swelling of 316 Stainless Steel," Proc. Symposium On Irradiation Behavior of Metallic Materials for Fast Reactor Core Components," Ajaccio, Corsica, June 5-7, 1979.

48. G. L. Hofman, L. C. Walters and G. L. McVay, J. Nucl. Mat., 67 (1977), p. 289. Also J. Nucl. Mat., 65 (1977), p. 200.

49. G. L. McVay, R. E. Einziger, G. L. Hofman and L. C. Walters, J. Nucl. Mat., 78 (1978), p. 201.

50. J. M. Dupouy, J. Lehman and J. L. Boutard, "Swelling and Irradiation Creep of 316 Stainless Steel," Proc. Conference on Reactor Materials Science, Vol. 5, p. 280, Alushta, USSR, 1978.

51. R. E. Einziger, D. L. Porter and B. R. Seidel, Trans ANS (Fall 1979), p. 284.

52. P. J. Alberry and C. W. Haworth, Metal Science, 8 (1974) p. 407.

53. J. L. Straalsund and J. F. Bates, Met. Trans, 5 (1974), p. 493.

54. F. H. Froes, M. G. H. Wells and B. R. Banerjee, Met. Sci. J., 2 (1968), p. 232.

55. L. A. Lawrence and J. W. Weber, Trans. ANS (poster session), San Diego, CA, June 18-23, 1978, p. 225.

56. R. A. Weiner and A. Boltax, "Comparison of High Fluence Swelling Behavior of Austenitic Stainless Steels," Ref. 2.

57. Y. Adda, "Report of the CEA Program of Investigations of Radiation-Induced Cavities in Metals: Presentations of Some Results," Proc. Symposium on Radiation-Induced Voids in Metals, June 9-11, 1971, Albany, NY, p. 31.

58. K. Uematsu, T. Kodama, Y. Ishida, K. Suzuki and M. Koyama, "Swelling Behavior of Cold-Worked Type 316 Stainless Steel," Ref. 1, p. 571.

59. K. D. Challenger and T. Lauritzen, "Effect of the Degree of Cold Work on the Irradiation-Induced Swelling of Type 316 Stainless Steel," ASTM STP 570 (1975), p. 388.

60. B. J. Makenas, J. W. Jost and J. W. Hales, Trans ANS, Las Vegas, NV, June 6-8, 1980, p. 256.

61. Supplied in advance of publication by D. L. Porter of Argonne National Laboratory, Idaho Falls.

62. J. F. Bates and D. S. Gelles, J. Nucl. Mat., 71 (1978), p. 365.

63. F. A. Garner, E. R. Gilbert, D. S. Gelles and J. P. Foster, "The Effect of Temperature Changes on Swelling and Creep of AISI 316," Ref. 2.

64. J. P. Foster and A. Boltax, Nucl. Tech., 47 (1980), p. 181.

65. J. F. Bates and M. K. Korenko, "Empirical Development of Irradiation-Induced Swelling Design Equation, Nucl. Tech., 48 (1980), p. 303.

66. J. M. Dupouy, J. Erler and R. Huillery, "Postirradiation Properties of Annealed and Cold Worked 316 Stainless Steel After Irradiation to High Fast Neutron Fluences," Ref. 1, p. 83.

67. G. D. Johnson, F. A. Garner, H. R. Brager and R. L. Fish, "A Microstructural Interpretation of the Fluence and Temperature Dependence of the Mechanical Properties of Irradiated AISI 316," Ref. 2.

68. F. A. Garner, E. R. Gilbert and D. L. Porter, "Stress-Enhanced Swelling of Metals During Irradiation," Ref. 2.

VII. FUTURE WORK

This effort will continue in order to incorporate an appropriate balance between microstructural and microchemical mechanisms in fission-fusion correlation models.

VIII. ACKNOWLEDGMENTS

The author is indebted to many persons for data, insight and thoughtful discussions. The majority of the experimental work on AISI 316 reported in this and earlier papers was performed in partnership with H. R. Brager. Other major experimental contributors who helped unravel the microchemical scenario were D. L. Porter, W. J. S. Yang, D. S. Gelles, L. E. Thomas, P. J. Maziasz, E. H. Lee, and C. Brown. Additional discussions with J. F. Bates, W. G. Wolfer and L. K. Mansur are gratefully acknowledged.

I. PROGRAM

Title: Irradiation Effects Analysis (AKJ)
Principal Investigator: D. G. Doran
Affiliation: Hanford Engineering Development Laboratory

II. OBJECTIVE

The objective of this effort is to determine the mechanisms which control precipitate and microstructural evolution in irradiated steels, and also to determine their parametric sensitivity so that extrapolations can be made to the behavior expected in fusion reactor environments.

III. RELEVANT OAFS PROGRAM TASK/SUBTASK

Subtask II.C.l.l Phase Stability Mechanism Experiments
Subtask II.C.4 Modeling

IV. SUMMARY

The γ' phase observed in AISI 316 is only stable during irradiation. It dissolves during annealing at the temperature of its formation in a manner which suggests that the dissolution rate is sensitive to the precipitate radius. The instability of this precipitate in the absence of irradiation confirms the expectation that this precipitate will exhibit a sensitivity to displacement rate.

V. ACCOMPLISHMENTS AND STATUS

Stability of the Radiation-Induced γ' Phase in 316 Stainless Steel -

H. R. Brager and F. A. Garner (HEDL)

1. Introduction

It has recently been shown that neutron irradiation of AISI 316 stainless steel leads to an extensive microchemical evolution involving primarily the removal of the elements nickel and silicon from the alloy matrix and their concentration into a variety of precipitate phases.[1-4] While most of these phases have been observed to form (often with different compositions) in unirradiated material, the γ' precipitates formed in this steel in the range 270-540°C cannot be produced at comparable temperatures and times in the absence of irradiation.[4-5] This phase has been shown to be nominally Ni_3Si with a small percentage of iron atoms. The formation of γ' requires the simultaneous segregation of moderately dilute solvent atoms (~13 atom % nickel) as well as very dilute solute atoms (1 atom % silicon).

One of the major unanswered questions about this phase has been whether it is nucleated at an enhanced rate during irradiation or whether the γ' **phase** is stable only under irradiation. Perhaps the kinetics *of* γ' formation in stainless steels are so sluggish that ex-reactor formation requires tens or hundreds of years and therefore γ' would eventually appear in components maintained at 250-550°C. Wolfer [6] had earlier suggested that the question of γ' stability could be addressed by annealing a specimen containing γ' in a furnace at its previous irradiation temperature and observing whether the γ' precipitates continue to grow, remain stable or dissolve. Such an experiment has now been performed and has shown that the γ' phase formed in AISI 316 is unstable in the absence of irradiation.

A survey of available specimens of 316 stainless steel containing γ' precipitates showed that the optimum available material to use was that from the X-157 experiment. This material was available in bulk and had been analyzed in detail in a previous study.[4] The specimens employed were derived from 20% cold worked N-lot (heat V87210) tubing irradiated in the EBR-II at zero stress and 475°C to a fluence of 1.0×10^{23} n/cm^2 ($E > 0.1$ MeV). They contained only 1.5% by volume of γ' and therefore the nickel and silicon removal function performed by γ' formation was still in progress. Since earlier studies had shown that ~4% γ' could be formed in this steel, less than half of the original matrix silicon content was concentrated into the γ' phase when the specimen was extracted

from the reactor.

Whereas the specimen from the X-157 experiment was midway in its progressofy' formation, a second tube from the RS-1 experiment was selected in which the γ' formation was essentially completed. This specimen is designated C-71 and was irradiated at 500°C to 13.5 x 10^{22} n/cm^2 (E >0.1 MeV). The lot of steel from which this specimen was formed is designated as CN-13 and is one of the FFTF first core heats of steel, all of which form γ' at lower fluences than does the N-lot heat of steel.

2. Experimental Procedures

Portions of two tubes made from the N-lot heat (designated AO and AN) from the X-157 experiment were encapsulated in an evacuated quartz tube and aged in a furnace at 475 ±5°C for either 300 or 1000 hours, respectively. After a slow cooling, the specimens were extracted from the tube and examined using conventional specimen preparation and transmission electron microscopy techniques. Aging at these conditions was not expected to produce any substantial change in the usual precipitate microstructure, i.e., no intermetallics were expected to form and the various carbide phases observed in the steel were known to be stable under these conditions. The aging period of 1000 hours was recognized as possibly being too short to allow differentiation between a stable γ' condition and one of continued growth, because the specimen had already accumulated about 15,000 hours exposure in reactor at the same temperature as that of the aging treatment. For such an eventuality, additional material was set aside to allow longer aging of specimens if necessary.

The C-71 specimen received a similar treatment but was aged at 900°F (487°C) for both 500 and 1000 hours.

3. Results

Figure 1, reproduced from reference 4, shows the contrast exhibited by γ' precipitates in dark field and also depicts the superlattice spots typical

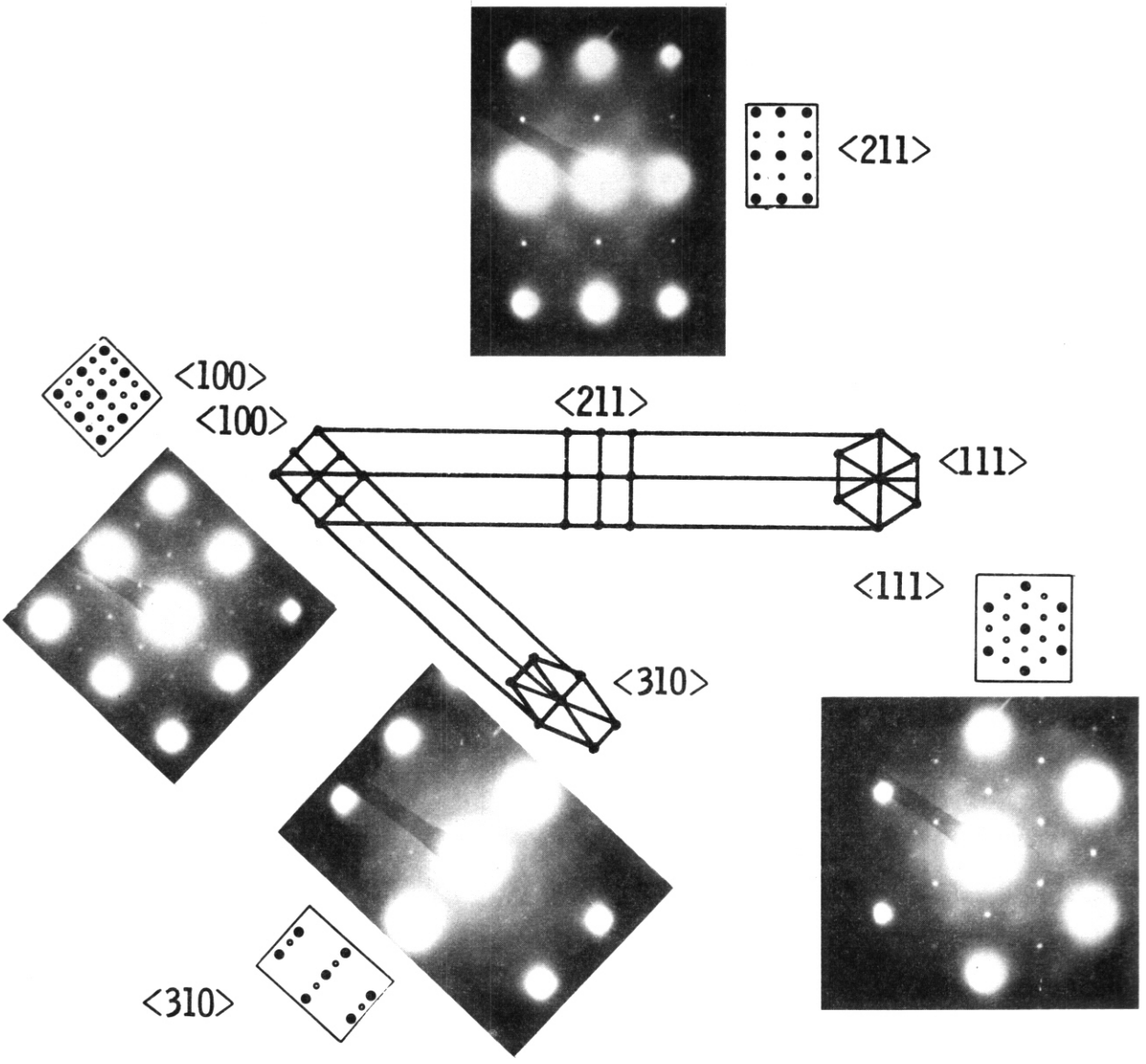

HEDL 7610-94

FIGURE 1. Four Low-Order Diffraction Patterns of the Same Grain Which Demonstrates That γ' is Produced in 20% CW 316 Stainless Steel (Heat 87210) Irradiated at 475°C to 1.0×10^{23} n/cm^2 (E >0.1 MeV). The solid dots and the open circles of the four diagrams provide schematic representation of diffraction from the austenite matrix and the γ' particles, respectively. (4)

of γ' in various low-order diffraction patterns. The precipitates are not readily visible in bright field except near the Bragg diffraction condition, $s = 0$. The specimen illustrated in Figure 1 and the X-157-AN specimen utilized in this study were all cut from the same tube.

In the aged X-157-AN specimen five separate grains were examined. Micrographs were taken for orientations in which either the <211>, <310>, or <100> zone axis was parallel to the electron beam. There was no visible γ' diffraction spots found for these grains in any of the diffraction patterns. By centering the diffraction aperature over the position where the γ' superlattice spot normally appears, one observed a few contrast features in the dark field micrographs that may or may not be due to γ' particles. As shown in Figure 2 the concentration of these contrast features is reduced by over two orders of magnitude from the 1.7×10^{16} cm^{-3} and ~ 7.4 nm diameter precipitates observed prior to the aging treatment. Therefore it is concluded that $\geq 99\%$ of the particles have dissolved during a time 1000 hours.

Examination of the X-157-A0 specimen aged for only 300 hours showed that the γ' phase was still present at densities and sizes that are indistinguishable fromthatof the unaged material.

When the other set of specimens (RS-1, C-71) were examined a similar pattern of behavior was observed in that 500 hours of aging at 482°C was insufficient to dissolve the γ' but 1000 hours of aging led to a complete removal of the γ' phase. Prior to aging the precipitates existed at 1.4×10^{16} cm^{-3} and 10 nm diameter. As shown in Figure 3 the γ' precipitates can still be observed after 500 hours of aging.

In both sets of specimens other precipitate phases existed at lower densities prior to aging, such as $M_{23}C_6$, G and η.[3] No determination was made of the fate of these phases upon aging.

4. Discussion

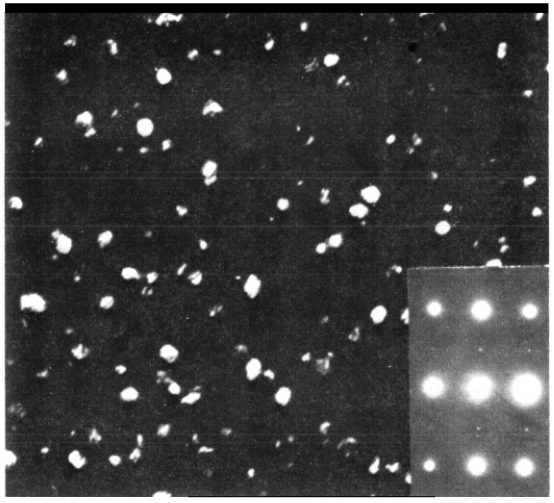

AFTER $1.0 \times 10^{23} n/cm^2$
AT 475°C

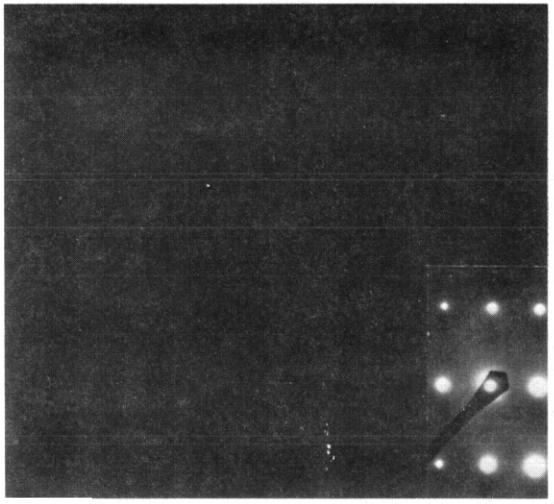

AFTER SPECIMEN ANNEALED
AT 475°C FOR 1000 HOURS

FIGURE 2 Micrographs Showing γ' Microstructure of Specimen AN Prior to Annealing and After Annealing for 1000 Hours at 475°C.

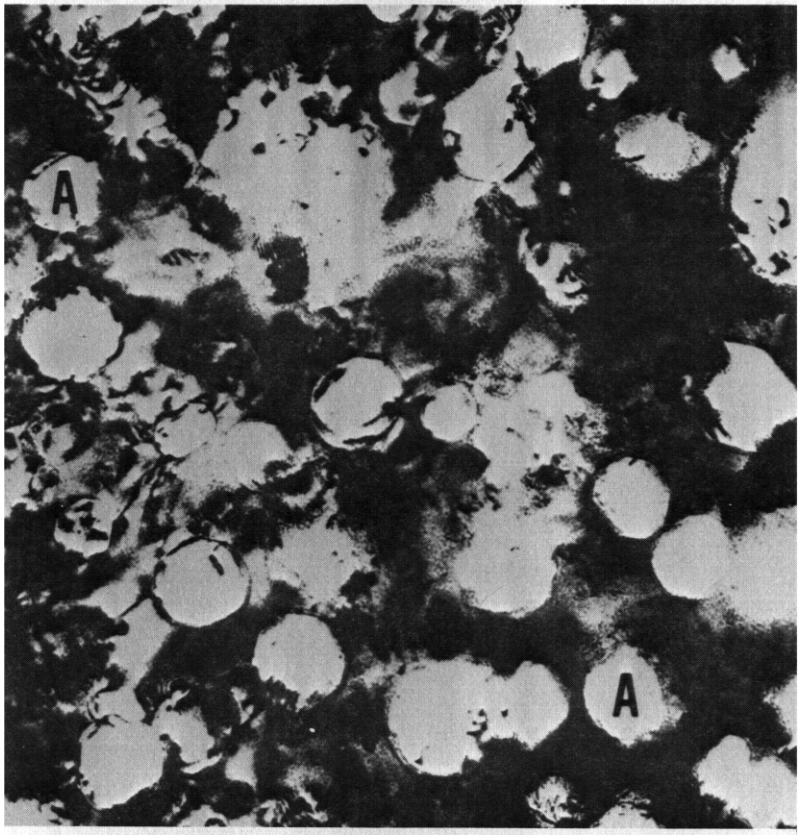

5662

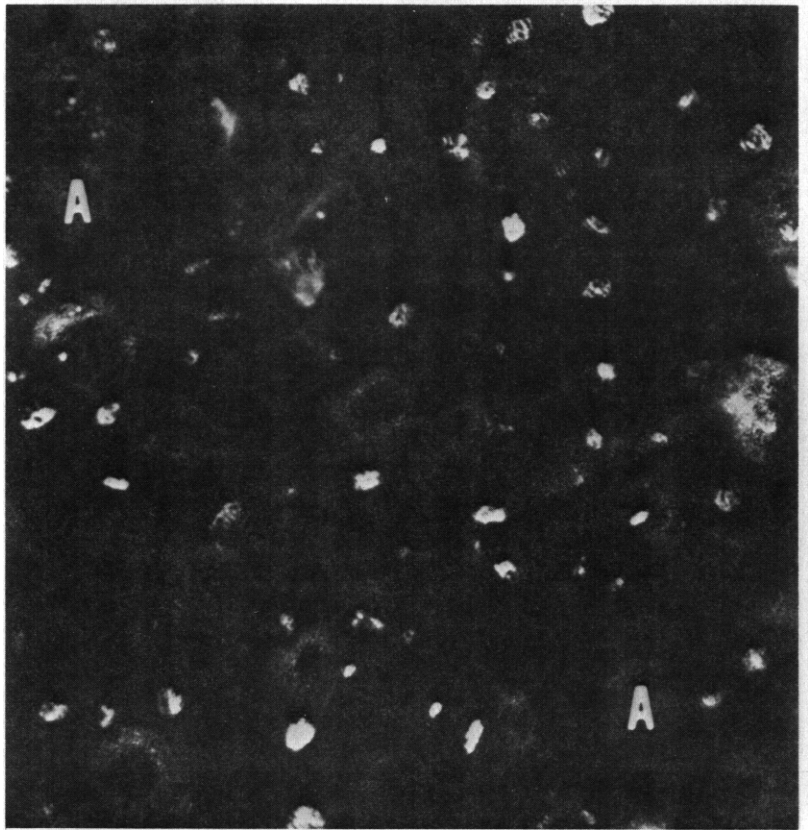

5663

HEDL 8008-300

FIGURE 3. Voids and γ' Precipitates Observed in Specimen C-71 After Annealing for 500 Hours at 483°C.

It appears that the γ' phase in 316 stainless steel is only stable under irradiation. Thus the equilibrium phase diagram for this steel (and probably others) is fundamentally altered by the presence of a displacive radiation field. Two other studies have earlier suggested that irradiation-induced phases which require the concentration of elements from dilute solution might not be stable in the absence of irradiation.[7-8] Both of these experiments involved the postirradiation annealing of charged particle bombarded specimens of nickel containing small amounts of silicon. The Ni_3Si precipitate layers formed by irradiation at the surface of such specimens dissolved during a very short annealing period. Such precipitates also require a relatively short time to form since only one element must be concentrated in contrast to the two required for γ' to form in AISI 316 stainless steel. The role of the surface as a point defect sink is crucial in the quick formation of such precipitates in the charged particle experiments, however, and may also be involved in the dissolution process. Since the AISI 316 stainless steel experiment involved annealing of bulk material with a relatively homogeneous distribution of γ' precipitates, the role of external surfaces on γ' stability in this steel can be discounted.

There is one observation made in this study which suggests that the surface of the γ' precipitate itself plays a large role in the precipitates rate of formation or dissolution. In each of the two annealing experiments no measurable dissolution was observed for times of 300-500 hours. Such an observation could be rationalized by surface tension/radius of curvature arguments similar to those invoked in void annealing experiments. In other words the dissolution rate increases with smaller radius. It is also interesting to note that the apparently abrupt dissolution behavior was observed in specimens which had completed γ' formation as well as those which had not.

If γ' is dissolved at times $\leq$1000 hours at the relatively low temperatures of 475 and 482°C then a shorter time is probably required for dissolution at higher temperatures. This leads to the interesting possibility that the upper temperature boundary observed at about 540°C for γ' formation in AISI 316 which contains about 1 atom % silicon (see Figure 4) may not be the actual phase boundary. Perhaps γ' forms at temperatures higher than $\sim$540°C but dissolves at

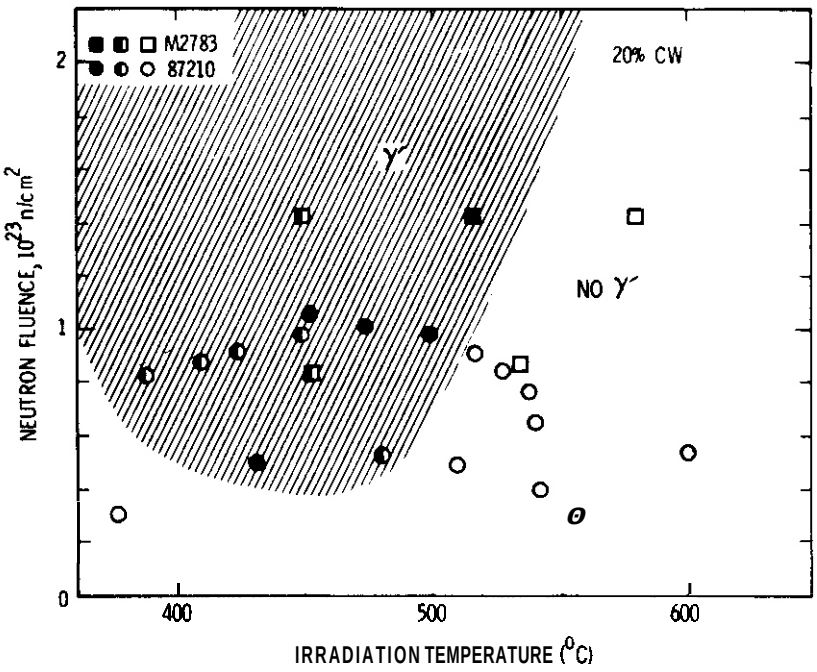

FIGURE 4. Temperature and Fluence Regime in Which γ' Phase Has Been Observed in N-lot and a Similar Steel.

relatively short times after reactor shutdown. It is therefore not necessarily a coincidence that the upper temperature limit of γ' observations in 316 stainless steel is essentially the temperature at which property changes which depend on self-diffusion normally accelerate ($\geq$550°C).

An alternate explanation of this high temperature boundary and the temperature dependence of the γ' regime invokes the different temperature dependencies involved in the segregation of nickel and silicon at sinks. Other studies [9-10] indicate that substantial radiation-induced segregation of nickel at such sinks occurs only at higher temperatures, most likely from the preferential out-migration of the faster diffusing elements chromium and iron. Silicon has not been found to segregate to a large extent at voids and dislocations at higher temperatures, but does segregate at such sinks at lower temperatures. The temperature regime between 450 and 550°C therefore may represent the temperature range wherein a substantial amount of both silicon and nickel can segregate simultaneously. The upper temperature limit of γ' formation is thus dictated by

the increasing mobility of silicon with temperature. Although silicon may segregate over a wide range of temperatures by binding with the interstitial current toward sinks, silicon will also out-migrate from such sinks by the inverse Kirkendall effect operating on the vacancy current to the same sinks.[10] At temperatures below 450°C both elements can segregate but at such a sluggish rate for nickel that γ' form at barely detectable levels.[4-5,9]

Since the formation of this phase requires radiation-induced transport or segregation of nickel and silicon, one would expect its formation and temperature regime to be influenced by the displacement rate, as observed by Martin and co-workers.[7] There is some circumstantial evidence that displacement rate influences the rate of formation of radiation-stable phases.[12] One would also expect that increasing the concentration of either nickel or particularly silicon would lead to an upward extension of the upper temperature limit of γ'. For silicon this prediction has been confirmed by recent experimental evidence.[13]

5. Conclusions

The γ' phase observed in AISI 316 is only stable during irradiation. It dissolves during annealing at the temperature of its formation in a manner which suggests that the dissolution rate is sensitive to the precipitate radius. The instability of this precipitate in the absence of irradiation is consistent with the observation that this precipitate exhibits a sensitivity to displacement rate.

VI. REFERENCES

1. H. R. Brager and F. A. Garner, "The Influence of Preirradiation Thermal Mechanical Treatment on Phase Stability and Swelling in 316 Stainless Steel," Trans. ANS, 28, p. 151 (1978).

2. H. R. Brager and F. A. Garner, "Dependence of Void Formation on Phase Stability in Neutron Irradiated Type 316 Stainless Steel," ASTM STP 683, Proc. ASTM 9th International Symposium on Effects of Radiation on Structural Materials, Richland, WA July 10, 1978, p. 207.

3. W. J. S. Yang, H. R. Brager and F. A. Garner, "Radiation-Induced Phase Development in AISI 316," Proc. Symposium on Irradiation Phase Stability, October 5-9, 1980, Pittsburgh, PA, AIME (in press).

4. H. R. Braaer and F. A. Garner. "Swellina as a Conseauence of Gamma Prime (γ') and $M_{23}(C,Si)_6$ Formation-in Neutron Irradiated 316 Stainless Steel, J. Nucl. Mat., 73, (1978) p. 9-19.

5. C. Cawthorne and C. Brown, J. Nucl. Mat., 66 (1977) p. 201.

6. W. G. Wolfer is Associate Professor, Department of Nuclear Engineering, University of Wisconsin, and is a consultant to the DAFS Program.

7. G. Martin, J. L. Bocquet, A. Barbu and Y. Adda. "Fundamental Aspects of and Phase Changes in Metals and Alloys Under Irradiation," Proc'. I——. ,national Conference on Radiation Effects in Breeder Reactor Structural Materials, June 19-23, 1977, Scottsdale, AL, p. 899.

8. L. E. Rehn, P. R. Okamoto, D. I. Potter and H. Wiedersich, "Irradiation-Induced Segregation in Ni-Si Alloys," ibid ref. 2.

9. H. R. Brager and F. A. Garner, "Analysis of Radiation-Induced Microchemical Evolution-in 300 Series Stainless Steel," Proc. Symposium on Advanced Technisues for the Characterization of Irradiated Materials, February 24-28, 1980, Las Vegas, NV, AIME (in press).

10. H. R. Brager and F. A. Garner, "Microchemical Evolution of Neutron-Irradiated 316 Stainless Steel," Effects on Radiation on Materials, ASTM STP 725, D. Kramer, H. R. Brager and J. S. Perrin (Eds), ASTM (1981).

11. P. R. Okamoto and L. E. Rehn, "Radiation-Induced Segregation in Binary and Ternary Alloys," to be published in J. Nucl. Mat. or part of Proceedinas Workshop on Solute Segregation and Phase Stability During Irradiation, Gatlinburg, TN, October 1978.

12. F. A. Garner, "The Microchemical Evolution of Irradiated Stainless Steels," included in reference 3.

13. H. R. Brager and F. A. Gamer, "Radiation-Induced Evolution of the Austenite Matrix in Silicon-Modified AISI 316 Alloys," included in reference 3.

VII. FUTURE WORK

No further work is planned.

I. PROGRAM

Title: Irradiation Effects Analysis (AKJ)
Principal Investigator: D. G. Doran
Affiliation: Hanford Engineering Development Laboratory

II. OBJECTIVE

The objectives of this effort are to identify the effects of applied and internal stresses on radiation-induced dimensional changes in metals and to predict the impact of these effects on fusion reactor design and performance.

III. RELEVANT DAFS PROGRAM TASK/SUBTASK

Task II.C.2.1 Effects of Material Parameters on Microstructure
Task II.C.2.5 Modeling

IV. SUMMARY

It is anticipated that stress-enhanced swelling may play a larger role in fusion devices than it does in breeder reactors. The need to extrapolate breeder-derived data from tensile experiments to the compressive and cyclic stress states expected in pulsed fusion reactors requires a reexamination of the phenomena involved. Recent data confirm the existence of both microstructurally-based and microchemically-based mechanisms. The latter is not anticipated to respond to compressive or cyclic stresses in the same manner as would the microstructurally-based mechanisms on which the current stress effects correlation is based.

V. ACCOMPLISHMENTS

Extrapolation of Stress-Affected Swelling Models Into Compressive and Cyclic Stress States - F. A. Garner (HEDL)

1. Introduction

In an earlier report [1] it was shown that many alloys exhibit an enhancement of irradiation-induced void swelling due to the application of biaxial tensile stresses during irradiation. For AISI 316 this enhancement was shown to arise from a shortening of the incubation period of void growth. No effect of stress was seen on the steady-state swelling rate. A correlation developed to describe this phenomenon is currently employed in the U.S. Breeder Reactor Program.[1]

Before this correlation can be employed in fusion reactor design studies, one must consider the impact of the differences in the two reactor environments and also make an assessment on how best to extrapolate the data into untested stress states. It is important to note that the total data base was developed from essentially isothermal irradiations of the walls of thin tubes subjected to a constant biaxial tensile stress. There are no previously published data on the effect of compressive or torsional stress states and no experiments which provide guidance on how to incorporate the effects of stress history. These considerations are potentially quite important for three reasons. First, the stresses anticipated in the first walls of Tokamak-type reactors will be time-dependent, cycling from tensile to compressive, and will not develop gradually like the fission gas loading typical of breeder reactor fuel pins. Second, there is some evidence which indicates that the current model (based only on microstructural concepts) incorrectly predicts that compressive stresses will delay swelling. These new data indicate that perhaps compressive or torsional stresses also accelerate swelling, particularly at higher temperatures. Third, the duration of the void incubation period of AISI 316 steel has been shown to be primarily determined by the microchemical evolution of the matrix, a process which is normally rather sluggish compared to the microstructural evolution.[2] The greatest sensitivities of the microchemical evolution appear to be associated with variations in flux, temperature and stress, all three of which will undergo pronounced simultaneous variations in the walls of pulsed reactors. The possible synergisms for such complex and sensitive

histories may lead to substantial changes in the rate of the microchemical evolution. Additional recent data presented in this report indicate that applied stresses accelerate the microchemical evolution at temperatures above 550°C.

In this report the status is reviewed of various ongoing data analysis, modeling and experimental activities concerning stress-affected swelling. These efforts are directed toward the development of models which can be confidently extrapolated into untested stress states, primarily those of compressive and/or cyclic nature.

2. Stress-Affected Swelling: Recently Acquired Data

Since the current stress-affected swelling model [1] was developed, some additional data have become available which will influence further model development. Much of the new data presented here has been supplied by its originators in advance of publication.

While much of the previous data were derived from relatively short irradiation creep capsules constructed from 20% cold worked AISI 316, significant additional insight was derived from irradiations of "long" tubes (~1 m) constructed of either 10%cold worked or 20% cold-worked and aged AISI 316.[1] These latter irradiations were conducted by D. L. Porter, G. McVay, and M. Takata of ANL-Idaho Falls. Figure 1 shows a previously published subset of their data with some additional new points added at 270 MPa. Not only do these new data conform to the trends observed in the earlier data but they reside in the near-incubation regime, confirming that the primary effect of the applied stress was to shorten the incubation period.

If the primary effect of stress is exerted on the incubation period of void growth one would expect that removal of the stress in the post-incubation period would lead to no visible effect on the swelling rate. While there are no AISI 316 data to support this contention, there are some relevant data on annealed AISI 304L. J. E. Flinn, M. Hall and L. C. Walters

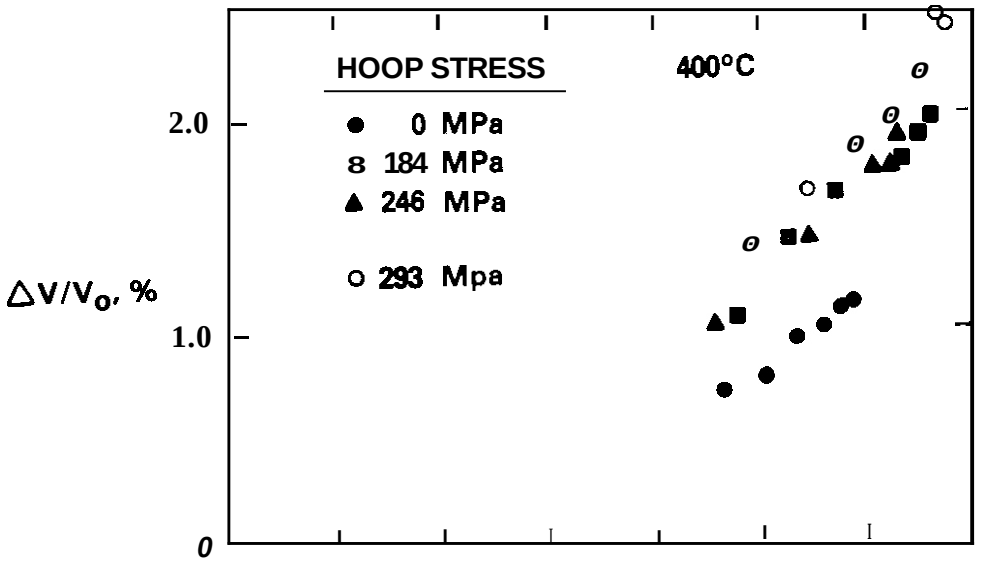

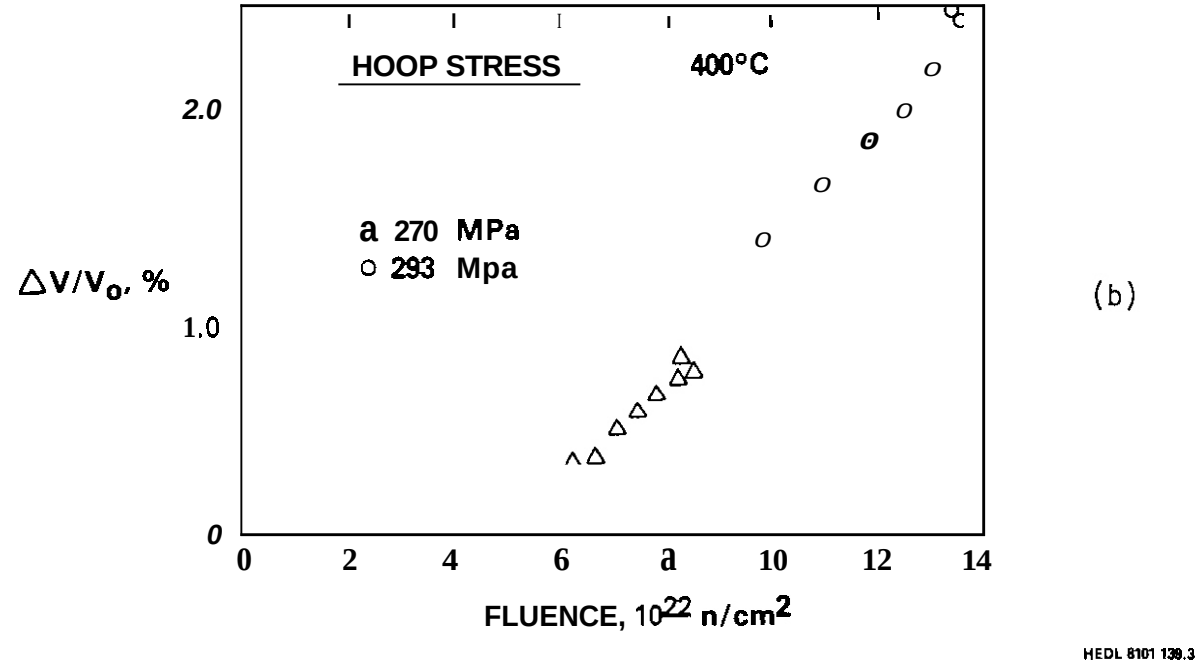

FIGURE 1. (a) Previously Published Data[1] on Stress-Affected Swelling of Long Tubes; (b) Additional New Swelling Data at 270 MPa and Lower Fluence Compared to Data at 293 MPa and Higher Fluence.

of ANL-Idaho Falls examined specimens of steel that comprised both the stressed cladding in fuel pin irradiations and the unstressed capsule material that surrounded the cladding.[3] Choosing specimens over a relatively narrow range of temperatures they established the swelling behavior of each steel. The different swelling rates shown in Figure 2 are thought by this author to reflect primarily the difference in composition (See Table 1) and not the differing stress state or temperature range. Each of these specimens was then reirradiated to higher fluences in the stress-free condition. Figure 3 shows that the swelling rate of the cladding material did not relax upon removal of the stress. This confirms the contention that the effect of applied stresses, once realized, is probably irreversible.

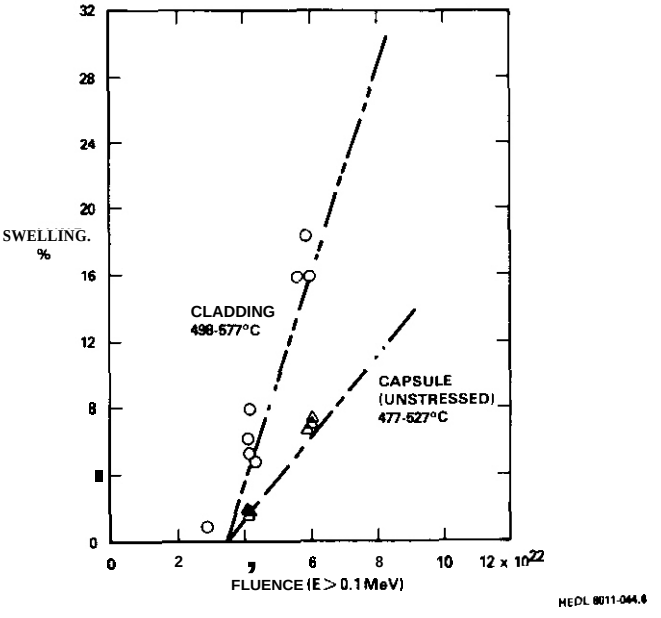

FIGURE 2. Post-Incubation Swelling of Two Different Annealed 304L Steels Observed by Flinn and Coworkers.[3] The claddingmaterial is stressed by fission gas pressure and possibly fuel-clad interaction during irradiation while the capsule material is essentially unstressed.

TABLE 1

COMPOSITION* OF 304L CLADDING AND CAPSULE TUBING (wt%)

	C	Mn	P	S	Si	Ni	Cr	Ti	cu	Mo	co
Cladding	0.03	1.66	0.16	0.014	0.59	10.6	18.3	<0.01	--	0.02	--
Capsule	0.03	1.37	0.01	0.007	0.62	9.26	18.3	0.02	0.074	0.02	0.05

*Note substantial differences in nickel and manganese content in the cladding and capsule materials. Both of these elements are important in the microchemical evolution of 300 series stainless steels.[2]

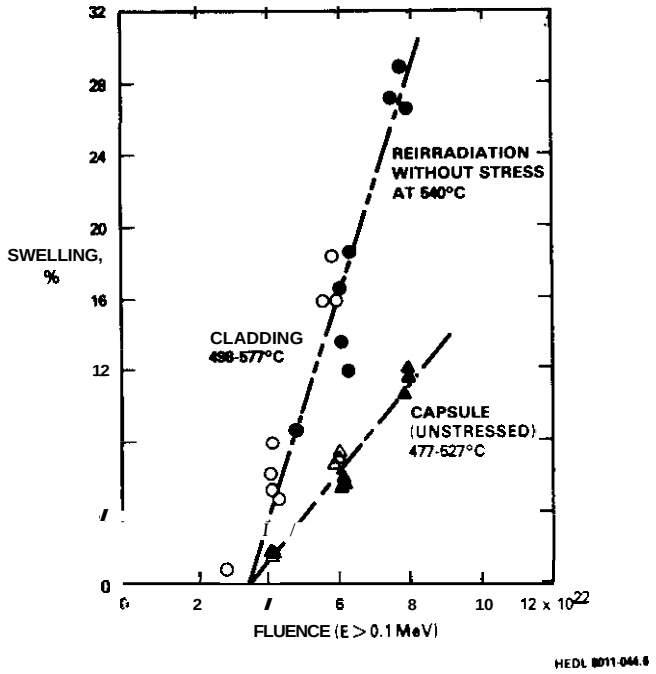

FIGURE 3. Subsequent Swelling Behavior of Specimens Shown in Figure 2.[3] Note that both steels were irradiated during this period without stress.

S. K. Khera, C. Schwaiger and H. Ullmaier[4] have recently published data which confirm many of the results of earlier microstructural studies of stress-affected swelling.[5-6] Using 6 MeV deuteron bombardment they demonstrated at 550°C in an Fe-Cr-Ni-Mo alloy (representative of AISI 316 without solute) that void nucleation was accelerated by application of a uniaxial tensile stress. It is important to note that no visible precipitation occurs in this steel, suggesting that the operating mechanism is probably not related to stress-affected microchemical evolution. The irradiation was performed at a calculated displacement rate typical of breeder reactors, although 0.75 MeV proton-generated displacements have been shown to be more effective in causing swelling per unit calculated displacement than were self-ion or neutron-induced displacements.[7] As shown in Figures 4 and 5 the void nucleation rate is accelerated but does not appear to lead to substantial enhancement in the eventual void density.

A similar conclusion concerning the stress insensitivity of the eventual void density was reached by Gelles and coworkers in the examination

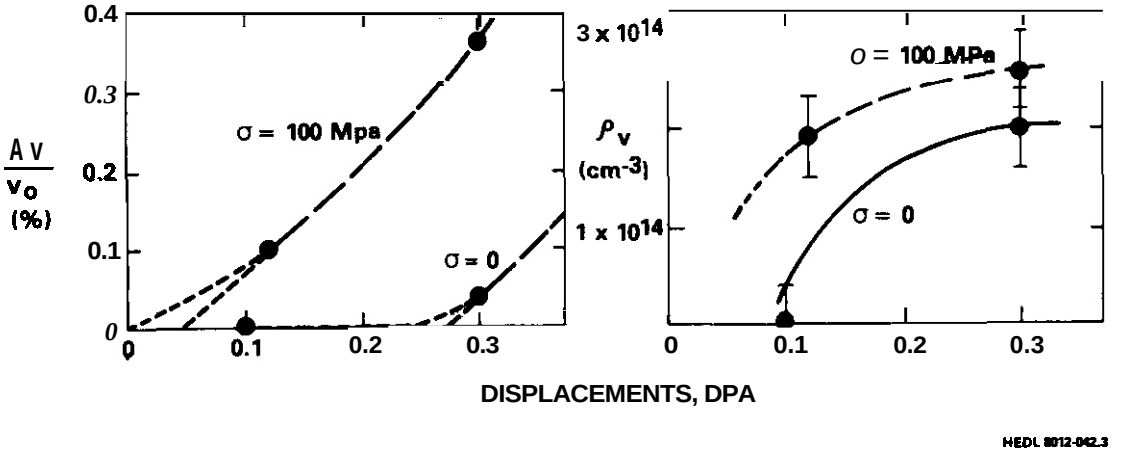

FIGURE 4. Stress-Affected Swelling Behavior Observed by Khera, Schwaiger and Ullmaier (4) in "Pure" AISI 316 During Deuteron Bombardment.

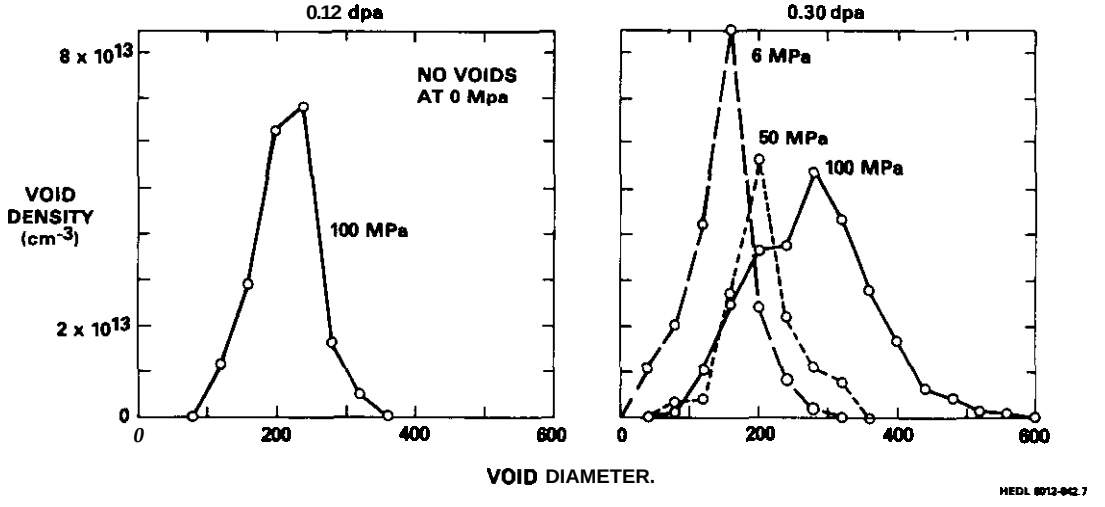

FIGURE 5. Details of Void Size Distribution for Materials Shown in Figure 4.(4)

of solution treated Inconel PE16.(8) In this alloy at 2 x 10^{22} n/cm^2 (E >0.1 MeV) and 550°C, application of a hoop stress of 167 MPa increased the void density from 1.2 x 10^{14} cm^{-3} (at zero stress) to only 1.7 x 10^{14} cm^{-3}. This small increase reflects the fact that the voids become visible around 1 x 10^{22} n/cm^2 and saturate in number shortly thereafter.

M. M. Hall of ANL-Idaho Falls has recently conducted an experiment on the effect of the nature of the stress state on stress-enhanced swelling

of annealed 304L. Although the findings are considered preliminary at this time, he has concluded that the swelling of this steel is accelerated for tensile, compressive or purely torsional stress states, with the enhancement increasing with increasing temperature. This is in contradiction to the predictions of the current stress-affected swelling model.[1] Torsional stresses are currently predicted to have no effect and compressive stresses are predicted to delay swelling.

There are two microstructurally-based mechanisms previously invoked to explain stress-enhanced swelling[6], neither of which would lead to predictions of Hall's findings. The first mechanism operates primarily at low temperatures (≤550°C) and arises from stress-induced changes in the interstitial capture efficiency of voids. The second operates most effectively at higher temperatures and involves stress-induced changes in vacancy emission at dislocations. Since these microstructural mechanisms cannot be invoked to explain Hall's data and no other microstructural mechanisms have been proposed, the possibility exists that the required mechanism is microchemical in nature. However, this does not preclude the possibility that the previously proposed microstructural mechanisms are also operating but not dominant under the particular conditions of Hall's experiment.

3. Experimental Evidence Supporting a Microchemical Mechanism

Brager and Garner[2,9] have recently shown that the radiation-stable phases found at low temperatures in AISI 316 do not appear to be sensitive to stress. There is some evidence however that the intermetallic phases at higher temperature are stress-sensitive in their rate of formation. Figure 6 shows that there is an apparent enhancement of swelling occurring at 3.7×10^{22} n/cm^2 (E >0.1 MeV) and 739°C, although all four density change data points represent a net densification of the steel. At elevated temperatures this steel is known to initially densify slightly due primarily to carbide precipitation and secondarily to recrystallization processes which occur both in and out of reactor.[10] Out of reactor this steel later increases volume as intermetallic phases form. As shown in Figure 7 the long-term "swelling" of the steel due to formation of intermetallics can be observed

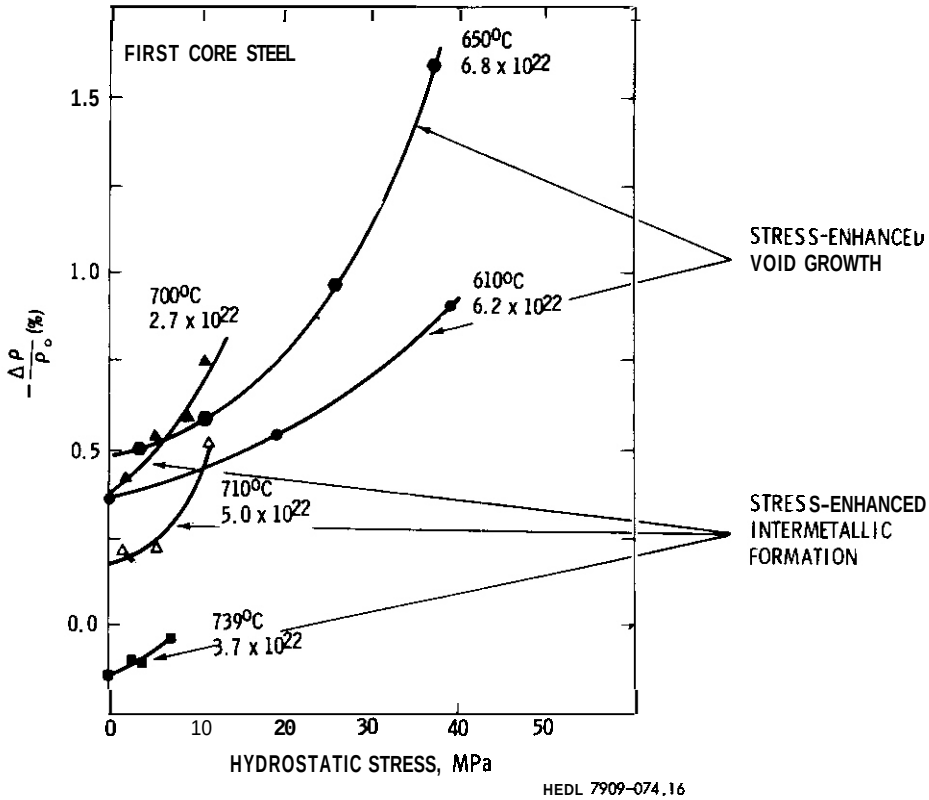

FIGURE 6. Swelling at High Temperature of AISI 316 in the 20% Cold-Worked Condition is Sensitive to the Stress Level and Consists of Contributions From Both Voidage and Phase Changes.

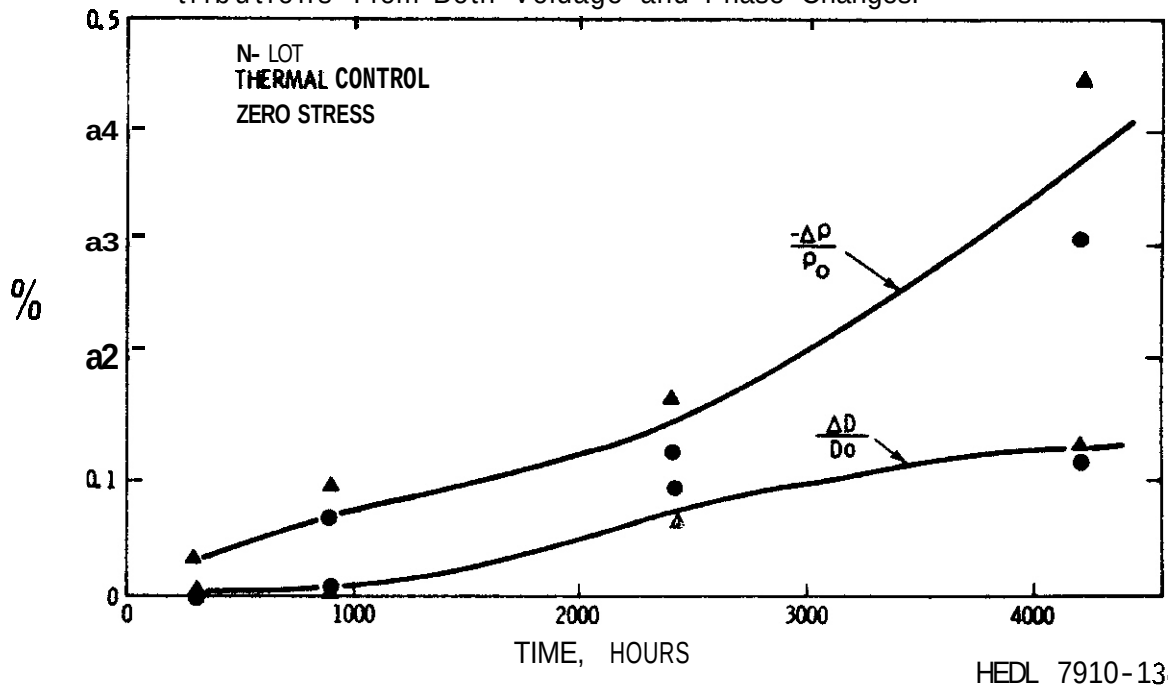

FIGURE 7. "Swelling" of 20% Cold-Worked AISI 316 Tubes Upon Thermal Aging at 700°C. The tube initially densified slightly and then became less dense ($-\frac{\Delta\rho}{\rho_o}$) and increased its diameter ($\Delta D/D$) upon long-term aging.

in unirradiated specimens and is much larger than that due to the carbide densification process.

In order to determine the cause of the stress-induced volume change at 739°C and 3.7 x 10^{22} n/cm^2, two specimens were chosen for examination, one irradiated at zero stress (designated AR7) and another irradiated at the highest hydrostatic stress level, 6.9 MPa, (designated AR2). The latter specimen had developed 11% diametral strain due to combined thermal and irradiation creep, and had been removed from the reactor in the anticipation that it might fail in the next reactor cycle. There was therefore the possibility that the observed stress-affected density change arose not from cavities or phase changes but from microcracks which develop prior to failure. While such microcracks would technically generate "swelling," such an effect would not continue with increasing stress but would'saturate at a relatively low level commensurate with failure of the tube.

Specimens were prepared for both light and electron microscopy as well as replication studies. Both the AR2 and AR7 tubes were irradiated side by side in the canister designed to reach 732°C in the AA-IIb experiment in capsule B-249. The ends of each capsule were removed and the density of each tube was measured by standard immersion techniques. The tubes were then sectioned. A transverse cut produced a 1/8 inch long ring. The ring was then quartered by longitudinal cutting and punched to yield TEM disks. Separate 1/4 inch rings were employed for replication studies. The latter type of ring was mounted and polished so as to yield a transverse section, and then cathodically etched in vacuum for 120 minutes. Cathodic etching is known to remove the polishing scratches, but will not enlarge any microcracks that are subsequently encountered. The resultant surfaces were then replicated with cellulose acetate and the replicas were examined by electron microscopy. Previous experience at this laboratory has shown that microcracks down to 20 nm can be resolved using this technique. The microscopy and replication studies were performed by B. Mastel of HEDL.

Microscopy Specimens. Small (~20 nm) cavities were found in both

specimens, but these were at very low and inhomogeneous number densities. There was no apparent pattern of association of these cavities with any particular microstructural component. The cavity volumes observed were too low to account for the apparent stress enhancement of density change. Therefore it was impossible to realistically analyze the micrographs for an effect of stress. It is the authors' opinion that the cavities in these specimens were helium bubbles and not voids. This heat of steel is known to resist swelling to much larger fluences at this temperature.[11]

Replication Specimens. No resolvable microcracks were detected in either specimen by replication techniques. It is judged unlikely that microcracks with dimensions smaller than the resolution limit could account for the observed stress enhancement of density change.

There was extensive formation of intermetallic phases in these specimens, however, and differences in sputtering rates of each phase during etching lead to a delineation of various microstructural features. Coventional light microscopy was therefore employed to evaluate the possible effect of stress on formation of intermetallic phases. Figures 8 and 9 are light micrographs of sections observed across the tube walls. Note that there appears to be an observable gradient in density of intermetallic phases across the unstressed tube wall, but that such a gradient does not exist in the stressed specimen. There also appears to be a larger mean precipitate size in the stressed specimen.

Analysis of Light Microscopy Data

The features shown in Figures 8 and 9 represent images not only of intermetallic precipitates but also twinned regions and small redeposition mounds. The latter arise from sputtered atoms which are scattered back toward the surface by subsequent collisions with gas atoms. In order to analyze the micrographs it was necessary to discriminate between the various microstructural features, and Figures 10(a) and 10(b) are the tracing of the features judged to be intermetallic precipitates. This step obviously

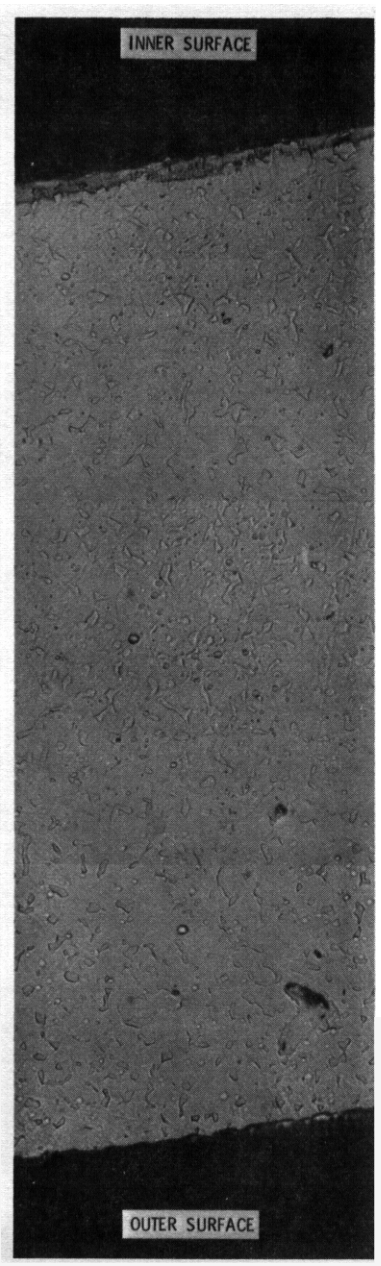

FIGURE 8. Light Micrograph Showing Cross Section of Tube Wall From Specimen AR7, Irradiated at Zero Stress.

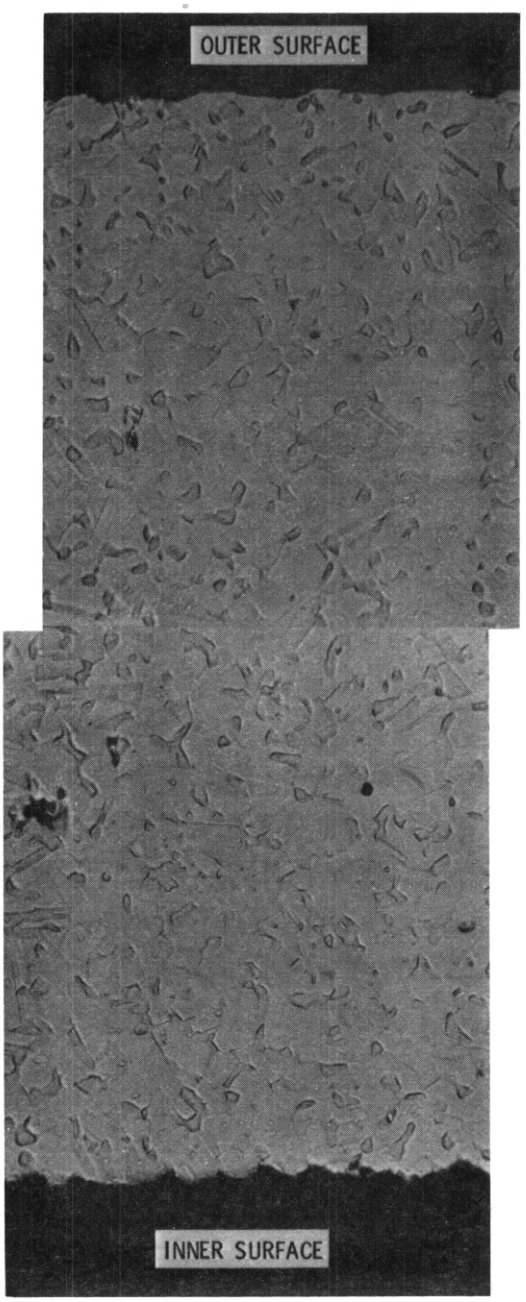

HEN 7902-055.5

FIGURE 9. Light Micrograph Showing Cross Section of Tube Wall From Specimen AR2, Irradiated at 6.9 MPa Hydrostatic Stress.

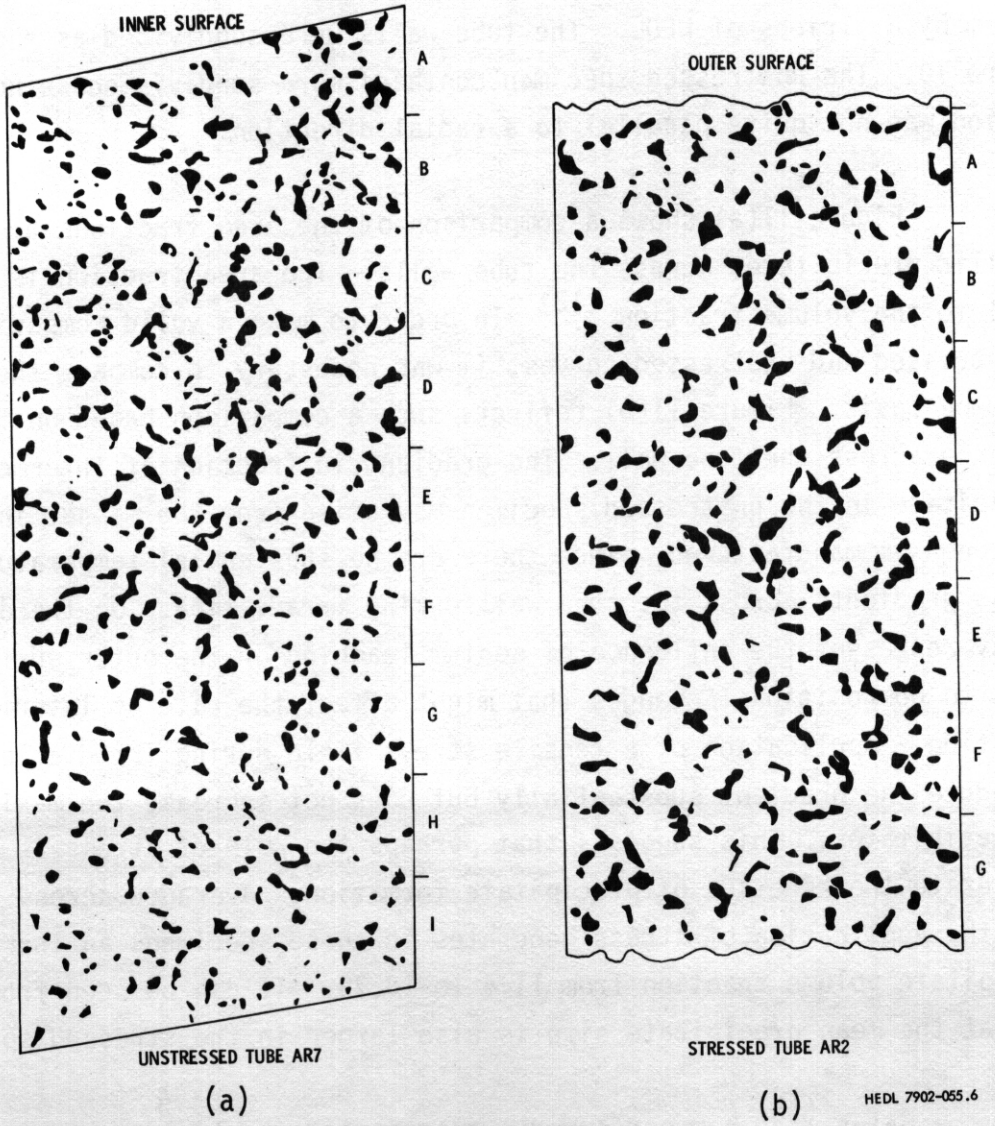

FIGURE 10. Tracing of Those Features of Figures 8 and 9 That Represent Intermetallic Precipitates.

involved substantial judgment and allows the possibility of some predjudice toward a preconceived answer. In order to avoid this possibility the discrimination and tracing were done by B. Mastel of HEDL who was not one of the persons involved in the data analysis.

The tracings were then analyzed using a Quantimet 720 image analysis system by H. Triebs of HEDL. The tube walls were subdivided as shown in Figure 10. The unstressed specimen contains more subdivisions since the section was not quite parallel to a radial direction.

Figure 11(a) shows a comparison of the area fractions of intermetallic precipitates across the tube walls. The area fraction is numerically equal to the volume fraction.[12] In order to make a valid comparison between the stressed and unstressed curves, it was necessary to compare the curves on a common basis. Figure 11(b) reflects such a comparison based on fractional distance across the tube wall. The gradient in fraction of intermetallic precipitate in the unstressed specimen may arise from the manner in which the tube was manufactured, since there are no substantial temperature or stress gradients across the tube wall during irradiation. On the other hand it may represent the influence of sodium leaching on the outer surface, which leads to compositional changes that might affect the rate of intermetallic formation. Application of a tensile stress field during irradiation appears to reduce the gradient substantially but does not increase the maximum level of precipitates. This suggests that perhaps the role of stress is only to accelerate the kinetics of precipitate formation. Averaged across the tube wall the application of stress generates in these specimens an increase in precipitate volume fraction from 11.4 to 13.7%. It can be seen from Figure 12 that the mean precipitate size is also larger in the stressed specimen.

Hales [13] has performed a quantitative analysis on the thermal development of such phases in two heats, one of which was the same heat examined in this study. As shown in Figure 13 she predicts that at comparable times (~8000 hours) the density of intermetallics should exceed 7%. In private communications Hales noted that maximum levels of 12-14%

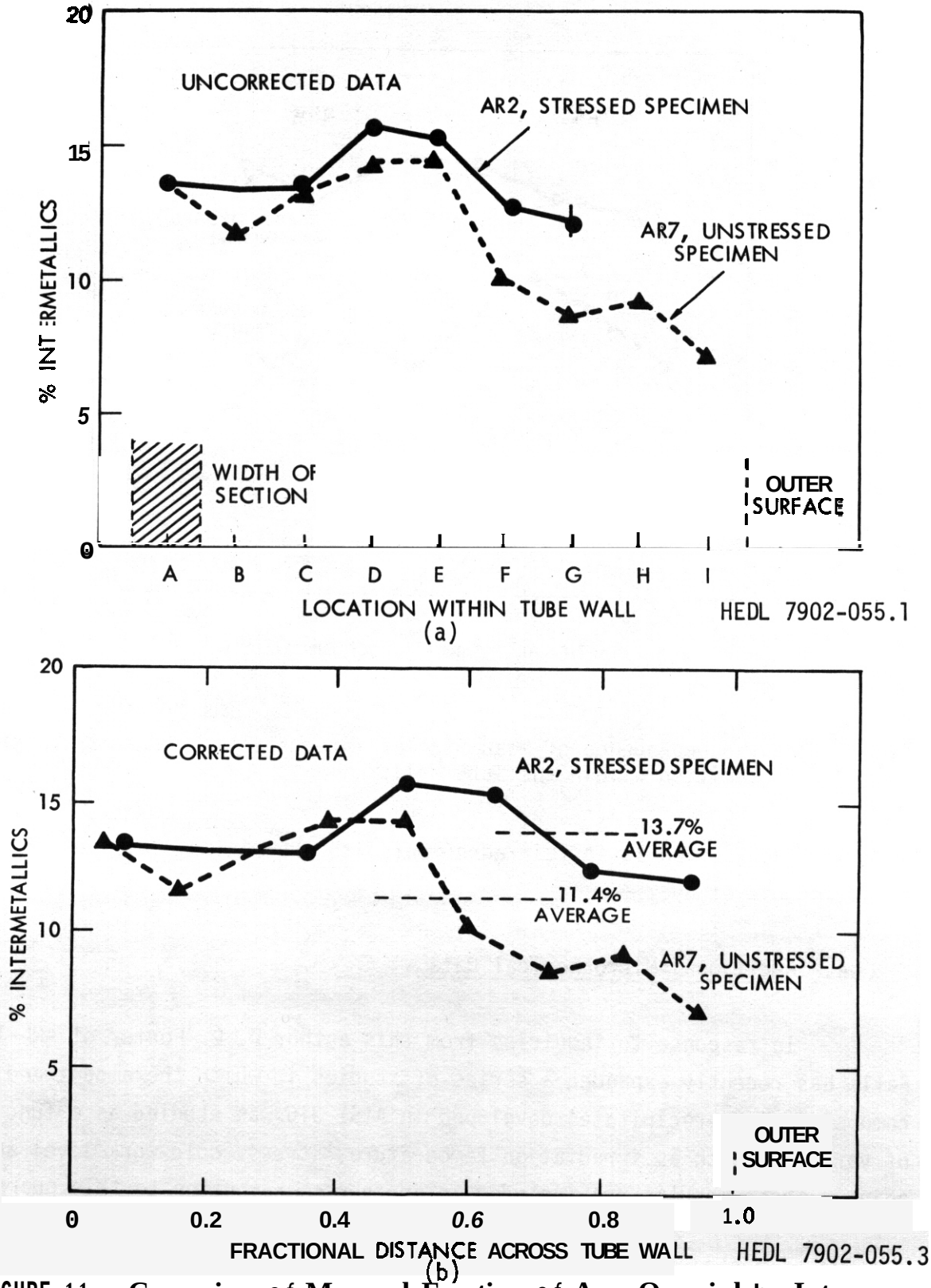

FIGURE 11. Comparison of Measured Fraction of Area Occupied by Intermetallic Phases in the Sections Shown in Figure 10.

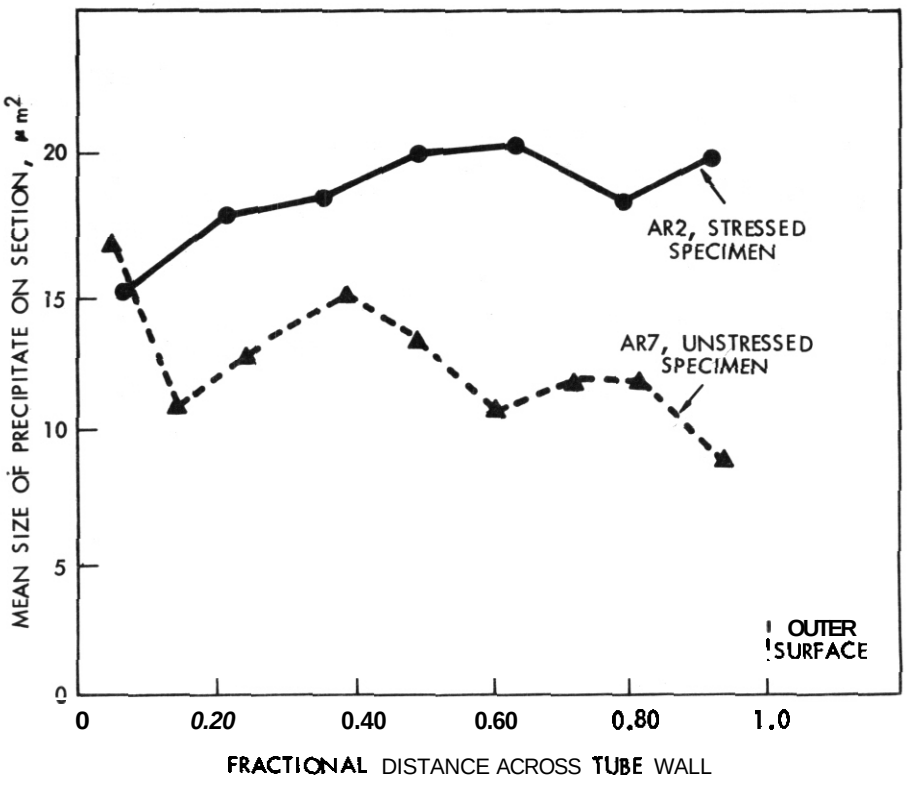

HEM 7902-055.2

FIGURE 12. The Dependence of Mean Size of Intermetallic Precipitates on Position Within the Tube Walls.

were observed, which is in fair agreement with the maximum level of 15% found in this study.

4. Additional Microchemical Data

In response to inquiries from this author D. L. Porter of ANL-Idaho Falls has recently expanded a series of studies in which the amount and composition of precipitates developed in AISI 316 was studied as a function of variables such as irradiation temperature, stress, cold-work level and aging. These results are included in another contribution to this quarterly report[14] and show that enhanced swelling is always correlated with enhanced removal of nickel into precipitates. At 400°C in either 10 or 20% cold-worked material, both the mole fraction of nickel of the precipitates and the volume

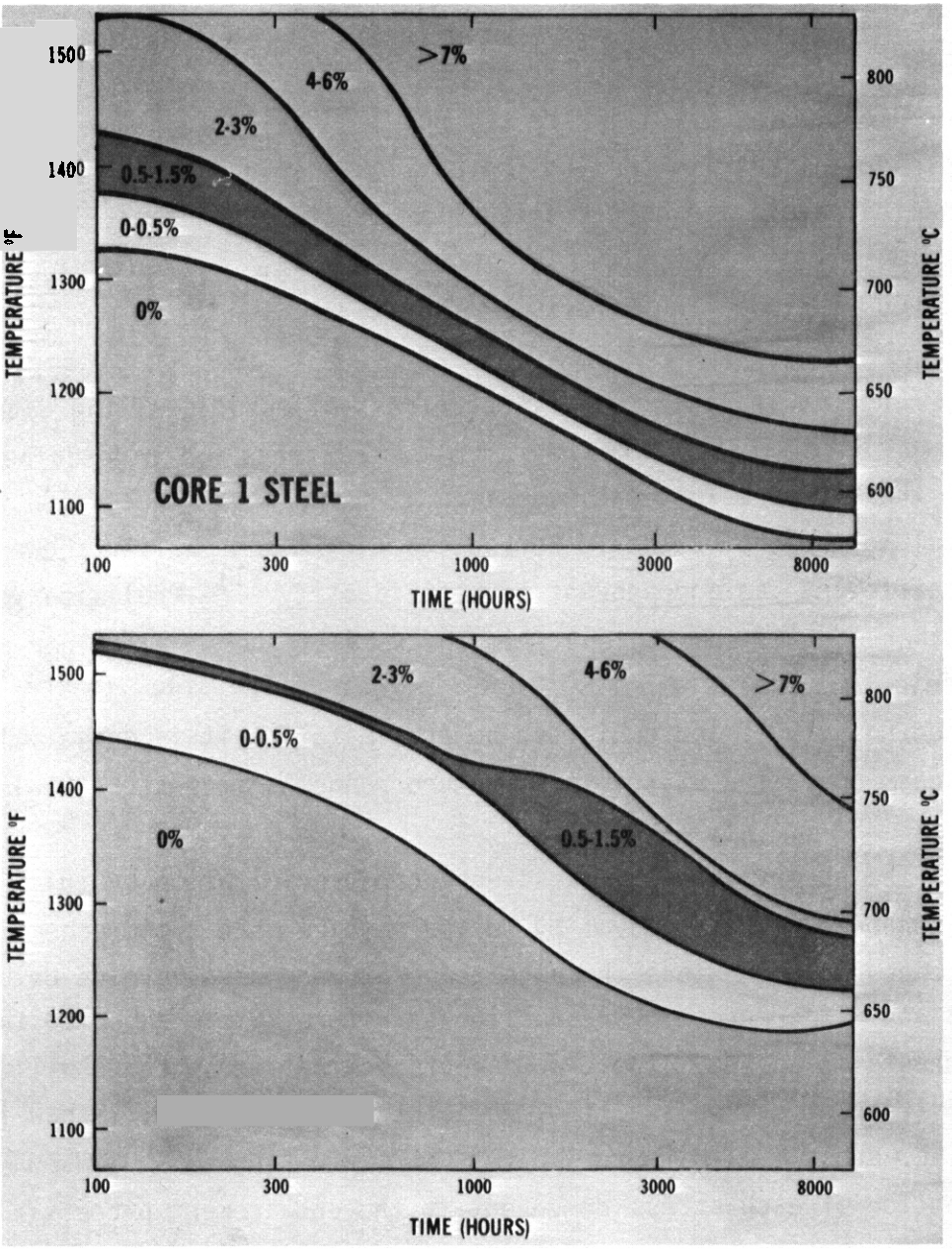

HEDL 7805-209.6

FIGURE 13. Second-Phase Precipitation Observed by Hales in Two Heats *of* 20% Cold-Worked AISI 316 During Thermal Aging.(13)

of the precipitates are independent of the stress level. The void swelling at this temperature is only weakly dependent on the stress level. At 550°C however both the swelling and the nickel removal process are enhanced by stress. This occurs due to stress-assisted increases in both precipitate volume and nickel content. The precipitates are not identified in these studies, but the experimental results confirm the earlier observation that stress-affected microchemical evolution occurs only at higher temperatures.

5. Current Modeling Efforts

Ongoing analysis of Porter's stress-affected swelling data in 10% cold worked AISI 316 indicates that the coefficients which describe the magnitude of the stress effect on incubation at temperatures below 500°C are identical to those of 20% cold-worked steel. It was earlier shown that this coefficient was independent of heat identity.[1] Preliminary estimates by this author of this coefficient from the work of Khera, Schwaiger and Ullmaier[4] also yield the same value of ~ 0.01 MPa^{-1}. Since the steel in the latter study contained no solutes and exhibited no precipitation it is anticipated that the process operating at this temperature range is microstructural in nature.

The observation of stress-enhanced precipitation by this author and stress-enhanced nickel removal by Porter require that a microchemical-based model be developed. Since the high temperature phases involve both volume changes and differences in crystalline structure, it is expected that both the hydrostatic and deviatoric components of the stress state will contribute to the stress effect on swelling. A joint modeling effort is now in progress with K. C. Russell of MIT that is directed toward predicting the relative contribution of each stress component to the enhancement process.

6. Conclusions

It is anticipated that stress-enhanced swelling may play a larger role in fusion devices that it does in breeder reactors. The need to extrapolate breeder-derived data from tensile experiments to compressive and

cyclic stress states anticipated in pulsed reactors requires a re-examination of the phenomena involved. Recent data confirm the existence of both microstructural-based and microchemically-based mechanisms. The latter is not anticipated to respond to compressive or cyclic stresses in the same manner as would microstructurally-based mechanisms.

VI. REFERENCES

1. F. A. Garner, E. R. Gilbert and D. L. Porter, "Stress-Enhanced Swelling of Metals During Irradiation," Proc. ASTM 10th International Symposium on Effects of Radiation on Materials, Savannah, GA, June 3-5, 1980, (in press).

2. F. A. Garner, "The Microchemical Evolution of Irradiated Stainless Steels," HEOL-SA-2159, Proceedings of AIME Symposium on Irradiation Phase Stability, October 5-9, 1980, Pittsburgh, PA.

3. J. E. Flinn and T. A. Kenfield, "Neutron Swelling Observations on Austenitic Stainless Steels Irradiated in EBR-II," Proceedings of Workshop on Correlation of Neutron and Charged Particle Damage, Oak Ridge, TN, June 8-10, 1976, p. 253, also in paper submitted to J. Nucl. Mat. by J. E. Flinn, M. Hall and L. C. Walters.

4. S. K. Khera, C. Schwaiger and H. Ullmaier, J. Nucl. Mat., 92, 299-305, 1980.

5. H. R. Brager, F. A. Garner and G. L. Guthrie, J. Nucl. Mat., 66, 301-321, 1977.

6. F. A. Garner, W. G. Wolfer and H. R. Brager, "A Reassessment of the Role of Stress in Development of Radiation-Induced Microstructure," ASTM STP 683, 160-183.

7. F. A. Garner et al., "Summary Report on the Alloy Development Intercorrelation Program Experiment, see Ref. 3, p. 147.

8. D. S. Gelles, F. A. Garner and H. R. Brager, "Frank Loop Formation in Irradiated Metals in Response to Applied and Internal Stresses," Proceedings ASTM 10th International Symposium on Effects of Radiation on Materials, Savannah, GA, June 3-5, 1980. (in press).

9. H. R. Brager and F. A. Garner, "Microchemical Evolution of Neutron Irradiated Stainless Steel," see Ref. 8.

10. F. A. Garner, W. V. Cummings, J. F. Bates and E. R. Gilbert, "Densification Induced Strains in 20% Cold Worked 316 Stainless Steel During Neutron Irradiation," HEDL-TME 78-9, June 1978.

11. J. F. Bates and M. K. Korenko, "Empirical Development of Irradiation-Induced Swelling Design Equation, J. Nucl. Tech., 48, 1980, p. 303.

12. R. T. DeHoff and F. N. Rhines, Quantitative Microscopy, 1968, p. 46, McGraw-Hill, New York.

13. J. Hales, "Second-Phase Precipitation in Irradiated Type 316 Stainless Steel Cladding," p. 153, ANS Transactions, 1978 Annual Meeting, San Diego, CA, June 18-22, 1970, Volume 28.

14. D. L. Porter and F. A. Garner, "The Influence of Microchemical Evolution on the Swelling of AISI 316 and its Dependence on Stress, Temperature and Heat Treatment, this report.

Expected Accomplishments in the Next Reporting Period

Modeling efforts will continue. Specimens irradiated at 700 and 710°C (see Figure 6) will be examined by microscopy to determine the relative contributions of voidage and phase changes to stress enhanced swelling.

I. PROGRAM

Title: Simulating the CTR Environment in the HVEM

Principal Investigators: W. A. Jesser and R. A. Johnson

Affiliation: University of Virginia

II. OBJECTIVE

The objective of this work is to model the role of helium in affecting microsctructural evolution.

111. RELEVANT OAFS PROGRAM TASK

Task II.C.2.4 Modeling

IV. SUMMARY

A kinetic model has been developed to study the growth of bubbles in thin specimens irradiated by helium ions. The materials parameters selected for the model are intended to pertain to type 316 stainless steel. For the case of 80 keV helium bombardment of planar specimens 0.25 μm thick at 250°, 400°, 550" and 700" C it was found that the ratio of helium ions to vacancies in clusters decreased with increasing temperature, being, for example, after a fluence of 7 dpa, 1.6 at 400° C and 0.63 at 550" C.

The model showed that the lack of swelling at low temperatures (e.g., 250° C) is not caused by thermal recombination of interstitials with vacancies but rather is a result of the decreased defect production rate associated with a high vacancy concentration. The presence of helium increased vacancy clustering at all temperatures investigated and eliminated the denuded zone which occurred at 700° C in the absence of helium.

V. ACCOMPLISHMENTS AND STATUS

A Kinetic Model for Helium Bombardment of Thin Foils, R. A. Johnson, Materials Science Department, University of Virginia, Charlottesville, Virginia 22901.

A kinetic model has been developed to study bubble growth in thin foils under He ion bombardment. While the primary purpose of the calculations is to obtain insight into the overall processes involved in such a situation, the specific case chosen is for bombardment by 80 keV He ions with a dose rate of 10^{14} ions/cm^2/sec, foil thickness of 0.1 and 0.25 μ, and the materials parameters are intended to pertain to type 316 stainless steel.

The kinetic problem becomes unmanageable if both bubble size and spatial distributions are treated. The emphasis in the present work is on the spatial distribution, and rather severe approximations had to be made pertaining to the effects of the size distribution. This was accomplished by varying the vacancy and He binding energies with the concentration of clustered vacancies and the ratio of clustered He to clustered vacancy concentrations.

With the bombardment conditions used, most He ions pass through the foil and there are more than 100 separated vacancy-interstitial pairs created per deposited He ion. Both the lattice defect creation rate and He deposition rate are peaked towards the back surface of the foil, with this effect being much greater with the He ions.

To study the effects of the deposited He, runs were made with just the lattice-defect production profile (the void case) and then with the deposited He present (the bubble case).

The calculations are not complete, but the first significant surprise involved the low temperature runs. It was found that the lack of swelling at low T (e.g., 250° C) is not caused by the thermal recombination of interstitials with the very high concentration of vacancies, but by a decrease in the defect production rate due to the high vacancy concentration.

Runs were made at T = 250°, 400°, 550°, and 700° C for the 0.25 μ foil thickness. Other parameters were, for example, a dislocation density of 10^9 cm/cm^3 and an interstitial bias factor for dislocations of 1.1. The irradiations were held for 53 minutes, which amounts to 7 dpa.

For the void case, nucleation occurred throughout the foils at all temperatures except in the front 250 Å at 700° C. The profile of clustered vacancies was peaked near the surfaces of the denuded zone. This tendency, which eventually disappears under very long irradiations, occurs because the foil surface acts as an excellent interstitial sink, so the interstitial concentration is low and consequently there is less recombination near the surfaces.

With the He present, the clustering was increased in all cases, by a greater ratio at the highest and lowest temperatures than for intermediate temperatures, and the denuded zone at 700' C disappeared. The ratio of He ions to vacancies in clusters decreased with increasing temperature, being, for example, 1.6 at 400' C and 0.63 at 550° C.

I. PROGRAM

Title: Effects of Near Surface Damage and Helium on the Performance of the First Wall

Principal Investigator: O.K. Harling

Affiliation: Nuclear Reactor Laboratory, Massachusetts Institute of Technology

II. OBJECTIVE

The objective of this study is to understand and quantify the effects of near surface damage and implanted gas on the performance of the fusion reactor first wall.

III. RELEVANT DAFS PROGRAM TASK/SUBTASK

TASK II.C.5 Effects of Cycling on Microstructure
II.C.8 Effects of Helium and Displacement on Fracture
II.C.12 Effects of Cycling on Flow and Fracture
II.C.13 Effects of Helium and Displacement on Crack Initiation and Propagation
II.C.15 Effects of Near Surface Damage on Fatigue

IV. SUMMARY

Neutron irradiation of a 316SS pressurized tube specimen with simultaneous ion bombardment and stress and temperature cycling was completed. This sample and a similar but non-ion-bombarded sample from an earlier experiment were sectioned and analyzed by optical microscopy and SEM. The outer surface of the ion-bombarded sample is more heavily cracked than that of the neutron bombarded specimen and there is preliminary evidence of surface damage from helium recoils on the specimen inner surfaces. Damage to vapor deposited boron layers on titanium substrates, which were irradiated with the stainless steel

specimens to produce ion bombardment, has also been observed.

V. ACCOMPLISHMENTS AND STATUS -- G. Kohse, S.G. DiPietro, O. Harling (M.I.T.), H. Andresen (M.I.T./Hahn-Meitner-Institut)

1. SS316 Pressure Capsule Irradiations

The facilities which have been set up at the MITR-II for surface and bulk irradiation of pressurized tube specimens with simultaneous temperature and stress cycling, and for intermittent characterization of sample dimensions and surfaces, are described in earlier reports.[1,2,3] In July, 1980, irradiation of two 316SS pressure capsules (see Fig. 1) was initiated in this apparatus. He and Li ion bombardment of the polished surfaces was produced by the reaction $^{10}B(n,\alpha)^{7}Li$ in a ^{10}B layer surrounding the samples. The irradiations were continued through November, 1980, with intermittent removal of the samples from the core for measurements, surface observations, and changes of ^{10}B layers.

The samples were temperature cycled between 350 and 600°C with an average period of 3.8 minutes. This produced a stress cycle from 210 to 295 MPa (30,500 to 42,800 psi). A total of approximately 16,000 cycles was accumulated, with an estimated dose of 4×10^{20} n/cm^2 (~0.1 MeV) and 2×10^{19} α/cm^2.

2. SS316 Pressure Capsule Characterizations

In order to characterize the radioactive pressure capsules in optical and scanning electron microscopy facilities, and in order to make cross-sections available for examination, the capsules were sectioned. One of the samples from the experiment described above, and a sample from a previous experiment which was treated similarly except that it was not ion bombarded,[4] were cut into 2 and 3 mm wide rings using a low speed diamond wafering saw set up for remote operation in a hot cell. To avoid deformation of the samples during cutting, the

inside was cast with epoxy following an initial cut close to the heavy end cap. Neither of the two samples had failed during irradiation, as was verified by initial opening of the sample filling tube under ethanol, with the observed escape of significant quantities of the pressurization gas.

The sample ring outer surfaces have been extensively examined by SEM, and interpretation of the results as well as correlation with optical microscope observations made periodically during the irradiations is continuing. Preliminary results do indicate the presence of a larger number of short cracks, of the type shown in Fig. 2, on the ion bombarded sample. The number density of these cracks correlates well with the increasing strain towards the thin-walled midsection of the sample. The details of the evolution of the surface morphology are somewhat obscured by oxidation effects, and further work is being planned.

More information, particularly concerning penetration and distribution of microcracks, is expected to be obtained from the samples by observation of the cut edges of the sectioned specimen rings, following polishing and, in some cases, etching. The necessary facilities for polishing radioactive specimens have been set up, and suitable techniques are being developed.

It is expected that the inner surfaces of the pressurized capsules will also provide useful data on the effects of multi-energy, multi-angle alpha bombardment, since the helium fill gas provides a source of energetic helium ions through fast neutron recoils. SEM observation of the inner surfaces has been initiated, and results to date indicate significant surface roughening, spalling and blistering.

3. Evaluation of Boron Coating Performance

As indicated above, ion bombardment of the outer surfaces of the 316SS pressure capsules is produced by surrounding them with a ^{10}B layer. This is accomplished by vapor deposition of boron onto semi-cyclindrical titanium foils, which are subsequently welded into the titanium can which contains the pressure capsules during irradiation.

Temperature cycling of the foils occurs in the same way as cycling of the pressure capsules (see Ref. 1). To date, three types of boron coated titanium foils have been irradiated; Table 1 gives irradiation data for the different layers. In each case, the layer thicknesses are in the range of 2 to 4 microns.

Due to the interest in boron as a possible low-Z coating in fusion devices, and in order to plan future irradiations using the $^{10}B(n,\alpha)^{7}Li$ reaction for surface bombardment, the titanium cans have also been sectioned using the low-speed diamond wafering saw, and have been examined by optical microscopy and SEM. In general, the layers deposited at 500°C (by Dr. Feldman, Applied Physics Lab, John Hopkins University) appeared to the naked eye to have held up reasonably well. The substrate was not exposed and no obvious flaking or peeling had occurred. This was not the case, however, with the layers deposited at lower temperature, where damage was readily visible. Microscopy revealed some damage in all cases. Fig. 3 shows a typical unirradiated boron surface, while Figs. 4 and 5 indicate some features typical of the post-irradiation appearance of the 19.8% ^{10}B and the 92% ^{10}B layers respectively (deposited at 500°C). Small pits, generally not penetrating down to the titanium substrate, were observed on the 19.8% ^{10}B coated foil. This removal of material seems to be the major result of the irradiation. The surface morphology of the 92% ^{10}B layer has, on the other hand, undergone drastic alterations. There is extensive roughening of the type shown in Fig. 5, although some boron seems to remain over the major part of the titanium substrate. Further experiments are under way or planned to determine more fully the nature of the irradiated layers, and additional results are expected from material in current and future irradiations.

VI. REFERENCES

1. H. Andresen, O.K. Harling, "Effects of Near Surface Damage and Helium on the Performance of the First Wall," DAFS Quarterly Progress Report, Oct.-Dec. 1978 (DOE/ET-0065/4).

2. H. Andresen et al, "Effects of Near Surface Damage and Helium on the Performance of the First Wall," DAFS Quarterly Progress Report, Apr.-June 1979 (DOE/ET-0065/6)

3. H. Andresen, O.K. Harling, "Fusion Reactor First-Wall Performance Under Ion Bombardment and Cyclic Stresses," invited paper, ANS Annual Meeting, Las Vegas, Nevada, June 1980.

4. H. Andresen et al, "Effects of Near Surface Damage and Helium on the Performance of the First Wall," DAFS Quarterly Program Report, Jan-Mar 1980 (DOE/ER-0046/1).

VII. FUTURE WORK

Further microscopic analysis of both the SS316 pressure capsules and the boron/titanium foils is planned. A new set of samples for irradiation is being prepared and should be in the reactor in the near future. The remaining sample from the experiment described above is continuing to be irradiated. A post-irradiation mechanical property test is planned for the SS316 pressure capsule rings. The current concept involves a fatigue test on quartered ring specimens. Designs for a prototype testing machine are being finalized and construction and testing should be well under way in the next quarter.

TABLE 1

BORON FILM IRRADIATION DATA

Layer Composition	Neutron Dose [n/m^2]		Temperature Cycling [°C]	Cycles	
	thermal	fast		length [sec]	No.
19.8% B-10 deposited at 500°C	2 x 10^{23}	6.7 x 10^{23}	140–380	~ 240	2800
92% B-10 deposited at 100°C	3 x 10^{23}	1.0 x 10^{24}	145–415	~ 220	1900
92% B-10 deposited at 500°C	4.1 x 10^{23}	1.4 x 10^{24}	165–490	~ 200	1320

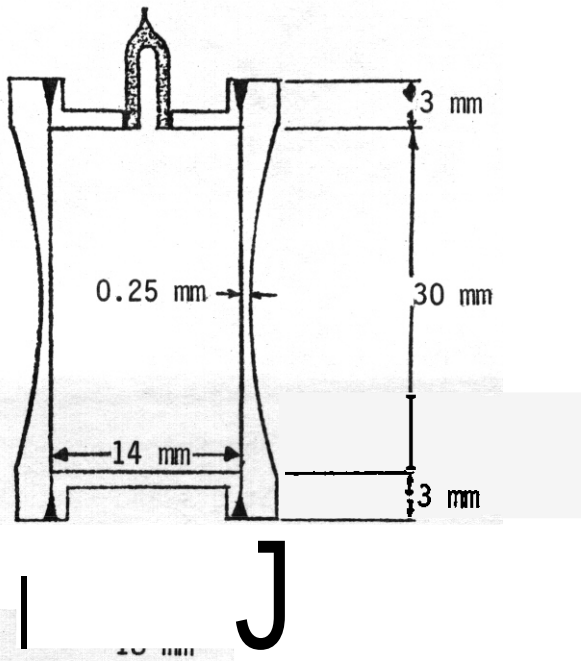

FIGURE 1. 316 SS Pressure Capsule.

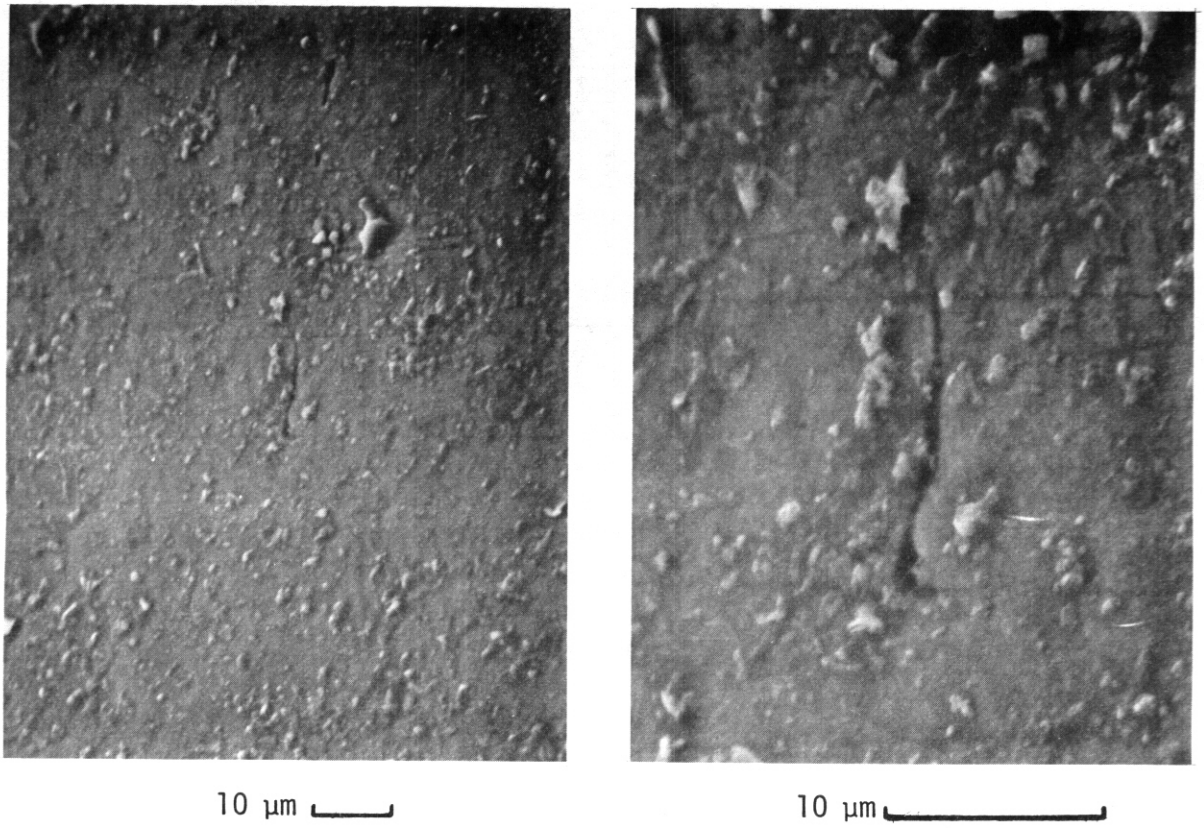

Figure 2. SEM Micrographs of SS316 Pressurized Tube Specimen - Neutron Irradiated, Ion Bombarded and Stress and Temperature Cycled.

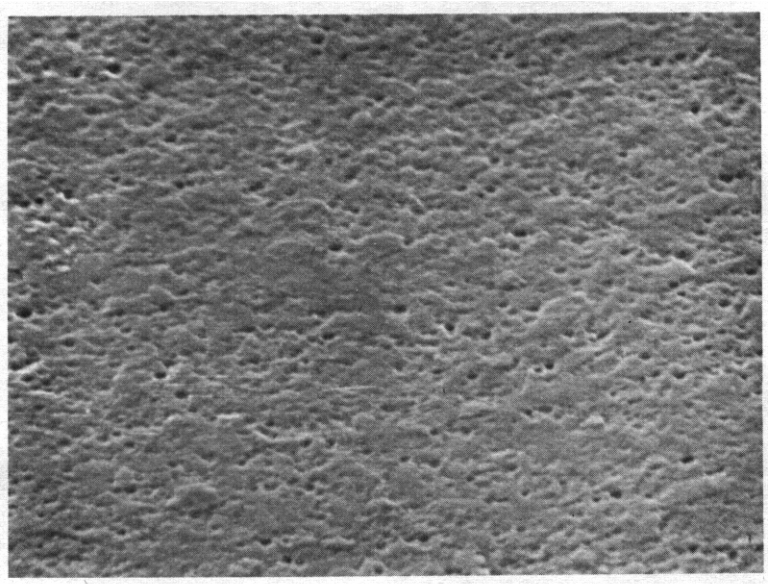

FIGURE 3. SEM Micrograph of Boron Vapor Deposited at 500°C on Titanium Substrate (Unirradiated).

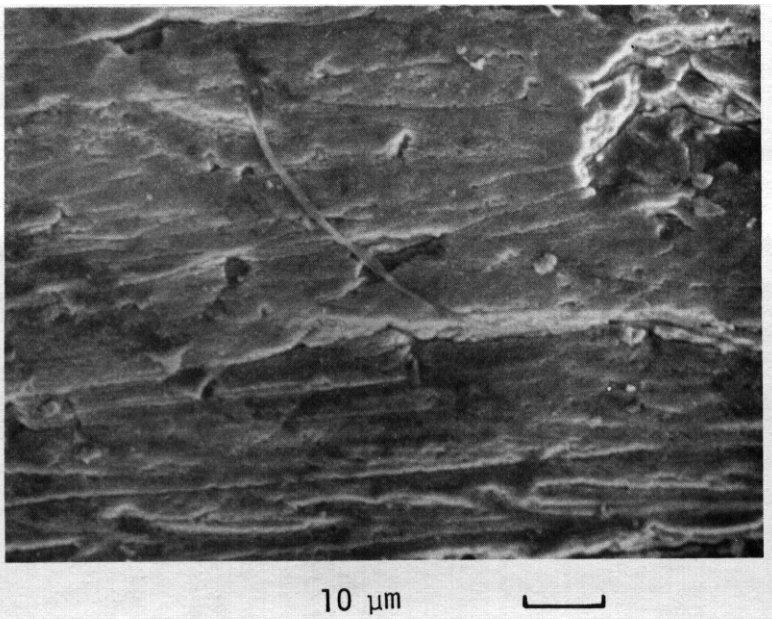

FIGURE 4. SEM Micrograph of 19.8% ^{10}B Vapor Deposited at 500°C on Titanium Substrate - Neutron Irradiated and Temperature Cycled.

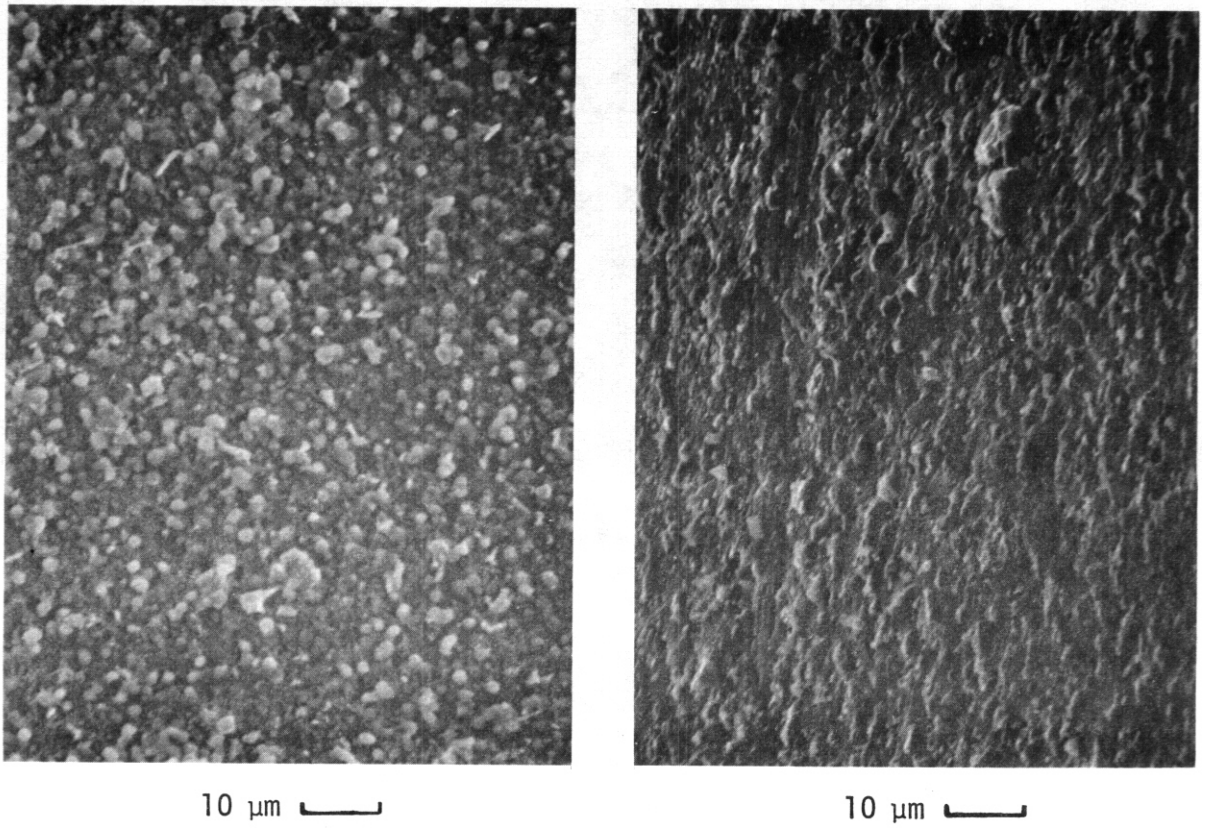

Figure 5: SEM Micrographs of 92% ^{10}B Vapor Deposited (at 500°C) on Titanium Substrate - Neutron Irradiated and Temperature Cycled.

I. PROGRAM

Title: Irradiation Effects Analysis (AKJ)
Principal Investigator: D. G. Ooran
Affiliation: Hanford Engineering Development Laboratory

II. OBJECTIVE

The objective of this work is to determine the effects of high energy neutrons on damage production and evolution, and the relationships of these effects to effects produced by fission reactor neutrons. Specific objectives of the current work are the planning and performance of irradiation programs using the Rotating Target Neutron Source (RTNS)-II at the Lawrence Livermore National Laboratory (LLNL) and the Omega West Reactor (OWR) at the Los Alamos National Laboratory (LANL).

III. RELEVANT OAFS PROGRAM PLAN TASK/SUBTASK

SUBTASK	II.B.3.2	Experimental Characterization of Primary Damage State; Studies of Metals
	II.C.6.3	Effects of Damage Rate and Cascade Structure on Microstructure; Low-Energy/High-Energy Neutron Correlations
	II.C.18.1	Relating Low- and High-Exposure Microstructures; Nucleation Experiments
	II.C.11.4	Effects of Cascades and Flux on Flow; High-Energy Neutron Irradiations

IV. SUMMARY

HEDL-IΩ, the first OAFS irradiation in the OWR thermal reactor facility at LANL, was completed on schedule. HEDL-VR, an ongoing irradiation experiment at the RTNS-II facility at LLNL, was reinitiated during this reporting period and is expected to attain a peak dose of 2.5 x 10^{18} n/cm^2, E∿14 MeV, during the next reporting period.

V. ACCOMPLISHMENTS AND STATUS

A. Status of OWR and RTNS-II Irradiation Programs - N. F. Panayotou (HEDL)

1. Introduction

HEDL-In was completed on schedule and is currently in transit to HEDL. The experiment was irradiated at 90°C and the expected dose is 2 x 10^{19} n/cm^2, E>0.1 MeV. The variation in dose within the specimen capsule is expected to be less than 10 percent. The experiment will be disassembled at HEDL. Dosimetry foils will be shipped to ANL for analysis. Post irradiation testing will be performed at HEDL. Another experiment will be assembled using, in part, specimens from HEDL-IΩ. A matrix for future OWR irradiations is being developed.

Afailedheater cable in the HEDL-VR experiment at RTNS-II was repaired during this reporting period and the irradiation of the experiment was re-initiated. The first goal dose level of 2.5 x 10^{19} n/cm^2, E∿14 MeV, will be attained during the next reporting period. At that time the experiment will be disassembled, new specimens loaded and the experiment reassembled, in preparation for continuation of the experiment to a peak dose level of 1 x 10^{19} n/cm^2, E∿14 MeV. The nominal irradiation temperaturesare 80 and 288°C for the HEDL-VR experiment.

VI. REFERENCES

None

VII. FUTURE WORK

Finalize matricies for the reconstitution of HEDL-In and HEDL-VR.

I. PROGRAM

Title: Irradiation Effects Analysis (AKJ)
Principal Investigator: D. G. Doran
Affiliation: Hanford Engineering Development Laboratory (HEDL)

II. OBJECTIVE

Determine the effect of pre-irradiation helium concentration and distribution on the microstructural development and material property changes in alloys of interest to the Fusion Energy Program.

III. RELEVANT DAFS PROGRAM PLAN TASK/SUBTASK

SUBTASK II.B.3.2 Experimental Characterization of Primary Damage State: Studies of Metals
II.C.1.2 Effects of Material Parameters on Microstructure: Modeling and Analysis
II.C.2.1 Effects of Helium on Microstructure: Mobility, Distribution and Bubble Nucleation.

IV. SUMMARY

Specimens of five alloys were irradiated in the ORR MFE-II test and sent to HEDL for distribution to other DAFS investigators or for examination. This experiment investigated the effect of helium concentration, initial helium distribution and material starting condition on the swelling and microstructural development in the materials. The specimens have been sorted, interested investigators have been notified and a selected number of specimens have been scheduled for immersion density, electron microscopy and microhardness measurements at HEDL.

V. ACCOMPLISHMENTS AND STATUS

A. ORR Irradiation of the MFE-II Experiment -- H. R. Brager and F. A. Garner (HEOL)

1. Irradiation Experiment

Specimens of five alloys in the form of TEM disks were irradiated in the ORR MFE-II experiment to a fluence of about 10 dpa in three capsules designed to operate at nominal temperatures of 350, 550 and 650°C. The alloys were Fe-17Cr-17Ni-2.5Mo ["pure 316", ORNL alloy P7] in the solution annealed (SA) and 20% cold worked condition, Fe-15Cr-20Ni (SA) [HEDL alloy E-191, V-20Ti (SA) [alloy HSV 3001, V-15Cr-5Ti (SA) [alloy HSL 3071, and Nb-1Zr (SA) [alloy 5301181. The specimens were prepared at ORNL and HEDL and then shipped to ANL for helium injection. Some of these specimens were aged prior to irradiation. This experiment was designed to investigate the effect of pre-irradiation helium concentration and distribution on the swelling and microstructural development.(1)

2. Post-Irradiation Activities

Table I summarizes the number of specimens irradiated in the ORR MFE-II experiment that have been identified; they are listed by alloy, treatment and irradiation condition. Note that in some instances none of the specimens of an alloy condition could be identified while in other cases there are more specimens than specified in reference 1.

Investigators located at ANL, BNL, HEDL and UCSB have expressed interest in the specimens and have been informed as to the availability of the material. Six different sets of Fe-17Cr-17Ni-2.5Mo specimens have been transferred to a HEOL hotcell where immersion density measurements will be performed on the TEM disks.

TABLE I

SUMMARY OF SPECIMENS IDENTIFIED AFTER IRRADIATION IN THE ORR MFE-II EXPERIMENT

Material	He Injection Level (appm)	Pre-Irrad. Heat Treatment Temp. (°C)	# specimens/ # specimens inserted sorted / into experiment		
			Irradiation Temperature (°C)		
			360°C	560°C	≤50°C
Fe-17Cr-17Ni-2.5Mo (SA)	0	-	4/4	4/4	2/4
	19-51	-	2/4	4/4	4/4
("Pure" 316)	25-45	-	0/4	3/4	4/4
	7-23	600	3/8		
[ORNL Alloy P7]	20-32	700	0/8		
	22-38	800	0/8		
	26-42	700		8/8	
	28-42	750		4/8	
	17-24	800		5/8	
	20-39	700			4/8
	22-37	800			4/8
	21-41	900			5/8
Fe-17Cr-17Ni-2.5Mo (CW)	0	-	2/4	3/4	1/4
	8-12	-	2/4	3/4	2/4
("Pure" 316)	29-34	-	3/4	3/4	4/4
Fe-15Cr-20Ni	0	-	0/4	0/4	1 or 2/4
	19-44	-	6/8		
[HEDL Alloy E-19]	24-55			3/8	
	27-50				3/8
	25-42	700	0/8		
	6-18	700		8/8	
	17-36	700			6/8

TABLE I (Cont'd)

SUMMARY OF SPECIMENS IDENTIFIED AFTER IRRADIATION IN THE ORR MFE-II EXPERIMENT

Material	He Injection Level (appm)	Pre-Irrad. Heat Treatment Temp. (°C)	# specimens sorted / *specimens inserted into experiment		
			Irradiation Temperature (°C)		
			450°C	550°C	650°C
V-20Ti (SA)	0	0	5/4	8/8	1/4
	8-12	-	6/4	7/8	3/4
[Alloy HSV 300]	20-40	-	7/4	7/8	3/4
	9-13	800	8/4	8/8	1/4
	23-45	800	3/4	9/8	3/4
V-15Cr-5Ti (SA)	0	-	3/4	3/4	1/4
	7-13	-	0/4	3/4	4/4
[Alloy HSC 307]	25-38	-	3/4	2/4	1/4
Nb-1Zr (SA)	0	-	7/4	6/4	4/4
	6-12	-	6/4	10/8	2/4
[Alloy 530118]	22-37	-	4/4	9/8	2/4

More effort should be expended on designing and implementing engraving identification codes in the future to minimize the number of identification engravings or markings of specimens and the effort required to identify the irradiated specimens. Some specimens had as many as nine markings on them.

VI. REFERENCES

1. G. R. Odette, R. W. Powell and F. V. Nolfi, "DAFS Experiment in the ORR MFE-II Test," DAFS Quarterly, Jan/-Mar.'79, DOE/ET-0065/5, p. 5.

VII. FUTURE WORK

Immersion density measurements will be performed on the selected Fe-17Cr-17Ni-2.5Mo specimens. Based on these data, transmission electron microscopy examination and hardness measurements will be performed. Specimens will be distributed to DAFS investigators who have indicated interest in the available specimens.

DISTRIBUTION

uc-20 (121)

UC-20c (77)

DOE/RRT-HQ (7)
Mail Stop B-107
Washington, DC 20545

Asst Director, Materials Tech
JF Clark, G-234
NA Davies
JF Decker
PB Hemmig
KG Moses
RE Price
FT Scott

DOE/RL (3)
Richland, WA 99352

HA House
GM Chenevert
LA Pasquini

Argonne National Laboratory (4)
9700 South Cass Avenue
Argonne, IL 60439

LR Greenwood
A. Taylor
APL Turner
H. Wiedersich

Brookhaven National Laboratory
Associated Universities
Upton, NY 11973

Chairman, Nuclear Energy Dept

Columbia University
Plasma Physics Laboratory
New York, NY 10027

RA Gross

General Atomics Company (3)
P.O. Box 81608
San Diego, CA 92138

GR Hopkins
JR Gilleland

INESCO
11011 Torreyana Rd
San Diego, CA 92121

RD Stevenson

Lawrence Livermore Laboratory (2)
P.O. Box 808
Livermore, CA 94550

MW Guinan
CM Logan

Los Alamos Scientific Laboratory (2)
P.O. Box 1663
Los Alamos, NM 87544

DJ Dudziak
CR Emigh

Massachusetts Institute of Technology (4)
77 Massachusetts Avenue
Cambridge, MA 02139

L. Lidsky
IW Chen
NJ Grant
DB Montgomery

McDonnell-Douglas Astronautics
P.O. Box 516
St. Louis, MO 63166

D. Kummer

Mound Laboratory
P.O. Box 32
Miamisburg, OH 45342

Manager, Tech Appl & Development

National Bureau of Standards
Gaithersburg, MD 20760

CD Bowman

DISTRIBUTION (Cont'd)

Naval Research Laboratory (2)
Metallurgy Division, Code 6390
Washington, OC 20375

I. Manning
JA Sprague

North Carolina State University
Department of Nuclear Engineering
Raleigh, NC 26707

JR Beeler, Jr.

Oak Ridge National Laboratory (8)
P.O. Box X
Oak Ridge, TN 37830

Director, Thermonuclear Div,
(Bldg 9201-2)
RJ Colchin, Bldg 9201-2
FG Perey
M. Roberts, Bldg 9204-1
J. Sheffield
JO Stiegler
C. Weisbin
FW Wiffen

Pacific Northwest Laboratory (4)
P.O. Box 999
Richland, WA 99352

JL Brimhall AB Johnson
T. Chikalla LC Schmid

Princeton University (3)
Plasma Physics Laboratory
Forrestal Campus
P.O. Box 451
Princeton, NJ 08540

C. Osgood
K. Wakefield
H. Furth

Rockwell International Energy Systems
8900 DeSoto Avenue
Canoga Park, CA 91304

D. Kramer

Sandia Laboratories (2)
Albuquerque, NM 87115

FL Vook

Sandia Laboratories
Livermore, CA 94550

WO Wilson

University of California
Los Angeles, CA 90024

RW Conn

University of Michigan
Nuclear Engineering Department
Ann Arbor, MI 48105

T. Kammash

University of Missouri
Dept of Mechanical and
Aerospace Engineering
1006 Engineering Bldg
Columbia, MO 65211

M. Jolles

University of Virginia
Charlottesville, VA 22901

WA Jesser

University of Wisconsin
1500 W. Johnson Drive
Madison, WI 53706

WG Wolfer

Westinghouse R&D Center (2)
Beulah Road
Pittsburgh, PA 15234

S. Wood
JA Spitznagel

DISTRIBUTION (Cont'd)

AERE-Harwell
Metallurgy Division
Building 388
Oxfordshire, OX11 ORA, UK

Dr. OR Harries

Commission for the European Communities
200, Rue de la Loi
B-1049 Brussels, Belgium

Dr. J. Darvas

ECN
Westerdionweg 3
NL-1755 ZG Petten, The Netherlands

Dr. B. Van Der Schaaf

EIR Swiss Federal Institute for Reactor Research
CH-5303 Wuerenlingen, Switzerland

Dr. WW Green

HMI - Berlin
Glienicherstrasse 100
0-1000 Berlin,
Federal Republic of Germany

Dr. H. Wollenberger

Japan Atomic Energy Research Institute
Physical Metallurgy Laboratory
Division of Nuclear Fuel Research
Fukoku Seimei Bldg
2-2, Uchisaiwai-cho 2-chome, Chiyoda-ki,
Tokyo 100, Japan

Dr. K. Shiraishi

KFA-IFF
Postfach 1913
0-517 Julich,
Federal Republic of Germany

Dr. H. Ullmaier

KFK-IMF II
Postfach 3640
0-7500 Karlsruhe 1,
Federal Republic of Germany

Dr. K. Ehrlich

Materials Science Division Joint Research Center
I-21020 Ispra, Varese, Italy

Dr. P. Schiller

National Research Council
Montreal Road
Ottawa, Canada

Dr. EV Kornelson

SCK/CEN
Boeretang 200
B-2400 Mol, Belgium

Dr. J. Nihoul

DISTRIBUTION (Cont'd)

HEDL (39)

HR Brager	W/A-64	EK Opperman	W/A-58
WL Bunch	W/C-47	NF Panayotou	W/A-65
LL Carter	W/C-47	EF Parker	W/E-17
DG Doran (5)	W/A-57	RW Powell	W/A-64
EA Evans	W/C-23	RJ Puigh	W/A-58
FA Garner	W/A-57	FH Ruddy	W/C-39
DS Gelles	W/A-64	FA Schmittroth	W/A-4
R. Gold	W/C-39	WF Sheely	W/C-62
HL Heinisch	W/A-57	RL Simons	W/A-57
DL Johnson	W/A-4	AL Trego	W/E-15
GD Johnson	W/A-65	GL Wire	W/A-58
NE Kenny	W/C-115	HH Yoshikawa	W/A-44
FM Mann	W/A-4	Central Files (5)	W/C-110
WN McElroy	W/C-39	Publ Services (2)	W/C-115
RE Nygren	W/A-58	Doc Management	W/C-125

'GPO 798-426 1981